UNIVERSITY OF CALIFORNIA
SANTA CRUZ

SOLVOTHERMAL METHODS FOR THE SYNTHESIS OF STRUCTURALLY DIVERSE EXTENDED MATERIALS

A dissertation submitted in partial satisfaction
of the requirements for the degree of

DOCTOR OF PHILOSOPHY

in

CHEMISTRY

by

Beatriz Ehlke Santi Grott

September 2023

The Dissertation of Beatriz Ehlke Santi Grott is approved by:

_____
Professor Scott Oliver

_____
Professor Yat Li

_____
Professor Jin Zhang

_____
Peter Biehl
Vice Provost and Dean of Graduate Studies

Table of Contents

List of Figures ..... **vi**
List of Tables ..... **xvi**
Abstract ..... **xviii**
Dedication ..... **xxi**
Acknowledgments ..... **xxii**

Chapter 1 - Introduction to the ionothermal synthesis of metal-doped aluminophosphates

Abstract **1**

1.1 Zeotype materials **2**
1.1.1 Zeolites 2
1.1.2 Aluminophosphates 6
1.1.3 Metal-doped aluminophosphates for catalytic applications 10

1.2 Synthesis of MAPOs **13**
1.2.1 Solvothermal methods 13
1.2.2 Mineralizer and the role of pH 19
1.2.3 The OSDA and the solvent competition 21
1.2.4 Ionothermal synthesis 24

1.3 Ionothermically synthesized MAPOs **26**
1.3.1 MgAPO 29
1.3.2 MnAPO 32
1.3.3 FeAPO 35
1.3.4 CoAPO 38
1.3.5 NiAPO 41
1.3.6 CuAPO 42
1.3.7 ZnAPO 43

1.4 Summary and Outcome **45**

1.5 References **47**

Chapter 2 - MAPO-5 Molecular Sieves from Alkylimidazolium Bromide Ionic Liquids

Abstract **72**

2.1 Introduction **73**

2.2 Experimental **76**
2.2.1 Reagents 76
2.2.2 MAPO-5 synthesis 77
2.2.3 Ionic liquid re-purification 78
2.2.4 Instrumentation 78

2.3 Results and Discussion 80
2.3.1 Water Studies 80
2.3.2 HF Studies 88
2.3.3 Modeling Data 94
2.3.4 TGA Analysis 97
2.3.5 In-depth Characterization of Mn-AFI 100
2.4 Conclusions and Future Directions 108
2.5 References 109

Chapter 3 - A flexible silver and bipyridine coordination polymer for the high-capacity trapping of perrhenate, a pertechnetate surrogate

Abstract 114
3.1 Introduction 115
3.2 Experimental 120
3.2.1 Materials 120
3.2.2 Synthesis of [Ag(2,4'-bipy)]NO_3 (SLUG-53) 120
3.2.3 Synthesis of [Ag(2,4'-bipy)]ReO_4 (SLUG-54) 121
3.2.4 Perrhenate uptake quantification 121
3.2.5 Selectivity studies 122
3.2.6 Instrumentation 123
3.3 Results and Discussion 128
3.3.1 Structural Description of SLUG-53 129
3.3.3 Anion Exchange with ReO_4^- 136
3.3.4 Structural description of SLUG-54 137
3.3.5 ReO_4^- Exchange Quantification 139
3.3.6 Thermostability analysis 146
3.4 Conclusions and Future Directions 149
3.5 References 150

Chapter 4 - A Crystal Structure of a Rippled Antiparallel Pauling-Corey Cross-β Dimer

Abstract 166
4.1 Introduction 167
4.2 Experimental 171
4.2.1 Peptide Synthesis 171
4.2.2 Crystallization 172
4.2.3 Single-Crystal X-ray Diffraction 173
4.2.4 Computational Chemistry 174
4.2.5 CSD Search 174
4.2.6 PDB Structural Database Mining 175
4.2.7 Considerations Regarding Nomenclature 175

4.3 Results and Discussion 176
4.3.1 Choice of system 176
4.3.2 The FFF:fff dimer structure 177
4.3.3 Crystal lattice analysis 182
4.3.4 Discussion 187
4.4 Conclusions and Future Directions 194
4.5 References 196

Chapter 5 – Summary and Future Directions

5.1 Summary 208
5.2 Metal-doped Aluminophosphates Project 208
5.3 Coordination Polymers Project 210
5.4 Pauling-Corey Rippled β-dimers Project 212
5.5 References 214

Appendix 217

List of Figures

Figure 1.1 Scheme showing the tiling built of pure silica zeolite STI. (a) All individual tiles presented in the STI framework and their [$M^m.N^n$…] identification; **(b)** Tile arrangement in the STI structure; **(c)** STI framework. Each vertex represents a SI atom. The b bridging oxygens are omitted for clarity. Adapted from the IZA database. 5

Figure 1.2 Structure schematics of AlPO4-5. **(a)** View along [100] detailing the 4-, 6- and 12- membered rings; **(b)** View normal to [001] showing the channel formed by the 12-membered rings; **(c)** Tiling construction of the framework; **(d)** Tile arrangement. Adapted from the IZA database. 8

Figure 1.3 Comparison between aluminosilicate zeolites and aluminophosphate tetrahedral building blocks and the overall charge of the respective frameworks. 9

Figure 1.4 Origin of the Brønsted acidity in MAPOs. 10

Figure 1.5 Scheme representing an MTO reaction over SAPO-34 catalyst.. 12

Figure 1.6 Methanol to Olefin (MTO) reactions. 13

Figure 1.7 Autogenic pressure generated in a hydrothermal system as a function of the temperature and the filling parameter. 14

Figure 1.8 Physicochemical properties of water under subcritical conditions present in hydrothermal methods. Left: density as a function of temperature

and pressure; right: dieletric constant as a function of temperature and pressure. 15

Figure 1.9 Free Gibbs energy (ΔG) diagram for the nucleation process in terms of nucleus radius (r). ΔGv = cohesive energy; ΔGs = surface energy; ΔGc = critical energy; r_c = critical radius. 18

Figure 1.10 Common IL cations. $[Emin]^+$ = 1-ethyl-3-methylimidazolium; $[Bmin]^+$ = 1-butyl-3-methylimidazolium; $[C_npyr]^+$ = 1-alkylpyridimium; $[C_4N]^+$ = tetraalkylammonium. 25

Figure 1.11 Structure of the ionic liquids' cations used by Benin et al. to investigate the influence of the OSDA's shape and size in the obtainment of MAPOs. All ILs had bromide as the anion. IL-A: 1-ethyl-2,3,4,5-tetramethylimidazolium, IL-B: 1,3-diethylimidazolium; IL-C: 1-isopropyl-3-ethylimidazolium; IL-D: 1,3-diisopropylimidazolium; IL-E: 1-isobutyl-3-isopropylimidazolium; IL-F: 1,3-diisobutylimidazolium; IL-G: 1,3-dicyclohexyllimidazolium. 32

Figure 1.12 Detail on the ordered arrangement of four $[DIPI]^+$ units inside the large cavity DFO ZnAPO described by Pinar et al. 44

Figure 2.1 PXRD comparison of Ni-AFI syntheses (blue upper patterns) and AFI syntheses (i.e. metal-free syntheses, black lower patterns) with DIPI as SDA: **(a)** 0.38 eq. Ni, 3.04 eq. water; **(b)** 0.25 eq. Ni, 2.51 eq. water; **(c)** 0.13 eq. Ni, 2.02 eq. water; tridymite and cristobalite peaks are denoted with asterisks and open circles, respectively. 81

Figure 2.2 PXRD comparison of Ni-AFI syntheses (green upper patterns) and AFI syntheses (black lower patterns) with DIBU as SDA: **(a)** 0.38 eq. Ni, 3.06 eq. water; **(b)** 0.25 eq. Ni, 2.57 eq. water; **(c)** 0.13 eq. Ni, 2.08 eq. water; cristobalite peaks are denoted with open circles. 82

Figure 2.3 ^{1}H-NMR spectra. Top: purified Ni-DIPI; bottom: as-made DIPI. .. 84

Figure 2.4 Corresponding PXRDs for Ni experiments using Ni-DIPI. All ratios can be found in Table 2.2. 85

Figure 2.5 PXRD comparison of Mn-AFI syntheses (blue upper patterns) and AFI syntheses (black lower patterns) with DIPI as SDA: **(a)** 0.39 eq. Mn, 3.06 eq. water; **(b)** 0.25 eq. Mn, 2.66 eq. water; **(c)** 0.13 eq. Mn, 2.00 eq. water; tridymite and cristobalite peaks are denoted with asterisks and open circles, respectively. tridymite peaks are denoted with asterisks. 87

Figure 2.6 PXRD comparison of Mn-AFI syntheses (green upper patterns) and AFI syntheses (black lower patterns) with DIBU as SDA: **(a)** 0.38 eq. Mn, 3.02 eq. water; **(b)** 0.25 eq. Mn, 2.74 eq. water; **(c)** 0.13 eq. Mn, 2.05 eq. water; cristobalite peaks are denoted with open circles. 87

Figure 2.7 PXRD comparison of Ni-AFI syntheses with varying HF equivalency and DIPI as SDA: **(a)** 0.60 HF eq.; **(b)** 0.48 HF eq.; **(c)** 0.36 HF eq.; **(d)** 0.24 HF eq.; **(e)** 0.12 HF eq.; **(f)** 0.00 HF eq.; all contained 2.14 water and 0.12 Ni equivalencies. 89

Figure 2.8 PXRD comparison of Ni-AFI syntheses with varying HF equivalency and DIBU as SDA: **(a)** 0.60 HF eq.; **(b)** 0.48 HF eq.; **(c)** 0.36 HF eq.; **(d)** 0.24

HF eq.; **(e)** 0.12 HF eq.; **(f)** 0.00 HF eq.; all contained 2.18 water and 0.12 Ni equivalencies. 89

Figure 2.9 PXRD comparison of Mn-AFI syntheses with varying HF equivalency and DIPI as SDA: (a) 0.60 HF eq.; (b) 0.48 HF eq.; (c) 0.36 HF eq.; (d) 0.24 HF eq.; (e) 0.12 HF eq.; (f) 0.00 HF eq.; all contained 2.2 water and 0.11 Mn equivalencies. 90

Figure 2.10 PXRD comparison of Mn-AFI syntheses with varying HF equivalency and DIBU as SDA: **(a)** 0.60 HF eq.; **(b)** 0.48 HF eq.; **(c)** 0.36 HF eq.; **(d)** 0.24 HF eq.; **(e)** 0.12 HF eq.; **(f)** 0.00 HF eq.; all contained 2.2 water and 0.11 Mn equivalencies. 91

Figure 2.11 PXRD comparison of the transition metal-free syntheses with varying HF equivalency and DIPI as SDA: **(a)** 0.60 HF eq.; **(b)** 0.48 HF eq.; **(c)** 0.36 HF eq.; **(d)** 0.24 HF eq.; **(e)** 0.12 HF eq.; **(f)** 0.00 HF eq.; all contained 2.2 water equivalencies. 92

Figure 2.12 PXRD comparison of the transition metal-free syntheses with varying HF equivalency and DIBU as SDA: **(a)** 0.60 HF eq.; **(b)** 0.48 HF eq.; **(c)** 0.36 HF eq.; **(d)** 0.24 HF eq.; **(e)** 0.12 HF eq.; **(f)** 0.00 HF eq.; all contained 2.2 water equivalencies; tridymite and cristobalite peaks are denoted with asterisks and open circles, respectively. 92

Figure 2.13 Modeling data with DIBU displaying the most favorable SDA interaction energy within the AFI framework. 95

Figure 2.14 TGA traces (solid lines; first derivatives are shown as dashed lines) for **(a)** DIBU and **(b)** DIPI. AFI is shown as blue lines and Mn-AFI is shown as black lines. Blue bars highlight the water loss region, yellow-orange bars highlight mass losses for AFI and brown bars highlight mass losses for Mn-AFI. 98

Figure 2.15 TGA of amorphous materials using DIPI SDA. Top: 0.25 eq. Mn, 2.66 eq. water; bottom: 0.39 eq. Mn, 3.06 eq. water. The % mass loss of the two materials from 160 to 600 °C were identical, indicating that the same amount of SDA existed in both materials. 99

Figure 2.16 EPR spectra at varying temperature. Left: RT; right: 121 °C. .. 100

Figure 2.17 ^{31}P MAS-NMR of Mn-AFI versus AFI, both made with DIBU SDA. 102

Figure 2.18 ^{55}Mn MAS-NMR of Mn-AFI made with DIBU SDA, before and after calcination. 103

Figure 2.19 ^{31}P MAS-NMR (left) and ^{27}Al MAS-NMR (right) of Mn-AFI (red) versus AFI (blue), both made with DIBU SDA. 105

Figure 2.20 ^{13}C CP-MAS-NMR of Mn-AFI (top, red) versus AFI (bottom, blue) synthesized with DIBU SDA. 106

Figure 2.21 EXAFS analysis was measured at room temperature and 373K, confirming Mn is present in the sample. 107

Figure 3.1 Coordination polymers based on 4,4'-bipyridine showing different dimensionalities: **(a)** 1D [Ni(L-Tyr)$_2$(4,4'-bipy)]·4H$_2$O; **(b)** 2D [Cu(4,4'-

bipy)$_2$(BF_4)$_2$]; **(c)** 3D [Cu(GeF_6)(4,4'-bipy)$_2$]·8H_2O. Hydrogen atoms omitted for clarity; color scheme: C – black; N – blue; O – red; Ni – light green; Cu – orange; F – magenta; B – yellow; Ge – dark green. 116

Figure 3.2 Common topologies adopted by 1D coordination polymers based on N-donor ligands. 117

Figure 3.3 Optical microscopy images depicting the morphology of crystals of **(a)** SLUG-53 and **(b)** SLUG-54. 127

Figure 3.4 Single crystal structure of SLUG-55. Although major disorders are observed in the extra-framework moieties, it is possible to conclude that a molecular structure was obtained. Hydrogen atoms omitted for clarity; color scheme: Ag – gray; N – blue; O – red; C – black. 128

Figure 3.5 PXRD patterns of reaction products using different molar ratios of AgNO3 to 2,4'-bipyridine: **(a)** Reference SLUG-53 phase obtained from the same sample solved by SCXRD; **(b)** Reference molecular structure obtained from the same sample solved by SCXRD; **(c)** 1:1 molar ratio, molecular phase; **(d)** 1.5:1 molar ratio, SLUG-53; **(e)** 2:1 molar ratio, SLUG-53; **(f)** 2.5:1 molar ratio, SLUG-53; **(g)** 3:1 molar ratio, SLUG-53; **(h)** 4:1 molar ratio, SLUG-53. 129

Figure 3.6 Crystal structure of SLUG-53 obtained by SCXRD at 100 K: **(a)** Projection along the b-axis, showing one polymeric zigzag chain formed by alternating Ag and 2,4'-bipy units. Nitrate anions reside in the pockets of the chain; **(b)** View parallel to the crystallographic (102) plane, showing the

stacking of zigzag chains through both argentophilic interactions (solid gray lines) and π-stacking (dashed green lines); **(c)** In the projection along the *c*-axis, the layers described in (*b*) interact with each other through additional π-stacking, here showed by dashed purple lines. Hydrogen atoms omitted for clarity; color scheme: Ag – gray; N – blue; O – red; C – black. 132

Figure 3.7 Powder X-ray diffractograms for SLUG-53. **(a)** experimental obtained at 287 K; **(b)** Calculated from SCXRD data collected at 287 K **(c)** Calculated from SCXRD data collected at 100 K. All calculated diffractograms were obtained using CSD Mercury. 134

Figure 3.8 PXRD comparison between **(a)** the starting material SLUG-53, and **(b)** the exchange product SLUG-54. 137

Figure 3.9 Crystal structure of SLUG-54 obtained by SCXRD at 100 K. Zigzag chains similar to SLUG-53 are again observed. However, the counter-anion now has a fundamental role in extending the structure through the formation of eight-membered rings containing silver atoms (emphasized as a blue rectangle). Color scheme: Ag – gray; N - blue; O - red; Re- light blue. All hydrogens are omitted for clarity. 139

Figure 3.10 UV-Vis analysis of the conversion reaction between SLUG-53 and SLUG-54 over time shows an increase in the nitrate peak (λ = 204 nm) as the reaction proceeds, indicating nitrate ions are being released in the anion exchange reaction. 140

Figure 3.11 Percentage of perrhenate removed by SLUG-53 as a function of time (inset: data fitting to pseudo-second-order model). 141

Figure 3.12 Adsorption capacity of SLUG-53 as a function of equilibrium concentration (inset: data fitting to Langmuir model). 143

Figure 3.13 Selectivity of SLUG-53 for the adsorption of perrhenate in the presence of sulfate (green – no sulfate; red – 50x molar excess sulfate; blue – 200x molar excess sulfate) at varying exchange time. 146

Figure 3.14 TGA analyses: solid blue - SLUG-53; dashed blue - 1st derivative of SLUG-53 trace; solid orange – SLUG-54; dashed orange – 1st derivative of SLUG-54 trace. 147

Figure 3.15 Ex situ VT-PXRD of SLUG-53. #: silver metal, COD ID: 901296. 148

Figure 3.16 Ex situ VT-PXRD of SLUG-54. #: silver metal, COD ID: 9012961.*: silver perrhenate, COD ID: 2008824. 148

Figure 4.1 Left panel: Antiparallel pleated sheet in different projections. Right panel: Antiparallel rippled sheet in different projections. A selected number of amino acid side chains are depicted as blue spheres on the left panel (pleated, along red vertical line) and on the right (rippled, along red diagonal), to reduce steric repulsion in each case. 169

Figure 4.2 Molecular graph of FFF with 50% thermal ellipsoids and H atoms shown as spheres of arbitrary radius. Color code: O red, N blue, C grey, H white. 180

Figure 4.3 Ball-and-stick depiction of the experimental rippled antiparallel FFF:fff cross-β dimer, shown in three orthogonal projections. The Pauling-Corey rippled antiparallel backbone dimer is shown in the inset, with apical carbon atoms added geometrically to facilitate comparison; (color code: C, gray; O, red; N, blue)..... 181

Figure 4.4 Top: Side and top views of the rippled antiparallel sheet structure predicted by Pauling and Corey [cf. Figure 1 from PNAS 1953, 39, 253]. Bottom: Side and top views of the rippled sheet structure formed by FFF:fff. Atoms of the polypeptide backbone are shown as ellipsoids (non-H) or spheres of arbitrary radius (H). Side-chain atoms are shown as sticks. Color code: O red, N blue, C grey, H white. Hydrogen bonds are shown as dashed lines. Boxed in green is the similar motif from the predicted (top) and experimentally observed (bottom) structure. 182

Figure 4.5 The rippled antiparallel FFF:fff cross-β dimer shown in contact with its direct neighbors. 183

Figure 4.6 Long-range packing of the FFF:fff lattice, shown in three orthogonal projections. The layer-to-layer distance is indicated in blue. 184

Figure 4.7 Packing diagram of FFF:fff highlighting that the layer-to-layer distance is the crystallographic lattice parameter a = 11.3563(5) Å. 185

Figure 4.8 A top-on view of a single layer containing the peptidic backbones. Individual rippled antiparallel FFF:fff cross-β dimers are centered about the unit

cell corners and center. L-peptides are shown in purple, and D-peptides are shown in blue. 186

Figure 4.9 Overlay of the crystallographic (orange) and the optimized (green; BP86-D3BJ/def2-SVP-CPCMwater) structure of the FFF:fff dimer. The polypeptide backbone is shown as thick sticks and the sidechains as thin sticks. 187

Figure 4.10 Detail of the antiparallel rippled motifs in the proteins selected by the PDB structural database mining. (**a)** glu-lys-glu-leu-val sequence in RV1738. **(b)** phe-phe-tyr sequence in ester insulin. **(c)** lys-gly-phe-arg sequence in Kaliotoxin. PDB codes PDB codes are displayed on the bottom right. 188

Figure 4.11 Ramachandran angle analysis for the rippled sheets noted with **(a)** the FFF:fff system; **(b)** racemic Ester Insulin (4IUZ); **(c)** racemic RV1738 (4WPY); D) racemic Kaliotoxin (3ODV). 190

Figure 4.12 Selected examples from Eisenberg and coworkers, of fibrils formed by aggregating enantiopure peptides in which pleated β-sheets display one-dimensional, long-range order. Color code: C, gray; O, red; N, blue. Water molecules and hydrogens are omitted for clarity. PDB codes are displayed on the bottom right of each structure. 191

Figure 5.1 Scheme of a methanol conversion reactor to be used for testing MnAPO-5 as a catalyst in MTO reactions. 210

List of Tables

Table 1.1 Summary of the ionothermal procedures described in the literature for the obtainment of MAPO materials 26

Table 2.1 Nickel versus water studies for DIPI and DIBU SDAs 82

Table 2.2 Summary of structure results with varying amount of Ni contributed by the Ni-DIPI versus $Ni(OAc)_2$ 85

Table 2.3 Manganese versus water studies for DIPI and DIBU SDAs 88

Table 2.4 HF studies for nickel systems 90

Table 2.5 HF studies for manganese systems. 91

Table 2.6 HF studies for no-metal systems 93

Table 2.7 MAPO compounds studied and NMR measurements 104

Table 2.8 Results of the EXAFS analysis. N: coordination number; R: distance between absorber and backscattering atoms; σ^2: Debye-Waller factor to account for thermal and structural disorders. Error bounds (accuracies) that characterize the structural parameters were estimated as R ± 0.01; σ^2 ± 0.0008; ΔE ± 0.8. S_0 was fixed at 0.64 as determined from Mn_2O_3 fitting (fitting range: 2.0 ≤ k(/Å) ≤ 10 and 1.0 ≤ R(Å) ≤ 2.0) 107

Table 3.1 Crystallographic parameters for SLUG-53 collected at 100 K and 287 K, and SLUG-54 collected at 100 K. 126

Table 3.2 Comparison of crystallographic parameters for the novel SLUG-53 and its previously reported polymorph 133

Table 3.3 Comparison of structural parameters between RT and 100 K SCXRD 135

Table 3.4 Perrhenate uptake quantification results for SLUG-53 141

Table 3.5 Kinetic parameters were obtained by fitting the adsorption data to a pseudo-second-order model. 142

Table 3.6 Adsorption parameters obtained by fitting the adsorption data to the Langmuir model 143

Table 3.7 ReO_4^-/TcO_4^- adsorption capacity of selected CPs/MOFs, polymeric and molecular materials (CPN = cationic polymeric network; iPOP = ionic porous organic polymers; MOC = metal-organic cage) in descending order 144

Table 3.8 Selectivity of SLUG-53 for the adsorption of perrhenate in the presence of sulfate 145

Table 4.1 of FFF.fff dimers 179

Table 4.2 Cartesian coordinates (Å) of the optimized (BP86-D3BJ/def2-SVP-$CPCM_{water}$) structure of FFF:fff. 217

Table A.1 Cartesian coordinates (Å) of the optimized (BP86-D3BJ/def2-SVP-$CPCM_{water}$) structure of FFF:fff.. 217

Table A.2 Chapter 2 synthetic details. 217

Table A.3 Chapter 3 synthetic details. 217

Abstract

Solvothermal Methods for the Synthesis of Structurally Diverse Extended Materials

by

Beatriz Ehlke Santi Grott

This dissertation will present three different variations of solvothermal methods for the obtainment of distinct classes of extended materials: the ionothermal synthesis of metal-doped nanoporous aluminophosphates, the hydrothermal synthesis of cationic coordination polymers, and the solvothermal synthesis for the crystallization of racemic polypeptide mixtures.

Chapter 1 introduces the field of metal-doped nanoporous aluminophosphates, a class of zeolitic material commonly used as catalysts in the petrochemical industry. The history that led to the development of these materials, their unique chemistry, and their synthetic details are discussed. Ionothermal synthesis is presented as an alternative to the usual hydrothermal method, and its concepts and advantages are detailed. The last section of this chapter is a literature review presenting – to the best of our knowledge – all the current reports of MAPOs synthesized via the ionothermal route.

Chapter 2 explores the ionothermal synthesis of $AlPO_4$-5 molecular sieves and the doping of its inorganic framework with Mn^{2+} or Ni^{2+}. The ionic liquids diisopropylimidazolium bromide (DIPI) and diisobutylimidazolium bromide (DIBU) were used as both the solvents and structure-directing agents, and HF was used as the mineralizer. Varying amounts of water, metal, and HF in the medium led to either AFI, cristobalite, or tridymite framework structures. The product's phase(s) were determined by powder X-ray diffraction (PXRD). Further structural insights were obtained by studying the coordination of Al^{3+}, P^{5+}, and F^- by solid-state nuclear magnetic resonance (SS-NMR) spectroscopy. Electron paragenetic resonance (EPR) spectroscopy and X-ray absorption spectroscopy (XAS) were used to investigate the metal incorporation in the framework. $AlPO_4$-5 and MnAPO-5 phases were isolated. Although there was no evidence of NiAPO-5 formation, the presence of Ni^{2+} in the reaction medium affected the phase selectivity. Lastly, the thermal stability of the products was determined by thermogravimetric analysis (TGA).

Chapter 3 describes the hydrothermal synthesis and single-crystal structure of the novel phase SLUG-53 [Ag(2,4'-bypiridine)NO_3]. Close examination of PXRD and single-crystal X-ray diffraction (SCXRD) data reveals the material behaves as a soft-porous crystal, as temperature perturbations led to anisotropic distortions of the unit cell. SLUG-53 undergoes an anion exchange reaction, where the nitrate ions are replaced by perrhenate, a surrogate for the radioactive and hazardous ion pertechnetate. The structure

of the resulting material, the novel SLUG-54 ([Ag(2,4'-bypiridine)ReO_4]), was also elucidated by SCXRD and revealed that an 8-membered inorganic ring is formed between perrhenate ions and two adjacent chains of polymeric Ag-2,4'-bipyridine. Kinetics studies showed that the exchange reaction follows a pseudo-second-order mechanism. The data was fitted to the Langmuir model to reveal that SLUG-53 shows a superior adsorption capacity of 764 mg ReO_4/g SLUG-53.

Chapter 4 presents the first high-resolution crystal structure study on the rippled β-sheet formation predicted in 1953 by Pauling and Corey to occur in racemic polypeptide mixtures. While other predictions of these scientists have now become textbook knowledge, such as the pleated β-sheet, the then theorized rippled arrangement was yet to be deeply investigated. The study presented here describes the solvothermal obtainment of [FFF.fff], where L,L,L-tripenhylalanine and D,D,D-triphenylalanine polypeptides strands were found to form dimers in an antiparallel rippled configuration for the first time. Such dimeric units are then further arranged in a herringbone fashion. Ramachandran angles were investigated for [FFF.fff] and three other racemic proteins presenting rippled motifs, which were selected after extensive database mining.

Chapter 5 presents a summary and describes future lines of investigation for each of the three projects discussed in this dissertation.

Dedication

To my Family

my mother Joeci

my brother Claudio

and my nephews Pipe and Cacá

Acknowledgments

To Dr. Scott R. J. Oliver, my most sincere gratitude. This thesis would not have been possible without your guidance, knowledge, and advice. Thank you for all the opportunities you have given me throughout my academic career and for all the support when I most needed it.

Thank you to my thesis committee, Dr. Yat Li and Dr Jin Zhang, for all the mentoring throughout every milestone of the graduate program.

To Dr. Stacey Zone, Dr. Tim Johnstone, Dr. Jevgenij Raskatov, Dr. Singaram Bakhtan, and Dr. Allen Oliver, thank you for all the mentoring and for allowing me to explore so many exciting fields of chemistry.

To my fellow Oliver Lab members Jerah, Kevin, Eaindar, Ana, Susan, Jesse and Ian. Thank you for all the training, companionship, and friendship. To my undergraduate students Cam, Tyler, Cherry, Jen, and Liber. This dissertation would not have been possible without your help, curiosity, and hard work.

To Eric Reinheimer, Dan Xie, Son-Jong Hwang, Andrew Ichimura, Xi Shibo, Brian Dreyer, and Daniel Droege, thank you for the aid with data collection and refinement.

I owe many thanks to my fellow graduate students at UCSC. To Ray, Melissa, Fran, Scott, Ariel, Anna, Eda, Danai, and Jake, thank you for inspiring

me to work hard week after week and for being there during graduate school's most challenging periods.

To all my family, especially my mother Joeci, my brother Claudio, and my sister-in-law Roberta for the unconditional love and support.

To my friends Josué, Juliana, Mariana Marçal, Mariana Limas, and Mariana Dias, for always being there for me, no matter how far we are. To Roberta, Lucas, Vini, Gen, Nil, Ankit, Ivo, Morteza, Abhi, and Keshav, thank you for making Santa Cruz my home away from home.

The text of this dissertation includes reprints of the following previously published material: Ehlke, B.*; Kuhn, A. J.*; Johnstone, T. C.; Oliver, S. R. J.; Raskatov, J. A. A Crystal-Structural Study of Pauling-Corey Rippled Sheet. *Chem. Sci.*, **2022**, *13*, 671-680. The co-authors listed in this publication directed and supervised the research which forms the basis for part of this dissertation.

Chapter 1 - Introduction to the ionothermal synthesis of metal-doped aluminophosphates

Abstract

Aluminophosphates (AlPOs) are a class of zeotype materials where phosphorus atoms replace the silicon in the aluminosilicate framework of zeolites. The further isomorphic substitution of Al^{3+} centers by M^{2+} metals leads to metal-doped aluminophosphates (MAPOs). Due to charge considerations, MAPOs present Brønsted acid sites, which can be tuned by the degree of M^{2+} doping. This tunable acidity, combined with their structural and porous versatility, makes MAPOs promising candidates as catalysts for a wide range of reactions, especially in the petrochemistry industry.

The synthesis of MAPOs (and zeolitic materials in general) is a complex process, with many moving pieces challenging synthetic control. The chemical source of the reagents used, pH, temperature, reaction time, mineralizer, structure-directing agent (SDA), solvent, and the molar ratio between all the reagents significantly impact the synthesis outcome. A particular issue is the competition that may arise between SDAs and the solvents, which can hinder formation of the framework target at the outset of the synthesis.

Much progress has been made in developing procedures to overcome the SDA/solvent competition in recent years. One of the most promising

strategies is ionothermal synthesis, a solvothermal method variation where an ionic liquid (IL) is used as the solvent. The bulky organic cations present in the majority of ILs show structure-directing properties. Therefore, ILs serve as solvents *and* organic structure-directing agents (OSDAs), eliminating the competition described above. Furthermore, ILs are also easily purified and reusable, possess inherent low vapor pressure and viscosity, and are greener alternatives to volatile or toxic traditional organic solvents. All these characteristics make ILs of great interest for industrial applications, as they allow a cheaper, greener, and safer synthesis.

This chapter introduces the structural features that make MAPOs unique materials for industrial catalytic applications. A detailed description of solvothermal synthesis is presented, including its variations (hydrothermal and ionothermal). The last section of this introduction discusses – to the best of our knowledge – all the current literature reports of MAPOs synthesized via the ionothermal route.

1.1 Zeotype materials

1.1.1 Zeolites

In 1753, the Swedish mineralogist Axel F. Cronstedt described the unique behavior of an unknown mineral that would show frothing when submitted to a flame. In his publication, Cronstedt named the material, now believed to be stilbite (STI), *zeolite*.[1,2] More than 250 years later and zeolites

are now used in several industrial applications. As of 2022, this market is valued at US 4.28 billion, and it is expected to be at US 5.71 billion by 2029.[3]

Zeolites are crystalline porous materials composed of tetrahedral TO_4 units, where oxygens bridge the adjacent T atoms. Although many compositional variations will be described in this chapter, zeolites were originally regarded as pure silicates or aluminosilicates. Their chemical structure is described as $A_{x/n}[Si_{1-x}Al_xO_2]\cdot mH_2O$ (where *A* is a metal with charge *n*). [4,5] The tetrahedral building blocks can be arranged in different ways, creating frameworks with diverse dimensionality and porous structure that may contain features such as cages, cavities, channels, and windows. The versatility of TO_4 building blocks leads to several unique frameworks. To date, the International Zeolite Organization (IZA) recognizes 248 different zeolite frameworks in its database. [a, 6]

The concept of tiling is commonly used to better illustrate the complex structure of zeolites and to describe each framework unambiguously. In simple

---

[a] The international Zeolite Associations uses three capital letter codes to refer to unique frameworks topologies of zeolite materials that refers to the abbreviation of the materials.[6] Some examples:

Code	Abbreviation	Full name
DFO	**D**A**F**-1 (**o**ne)	**Da**vy **F**araday Research Laboratory - **one**
DFT	**D**A**F**-2 (**t**wo)	**Da**vy **F**araday Research Laboratory - **two**
ITE	**I**TQ-**3** (**t**hre**e**)	**I**nstituto de **T**ecnologia **Q**uimica Valencia - three
AFI	**Al**PO_4-5 (**fi**ve)	Aluminophosphate-5
MFI	ZS**M**-5 (**fi**ve)	**Z**eolite **S**ocony **M**obil - five

terms, a tile is a cage whose faces can be described as [$M^m.N^n$…], where *m* and *n* are the number of faces in the tile that are *M*-rings and *N*-rings and so on. For example, the **t-bru** tile represented in Figure 1.1 is composed of two 4-membered rings (M = 2; m = 4) and four 5-membered rings (N = 4, n = 5) and can be described as $4^2.5^4$. Figure 1.1 further describes the other tiles in the STI framework and how they build the final zeolitic framework. The description of zeolite in terms of tiling is important as one can mathematically understand the topology of specific frameworks regarding the location and size of cavities, channels, and windows. Furthermore, unique frameworks that contain common tiles may present structural similarities and, consequently, use similar synthetic templates. It is possible, therefore, to investigate synthetic strategies for potential new frameworks that were hypothesized purely mathematically.[7]

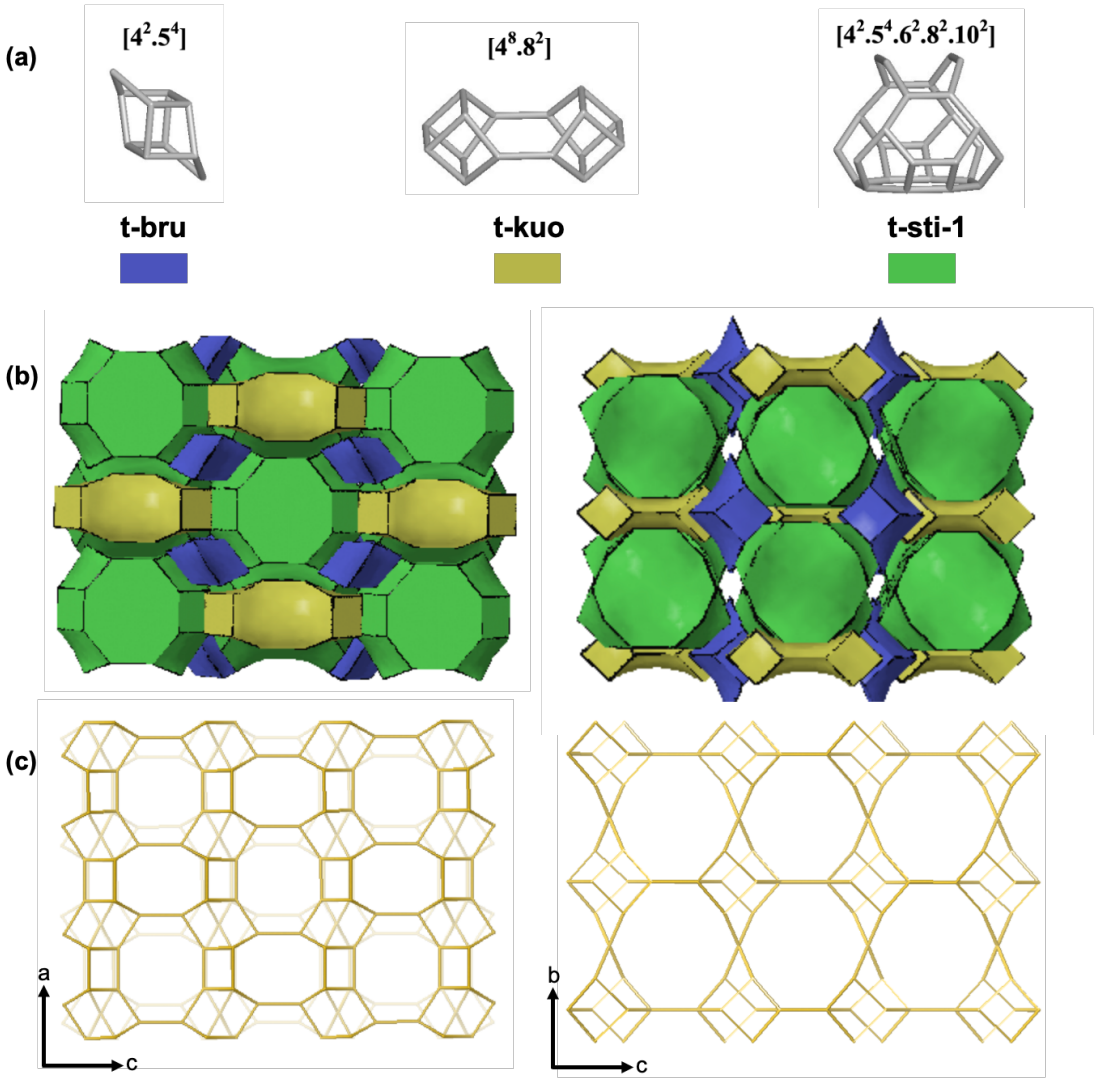

Figure 1.1 Scheme showing the tiling built of pure silica zeolite STI. (a) All individual tiles presented in the STI framework and their [$M^m.N^n$…] identification; **(b)** Tile arrangement in the STI structure; **(c)** STI framework. Each vertex represents a SI atom. The b bridging oxygens are omitted for clarity. Adapted from the IZA database.[6]

Zeolites' structural diversity allows them to be used for several applications, including catalysis and photocatalysis,[8] sorption[9–11] and carbon capture,[12,13] anti-corrosive coating,[14,15] and – due to their non-toxicity and biocompatibility – tissue engineering[16,17] and drug delivery.[18,19] Such a wide

range of applications has led the scientific community to explore further materials possessing structural frameworks analogs to zeolites.

1.1.2 Aluminophosphates

Because the original definition described zeolites as pure silicates or aluminosilicates, the term *zeotypes* or *zeolitic materials* is commonly used to refer to materials that are analogs to zeolites. The term was first used to describe aluminophosphates (AlPO), zeolite analogs where the silicon atoms are substituted by phosphorus.[20–22] Although many other structures are now considered zeotypes, such as gallosilicates,[23] gallophosphates,[24] gallogermanates,[25] borosilicates,[26] and zincophosphates,[27] AlPOs are the most investigated ones, and IZA recognizes more than 50 frameworks to date. They present much higher thermal stability than most zeotypes and their Al^{3+} centers can be directly substituted by divalent metals, which opens several possibilities in the field of catalysis.[22]

Aluminophosphates were first described in 1982 by the Flanigen group at Union Carbide Corporation. In their seminal work, the authors described twenty $AlPO_4$-n structures, some of them presenting novel topologies such as AFI framework.[21] Similarly to zeolites, AlPO frameworks consist of alternating Al- and P-centered polyhedral, each bridging to the other through oxygen. In AlPOs, there is a strict alternation of Al and P centers, no Al-O-Al being allowed due to Lowenstein's rule, which states that “whenever two tetrahedra are linked

by one oxygen bridge, the center of only one of them can be occupied by aluminum; the other center must be occupied by silicon, or another small ion of electrovalence four or more, e.g., phosphorus. Likewise, whenever two aluminum ions are neighbors to the same oxygen anion, at least one of them must have a coordination number larger than four, that is, five or six, towards oxygen".[28] The rule is valid for both aluminosilicate zeolites and AlPOs. In the latter, however, the existence of phosphorus in the framework allows unique coordination chemistry of the aluminum atoms.

Aluminum has more coordination modes with oxygen in AlPOs than in zeolites. It can form tetra - $AlO_{3b}(OH)$, AlO_{4b} - penta - AlO_{5b}, $AlO_{4b}(OH)$, or hexacoordinated - $AlO_{4b}(OH)_2$, $AlO_{4b}(H_2O)_2$, $AlO_{4b}(OH)(H_2O)$, $AlO_{5b}(OH)$, AlO_{6b} – spheres (b = bridging). In zeolites, aluminum strictly tetracoordinates. The fact that phosphorus, the other building block of AlPOs, also has a rich coordination chemistry, being able to form PO_{4b}, $PO_{3b}O_t$, $PO_{2b}O_{2t}$, and PO_bO_{3t} species (b = bridging; t = terminal), explains the structural versatility of these materials.[5]

The new chemistry introduced by phosphorus atoms led to many interesting findings. Novel structures not yet observed for pure silica or aluminosilicate materials have been obtained. $AlPO_4$-5 (Figure 1.2) was the first material with AFI framework, its pure silicate version (SSZ-24) only being reported years laters.[29,30]

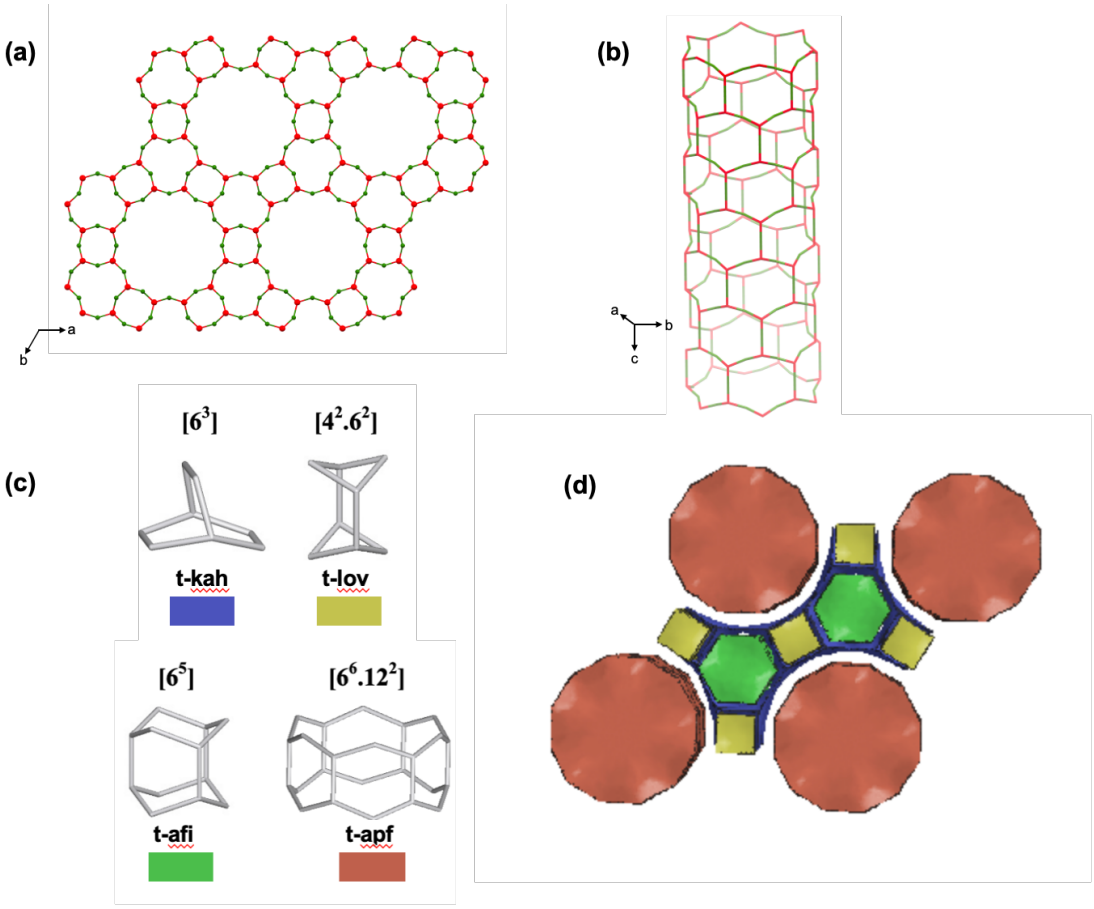

Figure 1.2 Structure schematics of AlPO4-5. **(a)** View along [100] detailing the 4-, 6- and 12- membered rings; **(b)** View normal to [001] showing the channel formed by the 12-membered rings; **(c)** Tiling construction of the framework; **(d)** Tile arrangement. Adapted from the IZA database.[6]

$AlPO_4$-5 contains three different ring sizes comprised of 4, 6, or 12 tetrahedral atoms. A 1D channel with a diameter of 11.3 Å is formed parallel to the crystallographic *c*-axis by the 12-membered rings. Computational geometry was used to elucidate the pore availability for the introduction of guest molecules. After considering physical dimensions as well as electrostatic interactions, it was concluded that the maximum diameter of a sphere that can be inserted in the channel is 8.3 Å while the maximum sphere diameter for

diffusion is 7.36 Å.[31] These values are important when considering the confinement effects that will be discussed later in this section.

Another crucial feature arises from replacing the Si^{4+} with P^{5+}. While aluminosilicate zeolites possess naturally negatively charged frameworks, aluminophosphates are neutral, as shown in Figure 1.3. When it comes to metal doping, it has been shown that only M^{3+} and M^{4+} cations can be introduced into zeolite frameworks. In AlPOs, however, doping is possible with M^{2+}, M^{3+}, M^{4+}, and M^{5+}.[b, 22]

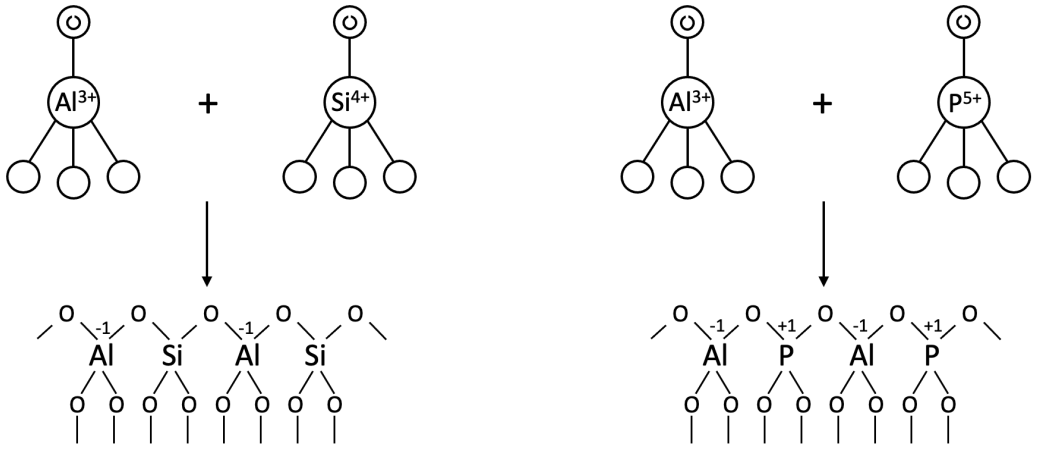

Figure 1.3 Comparison between aluminosilicate zeolites and aluminophosphate tetrahedral building blocks and the overall charge of the respective frameworks.

[b] Some few exceptions of the insertion of M^{2+} in zeolites[32–35] and M^{+} in AlPOs[36,37] have been reported.[22]

1.1.3 Metal-doped aluminophosphates for catalytic applications

Metal-doped aluminophosphates - MAPOs – are largely used in catalysis[38–42] mainly due to their Brønsted acidity tunability, which is achieved by isomorphically substituting Al^{3+} with M^{2+} metals ions.[c] A Brønsted acid can be defined as a proton donor. As exemplified in Figure 1.4, a less positive site is created when an M^{2+} replaces an Al^{3+}. The oxygens binding to such site will now withhold more of its electrons, creating a partial negative charge. Protons from the media will then loosely bind to the oxygens, and therefore MAPOs act as Brønsted acids.

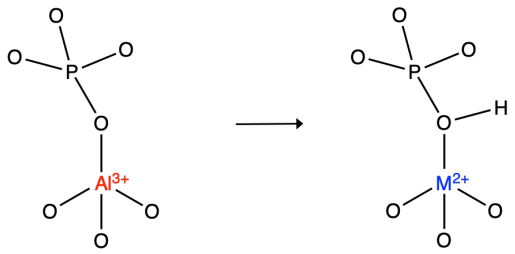

Figure 1.4 Origin of the Brønsted acidity in MAPOs.

.

The acidity of zeotypes will heavily depend on the chemical environment of the acid sites, namely bond angles and lengths, as well as the electrostatic potentials in the coordination spheres, and it has been shown that MAPOs may show higher acidity tunability than their respective zeolite analogs. In metal-

[c] Note on abbreviation. AlPO is used to refer to aluminophosphates. When aluminum atoms are substituted by M^{2+} metals, the compound is referred to as MAPO. It is possible to be more specific and use NiAPO for Ni^{2+},MnAPO for Mn^{2+}, etc. The number in the abbreviation refers to the type of IZA framework: -34 refers to CHA , -5 to AFI, etc. For example, MnAPO-5 is an Mn^{2+}dopped aluminophosphate with AFI framework.

doped zeolites, the acidic site will only present Si atoms in its first coordination sphere due to Lowenstein's rule. In MAPOs, this first coordination sphere can also contain P atoms. By controlling the first and second coordination spheres' composition, it is possible to also control the acidity.

The confinement effect is another essential feature of zeotype materials that makes them great catalyst candidates. For a successful reaction, the reactant must be able to access and adsorb onto the acidic sites. Therefore, the porous structure of the catalysts, namely the pore size, geometry, and electric field inside the pores, is of great importance in the process. These features will ultimately rule the enthalpy and entropy of the adsorption as they control both the rotational freedom of the adsorbed species and intermediates of the reaction as well as the degree of van der Waals and electrostatic interactions that hold such species in place.[43]

Due to the shape selectivity, some framework types will preferably produce certain products than others. For example, SAPO-34 (Figure 1.5), an aluminophosphate with CHA topology, presents high selectivity (>80%) for the production of ethylene and propylene in MTO (methanol to olefin) reactions.[44]

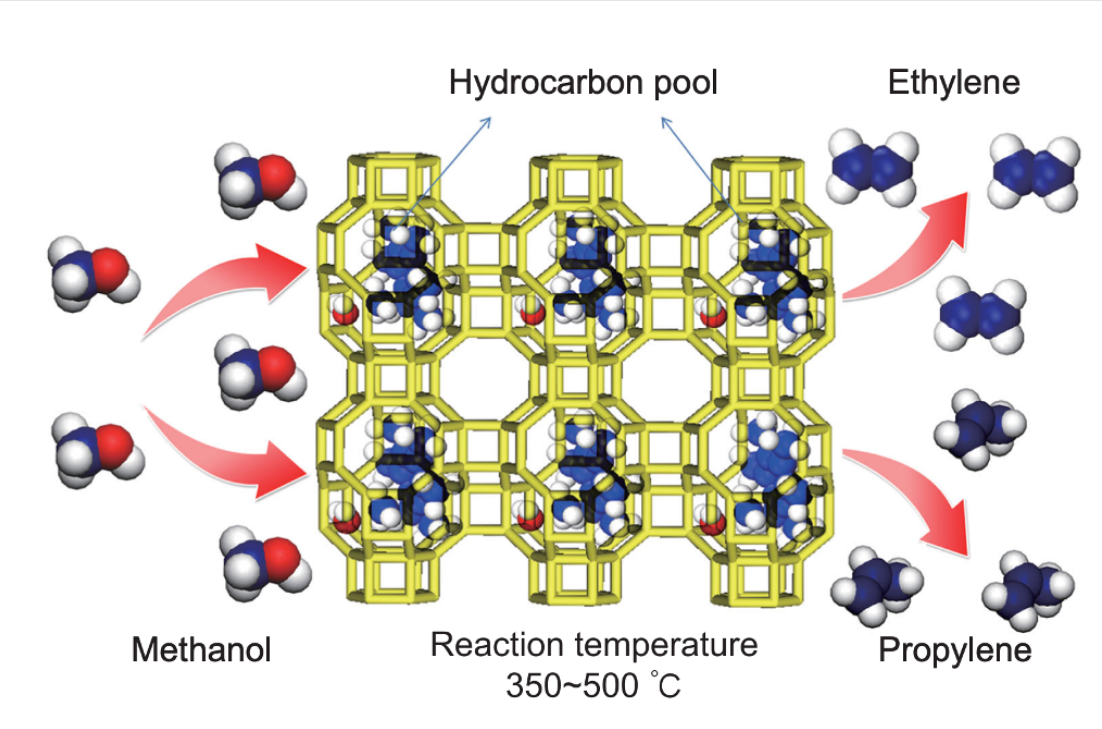

Figure 1.5 Scheme representing an MTO reaction over SAPO-34 catalyst.[44]

MTO is a type of MTH (methanol to hydrocarbon) reaction, invented by Mobil Corporation in 1977.[45,46] As shown in Figure 1.6, the reaction consists of obtaining olefins from methanol, which can be sourced from CO_2 capture[47], biomass waste,[48] and natural gas,[49] and coal.[50] MTO reactions are, therefore, a route to obtain petrochemicals from a non-oil source. Although much debate exists on the mechanism of MTO reactions,[43,51–55] two important features in a catalyst are agreed to be key for a successful process: shape selectivity and a source of protons. Hence MAPOs presenting Brønsted acidity are great candidates for this role.

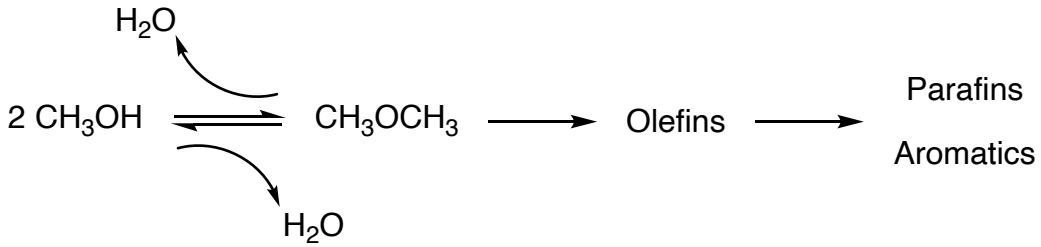

Figure 1.6 Methanol to Olefin (MTO) reactions.

1.2 Synthesis of MAPOs

1.2.1 Solvothermal methods

Solvothermal synthesis can be defined as "the synthesis by chemical reactions of substances in a sealed and heated aqueous solution or organic solvent at appropriate temperature (100-1000°C) and pressure (1-100 MPa)."[56] These reactions are usually held in Teflon-lined stainless-steel containers, commonly referred to as autoclaves, which are introduced to an external temperature source. Because the autoclaves are sealed, autogenous pressure is created. The magnitude of the pressure depends on the percentage to which the autoclave is filled with the reaction mixture.[56] Figure 1.7 details this phenomenon for a system using water as the solvent.

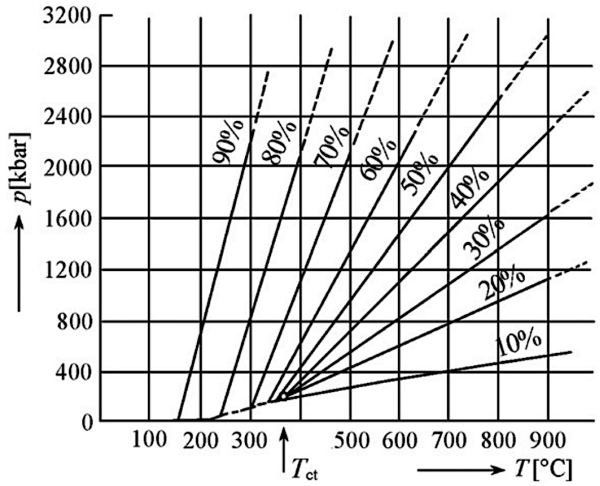

Figure 1.7 Autogenic pressure generated in a hydrothermal system as a function of the temperature and the filling parameter.[56]

The physicochemical properties of both the solvents and the precursors greatly affect the success of the solvothermal process. The solvent-precursor pair choice is crucial, as it directly influences the kinetics of the crystallization. The dissolution of the precursors and the distribution of the species in the solution dictate their availability to nucleate and later feed the crystal growth. Furthermore, solvation of the precursors may occur, changing their coordination spheres and possibly their reactivity.[57] Water is the most used solvent in these reactions, as it cheap and environmentally-friendly.[56] When the solvent is water, the process receives the specific name of hydrothermal synthesis.

The high temperature and pressure environment of solvothermal reactions are commonly referred to as subcritical conditions. Under such conditions, the solvents being used will present unique psychochemical properties. Water, for example, presents lower viscosity, density, and surface tension as well as higher vapor pressure, and ion product. Figure 1.8 further details the behavior of water under subcritical conditions.[56]

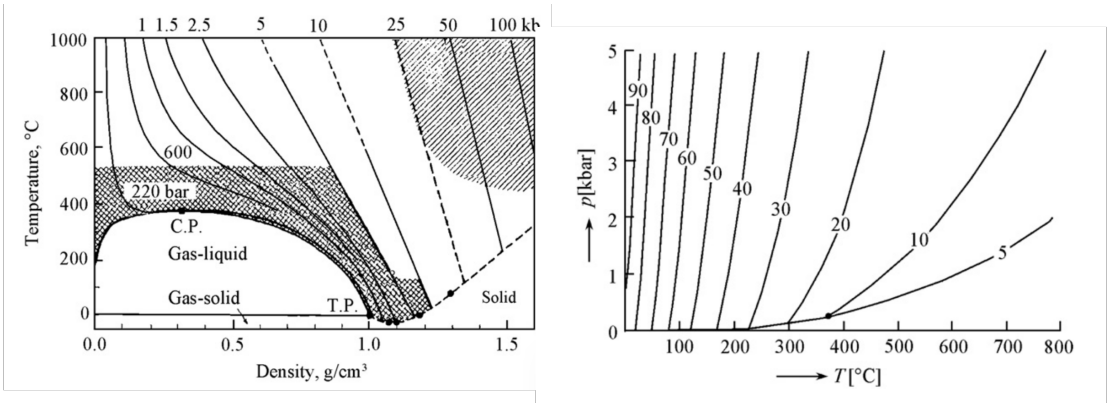

Figure 1.8 Physicochemical properties of water under subcritical conditions present in hydrothermal methods. Left: density as a function of temperature and pressure; right: dielectric constant as a function of temperature and pressure.[56]

The synthesis of zeolites via the hydrothermal route was beautifully discussed in a review by Cundy and Cox.[58] The authors provided extensive literature data that suggests zeolite crystallization follows the classical nucleation theory for precipitation reactions, which is also believed to be the same general mechanism for AlPO formation.[59] By this theory, the period from the start of the reaction until the appearance of the first crystal (induction period,

τ) can be decomposed into the relaxation time (t_r), nucleation time (t_n) and growth time (t_g), as shown in Equation 1.1.[58,60]

$$\tau = t_r + t_n + t_g \quad (1.1)$$

The relaxation time contemplates the very first physical and chemical changes following the act of adding the reagents to the mixture and include processes such as the dissolution of the starting materials, their distribution in the medium and the time that it takes for them to reach the system's temperature. Several studies, however, suggest that t_r can be further decomposed into a *primary* and *secondary* amorphous phase. The secondary amorphous phase is composed of a pseudo-steady-state intermediate. In this stage, there is a local organization of the reagents and the formation of aluminum and silicate tetrahedral subunits. Additionally, these subunits start a preliminary organization around templating groups (which will be discussed later in this chapter). It is important to emphasize that although structural order is observed at this stage, it is only local, and no extended periodic structure is yet observed. Therefore, the bulk phase is still amorphous at this point.[58]

The next step in the crystallization process regards the nucleation period (t_n, Equation 1.1). The high temperatures and pressures of solvothermal methods allows for supersaturation, which is one of the driving forces for the nucleation onset. The subunits formed during t_r are dynamically interacting to each other, constantly forming and breaking aggregates – or nuclei – of radius

r. Only nuclei that reach a critical radius r_c will further grow into crystals. Equation 1.2 described r_c for a spherical 3D nucleus,

$$r_c = \frac{2\omega\gamma_e}{kT \ln (S)} \quad (1.2)$$

where ω = molecular volume, γ_e = surface energy, k = Boltzmann constant, T = temperature, and S = supersaturation.[61]

The nucleation phenomenon can be further understood in terms of free Gibbs energy (Figure 1.9). When a subunit moves from the solution to an aggregate, a decrease in its free energy observed, which has a r^3 dependence (cohesive energy, ΔG_v in Figure 1.9). However, the newly formed nuclei will present an increase in its free energy, which in this case is dependent on r^2 (surface energy, ΔG_s in Figure 1.9). When $r = r_c$, the formation of a stable nucleus is energetically favorable, as the cohesive energy in forming a continuous motif is enough to outweigh the one necessary to split the nucleus into several smaller agglomerates. The nucleation rate can therefore be defined as the rate of formation of agglomerates with $r \geq r_c$.[58,60,61] For zeolites, r_c usually varies between one to eight unit cells.[62]

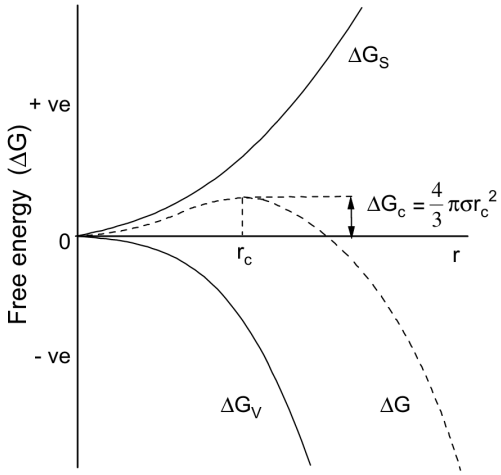

Figure 1.9 Free Gibbs energy (ΔG) diagram for the nucleation process in terms of nucleus radius (r). ΔGv = cohesive energy; ΔGs = surface energy; ΔGc = critical energy; r_c = critical radius.[58]

After nucleation, the crystal growth period (t_g in Equation 1.1) takes place. There are many models in the literature to explain the mechanism by which a certain crystal will grow, including surface energy theories, adsorption layer theories, kinematic theories, diffusion-reaction theories, and the birth and spread model.[60] For zeolites, the adsorption layer model, also known as the Gibbs-Volmer theory, is the most accepted mechanism for crystal growth.[58]

According to this thermodynamic model, when solute particles are in the interface of the crystal nuclei and the bulk solution, they will present a lower degree of freedom and diffuse on the surface of the nuclei, forming an adsorption layer that is in equilibrium with the solution. The particles will only adsorb to the crystal faces at *active sites*, which are optimal adsorption sites where the attraction forces are greater. This model was further elaborated by Kossel, who presented a more realistic crystal face containing not only flat

layers but also edge and layer vacancies, kinks, steps, and self-adsorbed growth units, which allow the crystal growth to occur simultaneously at different locations in the surface. The kinks were determined to be the preferred sites for the adsorption of solute particles, therefore greatly affecting the crystal growth rate.[58,60,63,64]

In a typical MAPO synthesis, the initial mixture to be placed in the autoclave consists of the inorganic precursors (aluminates, phosphates, and divalent metal salts), a solvent, a mineralizer, and a structure-directing agent (SDA). Besides the composition of the gel itself, pH, temperature, and reaction time also influence which of the hundreds of possible frameworks will be obtained.[59]

1.2.2 Mineralizer and the role of pH

The pH at which the synthesis of zeotypes materials is carried is of extreme importance. Because silica is more soluble at higher pH, the synthesis of zeotypes containing a large fraction of Si is usually carried in alkaline media with the presence of OH^- ions. The higher mobility of Si in these conditions allows it to move out of the initial gel phase and form Si-O-Si bonds, feeding the growing crystals. A limitation of this approach, however, is that many transition metals will form inert hydroxide compounds at higher pH. The obtainment of metal-doped zeotypes in basic conditions is, therefore, more challenging than obtaining pure or rich silica materials.[59]

An alternative strategy is using HF in the synthesis, a process commonly referred to as the “fluoride route.” In this methodology, the F^- acts as a mineralizing agent by forming hexafluoro complexes with Si. Such complexes are highly soluble, and their superior mobility facilitates the Si-O-Si formation. [59,65] In order to understand the role of HF in the crystallization process of AlPOs, it is common to employ SS-NMR spectroscopy to monitor the coordination environments and condensation degrees of ^{19}F, ^{27}Al and ^{31}P. For $AlPO_4$-5, it has been shown that the formation occurs in a multi-step fashion. Before hydrothermal treatment, the initial amorphous gel is composed of Al_{tet}-O-P_{par} and F-Al_{oct}-O-P_{par} units (tet = tetrahedral; oct = octahedral; par = partially condensed) as well as unreacted Al sources. Evidence of crystallization is obtained by the appearance of two microdomains: F-Al_{pen}-O-P_{ful} and Al_{tet}-O-P_{ful} (pen = pentacoordinate, ful = fully coordinated). As the reaction proceeds, the condensation degree of phosphorous species increases. The partially condensed units of the initial amorphous gels are replaced by fully condensed Al_{tet}-O-P_{ful}.[66]

In some contexts, F^- is considered a better mineralizer than OH^- as some structures can only be obtained via the fluoride route. Furthermore, HF can directly affect crystallization process. Due to its ability to lower the supersaturation of the medium, crystal growth is favored over nucleation. For example, when SAPO-34 is synthesized in the presence of fluoride, fewer but

bigger crystals are obtained if compared to syntheses using OH^- as the mineralizer.[67]

1.2.3 The OSDA and the solvent competition

Structure-directing agents are critical in the synthesis of zeotypes because – as the name suggests – they may represent the key to obtaining a particular desirable framework. Although many factors influence the complex crystallization of aluminophosphates - such as the mineralizer,[68,69] pH,[70,71] Al/P/M (M = doping heteroatom) ratio,[72,73] and temperature and reaction time[74,75] – organic structure-directing agents (OSDAs) are generally regarded as the most important factor in the successful obtainment of a certain framework.[76]

The concept of organic molecules aiding the crystallization of aluminosilicates was first introduced by Barrer and Denny in 1961.[77] Their work describes the use of methylammonium hydroxides for the obtainment of zeolitic materials. The methyl-substitution degree of the ammonium hydroxides (from mono- to tetra-substituted) influenced the obtainment of different zeolitic phases (FAU and LTA) and other mineral phases (bayerite, mica, harmotome, boehmite, sodalite, and montmorillonite). The authors discussed how the size, shape, and concentration of the base used greatly dictated which structure would be formed. Therefore, this work is considered the first study on organic structure-directing agents.[78]

The pioneering work of Barrer and Danny revolutionized the field. Two of the most important zeolites used nowadays in industrial catalysis, Zeolite Beta,[79] and ZSM-5,[80] were first synthesized using tetraethylammonium and tetrapropylammonium, respectively. The origin of the whole field of aluminophosphates can also be linked back to the discoveries of OSDAs, as the syntheses of the first AlPO materials[21] were aided by using organic amines and quaternary ammonium salts.[76]

It is important to point out, however, that other chemical species are commonly referred to as structure-directing agents. For example, alkali inorganic cations such as Li^+, Na^+, and K^+ not only counterbalance anionic frameworks but have also been shown to greatly affect the obtainment of silica-rich zeolites.[81] In alkaline media, their hydroxide form has been shown to affect the crystallization kinetics of pure silica zeolites.[82] The insertion of heteroatoms in the Al/Si or Al/P frameworks can also present a structure-directing effect with the rising of new coordination environments with unique bond lengths and angles. The introduction of Ge in zeolites has been shown to stabilize the formation of small 3- or 4-membered rings zeotypes.[83,84] Finally, the mineralizer agent itself may present SDA behavior. For example, fluoride has been show occupy the small D4R cages of silicate materials with ITW topology and to form ion pars with OSDA cations in the larger 10-MR channels of silicate MTT frameworks.[85]

Many physico-chemical properties of OSDAs influence their ability to dictate crystallization, such as size and shape, hydrophobicity,[86] hydrothermal stability,[87] and flexibility.[88] They can influence the synthesis via several simultaneous factors: (1) Templating effect: The structure obtained retains the geometry and electronic configuration of the OSDA; (2) Structure-directing effect: the OSDAs will still lead to specific topologies, but the resulting porous structure does not necessary retain the geometry and electronic configuration of the OSDA. The degree of host-guest interaction is lower than in true templates. For example, when acting by structure-directing the OSDA may freely rotate in the pores and therefore the pore formation is dependent on the volume caused by such rotation and not by the OSDA volume itself; (3) Pore-filling effect: Provides an increase in thermodynamic stability during the formation of the hydrophobic organic framework in aqueous media. The great majority of OSDAs will act by structure-directing and pore filling, true templates being much more rare.[89]

Although OSDAs have been shown to greatly aid crystallization, the solvent being used can compete as a structure-directing agent, creating a phase competition. Gomes et al. studied the use of the OSDAs triethylamine (TEA), benzylpyrrolidine (BP), and (S)-()-N-benzylpyrrolidine-2-methanol (BPM) for the aqueous synthesis of $AlPO_4$-5. They found that difference between OSDA/water competition or co-templating lies in the degree of interaction between the framework and OSDA. The highly-interacting bulky

BPM singly occupies the larger 12-MR channels while water preferably occupies the 6-MR channels of the structure. BP presented less interaction with the framework, and a clear BP/water competition for the same cavities was observed. TEA interaction degree lies between the ones for BPM and BP, and double occupancy with TEA and water simultaneously occluding a pore was observed.[90]

The solvent SDA competition can greatly hinder the selectivity of the synthesis. Therefore, many strategies for either solvent-free or template-free have been developed. [91,92] Of particular interest are the ionothermal reactions, where ionic liquids are used as both the solvent and the structure-directing agent.[93]

1.2.4 Ionothermal synthesis

Ionic Liquids (ILs) are generally defined as salts with low melting points (T_M < 100 °C). A subclass of ILs is the room-temperature ionic liquids which, as the name suggests, are in the liquid state at room temperature. Because of this, they can be explored as substitutes for common hazardous organic solvents. ILs are interesting for several reasons: (i) they are low-viscosity liquids with inherent low vapor pressure, which translate to safer processes in an industrial setting where high-temperature reactions are needed for larger scales; (ii) they are easily purified and can then be reusable, lowering overall

cost; (iii) they are greener alternatives to the toxic or volatile traditional organic solvents.

Ionic liquids are most commonly composed of at least one bulky organic ion. In general, bulkiness and some degree of asymmetry are the key points on the low melting point of salts, as such features hinder efficient packing in the solid state.[94] For example, it has been shown that highly-branched short alkyl chains in the amine lead to lower melting points.[95] The IL's ionic composition also dictates other important physicochemical properties, such as viscosity and heat capacity. Because it is possible to select ions for a specific application, ILs are commonly referred to as "designer solvents". [96] Some common IL cations are presented in Figure 1.10.

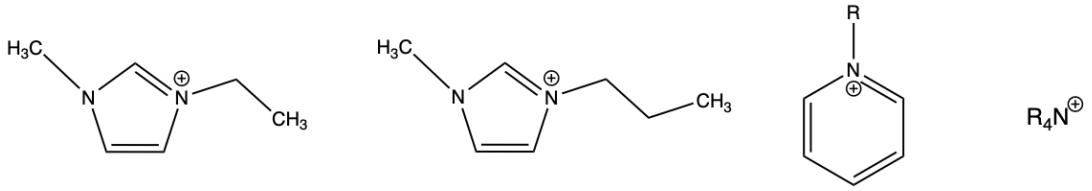

[Emin]$^+$ **[Bmin]$^+$** **[$C_n$pyr]$^+$** **[C_4N]$^+$**

Figure 1.10 Common IL cations. [Emin]$^+$ = 1-ethyl-3-methylimidazolium; [Bmin]$^+$ = 1-butyl-3-methylimidazolium; [$C_n$pyr]$^+$ = 1-alkylpyridimium; [C_4N]$^+$ = tetraalkylammonium.

When ILs replace the water in traditional hydrothermal synthesis, the process receives the name ionothermal synthesis. The term was coined in 2004 by Morris and co-workers in a paper describing the use of ILs for the first time for the synthesis of any zeolitic material. The group used 1-methyl-3-

ethylimidazolium bromide as the IL to obtain aluminophosphates a series of SIZ structures (**S**t. Andrews **I**onothermal **Z**eolite): SIZ-1 (interrupted structure), SIZ-3 ($AlPO_4$-11), SIZ-4 ($AlPO_4$-34) and SIZ-5 ($AlPO_4$-41). One of the most remarkable findings in this seminal paper is that the IL acted in the system both as a solvent and as an SDA. Therefore, it eliminated the SDA/solvent competition described earlier.[97] The possibility of a better synthetic control led to many studies exploring ionothermal synthesis.

1.3 Ionothermically synthesized MAPOs

This section highlights the current progress in the field by presenting – to the best of our knowledge – all the reports on the obtainment of MAPOs via the ionothermal route. Table 1.1 summarizes the structures that will be discussed, and the ionic liquids used for their obtainment.

Table 1.1 Summary of the ionothermal procedures described in the literature for the obtainment of MAPO materials

Ionic Liquid	Framework topologies* obtained with the respective IL**	Reference
Magnesium		
1-butyl-3-methylimidazolium bromide	AEL AFI	98
choline chloride and urea	AEL AEN GIS ALPO4-CJ2	99
1-butyl-3-methylimidazolium bromide	AEL AFI AEL	100

1-isopropyl-3methylimidazolium bromide	ATS CHA	
1-ethyl-2,3,4,5-tetramethylimidazolium	CHA	
1,3-diethylimidazolium	ATS	
1,3-diisopropylimidazolium	AFI	101
1-isobutyl-3-isopropylimidazolium	SAO DAF-1 AFI	
1,3-diisobutylimidazolium	AFI	
1-ethyl-3-methylimidazolium bromide	AEL	102
1-ethyl-2,3,4,5-tetramethylimidazolium	CHA	
1,3-diethylimidazolium	ATS	
1,3-diisopropylimidazolium	AFI	101
1-isobutyl-3-isopropylimidazolium	SAO+DAF-1+AFI	
1,3-diisobutylimidazolium	AFI	

Manganese

1-ethyl-3-methylimidazolium bromide	AFI	103
1-ethyl-3-methylimidazolium tosylate	LAU	104
1-ethyl-3-methylimidazolium bromide	SOD AEL CHA	105
1-butyl-3-methylimidazolium bromide	AFI	106

Iron

1-ethyl-3-methylimidazolium bromide	SOD	107
succinic acid-choline chloride	AST	108
succinic acid-choline chloride	AFI	109
succinic acid-choline chloride	AFI	110
1-butyl-3-methylimidazolium chloride	AFI	111
1-butyl-3-methylimidazolium bromide	SOD	106
succinic acid-choline chloride	AFI	112
succinic acid-choline chloride	LEV	113

1-ethyl-3-methylimidazolium bromide	CHA	114

Cobalt

1-ethyl-3-methylimidazolium bromide	AEI SOD SIV	115
Choline chloride and dicarboxylic acids	LEV SIZ-13	116
1-ethyl-3-methylimidazolium bromide 1-butyl-3-methylimidazolium tetrafluoroborate	SOD	107
1-ethyl-3-methylimidazolium bromide	AEL CHA CLO	117
1-ethyl-3-methylimidazolium bromide	SOD AEI	118
1-ethyl-3-methylimidazolium bromide	AEL CHA	119
1-butyl-3-methylimidazolium bromide	SOD LTA	106
1-ethyl-2,3,4,5-tetramethylimidazolium	CHA	101
1,3-diethylimidazolium	CHA	
1,3-diisopropylimidazolium	SSZ-85	
1-isobutyl-3-isopropylimidazolium	DAF-1	
1,3-diisobutylimidazolium	SAO AFI	
1,3-dicyclohexyllimidazolium	AFI	

Nickel

1-butyl-3-methylimidazolium bromide	LTA	106

Copper

1-butyl-3-methylimidazolium chloride	AFI	120
AFI	AFI	121

Zinc

1,3-diisopropylimidazolium bromide	DFO	122
1-ethyl-2,3,4,5-tetramethylimidazolium	CHA	123
1,3-diethylimidazolium	CHA	

1-isopropyl-3-ethylimidazolium	ATS
1,3-diisopropylimidazolium	DAF-1
1,3-diisobutylimidazolium	SAO DAF-1
1,3-dicyclohexyllimidazolium	AFI

*Mixed or pure phase. Dense phases not included.

**The multiple topologies described for one ionic liquid were obtained varying different reaction parameters such as molar ratios, precursor nature, mineralizer nature, temperature, time, and pH.

1.3.1 MgAPO

The first ionothermically synthesized MgAPOs were obtained by Wang et al. by using the ionic liquid 1-butyl 3-methylimidazolium bromide ([Bmim]Br) and MgO as the metal source. In the absence of Mg^{2+} ions in the reaction media, only condensed tridymite phase was isolated. The insertion of manganese led to the formation of mixed-phase AEL, AFI, and tridymite. Therefore, the manganese ions played a structure-directing role. Furthermore, the authors were able to tune the selectivity towards AEL topology by adding a second structure-directing agent, *n*-dipropylamine.[98]

Carvalho et al. used a factorial approach to investigate the formation of MgAPO in a deep-euthetic solvent (DES) composed of choline chloride and urea.[d] In general, lower amounts of manganese, higher amounts of DES, and shorter reaction times led to mixed-phase with AEL as the main topology.

[d] DES are many times regarded as a subclass of ionic liquids that are specifically composed of Lewis and Brønsted acids and bases. There is open discussion, however, on how to exactly classify these solvents.[124,125]

Different reaction parameters induced the formation of frameworks with smaller pores, such as AEN and GIS or condensed phase $AlPO_4$-CJ2.[99]

The fluoride-free synthesis of MgAPOs with topologies AEL, AFI, and ATS was described by Wei et al. Mixed phase AEL+AFI MgAPO was obtained when using [Bmim]Br and no HF. Interestingly, if using the same reaction conditions but the addition of Mg^{2+} was replaced by F^-, the same AEL +AFI topologies were obtained (now for AlPOs). It is possible, therefore, that Mg^{2+} and F^- play a similar role in the synthesis, as using either of them led to formation of the same AEL+AFI mixed phase. When 1-i-propyl-3methyl-imidazolium bromide ([iPrmin]Br) was used as IL, however, different results were observed. Mg^{2+} presence induced the formation of AEL+ATS while F^- generated pure CHA. Although specific details on how F^- leads to the formation of CHA were not investigated, it is possible that this anion causes the transalkylation of [iPrmin]Br to form dimethylimidazolium cations ($[Dmin]^+$), which have been shown to effectively template CHA in the AlPO SIZ-10.[126] It was again proposed that Mg^{2+} may have some structure-directing role as an increase in its concentration in the gel influenced the predominant phase. Thermogravimetric analysis showed that more IL cations were occluded when more Mg^{2+} was incorporated in the inorganic framework, which is explained in terms of the electrostatic stabilization of the organic cations by the now partially negative Mg-substituted inorganic framework.[100]

Wang et al. published an interesting study describing an extruding process for preparation of MgAPO with AEL topology using the ionic liquid [Emin]Br and di-n-propylamine. An initial gel composed of Al_2O_3:P_2O_5 :MgO:HF:DPA:[EMIm]Br:H_2O (molar ratio 1:1:0.03:0.18:0.4:1:45, respectively) was heated at 80°C to form a malleable solid to be extruded into a cylindrical shape. Only then the material was transferred to an autoclave to initiate the crystallization process. This pre-shaping methodology allows for a more straightforward application of molecular sieves in catalysis and eliminates the need for binders that can hinder the catalytic process. The extrudate obtained in this work was successfully applied for the hydroisomerization of n-dodecane, the process giving high conversion and selectivity.[102]

Benin et al. explored a variety of ionic liquids (Figure 1.11) to obtain MgAPOs with CHA (IL-A), ATS (IL-B), AFI (mixed with unknown phase) (IL-D), SAO+DAF-1+AFI mixed phase (IL-E) and AFI topologies (IL-F). The ionic liquids IL-C and IL-G led to tridymite and an unknow phase, respectively.[123]

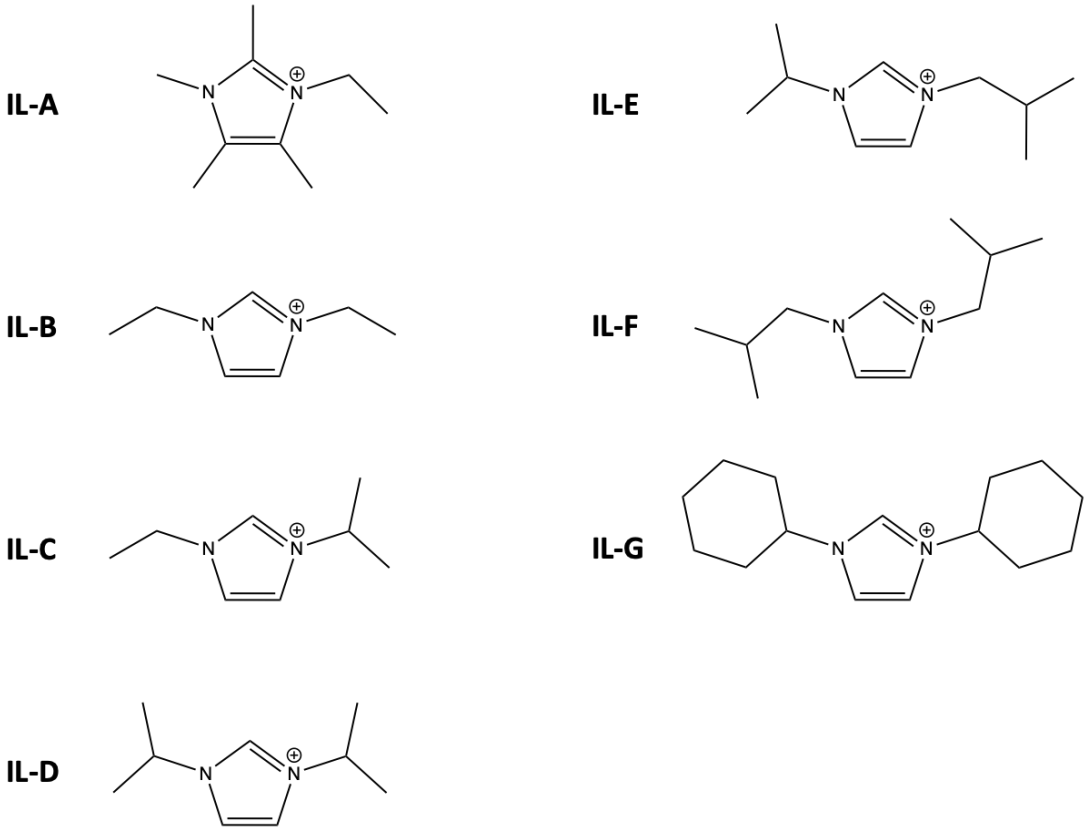

Figure 1.11 Structure of the ionic liquids' cations used by Benin et al. to investigate the influence of the OSDA's shape and size in the obtainment of MAPOs. All ILs had bromide as the anion. IL-A: 1-ethyl-2,3,4,5-tetramethylimidazolium, IL-B: 1,3-diethylimidazolium; IL-C: 1-isopropyl-3-ethylimidazolium; IL-D: 1,3-diisopropylimidazolium; IL-E: 1-isobutyl-3-isopropylimidazolium; IL-F: 1,3-diisobutylimidazolium; IL-G: 1,3-dicyclohexyllimidazolium. [123]

1.3.2 MnAPO

Ng et al. were the first to use an ionothermal strategy to obtain a MnAPO. The material with AFI topology was synthesized using 1-ethyl-2,3-dimethylimidazolium bromide ([Edmim]Br) as the IL. The crystallization mechanism was elucidated by characterizing the products of a 150 °C reaction at different times by PXRD, SEM and SS-NMR. The total dissolution of the

reagents was observed after 5 hours of reaction. Up to 25 hours, only amorphous phases were isolated. At 50 hours, a broad PXRD peak at angles characteristic of AFI framework is first seen. Between 50 and 90 h, all other AFI peaks start to show. The peaks also became narrower within this time interval, indicating larger crystals were formed and/or crystallinity increased, which was also confirmed by SEM. SS-NMR studies showed that tetrahedral Mn and P binding to Al octahedra start to form between the amorphous sample (25 h) and the first AFI peak (50 h). The small seeds consume soluble species nearby until 90 h, when spherical single-crystals are isolated. Interestingly, this is different from the usual needle morphology observed for other AFI materials such as Co-APO-5 obtained via usual hydrothermal reactions.[127] Macroscopic observations combined with time-resolved PXRD revealed the nucleation starts at the solid-liquid interphase, when the initially amorphous aluminophosphate phase organizes itself around $[Edmin]^+$ cations. The small crystals formed will then grow by consuming the remaining species in the amorphous phase that is now surrounded by crystal seeds. Therefore, the crystallization mechanism can be described as a surface-to-core reverse growth.[103]

The synthesis of MnAPO with LAU topology was investigated by Bieniok et al. in a system using the IL 1-ethyl-3-methylimidazolium-tosylate [Emin][tos]. The authors also added imidazole to the reaction, an OSDA known to well-template LAU structures. In this same work, the authors obtained - by solvothermal methods - the first FeAPO with LAU structure. The Mn material

obtained by ionothermal synthesis presented better crystallinity - both in size and quality – than the FeAPO obtained via the solvothermal route. The authors attribute such improvement to the existence of two organic species - $[Emin]^+$ and protonated imidazole – acting as co-OSDAs, as Raman spectroscopy showed that both occupy the porous structures of MnAPO. [104]

Liu et. al studied the use of different manganese sources and their possible role as SDAs for the obtainment of SOD topology MnAPO in a system with 1-ethyl-3-methylimidazolium bromide ([Emim]Br) as the ionic liquid. When Mn^{2+} ions were directly introduced via $MnCl_2 \cdot H_2O$, no SOD phase was observed, and a mix of AEL and CHA was isolated. However, the *in situ* generation of Mn^{2+} by using MnO or MnO_2 as the metal source led to SOD formation. SCXRD and crystallographic assessments indicate that manganese cations not only substitute Al^{3+} centers at a certain degree but are also part of the extraframework structure as hydrated ions occupying *sod* cages. [Emim]Br was not present in the porous structure of the final material but had an important role in the synthesis. The fact that SOD was only obtained when *in situ* Mn^{2+} was present indicates that the hydrated ions of manganese are the true SDAs. This is only possible in the weakly solvating solvent - [Emim]Br – as lesser solvation allows for stronger interactions between the metal cation and the inorganic framework and, therefore, a more effective structure-directing effect.[105]

The ability of manganese ions to act as SDA was also observed by Azim and Stark. The authors used an interesting approach by using MnF_3 in a system containing the ionic liquid [Bmim]Br. The MnF_3 had a triple role in the obtainment of MnAPO with AFI topology. It served as a source of manganese ions, as the mineralizer due to the presence of F^-, and as an SDA. An identical system, except for the presence of MnF_3, led to AEL topology.[106]

1.3.3 FeAPO

The ionothermal obtainment of FeAPO was first reported by Han et. al in 2008. The material presenting SOD topology was synthesized using [Emin]Br as the ionic liquid. The study shows that the initial Fe/Al can be used to control the degree of iron being doped. Furthermore, although higher additions of H_3PO_4 usually lead to better crystallinity as it promotes the hydrolyzation of the Al precursor, too much of the acid hindered the phase purity: when adding H_3PO_4, one will inevitably add more water. Additionally, the authors reported that higher contents of phosphoric acid led to amorphous phase instead of the SOD framework.[107] It has been shown that higher P:Al ratios affect the dimensionality of AlPOs and can, therefore, interfere with the crystallization process.[128]

The chemistry of FeAPO has been extensively studied by Zhao et al. The ability of ionic liquids to well absorb microwave radiation without decomposition was explored for the obtainment of FeAPO-16 (AST) in the

presence of a DES composed of 1:1 succinic acid and choline chloride. Upon varying several reaction conditions, different phases containing pure AST or mixed tridymite+AFI+quartz could be obtained. It was noticed that upon increasing the H_3PO_4 amount, the crystallinity of the AST phase improved. However, similarly to what was reported by Han et al.,[129] too much of the acid hindered phase selectivity and led to $AlPO_4$- quartz due to water being introduced into the system. Therefore, the once ionothermal synthesis starts to behave as a hydrothermal one. Furthermore, similarly to what was described for other MAPOs, the authors found evidence of the structure-directing behavior of the metal ion, as reactions without iron would lead to tridymite.[108] The same group also explored including tetraethylammonium bromide (TEABr) to the DES mixture as co-SDA to obtain FeAPO-5 (AFI). The authors confirmed the ability of TEABr to work as an effective OSDA toward the obtainment of the AFI. The framework was formed in the presence of the TEABr independently of the ferric source used. Furthermore, the H_3PO_4 molar ratio has been shown - once again - to greatly impact the crystallization, where an excess of it would lead to a dense phase, possibly due to the addition of water or over-acidic pH. [109] In a follow-up study, the group showed the FeAPO-5 material can be used as a catalyst for the hydroxylation of phenol, although FeAPO-5 obtained hydrothermally presented better catalytic performance.[110] They have also reported that introducing seed crystals in this system can affect the purity of the AFI phase and the catalyst's induction period.[112] Moreover, the group also

explored the use of the same DES mixture (succinic acid, choline chloride, and TEABr) to synthesize FeAPO with LEV topology. They also found that lower amounts of TEABr, as well as higher Fe_2O_3/Al_2O_3, tune the systems towards the obtainment of LEV instead of AFI and ATS phases.[113]

Ng et al. investigated the possibility of replacing H_3PO_4 with H_3PO_3 for the ionothermal obtainment of MAPO molecular sieves. This is an interesting approach to explore, as it allows for a lower releasing rate of P^{+5} in the system due to the fact that oxidation of P^{+3} to P^{5+} is first necessary. The methodology was applied for the successful synthesis of FeAPO-5 (AFI) using 1-benzyl-2,3-dimethylimidazolium chloride ([Bdmin]Cl) as the ionic liquid. The author found the presence of NKX-2, a one-dimensional intermediate containing 12-MR reported[130] to be formed in usual hydrothermal synthesis employing H_3PO_3 for obtaining $AlPO_4$-5. The iron ions were shown to be essential in the crystallization as they served as a medium for electron transfer associated with the oxidation of phosphorus.[111]

The synthesis of FeAPO with SOD topology using an organic source for the mineralizer F^- was reported by Azim and Stark. Tetramethylammonium fluoride ($[Me_4N]F$) was used not only as a mineralizer but also as co-OSDA in a system containing [Bmin]Br as the ionic liquid. The study resulted in a framework with high Fe/Al substitution (0.83) that was obtained at 160 °C in only 4 hours.[106]

More recently, Musa et al. reported the first ionothermically synthesized FeAPO materials with CHA framework by using the ionic liquid 1-ethyl-3-methylimidazolium chloride ([Emin]Cl) in the presence of ethylenediamine. Interestingly, dimethylimidazolium cations $[Dmin]^+$ instead of $[Emin]^+$ cations - originated from transalkylation reactions within the IL - were found occupying the pores of the structure. The ethylenediamine was not found in the final structure but aided the solubilization of iron ions, greatly interfering with its insertion in the framework, with no Fe^{2+} incorporation occurring in the absence of ethylenediamine.[114]

1.3.4 CoAPO

Parnham and Morris were the first to report the preparation of a CoAPO via ionothermal synthesis. The authors used the ionic liquid 1-methyl-3-ethyl imidazolium bromide to obtain SIZ-7 (SIV, novel), SIZ-8 (AEI), and SIZ-9 (SOD). Interestingly, it was noted that having Co^{2+} ions in the reaction medium interferes with the synthesis even if they are not incorporated in the final product, with lower amounts of the metal leading to SIZ-4 phase.[115]

Dryle and Morris et al. studied the use of three DES systems composed of choline chloride and succinic acid, glutaric acid, or citric acid to obtain SIZ-13 (novel) and SIZ-14 (LEV). Remarkably, rare Co-Cl bonds were found in the structure of product SIZ-13. Such bonds were not priorly found in MAPOs synthesized hydrothermally because they readily hydrolyze in water. The

findings corroborated the idea that ILs are capable of reducing the water's nucleophilicity and reactivity. It is proposed that IL's ions electrostatically interact with water and uniformly disperse its molecules without the formation of hydrophilic clusters usually observed in common organic solvents.[116,131]

Han and co-workers presented an extensive study on the influence of temperature in the crystallinity of SOD topology CoAlPO using four different ionic liquids: [Emim]Br, ([Bmim]Br), ([Bmim][BF_4]), and ([Bmim][PF_6]). More crystalline phases were obtained as the temperature was increased, reaching an optimal at 463 K. The authors attributed this phenomenon to the IL presenting lower viscosity at this temperature, which leads to a higher crystal growth ratio. Only the ([Bmim][PF_6]) system was not successful for the synthesis of CoAPO, which can be attributed to its higher ease of hydrolyzing and producing F^- even in a small amount of water, the latter usually introduced in the system through the use of aqueous acids such as H_3PO_4 and HF. Such hydrolyzation can greatly influence pH and diminishes synthetic control.[107]

CoDNL-1 with CLO topology that presents extra-large pores (20 MR) was obtained by Li et al. by employing a co-structure directing agent 1,6-hexadiamine (HDA) together with the ionic liquid [Emim]Br. The desired framework was obtained at HDA/Al 0.4 molar ratio, AEL and CHA being isolated at lower or higher ratios, respectively. Because HDA was previously shown to effectively template *ita* cages present in CLO topology,[132] the authors suggest that at HDA/Al small ratios, the templating was governed by $[Emim]^+$

species. At higher HAD/Al ratios, the decrease of pH due to more HDA in the medium led to CHA topology, commonly obtained in more acidic condition. Therefore, as expected, high amounts of HF also led to the formation of CHA. F^- ions were necessary for the obtainment of D4Rs building units that lead to the formation of the CLO framework, and reactions with low amounts of the mineralizer led to amorphous phases.[117] The [Emim]Br and HAD system was further studied by Musa et al. to better understand the selectivity towards CHA and AEL frameworks. Through NMR experiments, the authors showed that HDA was not incorporated into the final material but still greatly influenced which framework would be obtained. Only in the presence of HDA, CoAPO-34 (CHA) was isolated, while in its absence, cobalt-free $AlPO_4$-11 (AEL) was the final product. It was hypothesized by the authors that HDA influences the solubility of Co^{2+} in the [Emim]Br and allows it to be more available for incorporation in the tetrahedral sites of the aluminophosphates.[119]

Li et al. also studied the co-templating strategy to tune the selectivity in a [Emim]Br system by adding one of four different tetraalkylammonium hydroxides: tetramethylammonium hydroxide (TMAOH), tetraethylammonium hydroxide (TEAOH), tetrapropylammonium hydroxide (TPAOH), and tetrabutylammonium hydroxide (TBAOH). It was found that when the smaller TMAOH was used, SOD topology was obtained, while all other hydroxides led to the AEI phase. Not only the nature but also the amount of hydroxide was important for selectivity, as lower quantities led to either condensed or

interrupted phases. The authors also investigated the use of the different salts $Co(OH)_2$, $Co(OAc)_2{\cdot}4H_2O$, and $CoCl_2{\cdot}6H_2O$ as metal sources. Only $CoCl_2{\cdot}6H_2O$ did not yield SOD or AEI, and the phenomenon is attributed to the lesser availability of Co^{2+} as it is strongly coordinated to the chloride ions.[118] Interestingly, Azim and Stark later found that $CoCl_2{\cdot}6H_2O$ could lead to SOD/LTA mixed phase when a source of fluoride different than aqueous HF – tetramethylammonium fluoride ($[Me_4N]F$) – was used for the synthesis of CoAPOs with the ionic liquid [Bmim]Br and without the presence of tetraalkylammonium hydroxides.[106]

The use of bulkier ILs containing aromatic rings for the synthesis of CoAPO was recently introduced by Benin et al. Their study explored several substituted imidazolium bromide salts (Figure 1.11) to obtain a variety of framework topologies. A clear correlation between the ionic liquid used and the structure of the CoAPO isolated was observed. Cage-based CHA framework was obtained by using the smallest and more circular ILs *A* and *B*. The large IL *F* led to the mixed phase SAO and AFI, two large pore topologies, and the even larger *G* led to pure AFI phase. The intermediary ILs *C*, *D*, and *F* led to condensed SSZ-8 or DAF-1 phases.[123]

1.3.5 NiAPO

Azim and Stark reported the obtainment of a NiAPO with LTA topology by using the ionic liquid [Bmin]Br. $[Me_4N]F$ was added to the reaction mixture

to play the double role of co-OSDA and mineralizer, which is an interesting approach to explore fluoride sources other than the more toxic HF. The use of the different metal precursors $Ni(CH_3CO_2)_2 \cdot 4H_2O$ or $NiCl_2 \cdot 6H_2O$ was also investigated. The chloride salt led to a slightly higher nickel incorporation in the framework, which was attributed to its higher solubility when compared to the acetate form. This paper has been previously discussed in this chapter for the obtainment of Mn, Co and Fe MAPOs. The authors reported that the degree of doping follows the order $Fe^{2+} > Ni^{2+} > Mn^{2+} > Co^{2+}$ (for the respective topologies formed in each case) and that the substitution is preferred in the Al^{3+} sites.[106]

Benin et al. studied the Ni^{2+} doping in AlPOs with diverse framewroks with the use of a variation of imidazolium organo-cations. While NiAPO with LTA topology was successfully obtained, the authors were not able to isolate multidimensional large pores DFO and STO materials in the presence of nickel. Moreover, although an AFI product was obtained, extensive investigation of the Ni-AFI system by SS-NMR suggested no incorporation of nickel in this framework. This lack of incorporation was corroborated by analyses that did not identify the presence of acidity sites.[123]

1.3.6 CuAPO

The introduction of copper in the aluminophosphate framework is challenging due to the low electronic stability of Cu^{2+} at the high temperatures used for MAPOs synthesis and also due to its facile complexation with organic

species commonly used as OSDAs.[133] Nonetheless, Huang et al. presented the synthesis of CuAPO-5 (AFI) using [Bmin]Br as the ionic liquid in combination with TEAOH. X-ray fluorescence (XRF) revealed only small amounts were doped in the framework, even when the Cu^{2+} concentration in the medium was increased. Even though the metal was not inserted in the framework, its presence in the reaction medium greatly affect the porosity. The BET surface area increased with the addition of more copper. Too much metal precursor in the synthesis, however, led to a decrease in the surface area, possibly due to an accumulation of extra-framework copper species residing in the pores. NH_3 temperature-programmed desorption (NH_3-TPD) revealed the presence of acidic sites, corroborating the idea that copper was indeed able to replace aluminum centers. The material was then successfully used as the catalyst in the fructose dehydration reaction to produce 5-Hydroxymethylfurfural (HMF), an important platform chemical.[120]

CuAPO-5 was also obtained by Xin-Huang et al. using the DES succinic acid, choline chloride and TEABr. The authors used SEM and TEM to determine that the morphology of the crystallized molecular sieve is hexagonal nanometer-disc and both micro and mesoporous were found in its structure.[121]

1.3.7 ZnAPO

Pinar et al. were the first to report the use of the ionothermal route to obtain a ZnAPO. The material was synthesized using diisopropylimidazolium

bromide [DIPI]Br as the ionic liquid. It presents a DFO topology, which has only been found before for manganese-doped MAPOs. The authors extensively investigated the structural features using synchrotron XRD and SS-NMR. $[DIPI]^+$ cations were found residing in four different sites over two different channels. Remarkably, there is evidence that four $[DIPI]^+$ are ordered in the larger cavities of the structure, somehow working as a supramolecular OSDA (Figure 1.12). Water, F^- and OH^- were also found to be additional extra-framework species in other parts of the structure.[122]

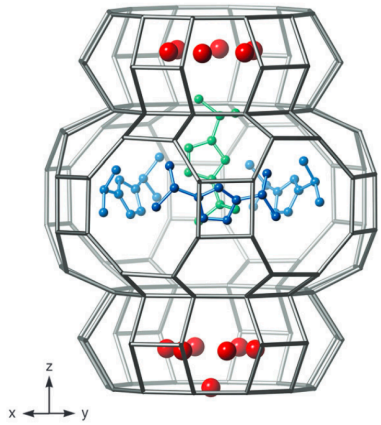

Figure 1.12 Detail on the ordered arrangement of four [DIPI]+ units inside the large cavity DFO ZnAPO described by Pinar et al.[122]

Benin et al. further contributed to the investigation of ionothermically synthesized ZnAPOs by using a series of imidazolium derived ionic liquids (Figure 1.11) to obtain materials with diverse topology (CHA, ATS, DFO, SAO, and AFI). As previously discussed in section 1.3.4, the shape and size of the ILs play an important role in directing the structure toward a specific topology. SS-NMR was used to study MAPOs obtained with the same ionic liquid but

containing different doped metals. The results showed that the metals themselves presented a structure-directing effect, as unique coordination ratios for P and Al were observed for each material, and the location of F^- has also been found to vary.[123]

1.4 Summary and Outcome

The literature review presented on this chapter showed the efficiency of the ionothermal route for the obtainment of MAPOs and at the same time underscored the complexity of the process. The ionic liquids have been shown to strongly direct the porous structure of the MAPOs in the majority of cases. Even when no IL is found occluded in the final framework, it still positively affects the synthesis as its low solvation properties makes the M^{2+} ions more available in the medium. Some of these metal ions exhibit a structure-directing effect even when not incorporated in the final framework, as reactions with and without them frequently leads to different zeolitic topologies.

The use of non-traditional starting materials led to many interesting results. Fluoride sources such as $[Me_4N]F$ and MnF_3 play not only the role of mineralizing agent but also act as SDA and, in the case of MnF_3, as the metal ion source. The successful FeAPO-5 synthesis from the metastable intermediate FeNKX-2, achieved when using H_3PO_3 instead of H_3PO_4, shows the phase transformation approach can be explored in ionothermal conditions.

The ionothermal strategy also unveiled novel and exciting structural features. The ionone liquid [DIPI]Br was used to obtain the first zinc-containing aluminophosphate with DFO topology. Remarkably, local ordering of four $[DIPI]^+$ groups was found in the larger cavities of the framework, showing supramolecular structure-directing effect is possible.

Ionothermal synthesis is an exciting strategy for the obtainment of MAPOs. Further studies on different systems are of interest in the field as they can bring insights on the importance of each reaction parameter and the crystallization mechanism itself. A deeper understanding on such topics will allow for a better synthetic design and open doors for the potential use of ionothermal methodologies in large scale industrial applications.

1.5 References

(1) Cronstedt, A. F. Rön Och Beskrifning - Om En Oberkant Barg Art, Som Kallas Zeolites, Kongl Vetenskaps Academiens Handlingar Stockholm, 17, 1756, p. 120.

(2) Colella, C.; Gualtieri, A. F. Cronstedt's Zeolite. *Microporous and Mesoporous Materials* **2007**, *105* (3), 213–221. https://doi.org/10.1016/j.micromeso.2007.04.056.

(3) *Zeolite Market Size, Share, Growth | Global Report [2022-2029]*. https://www.fortunebusinessinsights.com/industry-reports/zeolite-market-101921 (accessed 2023-06-11).

(4) Hartmann, M.; Kevan, L. Transition-Metal Ions in Aluminophosphate and Silicoaluminophosphate Molecular Sieves: Location, Interaction with Adsorbates and Catalytic Properties. *Chem. Rev.* **1999**, *99* (3), 635–664. https://doi.org/10.1021/cr9600971.

(5) Yu, J.; Xu, R. Rich Structure Chemistry in the Aluminophosphate Family. *Acc. Chem. Res.* **2003**, *36* (7), 481–490. https://doi.org/10.1021/ar0201557.

(6) IZA - International Zeolite Association. http://www.iza-structure.org/databases/ (accessed 2023-06-01).

(7) Blatov, V. A.; Delgado-Friedrichs, O.; O'Keeffe, M.; Proserpio, D. M. Three-Periodic Nets and Tilings: Natural Tilings for Nets. *Acta*

Crystallographica Section A **2007**, *63* (5), 418–425. https://doi.org/10.1107/S0108767307038287.

(8) Lo, A.-Y.; Taghipour, F. Review and Prospects of Microporous Zeolite Catalysts for CO2 Photoreduction. *Applied Materials Today* **2021**, *23*, 101042. https://doi.org/10.1016/j.apmt.2021.101042.

(9) Perego, C.; Bagatin, R.; Tagliabue, M.; Vignola, R. Zeolites and Related Mesoporous Materials for Multi-Talented Environmental Solutions. *Microporous and Mesoporous Materials* **2013**, *166*, 37–49. https://doi.org/10.1016/j.micromeso.2012.04.048.

(10) Dehghan, R.; Anbia, M. Zeolites for Adsorptive Desulfurization from Fuels: A Review. *Fuel Processing Technology* **2017**, *167*, 99–116. https://doi.org/10.1016/j.fuproc.2017.06.015.

(11) Ghasemi, Z.; Sourinejad, I.; Kazemian, H.; Rohani, S. Application of Zeolites in Aquaculture Industry: A Review. *Reviews in Aquaculture* **2018**, *10* (1), 75–95. https://doi.org/10.1111/raq.12148.

(12) Boer, D. G.; Langerak, J.; Pescarmona, P. P. Zeolites as Selective Adsorbents for CO2 Separation. *ACS Appl. Energy Mater.* **2023**, *6* (5), 2634–2656. https://doi.org/10.1021/acsaem.2c03605.

(13) Chatterjee, S.; Jeevanandham, S.; Mukherjee, M.; Vo, D.-V. N.; Mishra, V. Significance of Re-Engineered Zeolites in Climate Mitigation – A Review for Carbon Capture and Separation. *Journal of Environmental Chemical*

Engineering **2021**, *9* (5), 105957. https://doi.org/10.1016/j.jece.2021.105957.

(14) Calabrese, L. Anticorrosion Behavior of Zeolite Coatings Obtained by In Situ Crystallization: A Critical Review. *Materials* **2019**, *12* (1), 59. https://doi.org/10.3390/ma12010059.

(15) Calabrese, L.; Proverbio, E. A Brief Overview on the Anticorrosion Performances of Sol-Gel Zeolite Coatings. *Coatings* **2019**, *9* (6), 409. https://doi.org/10.3390/coatings9060409.

(16) Zarrintaj, P.; Mahmodi, G.; Manouchehri, S.; Mashhadzadeh, A. H.; Khodadadi, M.; Servatan, M.; Ganjali, M. R.; Azambre, B.; Kim, S.-J.; Ramsey, J. D.; Habibzadeh, S.; Saeb, M. R.; Mozafari, M. Zeolite in Tissue Engineering: Opportunities and Challenges. *MedComm* **2020**, *1* (1), 5–34. https://doi.org/10.1002/mco2.5.

(17) Serati-Nouri, H.; Jafari, A.; Roshangar, L.; Dadashpour, M.; Pilehvar-Soltanahmadi, Y.; Zarghami, N. Biomedical Applications of Zeolite-Based Materials: A Review. *Materials Science and Engineering: C* **2020**, *116*, 111225. https://doi.org/10.1016/j.msec.2020.111225.

(18) Hao, J.; Stavljenić Milašin, I.; Batu Eken, Z.; Mravak-Stipetic, M.; Pavelić, K.; Ozer, F. Effects of Zeolite as a Drug Delivery System on Cancer Therapy: A Systematic Review. *Molecules* **2021**, *26* (20), 6196. https://doi.org/10.3390/molecules26206196.

(19) Servatan, M.; Zarrintaj, P.; Mahmodi, G.; Kim, S.-J.; Ganjali, M. R.; Saeb, M. R.; Mozafari, M. Zeolites in Drug Delivery: Progress, Challenges and Opportunities. *Drug Discovery Today* **2020**, *25* (4), 642–656. https://doi.org/10.1016/j.drudis.2020.02.005.

(20) Wilson, S. T.; Lok, B. M.; Flanigen, E. M. Crystalline Metallophosphate Compositions. US-4310440-A.

(21) Wilson, S. T.; Lok, B. M.; Messina, C. A.; Cannan, T. R.; Flanigen, E. M. Aluminophosphate Molecular Sieves: A New Class of Microporous Crystalline Inorganic Solids. *J. Am. Chem. Soc.* **1982**, *104* (4), 1146–1147. https://doi.org/10.1021/ja00368a062.

(22) Sankar, G.; Sánchez-Sánchez, M. Metal-Substituted Microporous Aluminophosphates. In *Structure and Reactivity of Metals in Zeolite Materials*; Pérez Pariente, J., Sánchez-Sánchez, M., Eds.; Structure and Bonding; Springer International Publishing: Cham, 2018; pp 251–303. https://doi.org/10.1007/430_2018_25.

(23) Hussein, H.; Vivian, A.; Fusaro, L.; Devillers, M.; Aprile, C. Synthesis of Highly Accessible Gallosilicates via Impregnation Procedure: Enhanced Catalytic Performances in the Conversion of Glycerol into Solketal. *ChemCatChem* **2020**, *12* (23), 5966–5976. https://doi.org/10.1002/cctc.202001172.

(24) Tawbi, K.; Simon-Masseron, A.; Patarin, J. Synthesis of Microporous Gallophosphates Obtained by in Situ Decomposition of

Hexamethylphosphoramide. *Microporous and Mesoporous Materials* **2013**, *169*, 192–200. https://doi.org/10.1016/j.micromeso.2012.11.017.

(25) Li, L.; Pan, F.; Tanner, P. A.; Wong, K.-L. Tunable Dual Visible and Near-Infrared Persistent Luminescence in Doped Zinc Gallogermanate Nanoparticles for Simultaneous Photosensitization and Bioimaging. *ACS Appl. Nano Mater.* **2020**, *3* (2), 1961–1971. https://doi.org/10.1021/acsanm.9b02613.

(26) Qiu, B.; Lu, W.-D.; Gao, X.-Q.; Sheng, J.; Ji, M.; Wang, D.; Lu, A.-H. Boosting the Propylene Selectivity over Embryonic Borosilicate Zeolite Catalyst for Oxidative Dehydrogenation of Propane. *Journal of Catalysis* **2023**, *417*, 14–21. https://doi.org/10.1016/j.jcat.2022.11.031.

(27) Wang, G.-M.; Li, J.-H.; Gao, C.-L.; Zhang, J.-C.; Zhang, X.; Bao, Z.-Z.; Wang, Y.-X.; Lin, J.-H. Synthesis and Characterization of a Novel Inorganic–Organic Hybrid Open-Framework Zinc Phosphate with 16-Ring Channels. *Solid State Sciences* **2015**, *39*, 1–5. https://doi.org/10.1016/j.solidstatesciences.2014.11.007.

(28) Loewenstein, W. The Distribution of Aluminum in the Tetrahedra of Silicates and Aluminates. *American Mineralogist* **1954**, *39* (1–2), 92–96.

(29) BENNETT, J. M.; COHEN, J. P.; FLANIGEN, E. M.; PLUTH, J. J.; SMITH, J. V. Crystal Structure of Tetrapropylammonium Hydroxide—Aluminum Phosphate Number 5. In *Intrazeolite Chemistry*; ACS Symposium Series;

AMERICAN CHEMICAL SOCIETY, 1983; Vol. 218, pp 109–118. https://doi.org/10.1021/bk-1983-0218.ch006.

(30) Bialek, R.; Meier, W. M.; Davis, M.; Annen, M. J. The Synthesis and Structure of SSZ-24, the Silica Analog of AlPO4-5. *Zeolites* **1991**, *11* (5), 438–442. https://doi.org/10.1016/S0144-2449(05)80114-9.

(31) Foster, M. D.; Rivin, I.; Treacy, M. M. J.; Delgado Friedrichs, O. A Geometric Solution to the Largest-Free-Sphere Problem in Zeolite Frameworks. *Microporous and Mesoporous Materials* **2006**, *90* (1), 32–38. https://doi.org/10.1016/j.micromeso.2005.08.025.

(32) Annen, M. J.; Davis, M. E.; Higgins, J. B.; Schlenker, J. L. VPI-7: The First Zincosilicate Molecular Sieve Containing Three-Membered T-Atom Rings. *J. Chem. Soc., Chem. Commun.* **1991**, No. 17, 1175–1176. https://doi.org/10.1039/C39910001175.

(33) Annen, M. J.; Davis, M. E. Raman and 29Si MAS NMR Spectroscopy of Framework Materials Containing Three-Membered Rings. *Microporous Materials* **1993**, *1* (1), 57–65. https://doi.org/10.1016/0927-6513(93)80008-I.

(34) Takewaki, T.; Beck, L. W.; Davis, M. E. Zincosilicate CIT-6: A Precursor to a Family of *BEA-Type Molecular Sieves. *J. Phys. Chem. B* **1999**, *103* (14), 2674–2679. https://doi.org/10.1021/jp9845726.

(35) Zhang, X.; Liu, P.; Wu, Y.; Yao, Y.; Wang, J. Synthesis and Catalytic Performance of the Framework-Substituted Manganese β Zeolite. *Catal Lett* **2010**, *137* (3), 210–215. https://doi.org/10.1007/s10562-010-0367-3.

(36) Flanigen, E. M.; Lok, B. M.; Patton, R. L.; Wilson, S. T. Aluminophosphate Molecular Sieves and the Periodic Table. In *Studies in Surface Science and Catalysis*; Murakami, Y., Iijima, A., Ward, J. W., Eds.; New Developments in Zeolite Science and Technology; Elsevier, 1986; Vol. 28, pp 103–112. https://doi.org/10.1016/S0167-2991(09)60862-4.

(37) Qiu, S.; Tian, W.; Pang, W.; Sun, T.; Jiang, D. Synthesis and Characterization of Single Crystals of SAPO-5, BAPO-5, and LiAPO-5 Molecular Sieves. *Zeolites* **1991**, *11* (4), 371–375. https://doi.org/10.1016/0144-2449(91)80304-I.

(38) Xie, J.; Firth, D. S.; Cordero-Lanzac, T.; Airi, A.; Negri, C.; Øien-Ødegaard, S.; Lillerud, K. P.; Bordiga, S.; Olsbye, U. MAPO-18 Catalysts for the Methanol to Olefins Process: Influence of Catalyst Acidity in a High-Pressure Syngas (CO and H2) Environment. *ACS Catal.* **2022**, *12* (2), 1520–1531. https://doi.org/10.1021/acscatal.1c04694.

(39) Zhang, H. X.; Chokkalingam, A.; Subramaniam, P. V.; Joseph, S.; Takeuchi, S.; Wei, M. D.; Al-Enizi, A. M.; Jang, H.-G.; Kim, J.-H.; Seo, G.; Komura, K.; Sugi, Y.; Vinu, A. The Isopropylation of Biphenyl over Transition Metal Substituted Aluminophosphates: MAPO-5 (M: Co and Ni).

Journal of Molecular Catalysis A: Chemical **2016**, *412*, 117–124. https://doi.org/10.1016/j.molcata.2015.11.006.

(40) Feng, L.; Qi, X.; Li, J.; Zhu, Y.; Zhu, L. Synthesis of MgAPO-5 Molecular Sieves and Their Kinetic Behavior for n-Hexane Cracking. *React Kinet Catal Lett* **2009**, *98* (2), 327–339. https://doi.org/10.1007/s11144-009-0078-1.

(41) Maekawa, H.; Saha, S. K.; Mulla, S. A. R.; Waghmode, S. B.; Komura, K.; Kubota, Y.; Sugi, Y. Shape-Selective Alkylation of Biphenyl over Metalloaluminophosphates with AFI Topology. *Journal of Molecular Catalysis A: Chemical* **2007**, *263* (1), 238–246. https://doi.org/10.1016/j.molcata.2006.08.078.

(42) Fan, W.; Fan, B.; Song, M.; Chen, T.; Li, R.; Dou, T.; Tatsumi, T.; Weckhuysen, B. M. Synthesis, Characterization and Catalysis of (Co, V)-, (Co, Cr)- and (Cr, V)APO-5 Molecular Sieves. *Microporous and Mesoporous Materials* **2006**, *94* (1), 348–357. https://doi.org/10.1016/j.micromeso.2006.04.008.

(43) Chizallet, C.; Bouchy, C.; Larmier, K.; Pirngruber, G. Molecular Views on Mechanisms of Brønsted Acid-Catalyzed Reactions in Zeolites. *Chem. Rev.* **2023**, *123* (9), 6107–6196. https://doi.org/10.1021/acs.chemrev.2c00896.

(44) Sun, Q.; Xie, Z.; Yu, J. The State-of-the-Art Synthetic Strategies for SAPO-34 Zeolite Catalysts in Methanol-to-Olefin Conversion. *National Science Review* **2018**, *5* (4), 542–558. https://doi.org/10.1093/nsr/nwx103.

(45) Chang, C. D.; Silvestri, A. J. The Conversion of Methanol and Other O-Compounds to Hydrocarbons over Zeolite Catalysts. *Journal of Catalysis* **1977**, *47* (2), 249–259. https://doi.org/10.1016/0021-9517(77)90172-5.

(46) Evidence of Autocatalysis in Methanol to Hydrocarbon Reactions over Zeolite Catalysts. *Journal of Catalysis* **1979**, *59* (1), 123–129. https://doi.org/10.1016/S0021-9517(79)80050-0.

(47) Ye, R.-P.; Ding, J.; Gong, W.; Argyle, M. D.; Zhong, Q.; Wang, Y.; Russell, C. K.; Xu, Z.; Russell, A. G.; Li, Q.; Fan, M.; Yao, Y.-G. CO2 Hydrogenation to High-Value Products via Heterogeneous Catalysis. *Nat Commun* **2019**, *10* (1), 5698. https://doi.org/10.1038/s41467-019-13638-9.

(48) Gautam, P.; Neha; Upadhyay, S. N.; Dubey, S. K. Bio-Methanol as a Renewable Fuel from Waste Biomass: Current Trends and Future Perspective. *Fuel* **2020**, *273*, 117783. https://doi.org/10.1016/j.fuel.2020.117783.

(49) Salahudeen, N.; Rasheed, A. A.; Babalola, A.; Moses, A. U. Review on Technologies for Conversion of Natural Gas to Methanol. *Journal of Natural Gas Science and Engineering* **2022**, *108*, 104845. https://doi.org/10.1016/j.jngse.2022.104845.

(50) Wang, D.; Meng, W.; Zhou, H.; Yang, Y.; Xie, J.; Yang, S.; Li, G. Novel Coal-to-Methanol Process with near-Zero Carbon Emission: Pulverized Coal Gasification-Integrated Green Hydrogen Process. *Journal of Cleaner Production* **2022**, *339*, 130500. https://doi.org/10.1016/j.jclepro.2022.130500.

(51) Speybroeck, V. V.; Wispelaere, K. D.; Mynsbrugge, J. V. der; Vandichel, M.; Hemelsoet, K.; Waroquier, M. First Principle Chemical Kinetics in Zeolites: The Methanol-to-Olefin Process as a Case Study. *Chem. Soc. Rev.* **2014**, *43* (21), 7326–7357. https://doi.org/10.1039/C4CS00146J.

(52) Yarulina, I.; Chowdhury, A. D.; Meirer, F.; Weckhuysen, B. M.; Gascon, J. Recent Trends and Fundamental Insights in the Methanol-to-Hydrocarbons Process. *Nat Catal* **2018**, *1* (6), 398–411. https://doi.org/10.1038/s41929-018-0078-5.

(53) Wang, C.; Xu, J.; Deng, F. Mechanism of Methanol-to-Hydrocarbon Reaction over Zeolites: A Solid-State NMR Perspective. *ChemCatChem* **2020**, *12* (4), 965–980. https://doi.org/10.1002/cctc.201901937.

(54) Zhong, J.; Han, J.; Wei, Y.; Liu, Z. Catalysts and Shape Selective Catalysis in the Methanol-to-Olefin (MTO) Reaction. *Journal of Catalysis* **2021**, *396*, 23–31. https://doi.org/10.1016/j.jcat.2021.01.027.

(55) Hadi, N.; Farzi, A. A Review on Reaction Mechanisms and Catalysts of Methanol to Olefins Process. *Chemical Engineering Communications*

2022, *209* (12), 1664–1710. https://doi.org/10.1080/00986445.2021.1983547.

(56) Feng, S.-H.; Li, G.-H. Chapter 4 - Hydrothermal and Solvothermal Syntheses. In *Modern Inorganic Synthetic Chemistry (Second Edition)*; Xu, R., Xu, Y., Eds.; Elsevier: Amsterdam, 2017; pp 73–104. https://doi.org/10.1016/B978-0-444-63591-4.00004-5.

(57) Demazeau, G. Review. Solvothermal Processes: Definition, Key Factors Governing the Involved Chemical Reactions and New Trends. *Zeitschrift für Naturforschung B* **2010**, *65* (8), 999–1006. https://doi.org/10.1515/znb-2010-0805.

(58) Cundy, C. S.; Cox, P. A. The Hydrothermal Synthesis of Zeolites: Precursors, Intermediates and Reaction Mechanism. *Microporous and Mesoporous Materials* **2005**, *82* (1), 1–78. https://doi.org/10.1016/j.micromeso.2005.02.016.

(59) Wright, P. A. *Microporous Framework Solids*; RSC Materials Monographs; RSC Publishing: Cambrigde, UK, 2008.

(60) Mullin, J. W. *Crystallization*; Elsevier, 2001.

(61) Roberts, K. J.; Docherty, R.; Tamura, R. *Engineering Crystallography: From Molecule to Crystal to Functional Form*; NATO Science for Peace and Security Series; Springer, 2015.

(62) Thompson, R. W.; Dyer, A. A Modified Population Balance Model for Hydrothermal Molecular Sieve Zeolite Synthesis. *Zeolites* **1985**, *5* (5), 292–301. https://doi.org/10.1016/0144-2449(85)90161-7.

(63) Beischer, D. Kinetik Der Phasenbildung. Von Prof. Dr. M. Volmer. (Die Chemische Reaktion, Bd. 4.) 220 Seiten Mit 61 Abbildungen Und 15 Tabellen. Format 8°. Verlag Theodor Steinkopff, Dresden 1939. Preis Geb. RM 20.—, Brosch. RM 19 —. *Zeitschrift für Elektrochemie und angewandte physikalische Chemie* **1940**, *46* (5), 327–327. https://doi.org/10.1002/bbpc.19400460512.

(64) Kossel, W. Zur Energetik von Oberflächenvorgängen. *Annalen der Physik* **1934**, *413* (5), 457–480. https://doi.org/10.1002/andp.19344130502.

(65) Caullet, P.; Paillaud, J.-L.; Simon-Masseron, A.; Soulard, M.; Patarin, J. The Fluoride Route: A Strategy to Crystalline Porous Materials. *Comptes Rendus Chimie* **2005**, *8* (3), 245–266. https://doi.org/10.1016/j.crci.2005.02.001.

(66) Xu, J.; Chen, L.; Zeng, D.; Yang, J.; Zhang, M.; Ye, C.; Deng, F. Crystallization of AlPO4-5 Aluminophosphate Molecular Sieve Prepared in Fluoride Medium: A Multinuclear Solid-State NMR Study. *J. Phys. Chem. B* **2007**, *111* (25), 7105–7113. https://doi.org/10.1021/jp0710133.

(67) Xu, Y.; Maddox, P. J.; Couves, J. W. The Synthesis of SAPO-34 and CoSAPO-34 from a Triethylamine–Hydrofluoric Acid–Water System. *J.*

Chem. Soc., Faraday Trans. **1990**, *86* (2), 425–429. https://doi.org/10.1039/FT9908600425.

(68) Sierra, L.; Patarin, J.; Guth, J. L. Synthesis of Aluminophosphate and Derived Materials with the ZON Structure-Type. *Microporous and Mesoporous Materials* **2000**, *38* (2), 123–133. https://doi.org/10.1016/S1387-1811(99)00259-0.

(69) Pei, R.; Tian, Z.; Wei, Y.; Li, K.; Xu, Y.; Wang, L.; Ma, H. Ionothermal Synthesis of AlPO4-34 Molecular Sieves Using Heterocyclic Aromatic Amine as the Structure Directing Agent. *Materials Letters* **2010**, *64* (21), 2384–2387. https://doi.org/10.1016/j.matlet.2010.07.058.

(70) Newalkar, B. L.; Kamath, B. V.; Jasra, R. V.; Bhat, S. G. T. The Effect of Gel PH on the Crystallization of Aluminophosphate Molecular Sieve AlPO4-5. *Zeolites* **1997**, *18* (4), 286–290. https://doi.org/10.1016/S0144-2449(97)00015-8.

(71) García-Carmona, J.; Rodríguez-Clemente, R.; Gómez-Morales, J. Directed Crystallization of Selected Aluminophosphate Hydrates by PH Control. *Advanced Materials* **1998**, *10* (1), 46–49. https://doi.org/10.1002/(SICI)1521-4095(199801)10:1<46::AID-ADMA46>3.0.CO;2-8.

(72) Jiao, X.; Wang, Y.; Mu, Y.; Sun, Y.; Li, J. A New Magnesium-Containing Aluminophosphate with a Zeolite-like Structure. *RSC Adv.* **2015**, *6* (2), 1098–1102. https://doi.org/10.1039/C5RA22194C.

(73) Zhao, X.; Wang, Q.; Duan, W.; Li, G.; Ji, D.; Zhao, Y. Synthesis of ATN-Type FeAPO-39 Molecular Sieves without Solvent Using the Additional Structure-Directing Effect of the Iron Source. *European Journal of Inorganic Chemistry* **2018**, *2018* (39), 4331–4337. https://doi.org/10.1002/ejic.201800729.

(74) Grandjean, D.; Beale, A. M.; Petukhov, A. V.; Weckhuysen, B. M. Unraveling the Crystallization Mechanism of CoAPO-5 Molecular Sieves under Hydrothermal Conditions. *J. Am. Chem. Soc.* **2005**, *127* (41), 14454–14465. https://doi.org/10.1021/ja054014m.

(75) Simmance, K.; Beek, W. van; Sankar, G. Time Resolved in Situ X-Ray Diffraction Study of Crystallisation Processes of Large Pore Nanoporous Aluminophosphate Materials. *Faraday Discuss.* **2015**, *177* (0), 237–247. https://doi.org/10.1039/C4FD00179F.

(76) *Insights into the Chemistry of Organic Structure-Directing Agents in the Synthesis of Zeolitic Materials*; Gómez-Hortigüela, L., Ed.; Structure and Bonding; Springer International Publishing: Cham, 2018; Vol. 175. https://doi.org/10.1007/978-3-319-74289-2.

(77) Barrer, R. M.; Denny, P. J. 201. Hydrothermal Chemistry of the Silicates. Part IX. Nitrogenous Aluminosilicates. *J. Chem. Soc.* **1961**, No. 0, 971–982. https://doi.org/10.1039/JR9610000971.

(78) Vinaches, P.; Bernardo-Gusmão, K.; Pergher, S. B. C. An Introduction to Zeolite Synthesis Using Imidazolium-Based Cations as Organic Structure-

Directing Agents. *Molecules* **2017**, *22* (8), 1307. https://doi.org/10.3390/molecules22081307.

(79) Wadlinger, R. L.; Kerr, G. T.; Rosinski, E. W. Catalytic Composition of a Crystalline Zeolite. US-3308069-A.

(80) Argauer, R. J.; Landolt, G. R. Crystalline Zeolite Zsm-5 and Method of Preparing the Same. US-3702886-A, 1972.

(81) Nagy, J. B.; Bodart, P.; Collette, H.; Fernandez, C.; Gabelica, Z.; Nastro, A.; Aiello, R. Characterization of Crystalline and Amorphous Phases during the Synthesis of (TPA, M)-ZSM-5 Zeolites (M = Li, Na, K). *J. Chem. Soc., Faraday Trans. 1* **1989**, *85* (9), 2749–2769. https://doi.org/10.1039/F19898502749.

(82) Goepper, M.; Li, H.-X.; Davis, M. E. A Possible Role of Alkali Metal Ions in the Synthesis of Pure-Silica Molecular Sieves. *J. Chem. Soc., Chem. Commun.* **1992**, No. 22, 1665–1666. https://doi.org/10.1039/C39920001665.

(83) Corma, A.; Díaz-Cabañas, M. J.; Jiang, J.; Afeworki, M.; Dorset, D. L.; Soled, S. L.; Strohmaier, K. G. Extra-Large Pore Zeolite (ITQ-40) with the Lowest Framework Density Containing Double Four- and Double Three-Rings. *Proceedings of the National Academy of Sciences* **2010**, *107* (32), 13997–14002. https://doi.org/10.1073/pnas.1003009107.

(84) Corma, A.; Navarro, M. T.; Rey, F.; Valencia, S. Synthesis of Pure Polymorph C of Beta Zeolite in a Fluoride-Free System. *Chem. Commun.* **2001**, No. 16, 1486–1487. https://doi.org/10.1039/B104114M.

(85) Shayib, R. M.; George, N. C.; Seshadri, R.; Burton, A. W.; Zones, S. I.; Chmelka, B. F. Structure-Directing Roles and Interactions of Fluoride and Organocations with Siliceous Zeolite Frameworks. *J. Am. Chem. Soc.* **2011**, *133* (46), 18728–18741. https://doi.org/10.1021/ja205164u.

(86) Choi, M.; Na, K.; Kim, J.; Sakamoto, Y.; Terasaki, O.; Ryoo, R. Stable Single-Unit-Cell Nanosheets of Zeolite MFI as Active and Long-Lived Catalysts. *Nature* **2009**, *461* (7261), 246–249. https://doi.org/10.1038/nature08288.

(87) Villaescusa, L. A.; Camblor, M. A. Time Evolution of an Aluminogermanate Zeolite Synthesis: Segregation of Two Closely Similar Phases with the Same Structure Type. *Chem. Mater.* **2016**, *28* (9), 3090–3098. https://doi.org/10.1021/acs.chemmater.6b00507.

(88) Moliner, M.; González, J.; Portilla, M. T.; Willhammar, T.; Rey, F.; Llopis, F. J.; Zou, X.; Corma, A. A New Aluminosilicate Molecular Sieve with a System of Pores between Those of ZSM-5 and Beta Zeolite. *J. Am. Chem. Soc.* **2011**, *133* (24), 9497–9505. https://doi.org/10.1021/ja2015394.

(89) Davis, M. E.; Lobo, R. F. Zeolite and Molecular Sieve Synthesis. *Chem. Mater.* **1992**, *4* (4), 756–768. https://doi.org/10.1021/cm00022a005.

(90) Gómez-Hortigüela, L.; Pérez-Pariente, J.; Corà, F. Insights into Structure Direction of Microporous Aluminophosphates: Competition between Organic Molecules and Water. *Chemistry – A European Journal* **2009**, *15* (6), 1478–1490. https://doi.org/10.1002/chem.200801458.

(91) Zhang, X.; Yang, M.; Tian, P.; Liu, Z. Progress in Seed-Assisted Synthesis of (Silico)Aluminophosphate Molecular Sieves. *Chem. Res. Chin. Univ.* **2022**, *38* (1), 1–8. https://doi.org/10.1007/s40242-022-1407-4.

(92) Fan, D.; Barrier, N.; Vicente, A.; Gilson, J.-P.; Clevers, S.; Dupray, V.; Coquerel, G.; Valtchev, V. Organic Template-Free Synthesis of an Open Framework Silicoaluminophosphate (SAPO) with High Thermal Stability and High Ionic Conductivity. *Inorg. Chem. Front.* **2020**, *7* (2), 542–553. https://doi.org/10.1039/C9QI01223K.

(93) Wang, Y.; Xu, Y.; Tian, Z.; Lin, L. Research Progress in Ionothermal Synthesis of Molecular Sieves. *Chinese Journal of Catalysis* **2012**, *33* (1), 39–50. https://doi.org/10.1016/S1872-2067(11)60343-4.

(94) Morris, R. E. Ionothermal Synthesis—Ionic Liquids as Functional Solvents in the Preparation of Crystalline Materials. *Chem. Commun.* **2009**, No. 21, 2990–2998. https://doi.org/10.1039/B902611H.

(95) Eike, D. M.; Brennecke, J. F.; Maginn, E. J. Predicting Melting Points of Quaternary Ammonium Ionic Liquids. *Green Chem.* **2003**, *5* (3), 323–328. https://doi.org/10.1039/B301217D.

(96) Hallett, J. P.; Welton, T. Room-Temperature Ionic Liquids: Solvents for Synthesis and Catalysis. 2. *Chem. Rev.* **2011**, *111* (5), 3508–3576. https://doi.org/10.1021/cr1003248.

(97) Cooper, E. R.; Andrews, C. D.; Wheatley, P. S.; Webb, P. B.; Wormald, P.; Morris, R. E. Ionic Liquids and Eutectic Mixtures as Solvent and Template in Synthesis of Zeolite Analogues. *Nature* **2004**, *430* (7003), 1012–1016. https://doi.org/10.1038/nature02860.

(98) Wang, L.; Xu, Y.-P.; Wang, B.-C.; Wang, S.-J.; Yu, J.-Y.; Tian, Z.-J.; Lin, L.-W. Ionothermal Synthesis of Magnesium-Containing Aluminophosphate Molecular Sieves and Their Catalytic Performance. *Chemistry – A European Journal* **2008**, *14* (34), 10551–10555. https://doi.org/10.1002/chem.200801383.

(99) Carvalho, M. M.; Ruotolo, L. A. M.; Fernandez-Felisbino, R. Synthesis of Aluminophosphate by the Ionothermal Method Using Factorial Design. *Microporous and Mesoporous Materials* **2013**, *165*, 163–167. https://doi.org/10.1016/j.micromeso.2012.08.020.

(100) Wei, Y.; Zhang, L.; Tian, Z. Isomorphous Substitution Induced Ionothermal Synthesis of Magnesium Aluminophosphate Zeolites in Fluoride-Free Media. *RSC Adv.* **2016**, *6* (66), 61915–61919. https://doi.org/10.1039/C6RA12678B.

(101) Benin, A. I.; Hwang, S.-J.; Zones, S. I.; Xie, D.; Chaudhuri, K.; Lacheen, H. Structural and Compositional Studies of Crystalline MAPO Molecular

Sieves Formed in Ionothermal Synthesis Using Imidazolium Bromides. *Microporous and Mesoporous Materials* **2019**, *274*, 257–265. https://doi.org/10.1016/j.micromeso.2018.07.052.

(102) Wang, P.; Liu, H.; Wang, C.; Lv, G.; Wang, D.; Ma, H.; Tian, Z. Direct Synthesis of Shaped MgAPO-11 Molecular Sieves and the Catalytic Performance in n-Dodecane Hydroisomerization. *RSC Adv.* **2021**, *11* (41), 25364–25374. https://doi.org/10.1039/d1ra03758g.

(103) Ng, E.-P.; Itani, L.; Sekhon, S. S.; Mintova, S. Micro- to Macroscopic Observations of MnAlPO-5 Nanocrystal Growth in Ionic-Liquid Media. *Chemistry – A European Journal* **2010**, *16* (43), 12890–12897. https://doi.org/10.1002/chem.201001083.

(104) Bieniok, A.; Brendel, U.; Sereni, P.; Musso, M. Raman spectroscopy and crystal structure investigation of solvo- and ionothermally prepared microporous metal-aluminophosphates with the laumontite framework structure. *Zeitschrift für Kristallographie - Crystalline Materials* **2013**, *228* (8), 374–381. https://doi.org/10.1524/zkri.2013.1599.

(105) Liu, H.; Tian, Z.; Wang, L.; Wang, Y.; Li, D.; Ma, H.; Xu, R. Ionothermal Synthesis of MnAPO-SOD Molecular Sieve without the Aid of Organic Structure-Directing Agents. *Inorg. Chem.* **2016**, *55* (4), 1809–1815. https://doi.org/10.1021/acs.inorgchem.5b02700.

(106) Azim, M. M.; Stark, A. Ionothermal Synthesis and Characterisation of Mn-, Co-, Fe- and Ni-Containing Aluminophosphates. *Microporous and*

Mesoporous Materials **2018**, *272*, 251–259. https://doi.org/10.1016/j.micromeso.2018.06.045.

(107) Han, L.; Wang, Y.; Li, C.; Zhang, S.; Lu, X.; Cao, M. Simple and Safe Synthesis of Microporous Aluminophosphate Molecular Sieves by Ionothermal Approach. *AIChE Journal* **2008**, *54* (1), 280–288. https://doi.org/10.1002/aic.11363.

(108) Zhao, X.; Kang, C.; Wang, H.; Luo, C.; Li, G.; Wang, X. Ionothermal Synthesis of FeAlPO-16 Molecular Sieve by Microwave Irradiation in Eutectic Mixture. *J Porous Mater* **2011**, *18* (5), 615–621. https://doi.org/10.1007/s10934-010-9417-x.

(109) Zhao, X.; Wang, H.; Dong, B.; Sun, Z.; Li, G.; Wang, X. Facile Synthesis of FeAlPO-5 Molecular Sieve in Eutectic Mixture via a Microwave-Assisted Process. *Microporous and Mesoporous Materials* **2012**, *151*, 56–63. https://doi.org/10.1016/j.micromeso.2011.11.016.

(110) Zhao, X.; Sun, Z.; Zhu, Z.; Li, A.; Li, G.; Wang, X. Evaluation of Iron-Containing Aluminophosphate Molecular Sieve Catalysts Prepared by Different Methods for Phenol Hydroxylation. *Catal Lett* **2013**, *143* (7), 657–665. https://doi.org/10.1007/s10562-013-1027-1.

(111) Ng, E.-P.; Ghoy, J.-P.; Awala, H.; Vicente, A.; Adnan, R.; Ling, T. C.; Mintova, S. Ionothermal Synthesis of FeAPO-5 in the Presence of Phosphorous Acid. *CrystEngComm* **2015**, *18* (2), 257–265. https://doi.org/10.1039/C5CE01973G.

(112) Zhao, X.; Zhang, X.; Hao, Z.; Gao, X.; Liu, Z. Synthesis of FeAPO-5 Molecular Sieves with High Iron Contents via Improved Ionothermal Method and Their Catalytic Performances in Phenol Hydroxylation. *J Porous Mater* **2018**, *25* (4), 1007–1016. https://doi.org/10.1007/s10934-017-0511-1.

(113) Zhao, X.; Duan, W.; Wang, Q.; Ji, D.; Zhao, Y.; Li, G. Microwave-Assisted Ionothermal Synthesis of Fe-LEV Molecular Sieve with High Iron Content in Low-Dosage of Eutectic Mixture. *Microporous and Mesoporous Materials* **2019**, *275*, 253–262. https://doi.org/10.1016/j.micromeso.2018.09.005.

(114) Musa, M.; Dawson, D. M.; Morris, R. E.; Ashbrook, S. E. Synthesis of FeAPO-34 Molecular Sieve under Ionothermal Condition. *Inorg. Chem.* **2022**, *61* (42), 16685–16692. https://doi.org/10.1021/acs.inorgchem.2c02352.

(115) Parnham, E. R.; Morris, R. E. The Ionothermal Synthesis of Cobalt Aluminophosphate Zeolite Frameworks. *J. Am. Chem. Soc.* **2006**, *128* (7), 2204–2205. https://doi.org/10.1021/ja057933l.

(116) Drylie, E. A.; Wragg, D. S.; Parnham, E. R.; Wheatley, P. S.; Slawin, A. M. Z.; Warren, J. E.; Morris, R. E. Ionothermal Synthesis of Unusual Choline-Templated Cobalt Aluminophosphates. *Angewandte Chemie International Edition* **2007**, *46* (41), 7839–7843. https://doi.org/10.1002/anie.200702239.

(117) Li, D.; Xu, Y.; Wang, Y.; Liu, H.; Wang, B.; Ma, H.; Xu, R.; Tian, Z. Ionothermal Syntheses and Characterizations of Cobalt-Substituted Extra-Large Pore Aluminophosphate Molecular Sieves with -CLO Topology. *Microporous and Mesoporous Materials* **2014**, *198*, 153–160. https://doi.org/10.1016/j.micromeso.2014.07.029.

(118) Li, D.; Xu, Y.; Ma, H.; Xu, R.; Wang, Y.; Liu, H.; Wang, B.; Tian, Z. Ionothermal Syntheses of Transition-Metal-Substituted Aluminophosphate Molecular Sieves in the Presence of Tetraalkylammonium Hydroxides. *Microporous and Mesoporous Materials* **2015**, *210*, 125–132. https://doi.org/10.1016/j.micromeso.2015.02.028.

(119) Musa, M.; Dawson, D. M.; Ashbrook, S. E.; Morris, R. E. Ionothermal Synthesis and Characterization of CoAPO-34 Molecular Sieve. *Microporous and Mesoporous Materials* **2017**, *239*, 336–341. https://doi.org/10.1016/j.micromeso.2016.09.045.

(120) Huang, Y.; Zhang, P.; Hu, H.; Hu, D.; Yang, J.; Zhang, Y.; Chen, C.; Yang, Y.; Zhang, J.; Wang, L. Efficient Production of 5-Hydroxymethylfurfural from Fructose over CuAPO-5 Molecular Sieves Synthesized Using an Ionothermal Method. *RSC Adv.* **2019**, *9* (56), 32848–32853. https://doi.org/10.1039/C9RA07217A.

(121) Xin-Hong, Z.; Juan-Juan, W.; Jing, C.; Jiang-Bo, Z.; Yong-Dong, Q.; Gui-Xian, L. Ionothermal Synthesis of Hierarchical Structured CuAPO-5 Molecular Sieve. *Chin. J. Inorg. Chem.* **2015**, *31* (1), 29–36.

(122) Pinar, A. B.; McCusker, L. B.; Baerlocher, C.; Hwang, S.-J.; Xie, D.; Benin, A. I.; Zones, S. I. Synthesis and Structural Characterization of Zn-Containing DAF-1. *New J. Chem.* **2016**, *40* (5), 4160–4166. https://doi.org/10.1039/C5NJ02897C.

(123) Benin, A.; Hwang, S.-J.; Zones, S.; Xie, D.; Chaudhuri, K.; Lacheen, H. Structural and Compositional Studies of Crystalline MAPO Molecular Sieves Formed in Ionothermal Synthesis Using Imidazolium Bromides. *Microporous Mesoporous Mat.* **2019**, *274*, 257–265. https://doi.org/10.1016/j.micromeso.2018.07.052.

(124) Smith, E. L.; Abbott, A. P.; Ryder, K. S. Deep Eutectic Solvents (DESs) and Their Applications. *Chem. Rev.* **2014**, *114* (21), 11060–11082. https://doi.org/10.1021/cr300162p.

(125) Płotka-Wasylka, J.; de la Guardia, M.; Andruch, V.; Vilková, M. Deep Eutectic Solvents vs Ionic Liquids: Similarities and Differences. *Microchemical Journal* **2020**, *159*, 105539. https://doi.org/10.1016/j.microc.2020.105539.

(126) Parnham, E. R.; Morris, R. E. 1-Alkyl-3-Methyl Imidazolium Bromide Ionic Liquids in the Ionothermal Synthesis of Aluminium Phosphate Molecular Sieves. *Chem. Mater.* **2006**, *18* (20), 4882–4887. https://doi.org/10.1021/cm0615929.

(127) Zhao, R.; Dong, M.; Qin, Z.; Wang, J. Synthesis of Small Particle-Sized CoAPO-5 and CoAPO-20 by Surfactant-Assisted Method. *Materials*

Letters **2008**, *62* (30), 4573–4575. https://doi.org/10.1016/j.matlet.2008.08.055.

(128) Yu, J.; Xu, R.; Li, J. Structural Diversity of a Family of Aluminophosphates with Al/P Ratio of Non-Unity. *Solid State Sciences* **2000**, *2* (2), 181–192. https://doi.org/10.1016/S1293-2558(00)00120-5.

(129) Han, L.; Wang, Y.; Li, C.; Zhang, S.; Lu, X.; Cao, M. Simple and Safe Synthesis of Microporous Aluminophosphate Molecular Sieves by Ionothermal Approach. *AIChE Journal* **2008**, *54* (1), 280–288. https://doi.org/10.1002/aic.11363.

(130) Li, N.; Ma, Y.; Xiang, S.; Guan, N. Capturing an Aluminophosphite Intermediate in the New Route of Synthesizing Zeolite-like Aluminophosphates. *Chem. Mater.* **2006**, *18* (4), 975–980. https://doi.org/10.1021/cm052327a.

(131) Yasaka, Y.; Wakai, C.; Matubayasi, N.; Nakahara, M. Slowdown of H/D Exchange Reaction Rate and Water Dynamics in Ionic Liquids: Deactivation of Solitary Water Solvated by Small Anions in 1-Butyl-3-Methyl-Imidazolium Chloride. *J. Phys. Chem. A* **2007**, *111* (4), 541–543. https://doi.org/10.1021/jp0673720.

(132) Martineau, C.; Bouchevreau, B.; Tian, Z.; Lohmeier, S.-J.; Behrens, P.; Taulelle, F. Beyond the Limits of X-Ray Powder Diffraction: Description of the Nonperiodic Subnetworks in Aluminophosphate-Cloverite by NMR

Crystallography. *Chem. Mater.* **2011**, *23* (21), 4799–4809. https://doi.org/10.1021/cm2021033.

(133) Ke, Q.; Wu, M.; Yu, H.; Lu, G. Superior Catalytic Performance of Hierarchically Micro-Meso-Macroporous CuAlPO-5 for the Oxidation of Aromatic Amines under Mild Conditions. *ChemCatChem* **2017**, *9* (5), 733–737. https://doi.org/10.1002/cctc.201601157.

Chapter 2 - MAPO-5 Molecular Sieves from Alkylimidazolium Bromide Ionic Liquids

Abstract

MnAPO-5 (Mn-AFI) was synthesized via the ionothermal route using with two different ionic liquids (ILs), diisopropylimidazolium bromide (DIPI) and diisobutylimidazolium bromide (DIBU). Attempts were also made to synthesize NiAPO-5 (Ni-AFI) using the same ILs; although there is some evidence of nickel structure-directing capabilities, there was no data suggesting Ni framework incorporation. The ILs acted as both the solvent and the structure-directing agent (SDA). Each SDA demonstrated AFI to dense-phase cristobalite or tridymite phase formation when the level of nickel was increased in the reaction mixture. For increasing level of manganese, DIBU always yielded pure-phase Mn-AFI whereas DIPI led to amorphous product when more than 0.13 eq of Mn was added. The resulting products were analyzed by solid state NMR (SS-NMR) to gain mechanistic insight on product formation. By selecting both an appropriate SDA and tuning the amount of Mn in a given reaction, a pure-phase AFI material was reproducibly achieved by a simple one-pot method. Because of the vanishingly low vapor pressure of the ILs, the synthesis does not carry the risk of pressure build-up. Finally, the ILs were easily and fully recyclable and used for multiple syntheses. The MnAPO-5 material was characterized with powder X-ray diffraction (PXRD), thermogravimetric analysis (TGA),

electron paramagnetic resonance (EPR), multinuclear SS-NMR and extended X-ray absorption fine structure (EXAFS). These findings provide new insight into the ionothermal synthesis of metal-doped AFI frameworks with possible implications in catalytic applications.

2.1 Introduction

Zeolite and zeotype materials are widely used as catalysts for a large range of applications due to their molecular-sized pore structures and catalytic capabilities.[1,2] The aluminophosphate form (the first series from Union Carbide were labeled $AlPO_4$-n, where n = structure type) are comprised of AlO_4 and PO_4 tetrahedra connected *via* bridging oxygens. $AlPO_4$-n molecular sieves are neutral in charge and therefore as-prepared are not useful in catalysis. Isomorphic replacement of Al^{3+} with M^{2+} (M = metal), however, can afford metal-aluminophosphates (MAPOs) with Brønsted acidity. The benefit of MAPOs compared to the widely used silicoaluminophosphate molecular sieves (SAPOs) is the MAPO acidity can be tuned to the application for which the catalyst is needed. The appropriate substitutional metal is chosen, as different metals have been shown to provide varying catalytic strength.[3–7]

Traditionally, $AlPO_4$-n and MAPO-n materials are synthesized hydrothermally by adding the precursors along with a structure directing agent (SDA) into the water to make a heterogeneous mixture, then heating to 100-250 °C.[1] Hydrothermal syntheses are inherently high-pressure and therefore

have associated potential hazards, especially on the large scale. Additionally, because water is in far excess to the SDA, it can compete with the SDA in templating the resultant material. In 2004, Cooper *et al*. presented an alternate synthetic route to $AlPO_4$-n materials using ionic liquids (ILs), which they termed ionothermal synthesis.[8] Generally, ILs are salts with melting points below 100 °C. Consisting of simply an anion and cation, there are literally millions of possible ionic liquids. There are several benefits to ionothermal synthesis of aluminophosphates. ILs have virtually zero vapor pressure, are relatively non-toxic, and are easily reused.[3] Additionally, the organic cation of the IL can act as the SDA in the synthesis. Consequently, ionothermal synthesis not only removes the hazards of high-pressure hydrothermal synthesis, but it also eliminates competition between the solvent and the SDA since the solvent *is* the SDA. Since ionothermal synthesis represents a non-aqueous medium, water can be introduced as a reagent, which offers the opportunity to study its hydrolytic effects on the system. Finally, non-aqueous conditions can lead to new framework and low-dimensional phases not possible in hydrothermal syntheses.[9,10]

Studies have shown that both Ni and Mn incorporation into the $AlPO_4$-5 framework (AFI) are not very favorable. Although Ni substitution has been claimed, the evidence of actual tetrahedral framework incorporation is limited.[11,12] As a d^8 metal, it is challenging to force Ni^{2+} into a tetrahedral geometry over its preferred octahedral geometry. It is possible that the Ni

reported as being incorporated into the $AlPO_4$-5 framework was actually octahedral in geometry, either on the surface of the material or in a defect site within the structure. Some fairly extensive work has looked at Mn incorporation into the $AlPO_4$-5 framework. Evidence shows a larger degree of extra-framework presence as compared to actual framework incorporation, but nevertheless intraframework incorporation was 1-2%.[13–17] Although Mn has typically limited substitution into the tetrahedral $AlPO_4$-5 molecular sieve, the d^5 configuration may provide greater geometric flexibility, making it less challenging to incorporate than d^8 Ni^{2+}.

Recently, Benin *et al*. published a comprehensive study on the ionothermal synthesis of MAPOs using a variety of ionic liquids and several metals including nickel.[18] The researchers concluded nickel was not introduced into the tetrahedral framework for the $AlPO_4$-5 structure, but did find evidence of nickel incorporation into the LTA structure. Manganese was not explored in their study. Benin *et al*. made significant steps forward in understanding the effects of ionic liquid SDAs and the varying substitutional metals on the structure of the resulting molecular sieve, as well as possible location of catalytic sites within.[18] Still not well understood, however, is the effect of adding water into this non-aqueous system; nor is the effect of hydrofluoric acid (HF), which seems to be necessary as a mineralizer within the ionothermal system. Here, we studied two metals, Mn and Ni, for their influence on the synthesis of $AlPO_4$-5 versus that of water and HF. We use two similar ionic liquids as our

SDAs that are not commercially available, diisopropylimidazolium bromide (DIPI) and diisobutylimidazolium bromide (DIBU), to identify whether there are product selectivity differences between the two. Potential metal incorporation is explored for both Mn and Ni and the materials are characterized using a wide range of solid-state techniques.

2.2 Experimental

2.2.1 Reagents

Aluminum isopropoxide ($Al[OCH(CH_3)_2]_3$, TCI America, ≥ 98%), phosphoric acid (H_3PO_4, Sigma-Aldrich, 85 wt.% in H_2O), nickel(II) acetate tetrahydrate ($NiCH_3CO_2 \cdot 4H_2O$, Acros Organics, > 99%) manganese(II) acetate tetrahydrate ($MnCH_3CO_2 \cdot 4H_2O$, Sigma-Aldrich, > 99%) and hydrofluoric acid (HF, Acros Organics, 51 wt.% in H_2O) were used as-received for the syntheses.

Diisopropylimidazolium X^- (DIPI) and diisobutylimidazolium X^- (DIBU) were supplied by one of the co-authors (S. I. Z.) either as bromide or hydroxide salts solvated in excess water, prepared using previously published methods.[19] For the bromide salts in water, the solutions were placed on a low-pressure rotovap until most of the water was driven off. At this point, the IL was still liquid but much more viscous. The resulting solution was then placed in a vacuum oven overnight at 70 °C to drive off the remaining water. Once removed from the oven, the IL had solidified. To ensure the purity of the product, the IL was then purify by performing a Soxhlet extraction with methanol (MeOH) as the

solvent. It was again allowed to dry in a vacuum oven overnight after removal of most of the MeOH *via* rotary evaporation. The resulting IL purity was then confirmed via ^{1}H NMR in $CDCl_3$ solvent. For the hydroxide version, a titration with HBr was performed first, then the same procedure was followed. To complete the titration, concentrated HBr was added drop-wise while measuring the pH. The titration was complete when the pH reached 7. Often, the resulting solution would be acidic (pH 1 to 4) due to slight overshoot, but this acidity did not have any noticeable effect on the syntheses and was used directly without buffering back to neutral.

2.2.2 MAPO-5 synthesis

In a typical MAPO-5 synthesis, aluminum isopropoxide, metal acetate tetrahydrate (metal = Ni or Mn), IL SDA and H_3PO_4 were combined in a Teflon liner and mixed intimately. The HF was then added and the components mixed again. The molar ratios were approximately 1 : (0.1 to 0.4) : 10 : 1.3 : 0.12, respectively. The divalent metal had a range of equivalencies depending on the experiment. For the HF studies, the divalent metal equivalence was kept constant at 0.11 while the HF varied from 0.0 to 0.6. The liner was sealed in a stainless-steel jacket and placed in a 135 °C oven for 5 d. The resulting material was vacuum filtered and rinsed first with deionized water followed by acetone. The material was placed in a 90 °C oven for 30 min to dry prior to PXRD analysis.

2.2.3 Ionic liquid re-purification

IL already used for synthesis was re-purified *via* Soxhlet extraction with methanol as the solvent. The extractions were run overnight in all cases for a minimum of 18 h. A majority of the methanol was then evaporated under low pressure with a rotary evaporator and the remaining IL-methanol solution was placed in a vacuum oven at 70 °C overnight to evaporate the remaining methanol. The resulting purified IL was checked for purity using ^{1}H NMR in $CDCl_3$. It was found that excess metal ions remained in the purified IL as determined by ICP-OES. This excess was accounted for when completing further MAPO synthesis with the re-purified IL ("M-IL", see Supporting Information). To determine the amount of Ni^{2+} in "Ni-IL", 1.1 mg of the Ni-IL was added to a 10 mL volumetric flask. 1% nitric acid in 21 MΩ deionized water was added to the volumetric line, and the resulting solution was analyzed by ICP-OES.

2.2.4 Instrumentation

Powder X-ray diffraction

PXRD was measured on a Rigaku Americas Miniflex Plus diffractometer, scanning from 2° to 50° (2θ) at a rate of $2°\cdot min^{-1}$ with a 0.04° step size under Cu-Kα radiation (λ = 1.5418 Å).

Nuclear magnetic resonance spectroscopy

Initial studies of high-resolution ^{31}P and ^{55}Mn multinuclear magic angle spinning (MAS)-^{1} (CP)-NMR spectra were recorded with a 4 mm Bruker CP-MAS broadband probe on a Bruker AVANCE 500 spectrometer operating at frequencies of 202.49 MHz for ^{31}P and 123.96 MHz for ^{55}Mn. The 4 mm zirconia rotors were filled with 60 to 80 mg of dry sample and retained with Kel-F end caps. The chemical shift values were calibrated with external standards, namely concentrated phosphoric acid for ^{31}P and 0.1 M $KMnO_4$ for ^{55}Mn. For in-depth SS-NMR studies, the MAS-CP-NMR of the solids were taken on a Bruker DSX-500 MHz spectrometer using a Bruker 4 mm MAS probe. The operating frequencies were 500.2 MHz, 470.5 MHz, 125.4 MHz, 130.5 MHz, and 202.5 MHz for ^{1}H, ^{19}F, ^{13}C, ^{27}Al, and ^{31}P nuclei, respectively. Samples were spun at 12 to 14 kHz. Chemical shifts were reported in ppm after calibration to common references such as TMS for ^{1}H and ^{13}C, $CFCl_3$ for ^{19}F, 1.0 M aluminum nitrate aqueous solution for ^{27}Al and concentrated phosphoric acid for ^{31}P.

Thermogravimetric analysis

TGA was performed on a TA Instruments TGA Q500, heating from 25 °C to 550 °C at a rate of 5 °C·min^{-1} under nitrogen flow.

Electronic paramagnetic resonance spectroscopy

EPR analysis was obtained at room temperature and at 121K with a Bruker E580 CW-EPR spectrometer operating at the X-band frequency (~9.4 GHz) using an ER 4122SHQE Resonator (Bruker). The microwave power was set to 2 mW and the modulation amplitude was 5 Gauss.

X-ray absorption spectroscopy

EXFAS was performed at the XAFCA beam light at the Singapore Synchrotron Light Source. Data was collected in transmission mode at both room temperature and 100 K, processed with the ATHENA software and analyzed in the ARTEMIS program integrated with Demeter software package.[20] The theoretical phase and amplitude functions were calculated using FEFF 9.0.[21] For all samples, the EXAFS oscillations were extracted from the normalized XAS spectra by subtracting the atomic background using cubic split fit to k^3-weighted data, where k is the photoelectron wave number. The $\chi(k)$ functions were then Fourier transformed into R-space.

2.3 Results and Discussion

2.3.1 Water Studies

Ionothermal synthesis is a non-aqueous system, which lends excellent opportunity to study the effects of water as a reagent. Since our interest was metal-substitution (Ni^{2+} and Mn^{2+}) into the AFI framework, and the metal salts

used were polyhydrates, we conducted a comparative study on the syntheses with and without metal added. The corresponding amount of water was added to the metal-free syntheses since the metal salts all introduce water. In so doing, we were able to identify the role of the metal versus that of the water. The water introduced by H_3PO_4 and HF was constant since the same equivalency of these two reagents was used for all reactions. We compared both the DIPI and DIBU SDAs. The results of the nickel studies are summarized below in Figures 2.1 and 2.2, and Table 2.1.

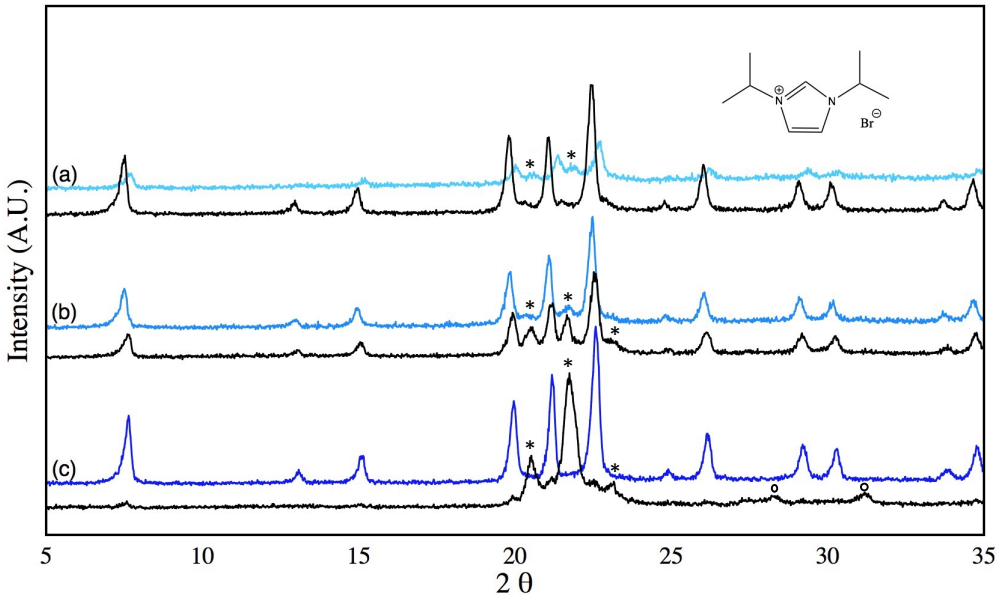

Figure 2.1 PXRD comparison of Ni-AFI syntheses (blue upper patterns) and AFI syntheses (i.e. metal-free syntheses, black lower patterns) with DIPI as SDA: **(a)** 0.38 eq. Ni, 3.04 eq. water; **(b)** 0.25 eq. Ni, 2.51 eq. water; **(c)** 0.13 eq. Ni, 2.02 eq. water; tridymite and cristobalite peaks are denoted with asterisks and open circles, respectively.

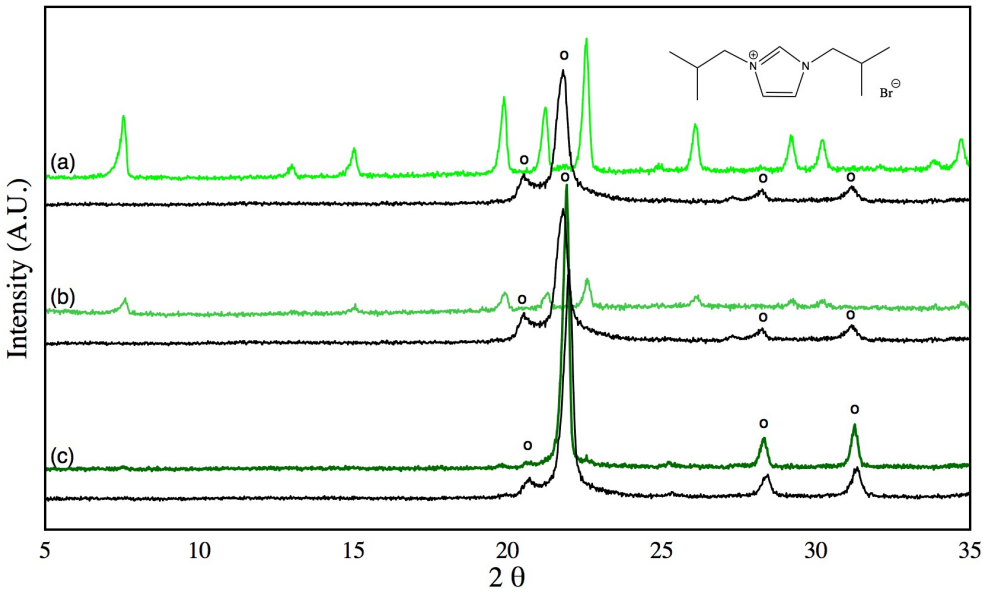

Figure 2.2 PXRD comparison of Ni-AFI syntheses (green upper patterns) and AFI syntheses (black lower patterns) with DIBU as SDA: **(a)** 0.38 eq. Ni, 3.06 eq. water; **(b)** 0.25 eq. Ni, 2.57 eq. water; **(c)** 0.13 eq. Ni, 2.08 eq. water; cristobalite peaks are denoted with open circles.

Table 2.1 Nickel versus water studies for DIPI and DIBU SDAs

Ref.	IL	Ni^{2+} eq.	H_2O eq.	Product	Product**
Fig. 2.1a	DIPI	0.38	3.04	AFI + dense*	AFI
Fig. 2.1b	DIPI	0.25	2.51	Mostly AFI	AFI + dense
Fig. 2.1c	DIPI	0.13	2.02	Pure-phase AFI	Mostly dense
Fig. 2.2a	DIBU	0.38	3.06	Pure-phase AFI	All dense-phase
Fig. 2.2b	DIBU	0.25	2.57	Mostly AFI	All dense-phase
Fig. 2.2c	DIBU	0.13	2.08	Mostly dense	All dense-phase

* dense-phase = cristobalite or tridymite
* no metal synthesis.

Interestingly, the two SDAs exhibit quite different behavior. The most representative PXRD patterns are shown in Figures 2.1 and 2.2 over several trials of each reaction. When examining the Ni influence, DIPI templates a high-

quality AFI pattern when a small amount of the metal is added to the reaction, but turns to mixed AFI/tridymite as more nickel is added (blue patterns, Figure 2.1a to c). DIBU, on the other hand, begins as dense-phase cristobalite when a small amount of nickel is in the reaction, becoming pure-phase AFI as more nickel is added (green patterns, Figure 2.2 a to c). When it comes to water content, the DIPI system is more sensitive to this variable: decreasing from 3.04 to 2.02 eq. water (black patterns, Figure 2.1a to c) changes the product from mixed AFI/tridymite to a near-pure AFI. Such trend is not observed in the DIBU system, as the cristobalite product was exclusively obtained no matter the water content tested (black patterns, Figure 2.2 a to c).

It has previously been demonstrated that nickel does not incorporate into an AFI framework using either DIPI or DIBU ILs[18] and our results also found this to be true. The role of nickel—or its acetate counterion—is therefore of interest in giving rise to such a range of products versus the amount of nickel added, especially for DIBU (Figure 2.2). AFI is only formed in the DIBU system if a minimum of 0.25 eq nickel acetate is added. In previously reported hydrothermal syntheses of Ni-AFI, the Ni precursors were dissolved in water prior to slow addition into the reaction mixture.[13,14] With this in mind, a series of reactions were run using the Ni-DIPI, with the hopes of possible incorporation due to the solvated Ni in the IL

The DIPI used for Ni-AFI syntheses was re-purified by Soxhlet extraction with methanol, as described in the experimental section. After recrystallization,

the IL was noticeably green/blue, signifying the presence of nickel. ^{1}H-NMR of this “Ni-DIPI” confirms there was no change to the DIPI structure and no added organic impurities (Figure 2.3). ICP-OES analysis on the Ni-DIPI showed the IL had a Ni loading of 1.36 mg/g.

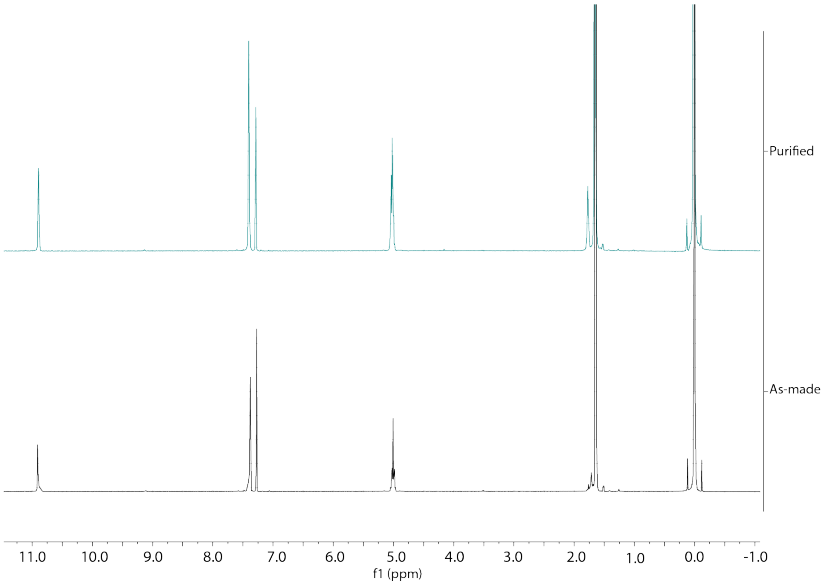

Figure 2.3 ^{1}H-NMR spectra. Top: purified Ni-DIPI; bottom: as-made DIPI.

The reaction ratios and corresponding PXRDs are summarized in Figure 2.4 and Table 2.2. Reagent amounts of water were added to make up the water difference that would have been added with the tetrahydrate salt. The total water in the ratios was from the acids, additional metal salt and added Millipore water.

Table 2.2 Summary of structure results with varying amount of Ni contributed by the Ni-DIPI versus $Ni(OAc)_2$

Reactant Ratios*	Ni^{2+} % in IL	Structure result
(a) 1 : 0.38 : 1.49 : 10.07 : 0.13 : 3.04	14.3%	Mostly AFI, some dense-phase
(b) 1 : 0.25 : 1.49 : 10.07 : 0.13 : 2.51	21.7%	Mostly AFI, some dense-phase
(c) 1 : 0.13 : 1.49 : 10.07 : 0.13 : 2.02	42.5%	Pure-phase AFI
(d) 1 : 0.05 : 1.49 : 10.07 : 0.13 : 2.02	100%	Mostly dense-phase

** $Al(^{i}PrO)_3$: $Ni^{2+}/Ni(OAc)_2 \bullet 4H_2O$: H_3PO_4 : Ni-DIPI : HF : total water*

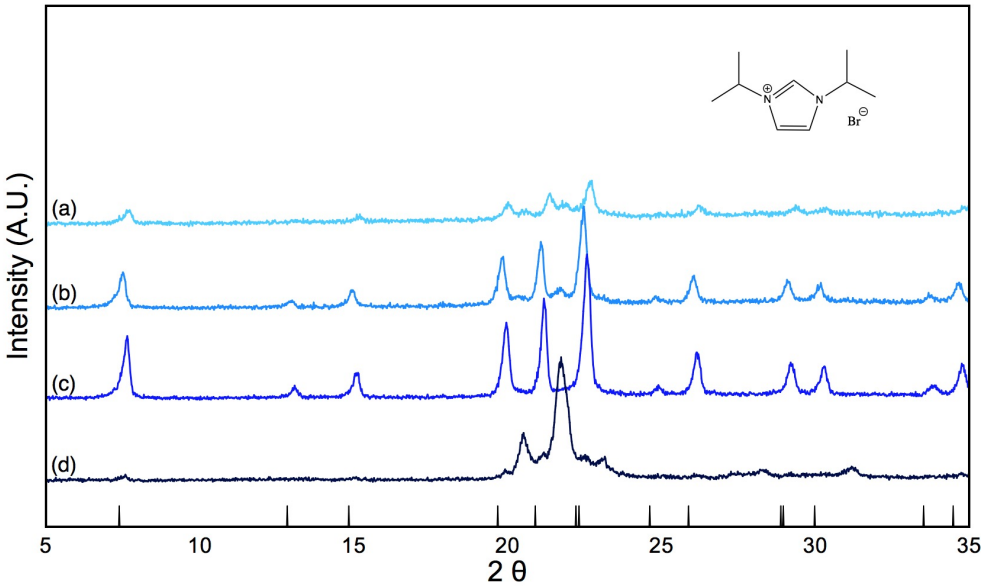

Figure 2.4 Corresponding PXRDs for Ni experiments using Ni-DIPI. All ratios can be found in Table 2.2.

As with the materials that utilized as-made DIPI, the materials synthesized with Ni-DIPI were characterized with acid site testing, SEM/EDX and MAS-NMR for ^{31}P and ^{27}Al nuclei to identify any Ni incorporation. Again, there was no evidence of Ni incorporation into the material.

For manganese, we again see different behavior between DIPI and DIBU, as well as differences in the system with no manganese (Figures 2.5 and 2.6, and Table 2.3). For DIPI with either added metal (Ni or Mn), a smaller amount (0.12 eq) led to high-purity AFI. When more metal was added, however, the DIPI system behaved differently between Ni and Mn. As previously mentioned, additional Ni (0.25 and 0.38 eq) led to a mixed AFI/tridymite product (Figure 2.1 a,b); additional Mn at the same equivalencies instead led to an amorphous product (Figure 2.5 a,b). This result is in contrast to DIBU, which produced a pure-phase Mn-AFI with all amounts of manganese (Figure 2.6) but transitioned from dense-phase cristobalite to AFI with increasing amounts of Ni (Figure 2.2). For both Figures 2.5 and 2.6, it is evident in the cristobalite patterns that a shift to lower angle occurs as the metal equivalence increases. Such a peak shift might be related to the α → β cristobalite phase transition, which is commonly reported in the literature and can be associated to the introduction of M^{2+} cations into the limited voids of the structure.[22] In the present study, we hypothesize the phase transition to be due the potential, but limited, insertion of Mn^{2+} cations into the tetrahedral framework of the aluminophosphate in replacement of aluminum.

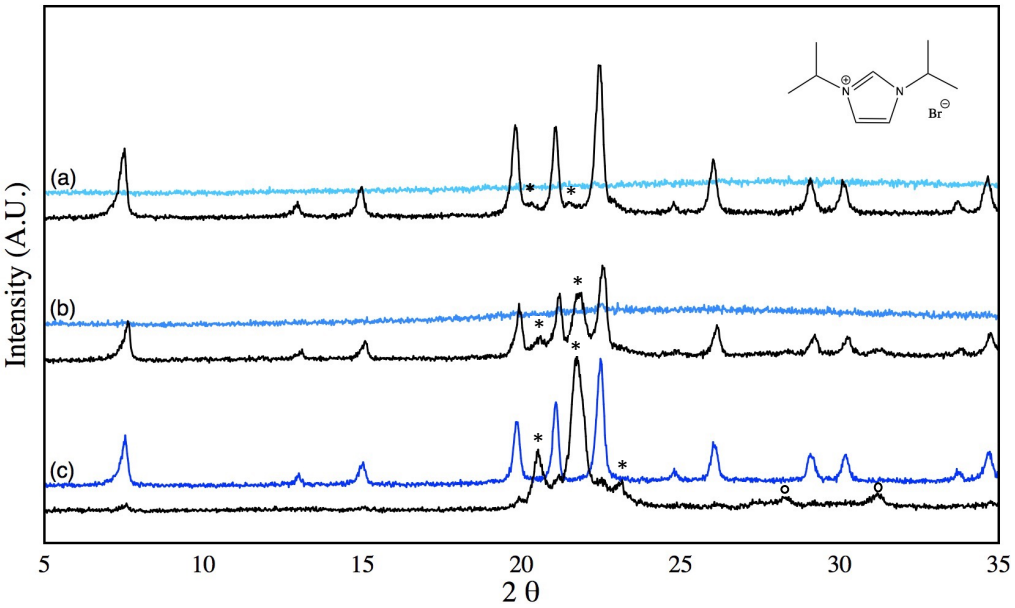

Figure 2.5 PXRD comparison of Mn-AFI syntheses (blue upper patterns) and AFI syntheses (black lower patterns) with DIPI as SDA: **(a)** 0.39 eq. Mn, 3.06 eq. water; **(b)** 0.25 eq. Mn, 2.66 eq. water; **(c)** 0.13 eq. Mn, 2.00 eq. water; tridymite and cristobalite peaks are denoted with asterisks and open circles, respectively. tridymite peaks are denoted with asterisks.

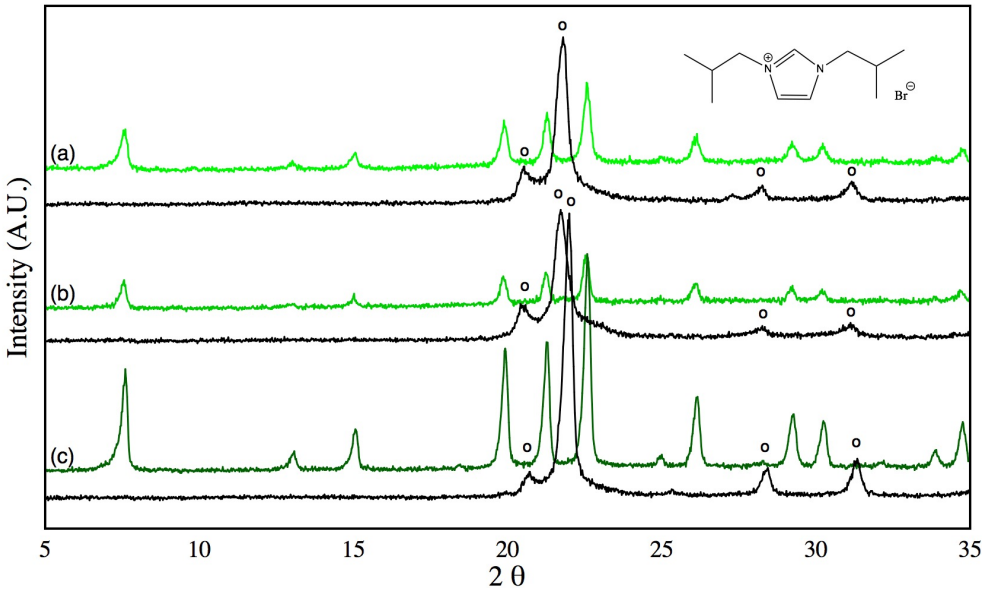

Figure 2.6 PXRD comparison of Mn-AFI syntheses (green upper patterns) and AFI syntheses (black lower patterns) with DIBU as SDA: **(a)** 0.38 eq. Mn, 3.02 eq. water; **(b)** 0.25 eq. Mn, 2.74 eq. water; **(c)** 0.13 eq. Mn, 2.05 eq. water; cristobalite peaks are denoted with open circles.

Table 2.3 Manganese versus water studies for DIPI and DIBU SDAs

Ref	IL	Mn^{2+} eq.	H_2O eq.	Product	Product**
Fig. 2.5a	DIPI	0.38	3.06	Amorphous	AFI
Fig. 2.5b	DIPI	0.25	2.66	Amorphous	AFI + dense*
Fig. 2.5c	DIPI	0.13	2.00	Pure-phase AFI	Mostly dense
Fig. 2.6a	DIBU	0.38	3.02	Pure-phase AFI	All dense-phase
Fig. 2.6b	DIBU	0.25	2.74	Pure-phase AFI	All dense-phase
Fig. 2.6c	DIBU	0.13	2.05	Pure-phase AFI	All dense-phase

* dense-phase = cristobalite or tridymite
* no metal synthesis.

2.3.2 HF Studies

HF has been shown to be an important reagent in the synthesis of aluminophosphate molecular sieves, aiding in precursor mineralization and can also play a part in structure directing.[9,18,23,24] The above water studies resulted in significant phase differences depending on whether substitutional metals were present in the reaction mixture while maintaining the same total water equivalencies. Likewise, it was also of interest to identify if the phase could be controlled by varying the amount of HF, while keeping equivalencies constant for both the water and substitutional metal (Ni or Mn). We again conducted studies with both Ni (Figures 2.7 and 2.8, Table 2.4) and Mn (Figures 2.9 and 2.10, Table 2.5) in order to compare the results with those achieved in the water studies. Additionally, we studied the influence of HF in systems without the addition of metals (Figures 2.11 and 2.12, Table 2.6).

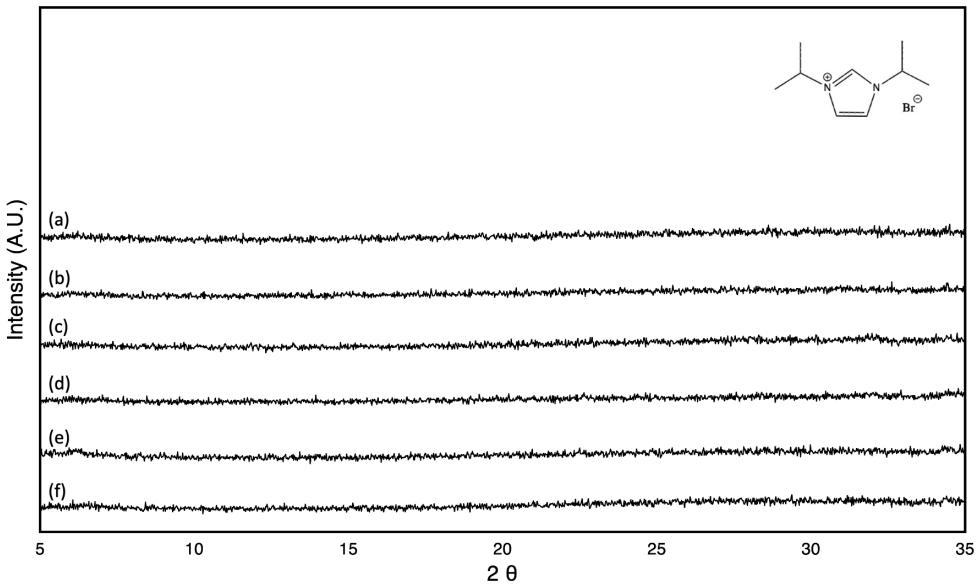

Figure 2.7 PXRD comparison of Ni-AFI syntheses with varying HF equivalency and DIPI as SDA: **(a)** 0.60 HF eq.; **(b)** 0.48 HF eq.; **(c)** 0.36 HF eq.; **(d)** 0.24 HF eq.; **(e)** 0.12 HF eq.; **(f)** 0.00 HF eq.; all contained 2.14 water and 0.12 Ni equivalencies.

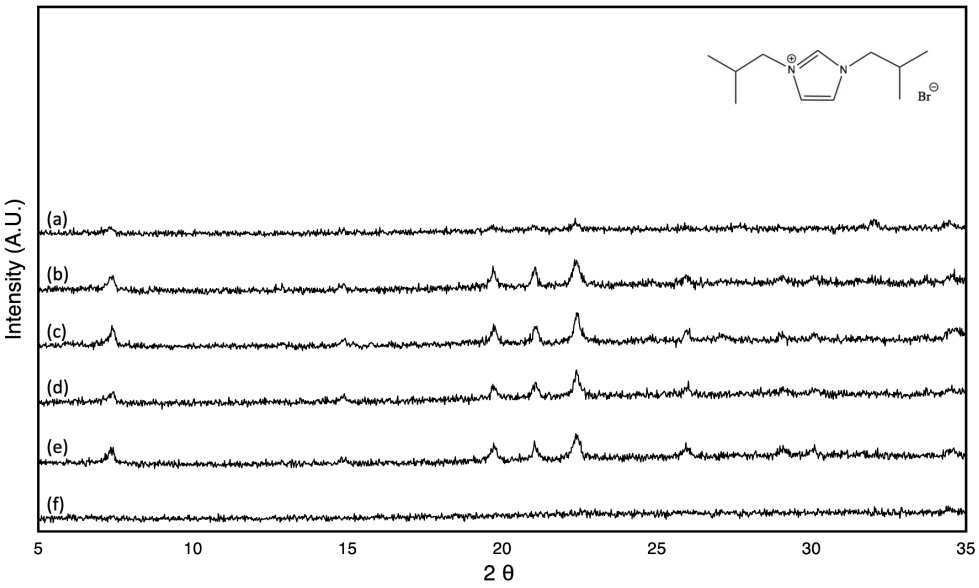

Figure 2.8 PXRD comparison of Ni-AFI syntheses with varying HF equivalency and DIBU as SDA: **(a)** 0.60 HF eq.; **(b)** 0.48 HF eq.; **(c)** 0.36 HF eq.; **(d)** 0.24 HF eq.; **(e)** 0.12 HF eq.; **(f)** 0.00 HF eq.; all contained 2.18 water and 0.12 Ni equivalencies.

Table 2.4 HF studies for nickel systems

Ref	SDA	Ni eq.	HF eq.	Structure
Fig. 2.7a	DIPI	0.10	0.60	Amorphous
Fig. 2.7b	DIPI	0.10	0.48	Amorphous
Fig. 2.7c	DIPI	0.10	0.36	Amorphous
Fig. 2.7d	DIPI	0.10	0.24	Amorphous
Fig. 2.7e	DIPI	0.10	0.12	Amorphous
Fig. 2.7f	DIPI	0.10	0.00	Amorphous
Fig. 2.8a	DIBU	0.10	0.60	AFI
Fig. 2.8b	DIBU	0.10	0.48	AFI
Fig. 2.8c	DIBU	0.10	0.36	AFI
Fig. 2.8d	DIBU	0.10	0.24	AFI
Fig. 2.8e	DIBU	0.10	0.12	AFI
Fig. 2.8f	DIBU	0.10	0.00	Amorphous

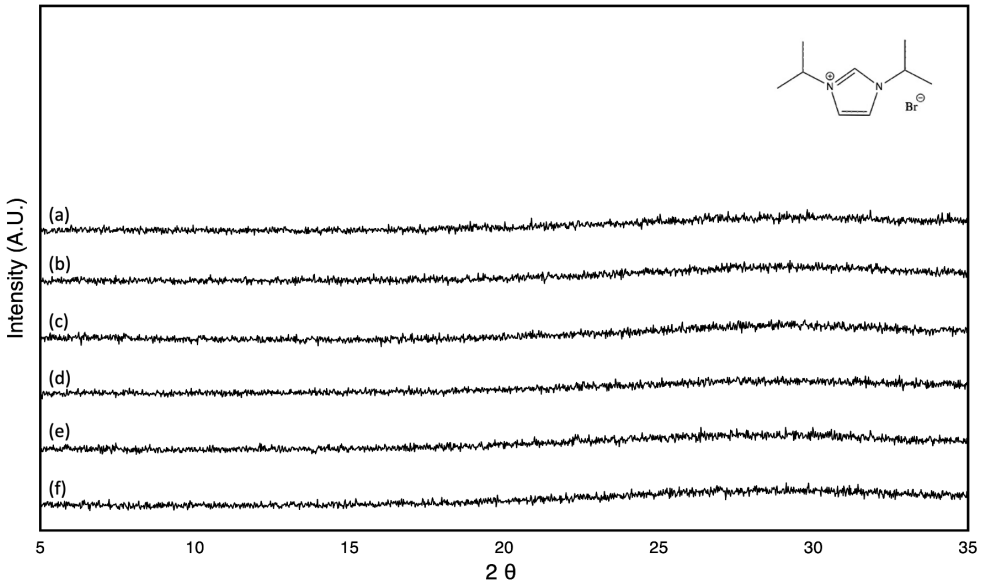

Figure 2.9 PXRD comparison of Mn-AFI syntheses with varying HF equivalency and DIPI as SDA: (a) 0.60 HF eq.; (b) 0.48 HF eq.; (c) 0.36 HF eq.; (d) 0.24 HF eq.; (e) 0.12 HF eq.; (f) 0.00 HF eq.; all contained 2.2 water and 0.11 Mn equivalencies.

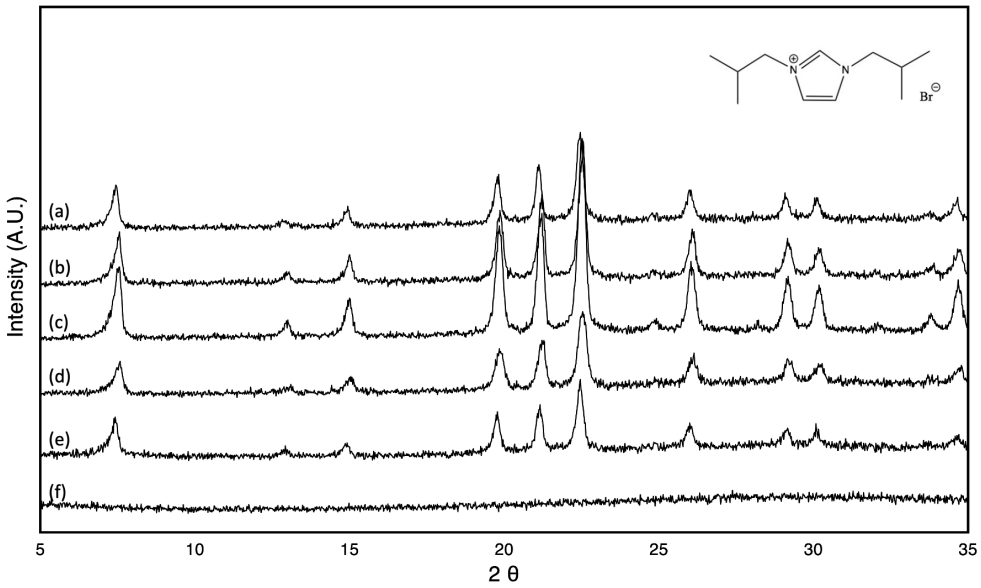

Figure 2.10 PXRD comparison of Mn-AFI syntheses with varying HF equivalency and DIBU as SDA: **(a)** 0.60 HF eq.; **(b)** 0.48 HF eq.; **(c)** 0.36 HF eq.; **(d)** 0.24 HF eq.; **(e)** 0.12 HF eq.; **(f)** 0.00 HF eq.; all contained 2.2 water and 0.11 Mn equivalencies.

Table 2.5 HF studies for manganese systems.

Ref	SDA	Mn eq.	HF eq.	Structure
Fig. 2.9a	DIPI	0.10	0.60	Amorphous
Fig. 2.9b	DIPI	0.10	0.48	Amorphous
Fig. 2.9c	DIPI	0.10	0.36	Amorphous
Fig. 2.9d	DIPI	0.10	0.24	Amorphous
Fig. 2.9e	DIPI	0.10	0.12	Amorphous
Fig. 2.9f	DIPI	0.10	0.00	Amorphous
Fig. 2.10a	DIBU	0.10	0.60	AFI
Fig. 2.10b	DIBU	0.10	0.48	AFI
Fig. 2.10c	DIBU	0.10	0.36	AFI
Fig. 2.10d	DIBU	0.10	0.24	AFI
Fig. 2.10e	DIBU	0.10	0.12	AFI
Fig. 2.10f	DIBU	0.11	0.00	Amorphous

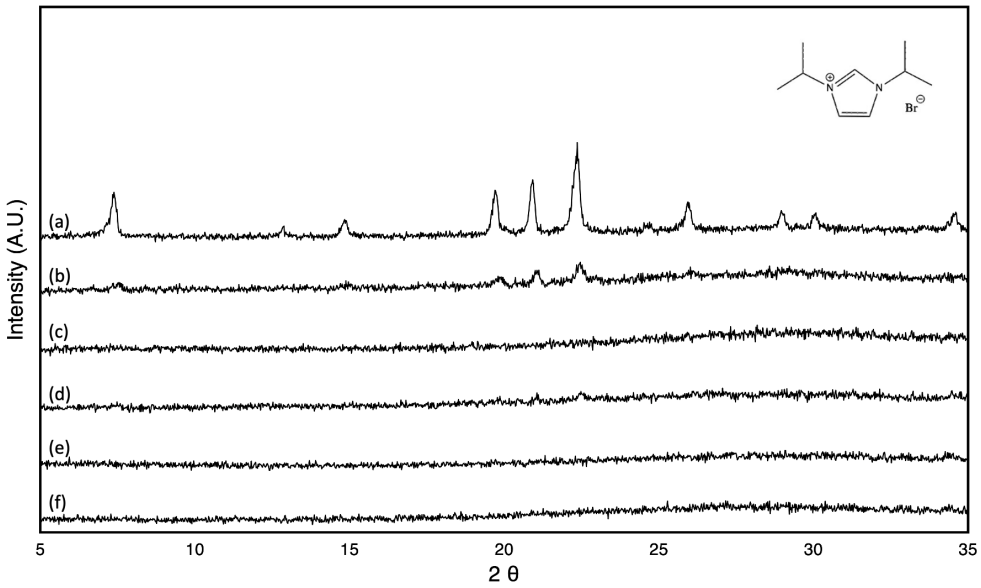

Figure 2.11 PXRD comparison of the transition metal-free syntheses with varying HF equivalency and DIPI as SDA: **(a)** 0.60 HF eq.; **(b)** 0.48 HF eq.; **(c)** 0.36 HF eq.; **(d)** 0.24 HF eq.; **(e)** 0.12 HF eq.; **(f)** 0.00 HF eq.; all contained 2.2 water equivalencies.

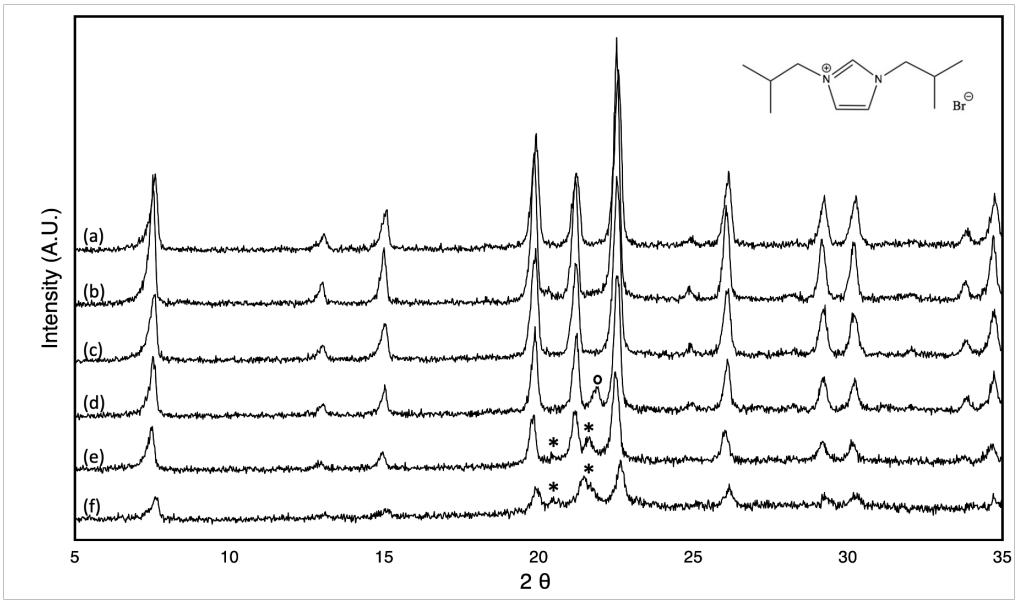

Figure 2.12 PXRD comparison of the transition metal-free syntheses with varying HF equivalency and DIBU as SDA: **(a)** 0.60 HF eq.; **(b)** 0.48 HF eq.; **(c)** 0.36 HF eq.; **(d)** 0.24 HF eq.; **(e)** 0.12 HF eq.; **(f)** 0.00 HF eq.; all contained 2.2 water equivalencies; tridymite and cristobalite peaks are denoted with asterisks and open circles, respectively.

Table 2.6 HF studies for no-metal systems

Ref	SDA	HF eq.	Structure
Fig. 11a	DIPI	0.60	AFI
Fig. 11b	DIPI	0.48	AFI
Fig. 11c	DIPI	0.36	Amorphous
Fig. 11d	DIPI	0.24	Amorphous
Fig. 11e	DIPI	0.12	Amorphous
Fig. 11f	DIPI	0.00	Amorphous
Fig. 12a	DIBU	0.60	AFI
Fig. 12b	DIBU	0.48	AFI
Fig. 12c	DIBU	0.36	AFI
Fig. 12d	DIBU	0.24	AFI + dense*
Fig. 12e	DIBU	0.12	AFI + dense
Fig. 12f	DIBU	0	AFI + dense

* dense-phase = cristobalite or tridymite

The HF data are in agreement with our previous results, suggesting that the DIPI SDA is not as efficient in templating AFI as DIBU. For both Ni and Mn reactions using DIPI as the SDA, no AFI product was recovered, with only amorphous phases being observed (Figures 2.7 and 2.9). Interestingly, when no metal is added to the DIPI system, we see the formation of the AFI framework at higher HF equivalences (Figure 2.11). For DIBU SDA, both Ni or Mn in the reaction mixture supported the formation of AFI with any amount of HF (Figures 2.8 and 2.10). When no Ni or Mn was introduced, it takes more than 0.24 eq of HF to achieve a quality AFI pattern with no dense-phase PXRD peaks (Figure 2.12). These HF experiments further confirm the stronger structure directing ability of the DIBU SDA compared to DIPI. Moreover, when the DIBU is paired with even a small addition of Mn in the reaction mixture, the

amount of HF needed to support an AFI pattern is reduced. These points will be further elucidated in the following sections.

2.3.3 Modeling Data

Since the DIBU was consistently more predictable in forming the AFI topology, we wanted to further understand this behavior. One possibility for the observed Mn-AFI products is the templating strength of the SDA. If one SDA has a better fit over another, there is likely an increased possibility of nucleation of the porous structure. For this reason, modeling of the fit was performed for DIPI, DIBU and dicyclohexylimidazolium (DICH) for comparison to an organic with bulky side groups (Figure 2.13).

SDA	vdW Interaction Energy (kJ/mol per Si)	Modeling
Diisopropylimidazolium (DIPI) 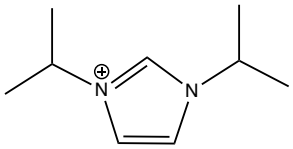	-5.68	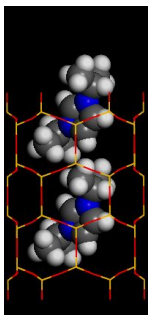
Diisobutylimidazolium (DIBU) 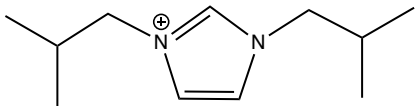	-6.89	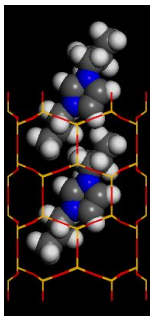
Dicyclohexylimidazolium (DICH) 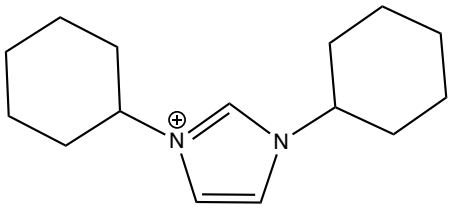	-6.34	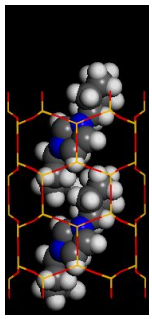

Figure 2.13 Modeling data with DIBU displaying the most favorable SDA interaction energy within the AFI framework.

Although DIBU does have the most favorable interaction energy within the AFI channels, the slight structural difference between DIBU and DIPI is not necessarily large enough to predict such a difference in results when adding Ni, Mn or water into the synthesis. Manganese certainly appears to play a role in the synthesis of an AFI structure. When Mn is not in the system, the majority phase is dense-phase tridymite or cristobalite for both DIPI and DIBU unless at least triple the amount of HF is added to the reaction mixture. Once Mn was introduced in a small amount (0.10 to 0.13 eq.), both SDAs readily form pure-phase AFI. When DIPI is used as the SDA, higher amounts of Mn (0.25 to 0.38 eq.) result in an amorphous phase, whereas DIBU still forms AFI with higher amounts of Mn. Mn^{2+} sites should introduce a negative charge (MnO_4^{2-} or MnO_4^- if accounting for oxygen sharing). Since the SDAs are cationic, it would be attracted to that negatively charged species, around which the precursors would form a porous network. The slight energy reduction with DIBU as compared with DIPI (Figure 2.13) may encourage faster nucleation, leading to pure AFI phase more quickly. The DIPI may simply need more time to form a framework, moving out of the amorphous stage of synthesis. Acetate was also being added to the reaction mixture as part of the metal salt. This would deprotonate at least some of the water, as acetic acid is a weak acid ($K_a = 1.8 \times 10^{-5}$). OH^- would then act as a mineralizer, perhaps promoting condensation polymerization into a porous phase. Both metal salts, however, are acetates and thus the metal itself is clearly a more important factor.

2.3.4 TGA Analysis

To test the above hypothesis of Mn acting as an anchor for the SDA, TGA was run for Mn-AFI and AFI products from both DIPI and DIBU. If the transition metal is charge-balancing the cationic SDA, it should be slightly more heat stable than the aluminophosphate material. As expected, the TGA curves for DIBU support this hypothesis (Figure 2.14 a). After water loss, the pure AFI and Mn-AFI both have two main mass losses. The first for Mn-free AFI occurs at ~ 270 °C (1.8% mass), but for Mn-AFI occurs at around 340 °C (5.2% mass). These losses are possibly related to neutral DIPI-Br salt molecules occluded in the pores. The second mass loss for Mn-free AFI occurs at 350 °C (8.2% mass), while for Mn-AFI it occurs at 410 °C (2.3% mass), possibly related to electrostatically bound DIBU ions within the framework.

TGA for the DIPI products (Figure 2.14 b) is markedly different for Mn-AFI, although the pure AFI data is similar. For Mn-AFI, there are four mass losses. The small, broad peak around 150 °C (0.6% mass) is likely chemisorbed water, while the event at 265°C (0.4 %) could be attributed to unbound DIBU-Br. The two higher temperature events are similar to the Mn-AFI obtained with DIBU but occur a little earlier, at 330 °C (1.4% mass) and 375 °C (0.3% mass), with lower mass loss as expected for a smaller organic molecule. As with the DIBU, the third and fourth mass losses from the DIPI synthesis are attributed to the potential SDA interaction with the Mn and Br salt, respectively. The amorphous products (blue patterns in Figure 2.5a,b) display

very different traces (Figure 2.15), with loss of water followed by a very gradual mass loss, likely due to condensation.

(a)

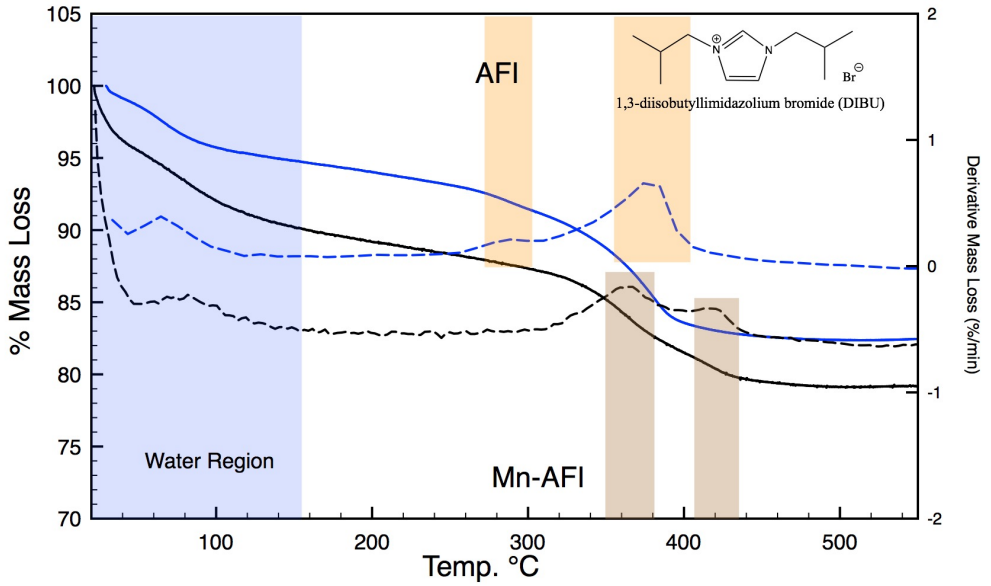

(b)

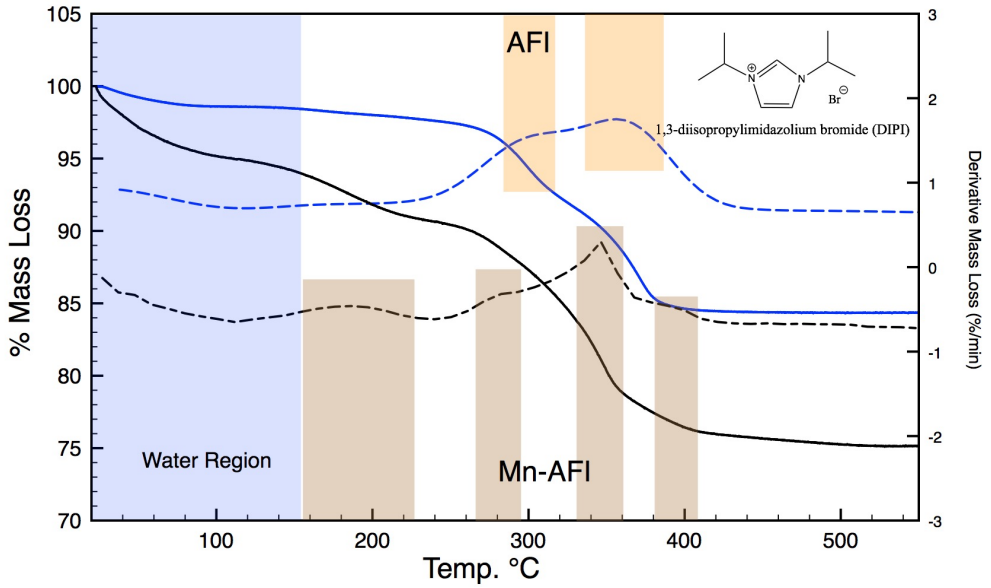

Figure 2.14 TGA traces (solid lines; first derivatives are shown as dashed lines) for **(a)** DIBU and **(b)** DIPI. AFI is shown as blue lines and Mn-AFI is

shown as black lines. Blue bars highlight the water loss region, yellow-orange bars highlight mass losses for AFI and brown bars highlight mass losses for Mn-AFI.

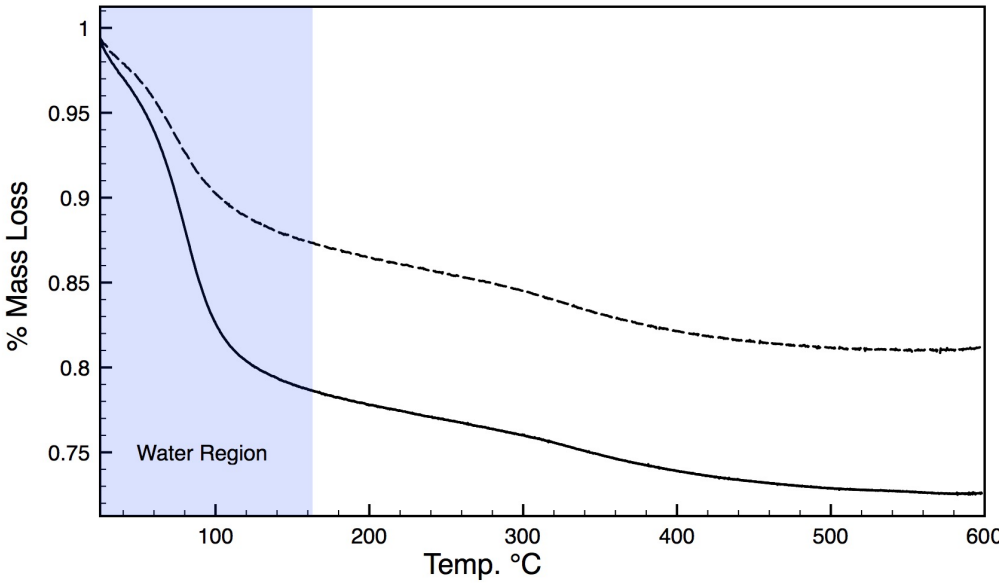

Figure 2.15 TGA of amorphous materials using DIPI SDA. Top: 0.25 eq. Mn, 2.66 eq. water; bottom: 0.39 eq. Mn, 3.06 eq. water. The % mass loss of the two materials from 160 to 600 °C were identical, indicating that the same amount of SDA existed in both materials.

Clearly, the introduction of metal into the syntheses plays a significant role in the resulting product. With this in mind, we were interested in determining if there was actual metal incorporation into the frameworks of these materials. We first studied the nickel syntheses for both DIPI and DIBU SDA. SEM/EDX mapping, ICP-OES elemental analysis, MAS-NMR and acid site testing all suggested there was no incorporation of Ni into the product, in agreement with the recent study by Benin at al.[18] Due to the seemingly strong

pairing of the DIBU SDA with manganese, further characterization studies were conducted for the Mn-AFI and AFI materials.

2.3.5 In-depth Characterization of Mn-AFI

EPR.

EPR analysis was conducted with the primary intention of establishing the presence of Mn in the material and the additional hope of identifying the geometry of the Mn. The sample for this analysis was Mn-AFI made with DIBU SDA (see PXRD, Figure 2.6c, green pattern). The anisotropic spectrum displays the six distinct hyperfine lines of paramagnetic Mn^{2+} (I = 5/2), confirming the presence of Mn (Figure 2.16). The g-value was calculated to be 1.9932±0.0005 for as-made Mn-AFI and 1.9925±0.0005 for calcined Mn-AFI, which is in line with the g-value for distorted octahedral Mn^{2+}.[25] The coupling constant for the hyperfine splitting was unable to be resolved, so the coordination environment could not be fully determined.[13,26]

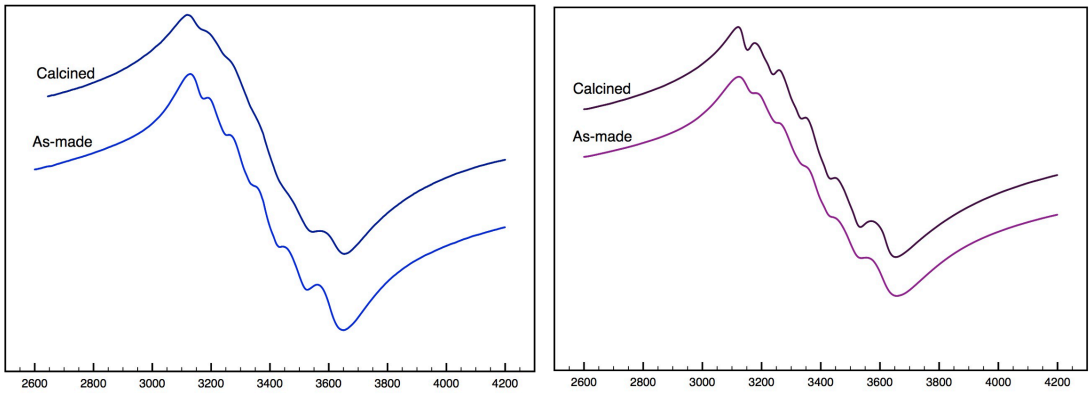

Figure 2.16 EPR spectra at varying temperature. Left: RT; right: 121 °C.

MAS-NMR

MAS-NMR spectra were collected for Mn-AFI and AFI made with DIBU SDA. Inspection of the ^{31}P spectra for AFI versus Mn-AFI suggests there is an influence on the environment for the phosphorous (Figure 2.17). In fact, the line shape appears to be very similar to that of the ^{31}P spectra of Co-AFI reported by Benin et al,[18] which shows evidence of Co within the molecular sieve. Additionally, ^{55}Mn NMR shows evidence of manganese in several different environments (Figure 2.18). Due to limited ^{55}Mn NMR literature on Mn-APO peak assignments, the actual coordination environments are difficult to directly assign. From previous literature on typical MAPO assignments, however, the peaks are anticipated to be associated with $Mn(H_2O)_6^{2+}$, MnO_6 and $MnO_4(H_2O)_6$.[18,27–29]

An extensive NMR study of MnAPO-5 by Goldfarb *et al*. suggests a small amount of Mn can incorporate into the AFI framework but Mn can also reside in an extra-framework position.[26] As mentioned previously, our Mn-AFI material was light pink in color after calcination. Their MnAPO-5 study discovered that the pink color is due to water adsorption and the resulting formation of extra-framework $[Mn(H_2O)_6]^{2+}$.[26] It has been shown that in an AFI framework, Mn often does not incorporate into tetrahedral sites but rather in a distorted octahedral environment, with weak interactions to Al and P.[13,30,31] Here, the ^{31}P spectra suggest the possibility of Mn substitution and the ^{55}Mn spectra show Mn in multiple environments. Most noticeably, after calcination

the peak at ~ 1200 ppm becomes much more prominent than in the pre-calcined material (Figure 2.18). This peak is very likely $Mn(H_2O)_6^{2+}$, given the light pink color of the calcined material. The remaining peaks around 400 and 600 ppm post-calcination, however, suggest some manganese may still reside within the structure of the molecular sieve.

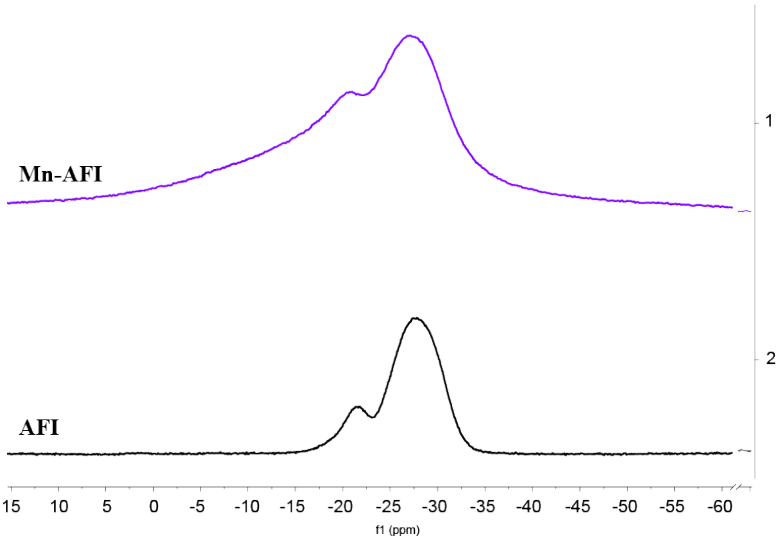

Figure 2.17 ^{31}P MAS-NMR of Mn-AFI versus AFI, both made with DIBU SDA.

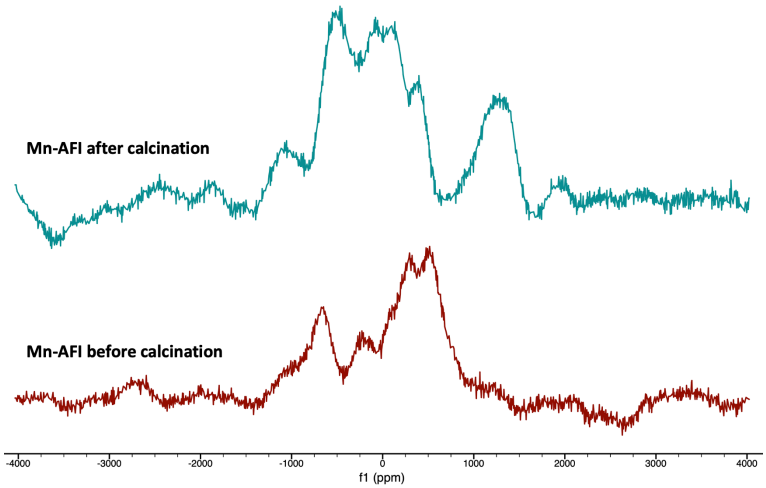

Figure 2.18 ^{55}Mn MAS-NMR of Mn-AFI made with DIBU SDA, before and after calcination.

With initial results showing promise for Mn incorporation into the AFI framework, a more in-depth NMR study was completed. We obtained SS-NMR data for ^{27}Al, ^{13}P, ^{19}F and ^{13}C and analyzed both crystalline and amorphous materials. Above, we saw a distinct difference in products obtained with the DIPI IL compared with the DIBU IL via PXRD (*vide supra*). By looking at the six-coordinate Al (AlO_6 or AlO_5F) NMR peaks versus four-coordinate (AlO_4) peaks, we were able to elucidate the quantitative amounts of amorphous versus crystalline material in the product. This method has been shown to be much more sensitive than PXRD: the PXRD had a pattern distinct to AFI, but SS-NMR reveals that the product was actually only 41% crystalline AFI (Table 2.7). When analyzing the products with and without Mn, a very interesting result was discovered. When Mn was introduced into the synthesis, the ^{31}P relaxation

times drop dramatically. For DIPI SDA, the difference in amorphous product changes from 23 s without metal to 6.5 s with metal. The DIBU AFI product changes from 58 s without Mn to a drastically reduced 3.2 s when Mn is present (Table 2.7), with increased crystallinity (*vide infra*). Although it would be interesting to identify whether an amorphous product from the Mn-DIBU system had reduced relaxation times, the only amorphous product we were able to obtain in this system was one that was formed without the use of HF, which would not be a direct comparison.

Table 2.7 MAPO compounds studied and NMR measurements

SDA	Mn	Phase	$[AlO_4]/[Total\ AlO_x]$	$^{31}P\ T_1$	$[^{31}P]$/unit mass
DIPI	no	amorphous	7.06%	23 s	65.4%
DIPI	yes	amorphous	7.07%	6.5 s	63.1%
DIPI	no	AFI	41.0%	35 s	80.9%
DIBU	no	AFI	83.6%	58 s	100%
DIBU	yes	AFI	72.9%	3.2 s	62.8%

Benin *et al*. observed a similar result for their Co-AFI product, but when Ni was added to the reaction, there was no drastic change in relaxation time.[18] Cobalt has been shown to readily substitute into an AFI framework whereas nickel has not. This further suggests Mn incorporation into our AFI framework. DIBU appears to crystallize AFI with much higher efficiency. ^{31}P NMR shows the majority of signal is around -30 ppm, indicating the dominant species is PO_4 (Figure 2.19). The resonance at -12 ppm indicates the presence of some amorphous phase, which could not be observed by PXRD. This peak is,

however, barely noticeable, estimated to be about ~ 5 %. Interestingly, the ^{31}P resonances are relatively well resolved, showing several different peaks for the crystalline PO_4 units, which has not been observed in other AFI products using smaller SDAs[18] and may help explain the success of the DIBU SDA.

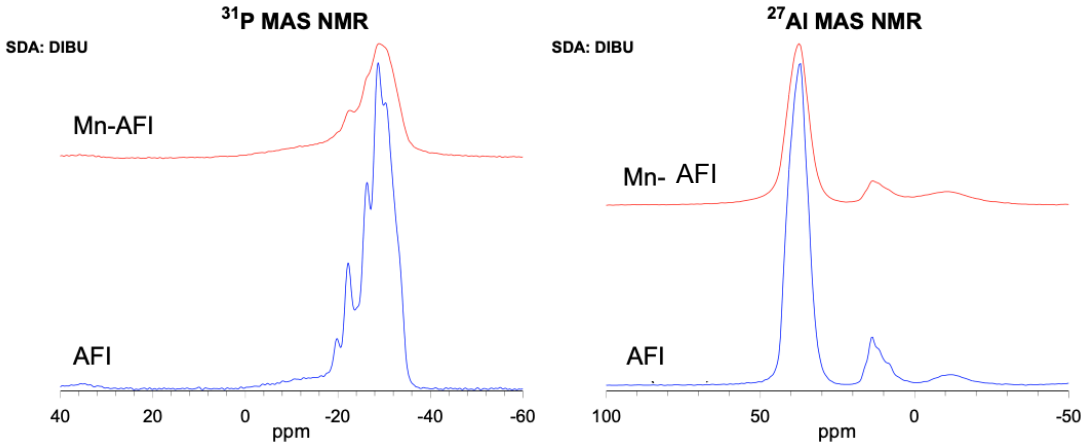

Figure 2.19 ^{31}P MAS-NMR (left) and ^{27}Al MAS-NMR (right) of Mn-AFI (red) versus AFI (blue), both made with DIBU SDA.

Analysis of ^{13}C CP-MAS-NMR confirms that the SDA is still intact and the weakening of the signal for Mn-AFI compared to AFI is indicative of the paramagnetic influence of Mn^{2+} (Figure 2.20). This result further suggests incorporation of Mn into the crystalline AFI framework.

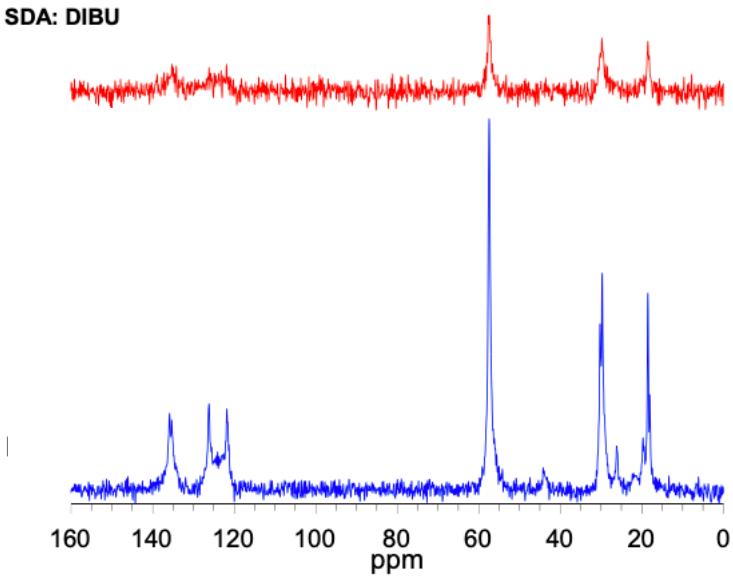

Figure 2.20 ^{13}C CP-MAS-NMR of Mn-AFI (top, red) versus AFI (bottom, blue) synthesized with DIBU SDA.

Analysis of the NMR data provides compelling evidence of Mn^{2+} incorporation into the AFI framework when the DIBU SDA is used as the template. MAS-NMR and EPR both point to intraframework Mn substitution, although the geometry of the Mn species is still in question. Furthermore, using DIBU as SDA led to a pure-phase or near pure-phase Mn-AFI every time. There is no doubt a synergistic effect is seen when pairing DIBU with Mn to produce an AFI product.

EXAFS analysis.

The Mn-AFI material was analyzed both at room temperature and at 373 K. As showed in Figure 2.21 and Table 2.8, the analysis confirmed the

presence of divalent manganese. The coordination of the metal was determined to be 3.8 ± 0.5 at 373 K, corroborating the presence of tetrahedrally coordinated manganese in the AFI material. At room temperature, however, the coordination was found to be 5.1 ± 0.5, which might simply be due to coordination of a water molecule.

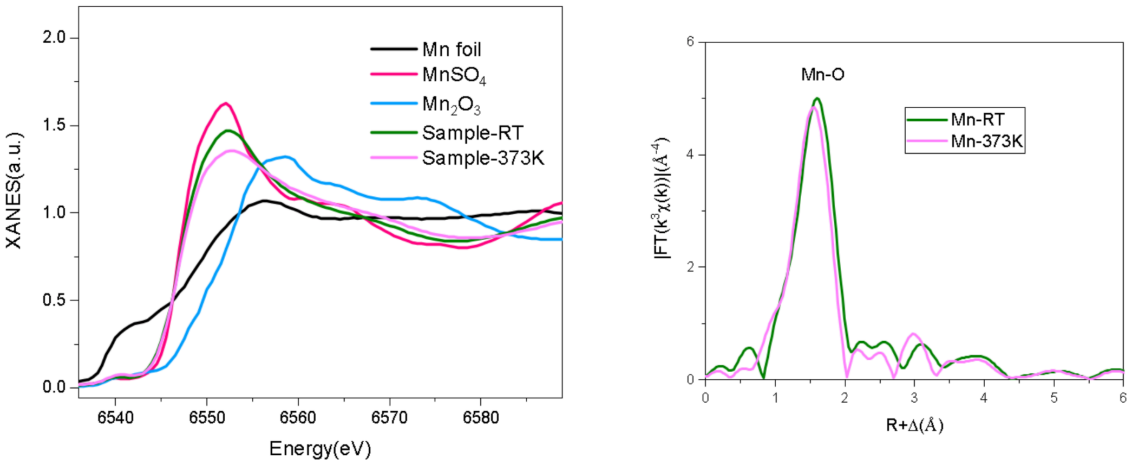

Figure 2.21 EXAFS analysis was measured at room temperature and 373K, confirming Mn is present in the sample.

Table 2.8 Results of the EXAFS analysis. N: coordination number; R: distance between absorber and backscattering atoms; σ^2: Debye-Waller factor to account for thermal and structural disorders. Error bounds (accuracies) that characterize the structural parameters were estimated as R ± 0.01; σ^2 ± 0.0008; ΔE ± 0.8. S_0 was fixed at 0.64 as determined from Mn_2O_3 fitting (fitting range: 2.0 ≤ k(/Å) ≤ 10 and 1.0 ≤ R(Å) ≤ 2.0)

Sample	Path	N	R (Å)	σ^2 (x10^{-3} Å^2)	ΔE_0(eV)	R(%)
Mn-RT	Mn-O	5.1±0.5	2.09	8.7	1.2	0.01
Mn-373K	Mn-O	3.8±0.5	2.05	5.1	-2.4	0.01

2.4 Conclusions and Future Directions

New, simple synthesis routes were discovered for MnAPO-5 using two different ionic liquids (ILs), DIPI and DIBU. Both Ni^{2+} and Mn^{2+} are challenging metals to substitute into tetrahedral frameworks due to their preferred octahedral geometries. We demonstrated that the presence of a transition metal influences the phase and crystallinity of the material. We have also found a strong synergistic effect when using DIBU and Mn together, resulting in pure-phase or near pure-phase Mn-AFI in all syntheses. There was compelling evidence of Mn incorporation into the framework by EPR, in-depth NMR and EXAFS. Each IL/SDA demonstrated opposite phase behavior when the syntheses included varying level of nickel in the reaction mixture. Future investigations include mode of formation and kinetic studies on the influence of the paramagnetic metal. Ionothermal synthesis is a simple one-pot reaction and has nearly zero vapor pressure making it a very promising route to MAPO-n syntheses.

2.5 References

(1) Davis, M. E. New Vistas in Zeolite and Molecular Sieve Catalysis. *Acc. Chem. Res.* **1993**, *26* (3), 111–115.

(2) Sherman, J. D. Synthetic Zeolites and Other Microporous Oxide Molecular Sieves. *Proc. Natl. Acad. Sci.* **1999**, *96* (7), 3471–3478.

(3) Mortén, M.; Mentel, Ł.; Lazzarini, A.; Pankin, I. A.; Lamberti, C.; Bordiga, S.; Crocellà, V.; Svelle, S.; Lillerud, K. P.; Olsbye, U. A Systematic Study of Isomorphically Substituted H-MAlPO-5 Materials for the Methanol-to-Hydrocarbons Reaction. *ChemPhysChem* **2017**, *19* (4), 484–495.

(4) Akolekar, D. B. Acidity and Acid Strength Distribution of the Crystalline Microporous MAPO-36 Molecular Sieve. *Zeolites* **1994**, *14* (1), 53–57.

(5) Akolekar, D. B. Acidity and Catalytic Properties of AlPO4-11, SAPO-11, MAPO-11, NiAPO-11, MnAPO-11 and MnAPSO-11 Molecular Sieves. *J. Mol. Catal. Chem.* **1995**, *104* (1), 95–102.

(6) Wang, C.-M.; Brogaard, R. Y.; Weckhuysen, B. M.; Nørskov, J. K.; Studt, F. Reactivity Descriptor in Solid Acid Catalysis: Predicting Turnover Frequencies for Propene Methylation in Zeotypes. *J. Phys. Chem. Lett.* **2014**, *5* (9), 1516–1521.

(7) Westgård Erichsen, M.; De Wispelaere, K.; Hemelsoet, K.; Moors, S. L. C.; Deconinck, T.; Waroquier, M.; Svelle, S.; Van Speybroeck, V.; Olsbye,

U. How Zeolitic Acid Strength and Composition Alter the Reactivity of Alkenes and Aromatics towards Methanol. *J. Catal.* **2015**, *328*, 186–196.

(8) Cooper, E. R.; Andrews, C. D.; Wheatley, P. S.; Webb, P. B.; Wormald, P.; Morris, R. E. Ionic Liquids and Eutectic Mixtures as Solvent and Template in Synthesis of Zeolite Analogues. *Nature* **2004**, *430* (7003), 1012.

(9) B. Pinar, A.; B. McCusker, L.; Baerlocher, C.; Hwang, S.-J.; Xie, D.; I. Benin, A.; I. Zones, S. Synthesis and Structural Characterization of Zn-Containing DAF-1. *New J. Chem.* **2016**, *40* (5), 4160–4166.

(10) Oliver, S.; Kuperman, A.; Ozin, G. A. A New Model for Aluminophosphate Formation: Transformation of a Linear Chain Aluminophosphate to Chain, Layer, and Framework Structures. *Angew. Chem. Int. Ed.* **1998**, *37* (1–2), 46–62.

(11) Zanjanchi, M. A.; Abdollahi, L. Preparation and Spectral Analysis of Nickel-Containing Aluminophosphate Molecular Sieves of Type-5. *J. Incl. Phenom. Macrocycl. Chem.* **2001**, *39* (1–2), 151–157.

(12) Amiri, M.; Sohrabnezhad, S.; Rahimi, A. Nickel (II) Incorporated AlPO-5 Modified Carbon Paste Electrode for Determination of Thioridazine in Human Serum. *Mater. Sci. Eng. C* **2014**, *37* (Supplement C), 342–347.

(13) Levi, Z.; Raitsimring, A. M.; Goldfarb, D. ESR and Electron Spin-Echo Studies of MnAlPO5. *J. Phys. Chem.* **1991**, *95* (20), 7830–7838.

(14) Wu, J.-Y.; Chien, S.-H.; Wan, B.-Z. Characterization of MnAPO-5 for Ethane Oxydehydrogenation. *Ind. Eng. Chem. Res.* **2001**, *40* (1), 94–100.

(15) Wan, B.-Z.; Huang, K. MnAPO-5 as a Catalyst for Ethane Oxydehydrogenation. *Appl. Catal.* **1991**, *73* (1), 113–124.

(16) Zhou, L.; Xu, J.; Chen, C.; Wang, F.; Li, X. Synthesis of Fe, Co, and Mn Substituted AlPO-5 Molecular Sieves and Their Catalytic Activities in the Selective Oxidation of Cyclohexane. *J. Porous Mater.* **2008**, *15* (1), 7–12.

(17) Ng, E.-P.; Sekhon, S. S.; Mintova, S. Discrete MnAlPO-5 Nanocrystals Synthesized by an Ionothermal Approach. *Chem. Commun.* **2009**, *0* (13), 1661–1663.

(18) Benin, A. I.; Hwang, S.-J.; Zones, S. I.; Xie, D.; Chaudhuri, K.; Lacheen, H. Structural and Compositional Studies of Crystalline MAPO Molecular Sieves Formed in Ionothermal Synthesis Using Imidazolium Bromides. *Microporous Mesoporous Mater.* **2019**, *274*, 257–265.

(19) Archer, R. H.; Zones, S. I.; Davis, M. E. Imidazolium Structure Directing Agents in Zeolite Synthesis: Exploring Guest/Host Relationships in the Synthesis of SSZ-70. *Microporous Mesoporous Mater.* **2010**, *130* (1–3), 255–265.

(20) Ravel, B.; Newville, M. ATHENA, ARTEMIS, HEPHAESTUS: Data Analysis for X-Ray Absorption Spectroscopy Using IFEFFIT. *J. Synchrotron Radiat.* **2005**, *12* (4), 537–541.

(21) Rehr, J. J.; Kas, J. J.; Vila, F. D.; Prange, M. P.; Jorissen, K. Parameter-Free Calculations of X-Ray Spectra with FEFF9. *Phys. Chem. Chem. Phys.* **2010**, *12* (21), 5503–5513.

(22) Chao, C.-H.; Lu, H.-Y. β-Cristobalite Stabilization in (Na2O+Al2O3)-Added Silica. *Metall. Mater. Trans. A* **2002**, *33* (8), 2703–2711.

(23) Morris, R. E.; Burton, A.; Bull, L. M.; Zones, S. I. SSZ-51A New Aluminophosphate Zeotype: Synthesis, Crystal Structure, NMR, and Dehydration Properties. *Chem. Mater.* **2004**, *16* (15), 2844–2851.

(24) Parnham, E. R.; Morris, R. E. Ionothermal Synthesis of Zeolites, Metal–Organic Frameworks, and Inorganic–Organic Hybrids. *Acc. Chem. Res.* **2007**, *40* (10), 1005–1013.

(25) Levanon, H.; Luz, Z. ESR and NMR of Mn(II) Complexes in Methanol. *J. Chem. Phys.* **1968**, *49* (5), 2031–2040.

(26) Goldfarb, D. MAS n.m.r. and e.s.r. Studies of MnAlPO5. *Zeolites* **1989**, *9* (6), 509–515.

(27) Lutz, O.; Steinkilberg, W. 55Manganese Nuclear Magnetic Resonance Studies. *Phys. Lett. A* **1969**, *30* (3), 183–184.

(28) Rentsch, D.; Hany, R.; Philipsborn, W. von. Transition Metal NMR Spectroscopy. 55Mn,13CO and 55Mn,31P Coupling Constants of Organomanganese Complexes: Comparison of NMR Results from Experiments in Solution and in the Solid State. *Magn. Reson. Chem.* **1997**, *35* (12), 832–838.

(29) Nakano, T. V-51 and Mn-55 NMR Studies of Metal Carbonyls. *Bull. Chem. Soc. Jpn.* **1977**, *50* (3), 661–665.

(30) Sinha, A. K.; Jacob, N. E.; Srinivas, D.; Sivasanker, S. Location of Mn in MnAPO-11: Influence of Synthesis from Aqueous and Non-aqueous Media. *Catal. Lett.* **1999**, *61* (3), 193–198.

(31) Sinha, A. K.; Satyanarayana, C. V. V.; Srinivas, D.; Sivasanker, S.; Ratnasamy, P. Location of Mn(II) Ions in Manganese Aluminophosphate Molecular Sieves: A Comparative Study of MnAPO-11 and MnAPO-41. *Microporous Mesoporous Mater.* **2000**, *35* (Supplement C), 471–481.

Chapter 3 - A flexible silver and bipyridine coordination polymer for the high-capacity trapping of perrhenate, a pertechnetate surrogate

Abstract

Pertechnetate, the most stable form of the radionuclide ^{99}Tc in aerobic aqueous systems, is a hazardous anion presented in nuclear waste. Its high mobility in water makes the remediation of the anion challenging. In the last decade, significant effort has been placed into finding materials capable of adsorbing this species. Here, we present the synthesis and high-resolution crystal structure of a new coordination polymer, [Ag(2,4'-bipyridine)]NO_3, which is capable of sequestering perrhenate—a pertechnetate surrogate—through anion exchange to form another new coordination polymer, [Ag(2,4'-bipyridine)]ReO_4. Both the beginning and end structures were solved by single crystal X-ray diffraction and the adsorption reaction was monitored through inductively coupled plasma - optical emission spectroscopy and UV-Vis spectroscopy. The exchange reaction follows a pseudo-second-order mechanism and the maximum adsorption capacity is 764 mg ReO_4/g [Ag(2,4'-bipyridine)]NO_3, one of the highest ever recorded for a coordination polymer or metal-organic framework. Further, the material has excellent selectivity towards perrhenate in the presence of up to 200× molar excess of sulfate. We also investigate the flexibility of [Ag(2,4'-bipyridine)]NO_3 through its anisotropic

thermal distortion and its ability to fold around perrhenate, thereby stabilizing the post-exchange coordination polymer.

3.1 Introduction

Coordination polymers (CPs) are hybrid organic/inorganic materials defined by IUPAC as “coordination compounds with repeating coordination entities extending in 1, 2, or 3 dimensions”. CPs’ polymeric structures are composed of metal centers covalently bridged to each other by organic ligands. Although the terms coordination polymer and metal-organic framework (MOF) are sometimes used interchangeably, in this Chapter, we will refer to MOFs as a subtype of CPs that present covalent polymeric growth in three dimensions, while CPs may possess lower covalent dimensionality. Due to their compositional and structural tunability, these materials have been studied in various applications, including gas adsorption,[1] energy storage,[2] catalysis,[3] luminescence,[4] sensing,[5] and selective anion crystallization.[6,7]

CP’s covalent dimensionality is generally ruled by the possible coordination modes of the metals used and the ligands’ hapticity and spatial orientation. For example, in $[Ni(_L\text{-Tyr})_2(4,4'\text{-bipy})]\cdot 4H_2O$, only two bidentate bipyridine (4,4'-bipy) ligands coordinate to Ni^{2+}, forming polymeric nearly linear 1D chains of alternating Ni^{2+} and 4,4'-bipy units. The other binding sites of the Ni^{2+} octahedral centers are occupied by tyrosine ligands, which do not allow further polymeric growth in other directions.[8] $[Cu(4,4'\text{-bipy})_2(BF_4)_2]$ also

contains the same bipyridine ligands. In this case, however, they bind to the metal centers in all four equatorial positions, while BF_4^- ions occupy the trans sites, resulting in a coordination polymer based on 2D square grids.[9,10] A strategy to increase the dimensionality of the Cu^{2+}/4,4'-bipy system using anions that can simultaneously coordinate to two 2D motifs. This is exemplified by GeF_6^{2-} in $[Cu(GeF_6)(4,4'\text{-bipy})_2]\cdot 8H_2O$, where each of its fluoride atoms binds to different Cu^{2+} centers.[11] Figure 3.1 shows the above coordination polymers based on 4,4'-bipy with different dimensionality.

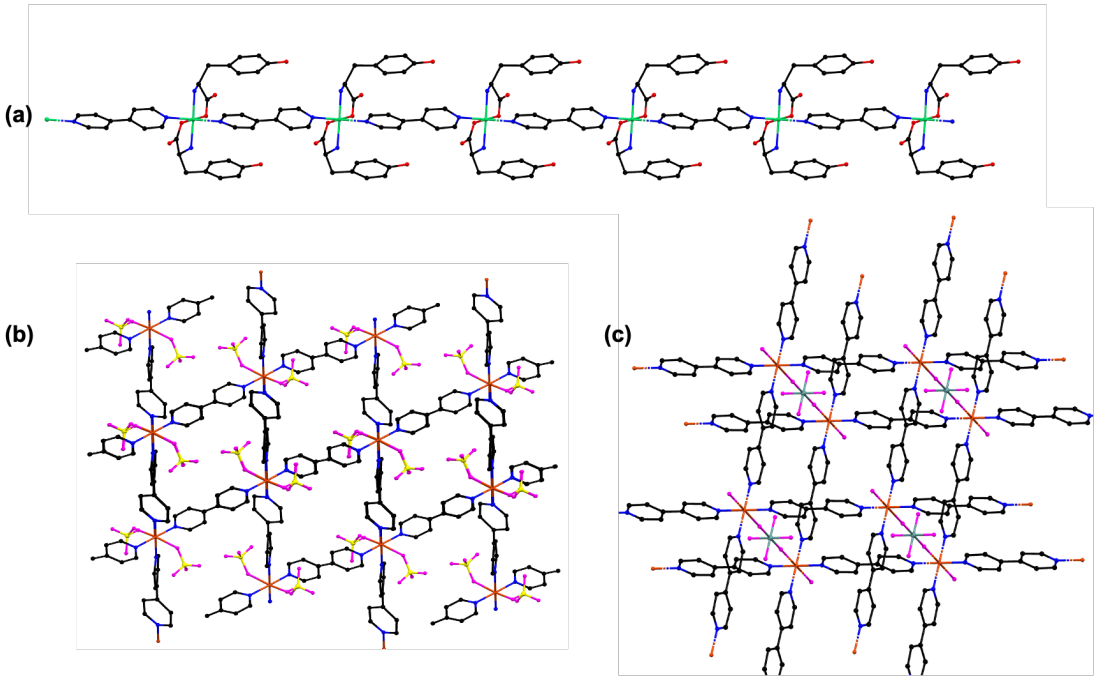

Figure 3.1 Coordination polymers based on 4,4'-bipyridine showing different dimensionalities: **(a)** 1D $[Ni(L\text{-}Tyr)_2(4,4'\text{-bipy})]\cdot 4H_2O$;[8] **(b)** 2D $[Cu(4,4'\text{-bipy})_2(BF_4)_2]$;[9,10] **(c)** 3D $[Cu(GeF_6)(4,4'\text{-bipy})_2]\cdot 8H_2O$.[11] Hydrogen atoms omitted for clarity; color scheme: C – black; N – blue; O – red; Ni – light green; Cu – orange; F – magenta; B – yellow; Ge – dark green.

One-dimensional CPs are of great interest as they are usually easier to crystallize than higher-dimensionality materials. Because of their simpler topology and fewer coordination array possibilities, better synthetic control is possible. Zhao et al. recently presented an extensive review of 1D CPs based on N-donor ligands. The authors reported five topologies commonly adopted by the 1D covalent chains: linear, zigzag, ribbon, ladder, and helical (Figure 3.2). These diverse topologies can be achieved using of ligands with different flexibilities and chiralities.[12]

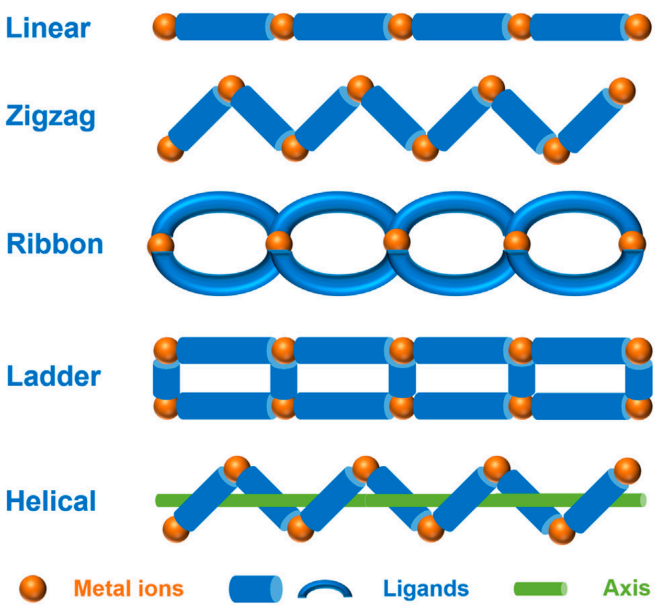

Figure 3.2 Common topologies adopted by 1D coordination polymers based on N-donor ligands.[12]

Besides the dimensionality of the structure, another feature that significantly affects the supramolecular chemistry of these compounds is the

overall charge of the covalent framework. By using low-valence cationic metals and neutral ligands, it is possible to obtain CPs with a positive charge, counter-balanced by anions residing in the structure's cavities. Because these anions are often weakly bound to the covalent framework via electrostatic interactions, cationic coordination polymers have been widely used in ion exchange applications.[13–15]

CPs are also unique because they may present higher structural flexibility and elasticity when compared to porous inorganic materials such as zeolites and aluminophosphates. Materials with such flexibility and elasticity are often referred to as soft porous crystals (SPCs), defined as "porous solids that possess both a highly ordered network and structural transformability".[16] One subtype of SPCs are the so-called flexible CPs, materials capable of changing crystallographic features such as unit cell volume through the adsorption/desorption of guest molecules.[17] This dynamic framework feature can make them capable of better accommodating species residing in their porous structures. Recent reports show that this class of materials can be used for the adsorption of a wide range of species, such as linear dicarboxylic acids,[18] hydrocarbon gases,[19] cobalt(II) ions,[20] and alkanes.[21]

The possible flexible porosity and positive charge of CPs make these materials great candidates for the adsorption of pollutant oxyanions, such as pertechnetate TcO_4^-. Technetium is a hazardous radionuclide introduced into nature mainly by anthropological sources, and it is estimated that 1 kg of

radionuclide is produced for every ton of enriched uranium fuel fissioned.[22] Once in aqueous systems, the most stable form of the long-lived ^{99}Tc is the pertechnetate ion TcO_4^-, with high water mobility due to its high solubility and weak coordination.[23] Currently, one of the most common strategies for the remediation of pertechnetate focus on the use of sorption methods. Recent studies employ bentonites,[24] carbazole derivatives,[25] cationic electrospun fibers,[26] modified commercial resins,[27,28] layered double hydroxides,[29] cationic polymeric networks,[30,31] mineral incorporation,[32] coordination polymers (CPs),[33] and metal-organic frameworks (MOFs).[34] To safely explore pertechnetate chemistry in a laboratory environment, it is common practice to use perrhenate as its surrogate, as TcO_4^- and ReO_4^- present the same geometry, charge and similar size.

Here, we report a flexible cationic coordination polymer [Ag(2,4'-bipyridine)]NO_3 (which we denote SLUG-53, for University of California, Santa Cruz, Structure No. 53) and its ability to sequester perrhenate through an anion exchange reaction. The rotational freedom of the central single carbon bond of the 2,4'-bipyridine ligand allows for a dynamic framework capable of uniquely accommodating the guest ion to form the new cationic CP [Ag(2,4'-bipyridine)]ReO_4 (which we denote SLUG-54).

3.2 Experimental

3.2.1 Materials

All reagents were used as-purchased: silver nitrate (Thermo Scientific, 99.9+%), 2,4'-bipyridine (2,4'-bipy, TCI), sodium perrhenate (Alfa Aesar, 99.95%) and sodium sulfate anhydrous (Fisher Scientific).

3.2.2 Synthesis of [Ag(2,4'-bipy)]NO_3 (SLUG-53)

5 mL aqueous solution of $AgNO_3$ (4.000 mmol, 0.6795 g) were added dropwise to 5 mL aqueous solution of 2,4'-bipyridine (1.000 mmol, 0.1562 g) under magnetic stirring. Upon addition, a white solid instantly precipitated. The resultant suspension was transferred to a Teflon-lined stainless-steel autoclave, placed in an oven at 145 °C for 5 d and then slowly cooled to room temperature at a rate of 0.1 °C/min. Colorless needle crystals suitable for single crystal X-ray diffraction (SCXRD) were isolated by vacuum filtration and rinsed with Milli-Q water. Yield based on 2,4'-bipyridine: 76.7%.

A polymorph material of SLUG-53 has been reported in the literature and will be discussed later in the paper. Such material was synthesized by combining methanolic equimolar solutions of $AgNO_3$ and 2,4'-bipyridine at 50 °C.[35]

3.2.3 Synthesis of [Ag(2,4'-bipy)]ReO_4 (SLUG-54)

An anion exchange reaction between SLUG-53 and $NaReO_4$ was prepared by placing 0.200 mmol (0.0652 g) of SLUG-53 in a beaker containing 10 mL of Milli-Q water and $NaReO_4$ (0.200 mmol, 0.0546 g), resulting in a white powder. Yield based on $NaReO_4$: 69.5%. The pH of the perrhenate solution was 5.7, and the pH of the mixture after 24 h reaction with SLUG-54 was 5.3. For large single crystals, an identical reaction mixture was transferred to a Teflon-lined stainless-steel autoclave, kept at 145 °C for 3 d and then slowly cooled to room temperature at a 0.1 °C/min rate. Colorless needle crystals suitable for single crystal X-ray diffraction (SCXRD) were isolated by vacuum filtration and rinsed with Milli-Q water. Yield based on $NaReO_4$: 43.3%.

3.2.4 Perrhenate uptake quantification

Adsorption kinetics were studied by performing an exchange reaction between SLUG-53 and $NaReO_4$ as described above. Aliquots were collected at 0.5, 1, 2, 3 and 4 h, syringe filtered and then analyzed by ICP-OES. The data was fitted to a pseudo-second-order model described in Equation 3.1.

$$\frac{t}{q_t} = \frac{1}{k_2 q_e^2} + \frac{t}{q_e} \tag{3.1}$$

where t is the reaction time (min), q_t is the material's adsorption at time t ($mg \cdot g^{-1}$), k_2 is the rate constant ($g \cdot mg^{-1} \cdot min^{-1}$), and q_e is the adsorption capacity at equilibrium ($mg \cdot g^{-1}$).

Sorption isotherms were obtained by placing 10 mg of CP in contact with 10 mL solutions of $NaReO_4$ with concentrations varying from 100 ppm to 1000 ppm. The reactions were kept under magnetic stirring for 24 h. Aliquots were collected for each reaction, syringe filtered and then analyzed by ICP-OES. The data was fitted to a Langmuir model as described in Equation 3.2.

$$\frac{C_e}{q_e} = \frac{1}{q_m K_L} + \frac{C_e}{q_m} \tag{3.2}$$

where C_e is the concentration of perrhenate ions at equilibrium ($mg \cdot L^{-1}$), q_m is the maximum adsorption capacity ($mg \cdot g^{-1}$), and K_L is the Langmuir model constant ($L \cdot mg^{-1}$). Both the adsorption kinetics and isotherms were obtained in triplicate.

3.2.5 Selectivity studies

SLUG-53 selectivity to uptake perrhenate was studied under two different molar excesses of sulfate. For a 50-fold excess, 0.4000 mmol (0.1304 g) of SLUG-53 was placed in a beaker containing 20 mL of Milli-Q water, $NaReO_4$ (0.4000 mol, 0.1093 g), and Na_2SO_4 (20.000 mmol, 2.8408 g). For a 200-fold excess, 0.4000 mmol (0.1304 g) of SLUG-53 was placed in a beaker

containing 50 mL of Milli-Q water, $NaReO_4$ (0.4000 mol, 0.1093 g), and Na_2SO_4 (50.0000 mol, 11.3632 g). A higher volume of water was used for the 200-fold excess reaction to guarantee the dissolution of the sulfate salt. Both reactions were performed in triplicate, syringe filtered, and the filtrate analyzed by inductively coupled plasma-optical emission spectroscopy (ICP-OES) for elemental quantification.

3.2.6 Instrumentation

Elemental Analysis

The concentrations of Re and Ag in the samples were obtained by ICP-OES on a PerkinElmer Optima 4300DV using yttrium as an internal standard and rhenium and silver solutions as external standards. The Re concentrations were then converted to perrhenate to be used in the kinetics and adsorption model studies. The equipment detection limits for Re and Ag were 5 ppb and 3 ppb, respectively.

Thermal stability analysis

Thermogravimetric analyses (TGA) were performed under nitrogen flow on a TA Instruments Q500 TGA with a temperature range of 25-500 °C at a heating rate of 10 °C/min.

Powder X-ray diffraction

Powder X-ray diffraction (PXRD) samples were prepared by grinding the synthetic products with a mortar and pistil and placing the resulting materials in an aluminum sample holder. The data was collected on a Rigaku Americas Miniflex Plus powder diffractometer under Cu Kα radiation (λ = 1.5418 Å) with a scanning range of 2° to 35° (2θ) at a rate of 2°/min with a 0.02° step size.

Variable temperature PXRD analysis

Ex situ variable temperature PXRD (VT-PXRD) was performed by heating the samples in a box furnace oven to 100, 200, 275, 300, 400 and 500 °C at a rate of 2°/min in air. The samples were analyzed on a Rigaku SmartLab X-ray Diffractometer with Cu Kα radiation (λ = 1.5418 Å) in parallel beam geometry from 2° to 50° (2θ) at a scan rate of 2°/min and 0.02° step size.

Single crystal X-ray diffraction (SCXRD)

Colorless crystals having dimensions 0.43 × 0.11 × 0.06 mm^3 (**SLUG-53-RT***), 0.50 × 0.06 × 0.05 mm^3 (**SLUG-53**) and 0.20 × 0.17 × 0.13 mm^3 (**SLUG-54**) were secured to Mitegen micromounts using Paratone oil and their SCXRD data was collected using a Rigaku Oxford Diffraction (ROD) Synergy-S X-ray diffractometer equipped with a HyPix-6000HE hybrid photon counting (HPC) detector and microfocused Cu $K_{\alpha 1}$ radiation (λ = 1.54184 Å). All data were collected at 100 K except for **SLUG-53-RT**, whose data was collected at

287 K. Data collection strategies for all samples to ensure completeness and desired redundancy were determined using CrysAlis^{Pro}.[36] Data processing was performed using CrysAlis^{Pro} and included numerical absorption corrections determined *via* face-indexing for samples **SLUG-53-RT** and **SLUG-54**. A multi-scan absorption correction was applied to **SLUG-53** using the SCALE3 ABSPACK scaling algorithm.[37] All structures were solved *via* intrinsic phasing methods using ShelXT[38] and refined using ShelXL[39] in the Olex2 graphical user interface.[40] Space groups were unambiguously verified by PLATON.[41] The final structural refinement included anisotropic temperature factors on all non-hydrogen atoms. All hydrogen atoms were attached *via* the riding model at calculated positions using suitable HFIX commands.

Selected crystallographic parameters are given in Table 3.1. Optical microscope images of SLUG-53 and SLUG-54 morphologies are depicted in Figure 3.3.

**SLUG-53 material was synthesized as described in the experimental section but with SCXRD data collected at room temperature.*

Table 3.1 Crystallographic parameters for SLUG-53 collected at 100 K and 287 K, and SLUG-54 collected at 100 K.

Compound	**SLUG-53 (100 K)**	**SLUG-53 (287 K)**	**SLUG-54**
Formula	$C_{10}H_8AgN_3O_3$	$C_{10}H_8AgN_3O_3$	$C_{10}H_8AgN_2O_4Re$
FW	326.06	326.06	514.25
T (K)	100	287	100
λ (Å)	1.54184	1.54184	1.54184
Crystal system	Monoclinic	Monoclinic	Monoclinic
Space group	$P2_1/c$	$P2_1/c$	$P2_1/n$
a (Å)	9.2352(7)	9.9566(3)	7.60620(10)
b (Å)	9.8442(7)	9.9051(2)	11.2555(2)
c (Å)	11.6191(8)	11.0666(3)	14.3200(2)
β (°)	99.343(7)	100.387(2)	101.094(2)
Volume (Å^3)	1042.32	1073.51(5)	1203.05(3)
Z	4	4	4
ρ_{calc} (mg/m^3)	2.078	2.017	2.839
Size (mm^3)	0.05 x 0.06 x 0.49	0.06 x 0.11 x 0.43	0.13 x 0.17 x 0.20
θ range (°)	5.85 – 66.40	4.52 – 66.96	5.03 – 67.07
Total data	7522	7818	8314
Unique data	1841	1908	2147
Parameters	154	155	164
Completeness	99.7%	99.9%	100%
R_{int}	6.50%	4.57%	4.36%
R_1 (I > 2σ)	3.88%	3.47%	3.54%
R_1 (all data)	4.13%	3.79%	3.59%
wR_2 (I > 2σ)	10.53%	9.64%	9.52%
wR_2 (all data)	10.74%	9.96%	9.58%
S	1.038	1.076	1.028
Min, max (e Å^{-3})	-0.848, 1.520	-0.964, 0.486	-0.954, 2.429

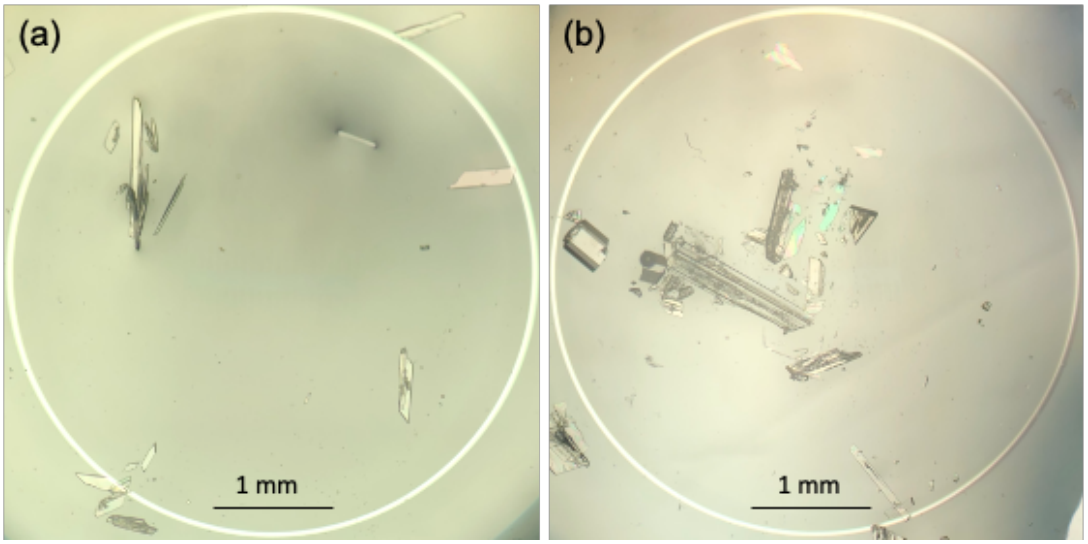

Figure 3.3 Optical microscopy images depicting the morphology of crystals of **(a)** SLUG-53 and **(b)** SLUG-54.

UV-Vis analysis

UV−Vis analysis was performed using quartz cuvettes on a Hewlett-Packard model 8452A UV−vis spectrophotometer with wavelength ranging from 190-820 nm.

Optical Microscopy

The morphologies of SLUG-53 and SLUG-54 crystals were examined on a Zeiss Axioskop 2 MAT microscope under bright-field light and 5x augmentation lenses.

3.3 Results and Discussion

[Ag(2,4'-bipy)]NO_3 (SLUG-53) was synthesized by the combination of the organic ligand 2,4'-bipyridine and silver nitrate. The low coordination number and +1 oxidation state of silver coupled with the neutral ligand allowed the formation of a coordination polymer with the cationic stoichiometry [Ag(2,4'-bipy)$^+$], counterbalanced by nitrate ions from the silver salt reagent. In order to guarantee an extended polymeric structure, a molar excess of silver nitrate in relation to 2,4'-bipy was necessary. Equimolar reactions led to the formation of a molecular solid (SLUG-55), as confirmed by SCRXD. Although showing significant disorder in the solvent molecules and nitrate groups, the structure was confirmed to have non-polymeric connectivity (Figure 3.4).

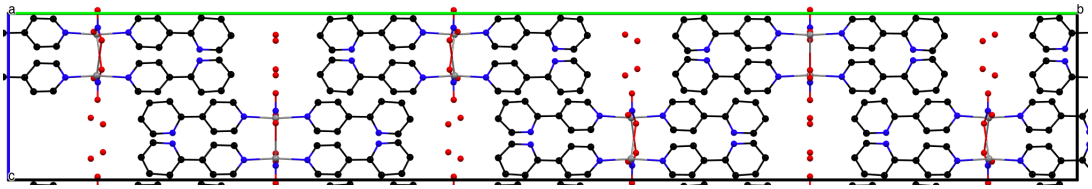

Figure 3.4 Single crystal structure of SLUG-55. Although major disorders are observed in the extra-framework moieties, it is possible to conclude that a molecular structure was obtained. Hydrogen atoms omitted for clarity; color scheme: Ag – gray; N – blue; O – red; C – black.

A molar excess of $AgNO_3$ as low as 1.5 times and as high as 4 times resulted in phase-pure SLUG-53 (Figure 3.5).

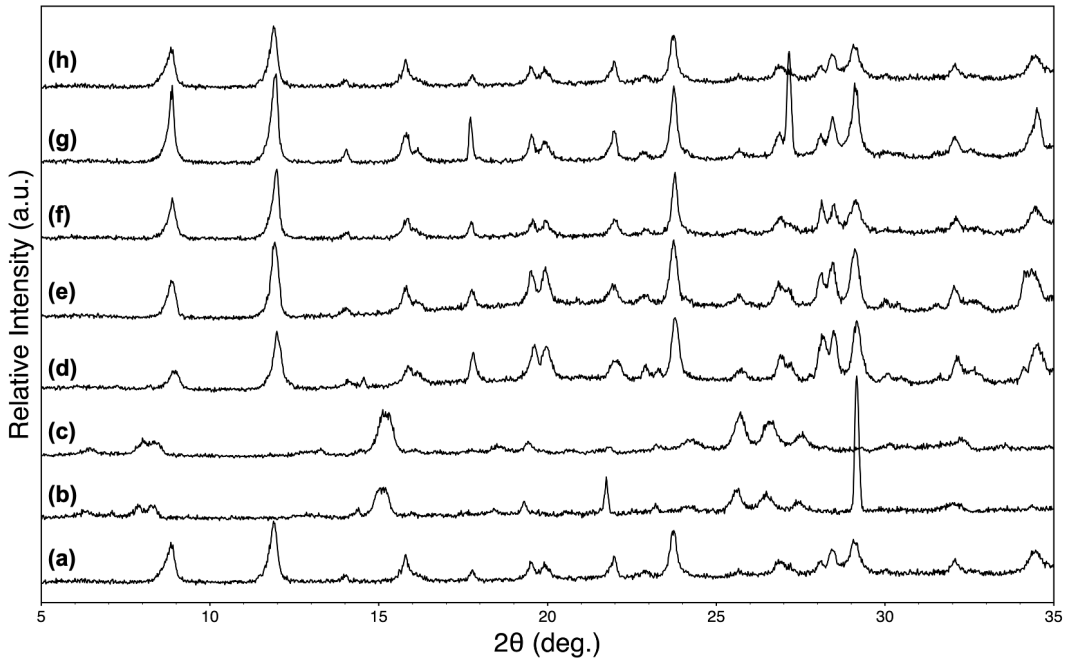

Figure 3.5 PXRD patterns of reaction products using different molar ratios of AgNO3 to 2,4'-bipyridine: **(a)** Reference SLUG-53 phase obtained from the same sample solved by SCXRD; **(b)** Reference molecular structure obtained from the same sample solved by SCXRD; **(c)** 1:1 molar ratio, molecular phase; **(d)** 1.5:1 molar ratio, SLUG-53; **(e)** 2:1 molar ratio, SLUG-53; **(f)** 2.5:1 molar ratio, SLUG-53; **(g)** 3:1 molar ratio, SLUG-53; **(h)** 4:1 molar ratio, SLUG-53.

3.3.1 Structural Description of SLUG-53

SLUG-53 crystallizes in space group $P2_1/c$ as colorless needle crystals. Its structure consists of zigzag chains growing in the direction of the crystallographic *b*-axis, formed by covalent bonds between silver and the nitrogen atoms of the 2,4'-bipy (Figure 3.6 a). Each silver atom connects to two ligands, binding through the nitrogen in the 4' position of one 2,4'-bipy (N2) and the 2 position of a second 2,4'-bipy (N3). Each ligand binds to another silver atom through its second nitrogen, leading to the modulating polymer. The Ag-

N3 bond length is 2.203(4) Å, and the Ag-N2 bond length is 2.179(3) Å. The silver also binds to one oxygen of a nitrate ion, with an Ag-O3 distance of 2.590(3) Å. The zigzag chains are not perfectly flat, with an N2-Ag-N3 angle of 163.73(13)°, resulting in a distorted T-shape geometry for the silver centers. The nitrate ions are positioned in the pockets of the zigzags, with only one of its oxygen atoms (O3) interacting with the silver. Therefore, the nitrates do not participate in extending the 1D zigzag chains into a 2D layer or 3D framework. Instead, the zigzag chains form a secondary structure by stacking upon each other through argentophilic interactions (Figure 3.6 b). Such interactions are generally accepted to occur whenever silver atoms with electronic configuration $[Kr]d^{10}$ are at a distance smaller than 3.44 Å – twice the van der Waals radius of Ag - in a crystal lattice.[42] Due to the asymmetry of the ligand and to maximize the argentophilic interactions, the zigzag chains are not perfectly parallel to each other but slightly shifted to allow closer contact between the silver centers. Further, neighboring zigzag chains are of opposite handedness and allow for a shorter Ag-Ag distance of 2.9949(6) Å. In addition to the argentophilic interactions, there is also interchain π-stacking of the 2,4'-bipy rings (green dashed lines, Figure 3.6 b). Because of the opposite handedness, this π-stacking occurs between the N2 and N3 rings, which are separated by 3.685(3) Å. Finally, a second π-stacking interaction connects the stacked zigzag layers, resulting in the overall 3D structure (orange dashed lines, Figure 3.6 c). This

interaction occurs between two N3 rings, each ring belonging to a different set of layered zigzag chains with a distance of 3.749(4) Å.

(a)

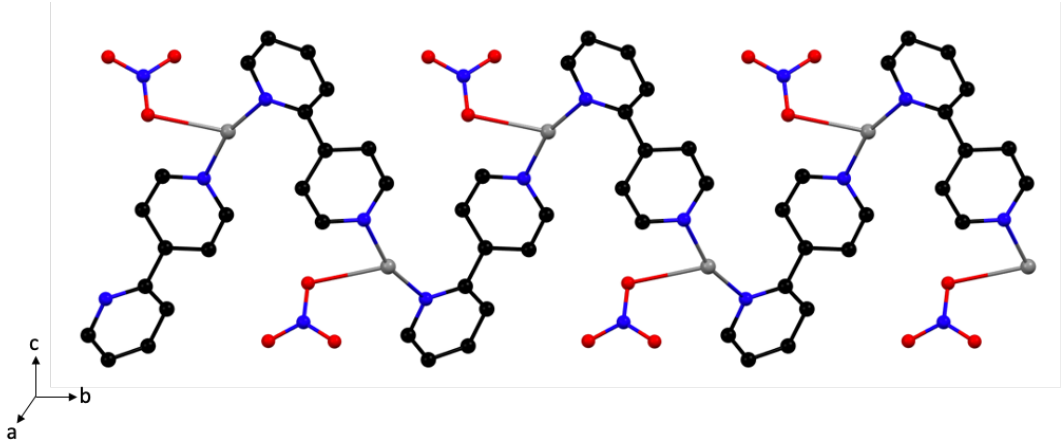

(b)

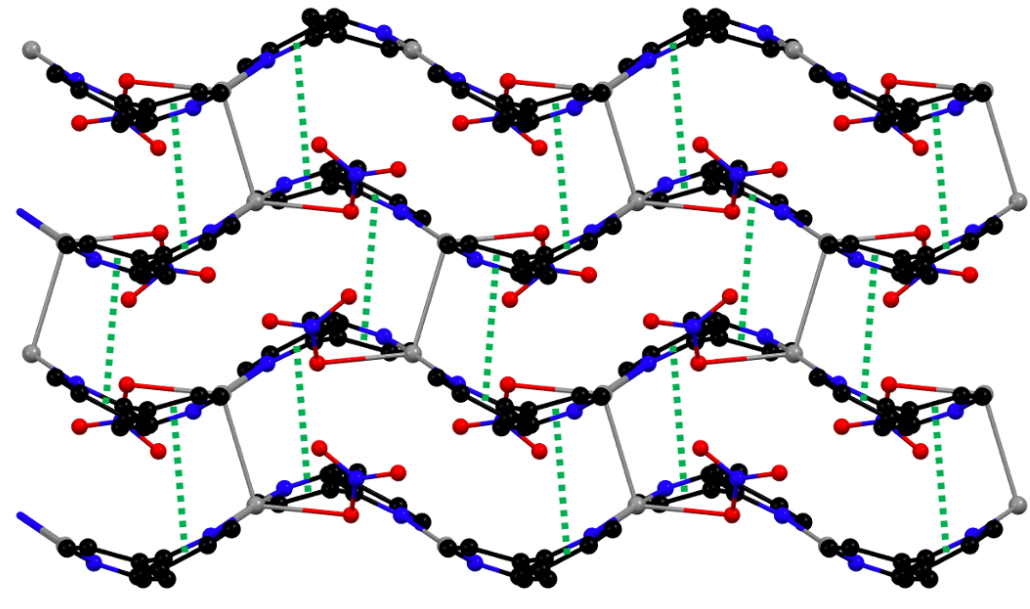

(c)

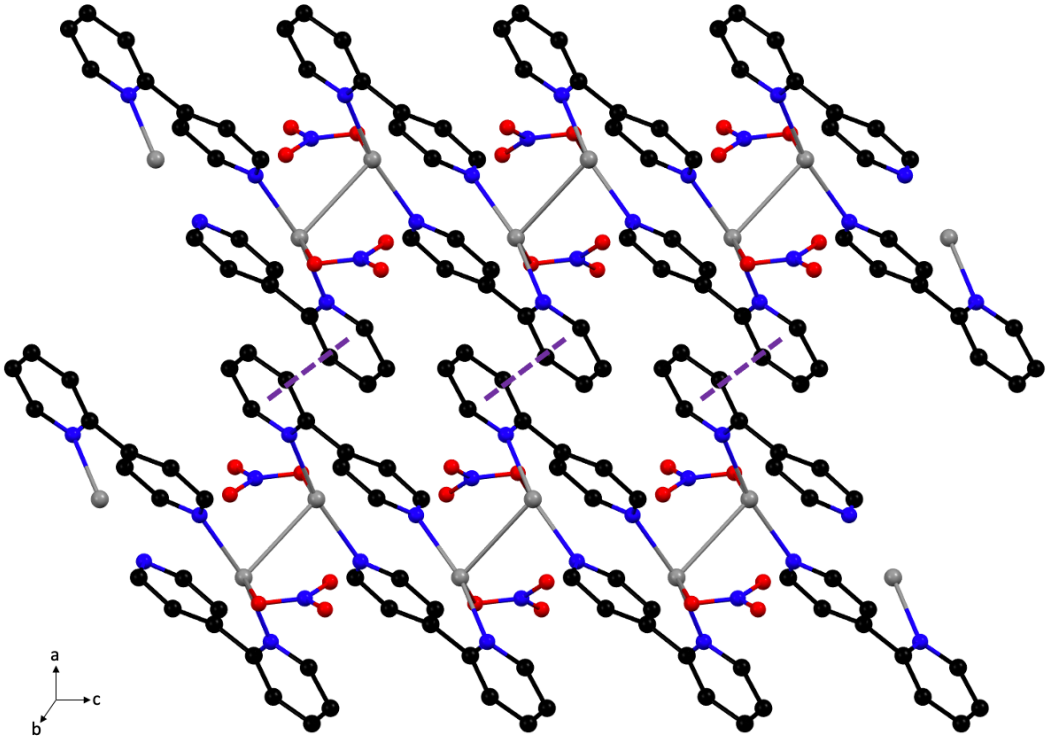

Figure 3.6 Crystal structure of SLUG-53 obtained by SCXRD at 100 K: **(a)** Projection along the b-axis, showing one polymeric zigzag chain formed by alternating Ag and 2,4'-bipy units. Nitrate anions reside in the pockets of the chain; **(b)** View parallel to the crystallographic (102) plane, showing the stacking of zigzag chains through both argentophilic interactions (solid gray lines) and π-stacking (dashed green lines); **(c)** In the projection along the *c*-axis, the layers described in (*b*) interact with each other through additional π-stacking, here showed by dashed purple lines. Hydrogen atoms omitted for clarity; color scheme: Ag – gray; N – blue; O – red; C – black.

A polymorphic CP of SLUG-53 crystallizes in the *Pbca* space group and has been reported in the literature. In that compound, the silver atoms still bind to two nitrogens from the ligands and one oxygen from NO_3^-, resulting in a distorted T-shape geometry. The zigzag chains of alternating Ag and 2,4'-bipy are again observed; however, the fashion in which they are arranged differs as

they are no longer shifted towards each other to maximize argentophilic interactions. As a result, the Ag-Ag distance is increased to 3.9868(5) Å, outside the covalent range. Further crystallographic comparison is given in Table 3.2.

Table 3.2 Comparison of crystallographic parameters for the novel SLUG-53 and its previously reported polymorph[35]

	SLUG-53	**Polymorph**
Crystal System	Monoclinic	Orthorhombic
Space Group	P21/c	Pbca
Unit cell parameters (Å)	9.2352(7); 9.8442(7); 11.6191(8) 90º; 99.343(7)º; 90º	11.2884(7); 11.3981(10); 16.5299(13) 90º; 90º; 90º
Volume (Å^3)	1042.32(13)	2126.8(3)
Ag1-Ag1 distance (Å)	2.9949(6)	3.9868(5)
N2-Ag1-N3 angle	163.7(13)°	169.03(8)°
Ligand torsion (N3-C6-C5-C4)	133.0(4)°	146.9(2)°

3.3.2 Thermal distortion of the SLUG-53 unit cell

In order to determine if the single crystal collected for SCXRD was representative of the bulk sample, we compared the theoretical powder pattern calculated from the single crystal data to that obtained experimentally by PXRD of the SLUG-53 needle crystals. Observing Bragg's Law, slight 2θ angle shifts are expected when comparing calculated versus theoretical patterns since PXRD and SCXRD data were collected at different temperatures (287 K and

100 K, respectively). Usually, there is a shrinking of the unit cell at lower temperatures and, consequently, the diffraction planes are close together. However, a significant mismatch of diffraction peaks was noticed when we compared the theoretical and experimental patterns for SLUG-53 (Figure 3.7). Because of that, a new SCXRD analysis on a different crystal was performed at room temperature.

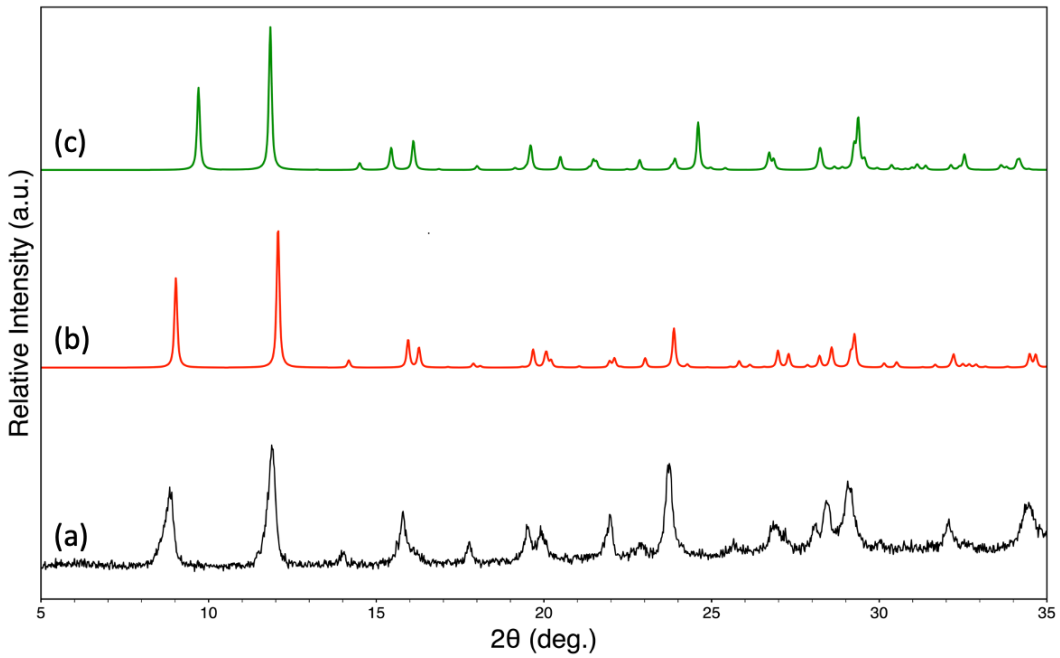

Figure 3.7 Powder X-ray diffractograms for SLUG-53. **(a)** experimental obtained at 287 K; **(b)** Calculated from SCXRD data collected at 287 K **(c)** Calculated from SCXRD data collected at 100 K. All calculated diffractograms were obtained using CSD Mercury.[43]

The room temperature SCXRD analysis revealed an anisotropic thermal distortion of the unit cell. Rather than uniformly shrinking at lower temperatures, an overall deformation occurred with the crystallographic *a*-axis decreasing by

7%, the crystallographic *b*-axis decreasing by 0.6%, and the crystallographic *c*-axis *increasing* by 5 %. Although unusual, particularly the increase of the unit cell along the *c*-axis, these distortions correlate well with the chemical structure of SLUG-53. The polymeric chain possesses stronger Ag-N covalent bonds in the *b* direction, while in the *a* and *c* directions are weaker van der Waals interactions. As a result, the latter two axes would be more susceptible to temperature-related distortions. Selected structural parameters are displayed in Table 3.3.

Table 3.3 Comparison of structural parameters between RT and 100 K SCXRD

	SLUG-53 100K	**SLUG-53 RT**
Crystal System	Monoclinic	Monoclinic
Space Group	$P2_1/c$	$P2_1/c$
Unit cell parameters (Å)	9.2352(7) 9.8442(7) 11.6191(8) 90° 99.343(7)°; 90°	9.9566(3) 9.9051(2) 11.0666(3) 90° 100.387(2)° 90°
Volume (Å^3)	1042.32(13)	1073.52(5)
Ag1-Ag1 distance (Å)	2.9949(6)	3.0792(7)
N2-Ag1-N3 angle	163.73(13)°	164.63(11)°
Ring distance N3-N3 rings (Å)	3.749(4)	3.761(3)
Ring distance N2-N3 rings (Å)	3.685(3)	3.775(2)
N3-C6-C5-C1 angle	46.5(5)°	45.6(5)°

3.3.3 Anion Exchange with ReO_4^-

The novel CP SLUG-53 successfully exchanges its nitrate for the hazardous perrhenate ion. The powder pattern of the exchange product is very similar to that of SLUG-53, but there is an important shift of the earlier peaks to higher angles (Figure 3.8). The similarity between the patterns suggests the covalent framework is preserved, while the shifts indicate that the new framework is likely wrapping around the incoming perrhenate ions. To strengthen this theory, we were able to recrystallize the exchange product and solve the compound as [Ag(2,4'-bipy)]ReO_4. The initial exchange product and the recrystallized material presented the same PXRD pattern, confirming that no phase change was observed after hydrothermal treatment.

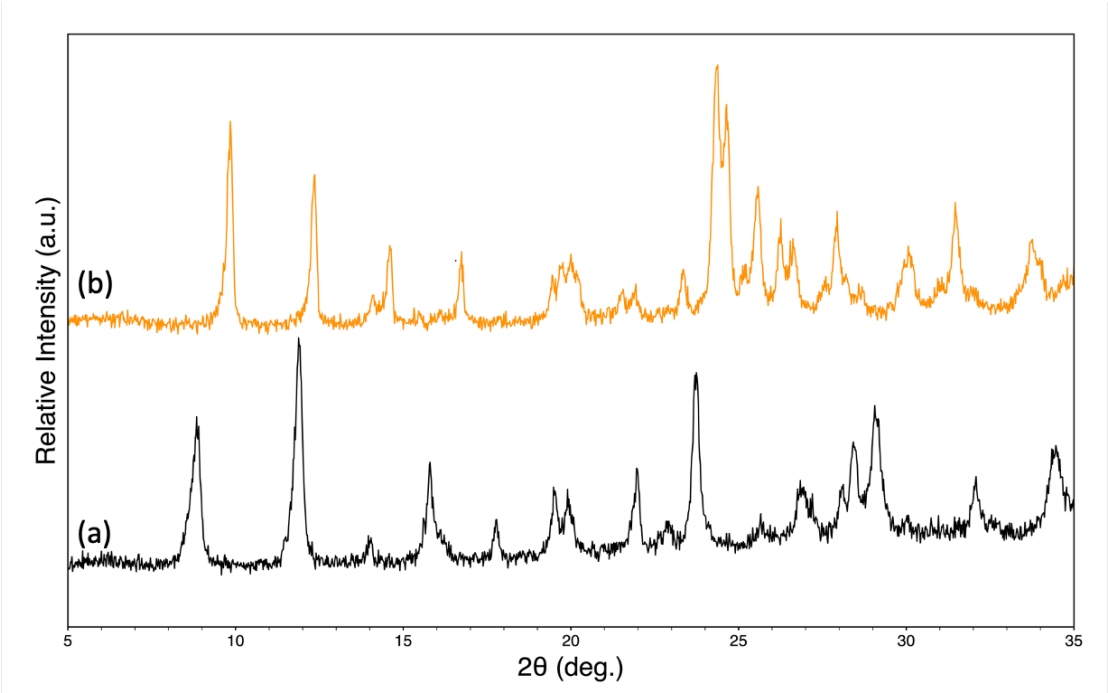

Figure 3.8 PXRD comparison between **(a)** the starting material SLUG-53, and **(b)** the exchange product SLUG-54.

3.3.4 Structural description of SLUG-54

The structure of SLUG-54 is presented in Figure 3.9. It also consists of polymeric zigzag chains built by the alternation of silver and 2,4'- bipyridine units in a similar fashion to SLUG-53, as expected by the powder pattern. The Ag-N1 distance is 2.202(5) Å and Ag-N2 is 2.183(5) Å (N1 and N2 being the 2 and 4' nitrogens of 2,4'-bipy, respectively). Once again, the chains are not perfectly planar, with an N1-Ag-N2 angle of 165.9(2)°. The main difference between the two CPs is the role of the counter-anion in building the overall structure. In SLUG-53, the nitrate ions resided in the zigzag pockets and interacted with only one silver atom. In SLUG-54, the perrhenate ions are the

primary units responsible for connecting adjacent chains. Due to its much larger size, perrhenate ions do not fit in the zigzag pockets the same way the nitrate ions did. The rhenium atom resides in the same plane as the zigzag chains, while the oxygen atoms reside in the interchain spacing. An eight-membered ring is thereby formed by two ReO_4 units bridging two silver atoms from adjacent zigzag chains, with bond lengths Re-O1 = 1.733(4) Å, Re-O4 = 1.730(5) Å, Ag-O4 = 2.617(5) Å and Ag-O1 = 2.588(5) Å. The other two oxygens of the perrhenate ion, O2 and O3, do not covalently interact. No argentophilic interactions are present, with the closest Ag atoms standing at 4.2693(8) Å apart.

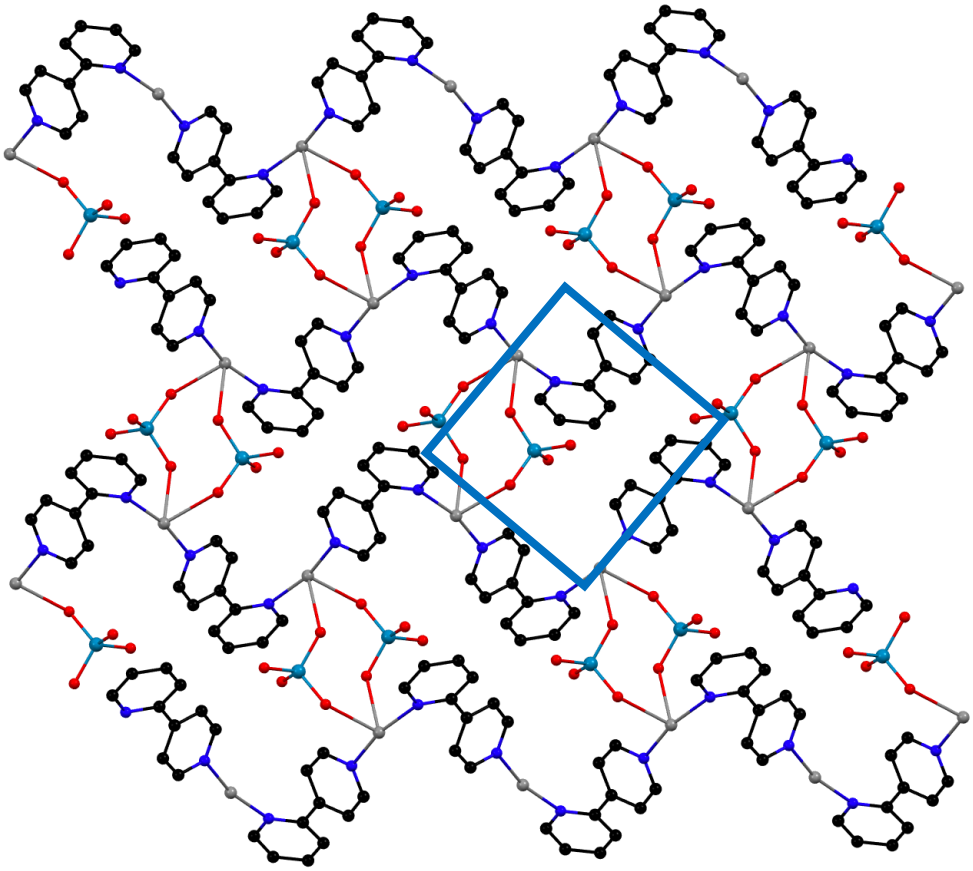

Figure 3.9 Crystal structure of SLUG-54 obtained by SCXRD at 100 K. Zigzag chains similar to SLUG-53 are again observed. However, the counter-anion now has a fundamental role in extending the structure through the formation of eight-membered rings containing silver atoms (emphasized as a blue rectangle). Color scheme: Ag – gray; N - blue; O - red; Re- light blue. All hydrogens are omitted for clarity.

3.3.5 ReO_4^- Exchange Quantification

To better understand the dynamics of the conversion of SLUG-53 to SLUG-54, we investigated the exchange reactions over different periods of time. The UV-Vis analysis of the filtrates of these reactions revealed the

increase of the nitrate peak intensity, indicating the release of this species upon the adsorption of perrhenate (Figure 3.10).

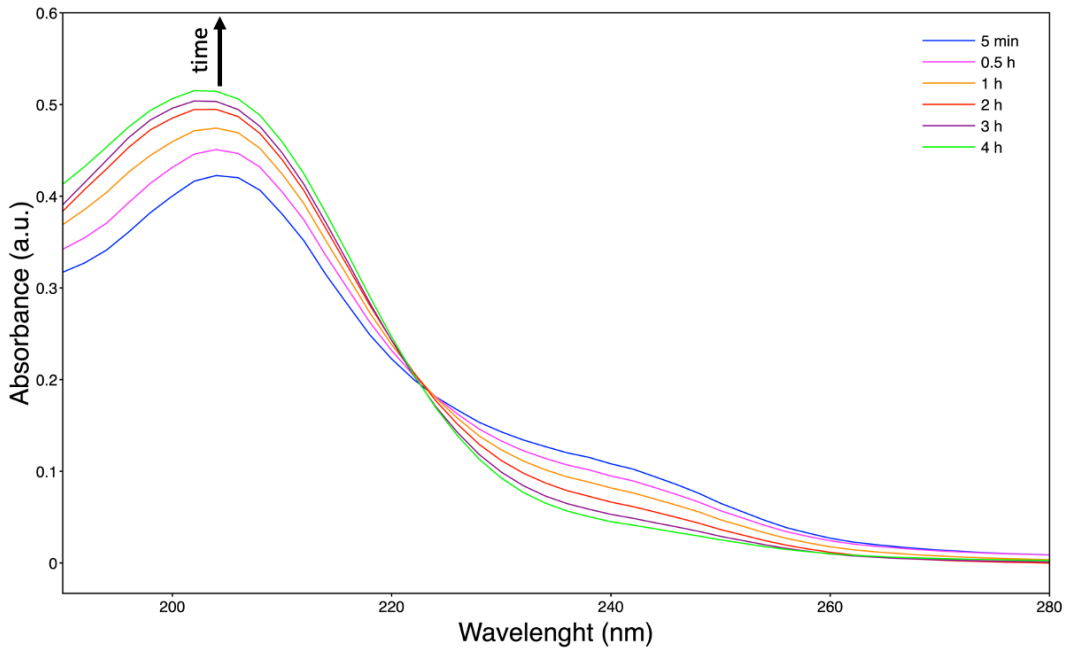

Figure 3.10 UV-Vis analysis of the conversion reaction between SLUG-53 and SLUG-54 over time shows an increase in the nitrate peak (λ = 204 nm) as the reaction proceeds, indicating nitrate ions are being released in the anion exchange reaction.

ICP-OES was used to quantify the perrhenate uptake. The percentage removals and adsorption capacities for the reactions at different times are given in Table 3.4.

Table 3.4 Perrhenate uptake quantification results for SLUG-53

Time (min)	% ReO_4^- removed	mg ReO_4^-/g SLUG-53
5	44.2 ± 2.6	341 ± 21
30	52.1 ± 1.7	404 ± 12
60	58.2 ± 1.7	448 ± 10
120	66.2 ± 2.7	510 ± 17
180	73.3 ± 3.4	564 ± 23
240	76.9 ± 4.7	592 ± 37
480	79.4 ± 9.5	611 ± 70
960	87.5 ± 6.3	673 ± 45
1440	90.6 ± 5.1	692 ± 36

Figure 3.11 and Table 3.5 show that the data fits well as a pseudo-second-order reaction.

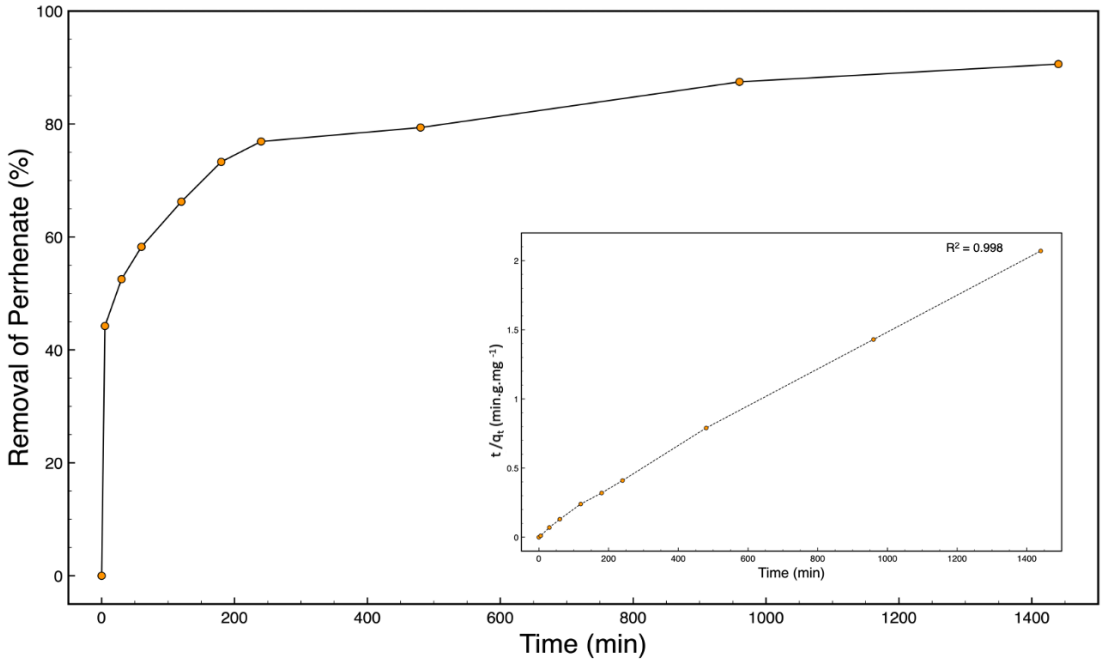

Figure 3.11 Percentage of perrhenate removed by SLUG-53 as a function of time (inset: data fitting to pseudo-second-order model).

Table 3.5 Kinetic parameters were obtained by fitting the adsorption data to a pseudo-second-order model.

R^2	k_2 (g mg^{-1} min^{-1})	q_e (mg g^{-1})
0.998	$4.58x10^{-5}$	702

To determine the maximum adsorption capacity, sorption isotherms were obtained by adding 10 mg of SLUG-53 to 10 mL of perrhenate with concentrations varying from 100 to 1000 ppm. The reactions were kept under stirring for 24h to guarantee equilibrium was reached. The data fit well with the Langmuir model (Figure 3.12, Table 3.6), and the maximum adsorption capacity was calculated to be 764 mg/g. This value is very close to the theoretical maximum adsorption (767 mg/g) calculated by assuming 1 mol of SLUG-53 could uptake 1 mol of perrhenate.

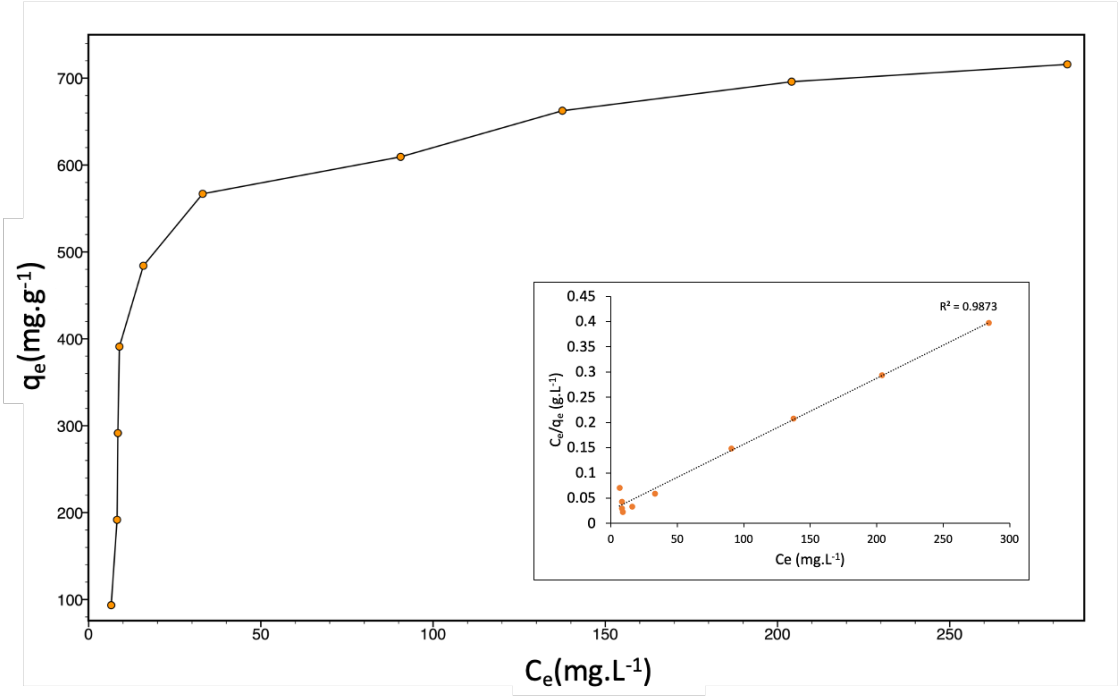

Figure 3.12 Adsorption capacity of SLUG-53 as a function of equilibrium concentration (inset: data fitting to Langmuir model).

Table 3.6 Adsorption parameters obtained by fitting the adsorption data to the Langmuir model

R^2	K_L (L mg^1)	q_m (mg g^{-1})
0.987	5.02x10^{-2}	764

Although the percentage removal of perrhenate is still lower than some commercial resins,[44] SLUG-53 adsorption capacity is incredibly high and superior to most of the CP/MOF materials reported to date (Table 3.7).

Table 3.7 ReO_4^-/TcO_4^- adsorption capacity of selected CPs/MOFs, polymeric and molecular materials (CPN = cationic polymeric network; iPOP = ionic porous organic polymers; MOC = metal-organic cage) in descending order

Material	Adsorption Capacity (mg ReO_4^- /g materials)	Class	Reference
SCU-CPN -2	1,467	CPN	[45]
SCU-CPN-1	999	CPN	[30]
MOR-2	876	CP/MOF	[46]
SPN	818	CP/MOF	[13]
Ni_3Th_6 MOF(1)*	807	CP/MOF	[47]
SBN	786	CP/MOF	[33]
SLUG-53	**764**	**CP/MOF**	**This work**
Purolite A530E	707	Resin	[44]
CAU-1	692	CP/MOF	[48]
iMOF-2C	691	CP/MOF	[49]
SLUG-21	602	CP/MOF	[50]
Th-MOF-68	560	CP/MOF	[51]
SCU-100	541	CP/MOF	[52]
ZJU-X11	518	CP/MOF	[53]
iPOP-3	516	iPOP	[54]
ZJU-X6	507	Cp/MOF	[55]
CL-*a*MOC-1	453	MOC	[56]
Purolite A532E	446	Resin	[44]
SCU-CPN-4	437	CPN	[57]
MILP-3	435	CP/MOF	[58]
TJNU-216	417	CP/MOF	[59]
Mn-MOF	403	CP/MOF	[60]
BUC-17	402	CP/MOF	[61]
ZJU-X4	395	CP/MOF	[62]
iPOP-4	350	iPOP	[54]
TNU-132	319	CP/MOF	[63]
SCU-103	318	CP/MOF	[31]
SCU-102	291	CP/MOF	[64]
Ag-TPPE	251	CP/MOF	[65]
Cu_8Cu_{18} MOF(1)**	218	CP/MOF	[66]
TJNU-302	211	CP/MOF	[67]

SCP-IHEP-1	211	CP/MOF	[68]
NU-1000	210	CP/MOF	[69]
IHEP-11	206	CP/MOF	[70]
UiO-66-NH_3^+	159	CP/MOF	[71]
ZJU-X12	150	CP/MOF	[53]
MIL-101-Cr-NO_3-CTAB	139	CP/MOF	[72]
Zr-tcbp-Me	128	CP/MOF	[73]
Zr-tcpp-Me	121	CP/MOF	[73]

* $\{[Ni_3Th_6(\mu_3\text{-}O)_4(\mu_3\text{-}OH)_4(IN)_{12})(H_2O)_{12}]\cdot(OH)_6\cdot 5DMF\cdot 2\ H_2O\}_n$
** $\{[Cu^{I}Cu_4^{II}(XN)_4(PTA)_4(H_2O)_4]0.5SO_4\cdot 5H_2O\cdot EtOH\}_n$

Sulfate ions may be present in great amounts in pertechnetate-containing waste.[63] Because of SO_4^{2-} charge density, they have been shown to be more favorably adsorbed by other materials designed for the removal of the TcO^{4-}. [74] SLUG-53, however, has shown good selectivity to adsorbing perrhenate in the presence of a molar excess of sulfate up to 200-fold (Table 3.8, Figure 3.13).

Table 3.8 Selectivity of SLUG-53 for the adsorption of perrhenate in the presence of sulfate

	50× SO_4^- excess		**200× SO_4^- excess**	
Time (min)	**% ReO_4^- removed**	**mg ReO_4^-/ g SLUG-53**	**% ReO_4^- removed**	**mg ReO_4^-/ g SLUG-53**
5	45.6 ± 5.2	349 ± 39	47.2 ± 8.2	403 ± 41
30	52.9 ± 5.2	405 ± 40	52.8 ± 11.3	451 ± 79
60	55.8 ± 5.0	427 ± 38	55.1 ± 11.5	478 ± 74
120	60.9 ± 4.1	466 ± 31	57.9 ± 11.9	501 ± 75
180	64.1 ± 5.1	491 ± 38	60.1 ± 11.4	500 ± 98
240	69.3 ± 3.1	530 ± 24	60.7 ± 12.0	521 ± 95

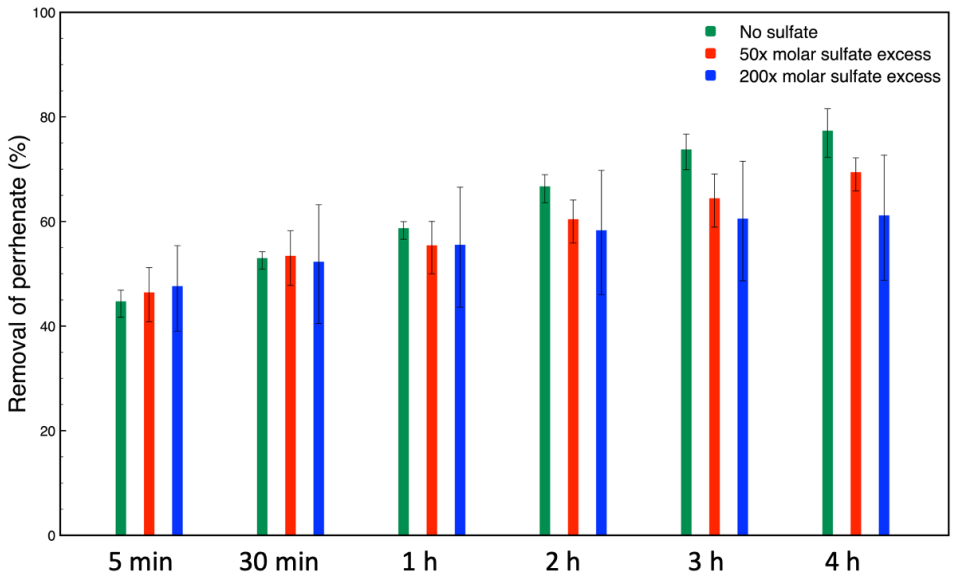

Figure 3.13 Selectivity of SLUG-53 for the adsorption of perrhenate in the presence of sulfate (green – no sulfate; red – 50x molar excess sulfate; blue – 200x molar excess sulfate) at varying exchange time.

3.3.6 Thermostability analysis

The thermogravimetric analyses show that SLUG-54 is more stable than SLUG-53 (Figure 3.14), which would facilitate perrhenate abatement. For SLUG-53, one main event is observed at 215 °C and corresponds to the loss of 2,4'-bipyridine (mass loss observed: 49.13%; calculated: 47.90%). For SLUG-54, the same event is observed but at 295 °C (mass loss observed: 30.26%; calculated: 30.37%). As expected, no water loss peak was observed in the thermal profiles since there is no crystallographic water in the structures. The higher stability of the perrhenate CP can be hypothesized to be due to the eight-membered inorganic ring (Figure 3.9), which would more efficiently hold

the framework together when compared to the soft argentophilic interactions of SLUG-53. The TGA results correlate well with VT-PXRD analyses. For SLUG-53 (Figure 3.15), the usual powder pattern for the material is observed up to 200 °C. At 275 °C, there is a mixture of SLUG-53 and silver metal phases. Finally, only silver metal peaks are observed at 300 °C and above. For SLUG-54, the pure CP phase is observed until 300 °C (Figure 3.16). Starting at 400 °C, a mixture of silver metal and silver perrhenate phases is observed.

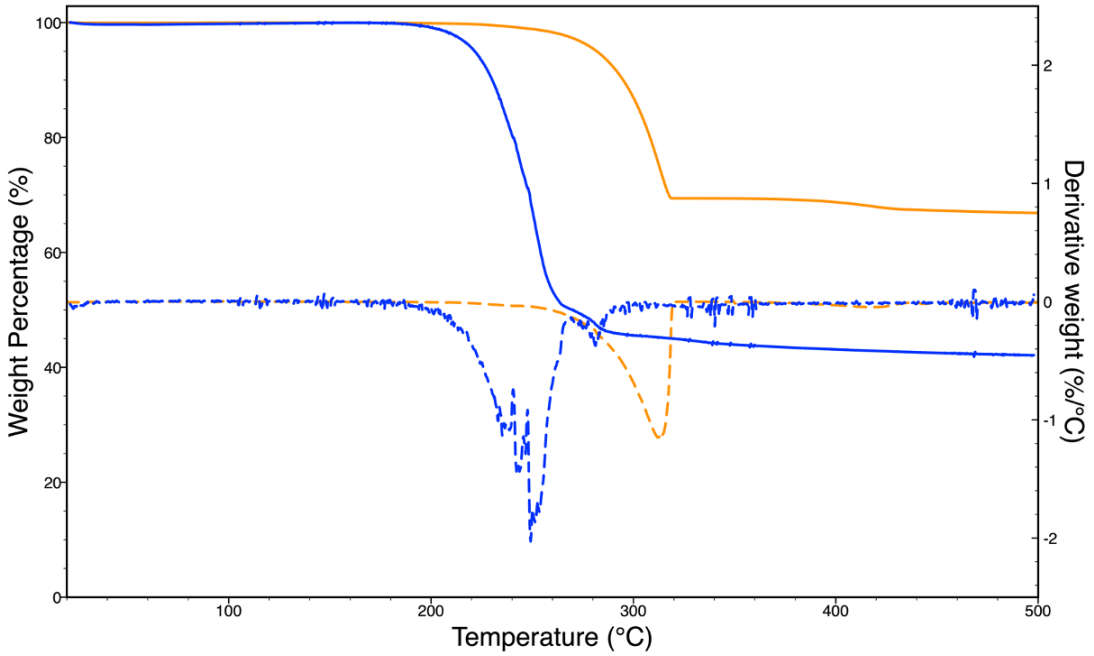

Figure 3.14 TGA analyses: solid blue - SLUG-53; dashed blue - 1st derivative of SLUG-53 trace; solid orange – SLUG-54; dashed orange – 1st derivative of SLUG-54 trace.

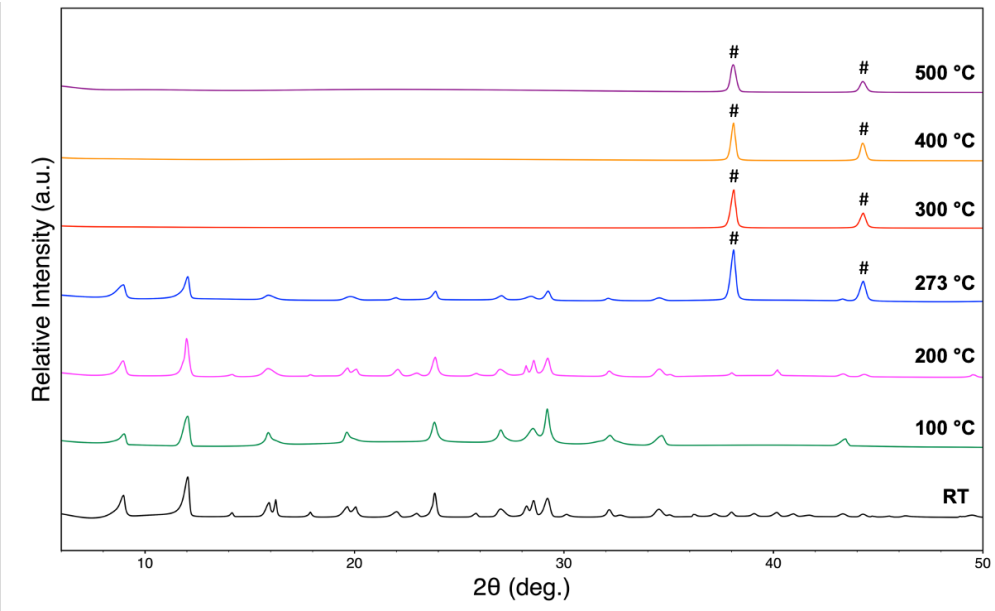

Figure 3.15 Ex situ VT-PXRD of SLUG-53. #: silver metal, COD ID: 901296.[75]

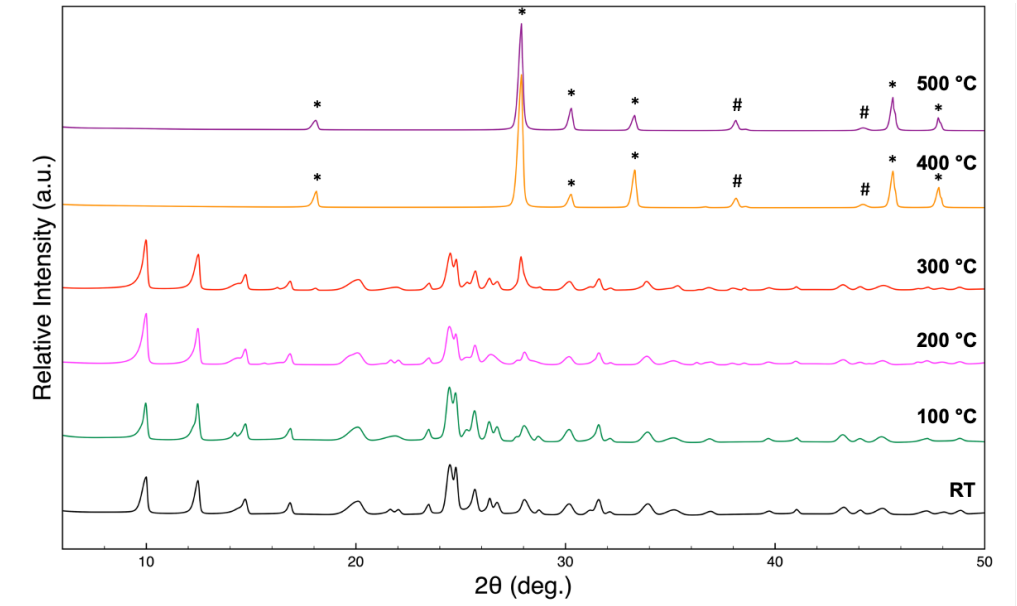

Figure 3.16 Ex situ VT-PXRD of SLUG-54. #: silver metal, COD ID: 9012961.[15] *: silver perrhenate, COD ID: 2008824.[76]

3.4 Conclusions and Future Directions

We presented two new [Ag(2,4'-bipyridine)]$^{+}$ CPs, both before and after the exchange of the counter-anion nitrate for perrhenate. The structural features of both materials allowed for the high-capacity sequestration of the incoming ReO_4^- . SLUG-53 is thus a promising material to be applied in the remediation of the perrhenate analog pertechnetate. Our materials were all obtained and crystallized in aqueous media, avoiding the use of organic solvents. The flexibility of the ligand 2,4'-bipyridine can be combined with the use of metals with open coordination sites, such as silver, to obtain a breathable cationic CP capable of folding around the guest perrhenate ion. The present study expands the current understanding of soft porous crystals and can aid the development of future cationic CP materials for anion trapping.

3.5 References

(1) Furukawa, H.; Ko, N.; Go, Y. B.; Aratani, N.; Choi, S. B.; Choi, E.; Yazaydin, A. O.; Snurr, R. Q.; O'Keeffe, M.; Kim, J.; Yaghi, O. M. Ultrahigh Porosity in Metal-Organic Frameworks. *Science* **2010**, *329* (5990), 424–428. https://doi.org/10.1126/science.1192160.

(2) Wang, L.; Han, Y.; Feng, X.; Zhou, J.; Qi, P.; Wang, B. Metal–Organic Frameworks for Energy Storage: Batteries and Supercapacitors. *Coordination Chemistry Reviews* **2016**, *307*, 361–381. https://doi.org/10.1016/j.ccr.2015.09.002.

(3) Liu, J.; Chen, L.; Cui, H.; Zhang, J.; Zhang, L.; Su, C.-Y. Applications of Metal–Organic Frameworks in Heterogeneous Supramolecular Catalysis. *Chem. Soc. Rev.* **2014**, *43* (16), 6011–6061. https://doi.org/10.1039/C4CS00094C.

(4) Allendorf, M. D.; Bauer, C. A.; Bhakta, R. K.; Houk, R. J. T. Luminescent Metal–Organic Frameworks. *Chem. Soc. Rev.* **2009**, *38* (5), 1330–1352. https://doi.org/10.1039/B802352M.

(5) Lustig, W. P.; Mukherjee, S.; Rudd, N. D.; Desai, A. V.; Li, J.; Ghosh, S. K. Metal-Organic Frameworks: Functional Luminescent and Photonic Materials for Sensing Applications. *Chem. Soc. Rev.* **2017**, *46* (11), 3242–3285. https://doi.org/10.1039/c6cs00930a.

(6) Custelcean, R.; Haverlock, T. J.; Moyer, B. A. Anion Separation by Selective Crystallization of Metal−Organic Frameworks. *Inorg. Chem.* **2006**, *45* (16), 6446–6452. https://doi.org/10.1021/ic060958g.

(7) Custelcean, R.; Moyer, B. A. Anion Separation with Metal–Organic Frameworks. *European Journal of Inorganic Chemistry* **2007**, *2007* (10), 1321–1340. https://doi.org/10.1002/ejic.200700018.

(8) *Structural, spectroscopic, magnetic behavior and DFT investigations of l-tyrosinato nickel(ii) coordination polymer - New Journal of Chemistry (RSC Publishing)*. https://pubs.rsc.org/en/content/articlelanding/2015/NJ/C5NJ00972C (accessed 2023-07-22).

(9) Cheng, Y.; Kondo, A.; Noguchi, H.; Kajiro, H.; Urita, K.; Ohba, T.; Kaneko, K.; Kanoh, H. Reversible Structural Change of Cu-MOF on Exposure to Water and Its CO2 Adsorptivity. *Langmuir* **2009**, *25* (8), 4510–4513. https://doi.org/10.1021/la803818p.

(10) Kondo, A.; Noguchi, H.; Ohnishi, S.; Kajiro, H.; Tohdoh, A.; Hattori, Y.; Xu, W.-C.; Tanaka, H.; Kanoh, H.; Kaneko, K. Novel Expansion/Shrinkage Modulation of 2D Layered MOF Triggered by Clathrate Formation with CO2 Molecules. *Nano Lett.* **2006**, *6* (11), 2581–2584. https://doi.org/10.1021/nl062032b.

(11) Noro, S.; Kitaura, R.; Kondo, M.; Kitagawa, S.; Ishii, T.; Matsuzaka, H.; Yamashita, M. Framework Engineering by Anions and Porous

Functionalities of Cu(II)/4,4‘-Bpy Coordination Polymers. *J. Am. Chem. Soc.* **2002**, *124* (11), 2568–2583. https://doi.org/10.1021/ja0113192.

(12) Zhao, J.; Yuan, J.; Fang, Z.; Huang, S.; Chen, Z.; Qiu, F.; Lu, C.; Zhu, J.; Zhuang, X. One-Dimensional Coordination Polymers Based on Metal–Nitrogen Linkages. *Coordination Chemistry Reviews* **2022**, *471*, 214735. https://doi.org/10.1016/j.ccr.2022.214735.

(13) Soe, E.; Ehlke, B.; Oliver, S. R. J. A Cationic Silver Pyrazine Coordination Polymer with High Capacity Anion Uptake from Water. *Environ. Sci. Technol.* **2019**, *53* (13), 7663–7672. https://doi.org/10.1021/acs.est.9b01633.

(14) Citrak, S. C.; Bdeir, K.; Delgado-Cunningham, K.; Popple, D.; Oliver, S. R. J. Exchange Capability of Cationic Silver 4,4′-Bipyrdine Materials for Potential Water Remediation: Structure, Stability, and Anion Exchange Properties. *Inorg. Chem.* **2019**, *58* (11), 7189–7199. https://doi.org/10.1021/acs.inorgchem.9b00115.

(15) Chatenever, A. R. K.; Abdollahian, Y.; Oliver, A. G.; Oliver, S. R. J. Three Neodymium-Based Cationic Layered Inorganic Materials Capable of Anion Exchange. *Inorganica Chimica Acta* **2019**, *498*, 119171. https://doi.org/10.1016/j.ica.2019.119171.

(16) Horike, S.; Shimomura, S.; Kitagawa, S. Soft Porous Crystals. *Nature Chem* **2009**, *1* (9), 695–704. https://doi.org/10.1038/nchem.444.

(17) Schneemann, A.; Bon, V.; Schwedler, I.; Senkovska, I.; Kaskel, S.; Fischer, R. A. Flexible Metal–Organic Frameworks. *Chem. Soc. Rev.* **2014**, *43* (16), 6062–6096. https://doi.org/10.1039/C4CS00101J.

(18) Qin, J.-S.; Yuan, S.; Alsalme, A.; Zhou, H.-C. Flexible Zirconium MOF as the Crystalline Sponge for Coordinative Alignment of Dicarboxylates. *ACS Appl. Mater. Interfaces* **2017**, *9* (39), 33408–33412. https://doi.org/10.1021/acsami.6b16264.

(19) Hähnel, T.; Kalies, G.; Krishna, R.; Möllmer, J.; Hofmann, J.; Kobalz, M.; Krautscheid, H. Adsorptive Separation of C2/C3/C4-Hydrocarbons on a Flexible Cu-MOF: The Influence of Temperature, Chain Length and Bonding Character. *Microporous and Mesoporous Materials* **2016**, *224*, 392–399. https://doi.org/10.1016/j.micromeso.2015.12.056.

(20) Li, M.; Yuan, G.; Zeng, Y.; Peng, H.; Yang, Y.; Liao, J.; Yang, J.; Liu, N. Efficient Removal of Co(II) from Aqueous Solution by Flexible Metal-Organic Framework Membranes. *Journal of Molecular Liquids* **2021**, *324*, 114718. https://doi.org/10.1016/j.molliq.2020.114718.

(21) Velasco, E.; Xian, S.; Wang, H.; Teat, S. J.; Olson, D. H.; Tan, K.; Ullah, S.; Osborn Popp, T. M.; Bernstein, A. D.; Oyekan, K. A.; Nieuwkoop, A. J.; Thonhauser, T.; Li, J. Flexible Zn-MOF with Rare Underlying Scu Topology for Effective Separation of C6 Alkane Isomers. *ACS Appl. Mater. Interfaces* **2021**, *13* (44), 51997–52005. https://doi.org/10.1021/acsami.1c08678.

(22) Icenhower, J. P.; Qafoku, N. P.; Zachara, J. M.; Martin, W. J. The Biogeochemistry of Technetium: A Review of the Behavior of an Artificial Element in the Natural Environment. *American Journal of Science* **2010**, *310* (8), 721–752. https://doi.org/10.2475/08.2010.02.

(23) Desmet, G.; Myttenaere, C. *Technetium in the Environment*; Springer Science & Business Media, 2012.

(24) Buzetzky, D.; Kovács, E. M.; Nagy, M. N.; Kónya, J. Sorption of Pertechnetate Anion by Cation Modified Bentonites. *J Radioanal Nucl Chem* **2019**, *322* (3), 1771–1776. https://doi.org/10.1007/s10967-019-06852-8.

(25) Shu, X.; Xu, Y.; Liu, L.; Fan, Y.; Zhuang, X.; Huang, C.; Chen, S.; Zheng, C.; Jin, Y.; Xia, C. Synthesis of New Carbazole Derivative Extractants and Study on Extraction of Perrhenate/Pertechnetate. *Polyhedron* **2022**, *214*, 115641. https://doi.org/10.1016/j.poly.2021.115641.

(26) Zhao, R.; Chen, D.; Gao, N.; Yuan, L.; Hu, W.; Cui, F.; Tian, Y.; Shi, W.; Ma, S.; Zhu, G. Porous Cationic Electrospun Fibers with Sufficient Adsorption Sites for Effective and Continuous 99TcO4− Uptake. *Advanced Functional Materials* **2022**, *32* (26), 2200618. https://doi.org/10.1002/adfm.202200618.

(27) Zhang, P.; Chen, Y.-Z.; Weng, H.-Q.; Guo, Z.-F.; Chen, J.-L.; Zhao, X.; Ye, G.-A.; Lin, M.-Z. Dication-Accelerated Anion Transport inside

Micropores for the Rapid Decontamination of Pertechnetate. *NUCL SCI TECH* **2022**, *33* (4), 42. https://doi.org/10.1007/s41365-022-01026-w.

(28) Bonnesen, P. V.; Brown, G. M.; Alexandratos, S. D.; Bavoux, L. B.; Presley, D. J.; Patel, V.; Ober, R.; Moyer, B. A. Development of Bifunctional Anion-Exchange Resins with Improved Selectivity and Sorptive Kinetics for Pertechnetate: Batch-Equilibrium Experiments. *Environ. Sci. Technol.* **2000**, *34* (17), 3761–3766. https://doi.org/10.1021/es990858s.

(29) Celik, A.; Li, D.; Quintero, M. A.; Taylor-Pashow, K. M. L.; Zhu, X.; Shakouri, M.; Roy, S. C.; Kanatzidis, M. G.; Arslan, Z.; Blanton, A.; Nie, J.; Ma, S.; Han, F. X.; Islam, S. M. Removal of CrO42–, a Nonradioactive Surrogate of 99TcO4–, Using LDH–Mo3S13 Nanosheets. *Environ. Sci. Technol.* **2022**, *56* (12), 8590–8598. https://doi.org/10.1021/acs.est.1c08766.

(30) Li, J.; Dai, X.; Zhu, L.; Xu, C.; Zhang, D.; Silver, M. A.; Li, P.; Chen, L.; Li, Y.; Zuo, D.; Zhang, H.; Xiao, C.; Chen, J.; Diwu, J.; Farha, O. K.; Albrecht-Schmitt, T. E.; Chai, Z.; Wang, S. 99TcO4− Remediation by a Cationic Polymeric Network. *Nat Commun* **2018**, *9* (1), 3007. https://doi.org/10.1038/s41467-018-05380-5.

(31) Shen, N.; Yang, Z.; Liu, S.; Dai, X.; Xiao, C.; Taylor-Pashow, K.; Li, D.; Yang, C.; Li, J.; Zhang, Y.; Zhang, M.; Zhou, R.; Chai, Z.; Wang, S. 99TcO4− Removal from Legacy Defense Nuclear Waste by an Alkaline-

Stable 2D Cationic Metal Organic Framework. *Nat Commun* **2020**, *11* (1), 5571. https://doi.org/10.1038/s41467-020-19374-9.

(32) Boglaienko, D.; Levitskaia, T. G. The Abiotic Reductive Removal and Subsequent Incorporation of Tc(IV) into Iron Oxides: A Frontier Review. *Environ. Sci.: Nano* **2019**, *6* (12), 3492–3500. https://doi.org/10.1039/C9EN00903E.

(33) Zhu, L.; Xiao, C.; Dai, X.; Li, J.; Gui, D.; Sheng, D.; Chen, L.; Zhou, R.; Chai, Z.; Albrecht-Schmitt, T. E.; Wang, S. Exceptional Perrhenate/Pertechnetate Uptake and Subsequent Immobilization by a Low-Dimensional Cationic Coordination Polymer: Overcoming the Hofmeister Bias Selectivity. *Environ. Sci. Technol. Lett.* **2017**, *4* (7), 316–322. https://doi.org/10.1021/acs.estlett.7b00165.

(34) Xiao, C.; Khayambashi, A.; Wang, S. Separation and Remediation of 99TcO4– from Aqueous Solutions. *Chem. Mater.* **2019**, *31* (11), 3863–3877. https://doi.org/10.1021/acs.chemmater.9b00329.

(35) Tong, M.-L.; Chen, X.-M.; Ye, B.-H.; Ng, S. W. Helical Silver(I)−2,4‘-Bipyridine Chains Organized into 2-D Networks by Metal−Counterion or Metal−Metal Bonding. Structures of [Ag(2,4‘-Bipyridine)]X (X- = NO3- or ClO4-). *Inorg. Chem.* **1998**, *37* (20), 5278–5281. https://doi.org/10.1021/ic971579d.

(36) CrysAlisPro, Rigaku Oxford Diffraction, Version 171.41.103a, 2021.

(37) SCALE3 ABSPACK – A Rigaku Oxford Diffraction Program for Absorption Corrections, Rigaku Oxford Diffraction, 2017.

(38) Sheldrick, G. M. SHELXT – Integrated Space-Group and Crystal-Structure Determination. *Acta Cryst A* **2015**, *71* (1), 3–8. https://doi.org/10.1107/S2053273314026370.

(39) Sheldrick, G. M. Crystal Structure Refinement with SHELXL. *Acta Cryst C* **2015**, *71* (1), 3–8. https://doi.org/10.1107/S2053229614024218.

(40) Dolomanov, O. V.; Bourhis, L. J.; Gildea, R. J.; Howard, J. a. K.; Puschmann, H. OLEX2: A Complete Structure Solution, Refinement and Analysis Program. *J Appl Cryst* **2009**, *42* (2), 339–341. https://doi.org/10.1107/S0021889808042726.

(41) Spek, A. L. Structure Validation in Chemical Crystallography. *Acta Cryst D* **2009**, *65* (2), 148–155. https://doi.org/10.1107/S090744490804362X.

(42) Schmidbaur, H.; Schier, A. Argentophilic Interactions. *Angewandte Chemie International Edition* **2015**, *54* (3), 746–784. https://doi.org/10.1002/anie.201405936.

(43) Macrae, C. F.; Sovago, I.; Cottrell, S. J.; Galek, P. T. A.; McCabe, P.; Pidcock, E.; Platings, M.; Shields, G. P.; Stevens, J. S.; Towler, M.; Wood, P. A. Mercury 4.0: From Visualization to Analysis, Design and Prediction. *J Appl Cryst* **2020**, *53* (1), 226–235. https://doi.org/10.1107/S1600576719014092.

(44) Li, J.; Zhu, L.; Xiao, C.; Chen, L.; Chai, Z.; Wang, S. Efficient Uptake of Perrhenate/Pertechnenate from Aqueous Solutions by the Bifunctional Anion-Exchange Resin. *Radiochimica Acta* **2018**, *106* (7), 581–591. https://doi.org/10.1515/ract-2017-2829.

(45) Li, J.; Chen, L.; Shen, N.; Xie, R.; Sheridan, M. V.; Chen, X.; Sheng, D.; Zhang, D.; Chai, Z.; Wang, S. Rational Design of a Cationic Polymer Network towards Record High Uptake of 99TcO4− in Nuclear Waste. *Sci. China Chem.* **2021**, *64* (7), 1251–1260. https://doi.org/10.1007/s11426-020-9962-9.

(46) Rapti, S.; Diamantis, S. A.; Dafnomili, A.; Pournara, A.; Skliri, E.; Armatas, G. S.; Tsipis, A. C.; Spanopoulos, I.; Malliakas, C. D.; Kanatzidis, M. G.; Plakatouras, J. C.; Noli, F.; Lazarides, T.; Manos, M. J. Exceptional TcO4− Sorption Capacity and Highly Efficient ReO4− Luminescence Sensing by Zr4+ MOFs. *J. Mater. Chem. A* **2018**, *6* (42), 20813–20821. https://doi.org/10.1039/C8TA07901C.

(47) Xu, H.; Cao, C.-S.; Hu, H.-S.; Wang, S.-B.; Liu, J.-C.; Cheng, P.; Kaltsoyannis, N.; Li, J.; Zhao, B. High Uptake of ReO4− and CO2 Conversion by a Radiation-Resistant Thorium–Nickle [Th48Ni6] Nanocage-Based Metal–Organic Framework. *Angewandte Chemie International Edition* **2019**, *58* (18), 6022–6027. https://doi.org/10.1002/anie.201901786.

(48) Zhong, X.; Liang, W.; Wang, H.; Xue, C.; Hu, B. Aluminum-Based Metal-Organic Frameworks (CAU-1) Highly Efficient UO22+ and TcO4− Ions Immobilization from Aqueous Solution. *Journal of Hazardous Materials* **2021**, *407*, 124729. https://doi.org/10.1016/j.jhazmat.2020.124729.

(49) Dutta, S.; Samanta, P.; Joarder, B.; Let, S.; Mahato, D.; Babarao, R.; Ghosh, S. K. A Water-Stable Cationic Metal–Organic Framework with Hydrophobic Pore Surfaces as an Efficient Scavenger of Oxo-Anion Pollutants from Water. *ACS Appl. Mater. Interfaces* **2020**, *12* (37), 41810–41818. https://doi.org/10.1021/acsami.0c13563.

(50) Fei, H.; Bresler, M. R.; Oliver, S. R. J. A New Paradigm for Anion Trapping in High Capacity and Selectivity: Crystal-to-Crystal Transformation of Cationic Materials. *J. Am. Chem. Soc.* **2011**, *133* (29), 11110–11113. https://doi.org/10.1021/ja204577p.

(51) Feng, H.; Xiong, X.; Gong, L.; Zhang, H.; Xu, Y.; Feng, X.; Luo, F. Rational Tuning of Thorium-Organic Frameworks by Reticular Chemistry for Boosting Radionuclide Sequestration. *Nano Res.* **2022**, *15* (2), 1472–1478. https://doi.org/10.1007/s12274-021-3690-7.

(52) Sheng, D.; Zhu, L.; Xu, C.; Xiao, C.; Wang, Y.; Wang, Y.; Chen, L.; Diwu, J.; Chen, J.; Chai, Z.; Albrecht-Schmitt, T. E.; Wang, S. Efficient and Selective Uptake of TcO4– by a Cationic Metal–Organic Framework Material with Open Ag+ Sites. *Environ. Sci. Technol.* **2017**, *51* (6), 3471–3479. https://doi.org/10.1021/acs.est.7b00339.

(53) Kang, K.; Li, L.; Zhang, M.; Zhang, X.; Lei, L.; Xiao, C. Constructing Cationic Metal–Organic Framework Materials Based on Pyrimidyl as a Functional Group for Perrhenate/Pertechnetate Sorption. *Inorg. Chem.* **2021**, *60* (21), 16420–16428. https://doi.org/10.1021/acs.inorgchem.1c02257.

(54) Sen, A.; Dutta, S.; Dam, G. K.; Samanta, P.; Let, S.; Sharma, S.; Shirolkar, M. M.; Ghosh, S. K. Imidazolium-Functionalized Chemically Robust Ionic Porous Organic Polymers (IPOPs) toward Toxic Oxo-Pollutants Capture from Water. *Chemistry – A European Journal* **2021**, *27* (53), 13442–13449. https://doi.org/10.1002/chem.202102399.

(55) Kang, K.; Shen, N.; Wang, Y.; Li, L.; Zhang, M.; Zhang, X.; Lei, L.; Miao, X.; Wang, S.; Xiao, C. Efficient Sequestration of Radioactive 99TcO4- by a Rare 3-Fold Interlocking Cationic Metal-Organic Framework: A Combined Batch Experiments, Pair Distribution Function, and Crystallographic Investigation. *Chemical Engineering Journal* **2022**, *427*, 130942. https://doi.org/10.1016/j.cej.2021.130942.

(56) Deng, S.-Q.; Li, D.-M.; Mo, X.-J.; Miao, Y.-L.; Cai, S.-L.; Fan, J.; Zhang, W.-G.; Zheng, S.-R. Covalent Cross-Linking of Metal-Organic Cages: Formation of an Amorphous Cationic Porous Extended Framework for the Uptake of Oxo-Anions from Water. *ChemPlusChem* **2021**, *86* (5), 709–715. https://doi.org/10.1002/cplu.202000570.

(57) Li, J.; Li, B.; Shen, N.; Chen, L.; Guo, Q.; Chen, L.; He, L.; Dai, X.; Chai, Z.; Wang, S. Task-Specific Tailored Cationic Polymeric Network with High Base-Resistance for Unprecedented 99TcO4– Cleanup from Alkaline Nuclear Waste. *ACS Cent. Sci.* **2021**, *7* (8), 1441–1450. https://doi.org/10.1021/acscentsci.1c00847.

(58) Li, J.; Zhang, Y.; Zhou, Y.; Fang, F.; Li, X. Tailored Metal-Organic Frameworks Facilitate the Simultaneously High-Efficient Sorption of UO22+ and ReO4− in Water. *Science of The Total Environment* **2021**, *799*, 149468. https://doi.org/10.1016/j.scitotenv.2021.149468.

(59) Li, C.-P.; Ai, J.-Y.; Zhou, H.; Chen, Q.; Yang, Y.; He, H.; Du, M. Ultra-Highly Selective Trapping of Perrhenate/Pertechnetate by a Flexible Cationic Coordination Framework. *Chem. Commun.* **2019**, *55* (12), 1841–1844. https://doi.org/10.1039/C8CC09364D.

(60) Hu, Q.-H.; Shi, Y.-Z.; Gao, X.; Zhang, L.; Liang, R.-P.; Qiu, J.-D. An Alkali-Resistant Metal–Organic Framework as Halogen Bond Donor for Efficient and Selective Removing of ReO4−/TcO4−. *Environ Sci Pollut Res* **2022**. https://doi.org/10.1007/s11356-022-21870-y.

(61) Ma, J.; Wang, C.-C.; Zhao, Z.-X.; Wang, P.; Li, J.-J.; Wang, F.-X. Adsorptive Capture of Perrhenate (ReO4−) from Simulated Wastewater by Cationic 2D-MOF BUC-17. *Polyhedron* **2021**, *202*, 115218. https://doi.org/10.1016/j.poly.2021.115218.

(62) Kang, K.; Li, L.; Zhang, M.; Miao, X.; Lei, L.; Xiao, C. Two-Fold Interlocking Cationic Metal–Organic Framework Material with Exchangeable Chloride for Perrhenate/Pertechnetate Sorption. *Inorg. Chem.* **2022**, *61* (29), 11463–11470. https://doi.org/10.1021/acs.inorgchem.2c01846.

(63) Ming, M.; Zhou, H.; Mao, Y.-N.; Li, H.-R.; Chen, J. Selective Perrhenate/Pertechnetate Removal by a MOF-Based Molecular Trap. *Dalton Trans.* **2022**, *51* (11), 4458–4465. https://doi.org/10.1039/D1DT04175D.

(64) Sheng, D.; Zhu, L.; Dai, X.; Xu, C.; Li, P.; Pearce, C. I.; Xiao, C.; Chen, J.; Zhou, R.; Duan, T.; Farha, O. K.; Chai, Z.; Wang, S. Successful Decontamination of 99TcO4− in Groundwater at Legacy Nuclear Sites by a Cationic Metal-Organic Framework with Hydrophobic Pockets. *Angewandte Chemie International Edition* **2019**, *58* (15), 4968–4972. https://doi.org/10.1002/anie.201814640.

(65) Kang, K.; Liu, S.; Zhang, M.; Li, L.; Liu, C.; Lei, L.; Dai, X.; Xu, C.; Xiao, C. Fast Room-Temperature Synthesis of an Extremely Alkaline-Resistant Cationic Metal–Organic Framework for Sequestering TcO4− with Exceptional Selectivity. *Advanced Functional Materials n/a* (n/a), 2208148. https://doi.org/10.1002/adfm.202208148.

(66) Qiao, W.-Z.; Song, T.-Q.; Cheng, P.; Zhao, B. Highly Selective Enamination of β-Ketoesters Catalyzed by Interlocked [Cu8] and [Cu18]

Nanocages. *Angewandte Chemie International Edition* **2019**, *58* (38), 13302–13307. https://doi.org/10.1002/anie.201906306.

(67) Li, C.-P.; Zhou, H.; Chen, J.; Wang, J.-J.; Du, M.; Zhou, W. A Highly Efficient Coordination Polymer for Selective Trapping and Sensing of Perrhenate/Pertechnetate. *ACS Appl. Mater. Interfaces* **2020**, *12* (13), 15246–15254. https://doi.org/10.1021/acsami.0c00775.

(68) Mei, L.; Li, F.; Lan, J.; Wang, C.; Xu, C.; Deng, H.; Wu, Q.; Hu, K.; Wang, L.; Chai, Z.; Chen, J.; Gibson, J. K.; Shi, W. Anion-Adaptive Crystalline Cationic Material for 99TcO4− Trapping. *Nat Commun* **2019**, *10* (1), 1532. https://doi.org/10.1038/s41467-019-09504-3.

(69) Drout, R. J.; Otake, K.; Howarth, A. J.; Islamoglu, T.; Zhu, L.; Xiao, C.; Wang, S.; Farha, O. K. Efficient Capture of Perrhenate and Pertechnetate by a Mesoporous Zr Metal–Organic Framework and Examination of Anion Binding Motifs. *Chem. Mater.* **2018**, *30* (4), 1277–1284. https://doi.org/10.1021/acs.chemmater.7b04619.

(70) Kong, X.; Hu, K.; Huang, Z.; Wu, Q.; Yu, J.; Mei, L.; Chai, Z.; Nie, C.; Shi, W. Stepwise Assembly of a Multicomponent Heterometallic Metal–Organic Framework via Th6-Based Metalloligands. *Inorg. Chem.* **2021**, *60* (19), 14535–14539. https://doi.org/10.1021/acs.inorgchem.1c02082.

(71) Banerjee, D.; Xu, W.; Nie, Z.; Johnson, L. E. V.; Coghlan, C.; Sushko, M. L.; Kim, D.; Schweiger, M. J.; Kruger, A. A.; Doonan, C. J.; Thallapally, P. K. Zirconium-Based Metal–Organic Framework for Removal of Perrhenate

from Water. *Inorg. Chem.* **2016**, *55* (17), 8241–8243. https://doi.org/10.1021/acs.inorgchem.6b01004.

(72) Li, D.; Shustova, N. B.; Martin, C. R.; Taylor-Pashow, K.; Seaman, J. C.; Kaplan, D. I.; Amoroso, J. W.; Chernikov, R. Anion-Exchanged and Quaternary Ammonium Functionalized MIL-101-Cr Metal-Organic Framework (MOF) for ReO4−/TcO4− Sequestration from Groundwater. *Journal of Environmental Radioactivity* **2020**, *222*, 106372. https://doi.org/10.1016/j.jenvrad.2020.106372.

(73) Zhang, G.; Tan, K.; Xian, S.; Xing, K.; Sun, H.; Hall, G.; Li, L.; Li, J. Ultrastable Zirconium-Based Cationic Metal–Organic Frameworks for Perrhenate Removal from Wastewater. *Inorg. Chem.* **2021**, *60* (16), 11730–11738. https://doi.org/10.1021/acs.inorgchem.1c00512.

(74) Wang, S.; Yu, P.; Purse, B. A.; Orta, M. J.; Diwu, J.; Casey, W. H.; Phillips, B. L.; Alekseev, E. V.; Depmeier, W.; Hobbs, D. T.; Albrecht-Schmitt, T. E. Selectivity, Kinetics, and Efficiency of Reversible Anion Exchange with TcO4− in a Supertetrahedral Cationic Framework. *Advanced Functional Materials* **2012**, *22* (11), 2241–2250. https://doi.org/10.1002/adfm.201103081.

(75) Owen, E. A.; Yates, E. L. XLI. *Precision Measurements of Crystal Parameters*. *The London, Edinburgh, and Dublin Philosophical Magazine and Journal of Science* **1933**, *15* (98), 472–488. https://doi.org/10.1080/14786443309462199.

(76) Naumov, D. Yu.; Virovets, A. V.; Korenev, S. V.; Gubanov, A. I. Silver Perrhenate, AgReO4. *Acta Crystallographica Section C* **1999**, *55* (8), IUC9900097–IUC9900097. https://doi.org/10.1107/S0108270199099138.

Chapter 4 - A Crystal Structure of a Rippled Antiparallel Pauling-Corey Cross-β Dimer

Abstract

This work has been published on the Chemical Sciences journal in collaboration with co-first-author Dr. Ariel Kuhn and co-authors Dr. Tim Johnstone, Dr. Scott Oliver, and Dr. Jevgenij Raskatov.[1]

Following the seminal theoretical work on the pleated β-sheet published by Pauling and Corey in 1951, the rippled β-sheet was hypothesized by the same authors in 1953. In the pleated β-sheet the interacting β-strands have the same chirality, whereas in the rippled β-sheet the interacting β-strands are mirror images. Unlike the pleated β-sheet that is now common textbook knowledge, the rippled β-sheet has been much slower to evolve. Much of the experimental work on rippled sheets came from groups that study aggregating racemic peptide systems over the course of the past decade. This includes MAX1/ DMAX hydrogels (Schneider), L/D-KFE8 aggregating systems (Nilsson), and racemic Amyloid b mixtures (Raskatov). Whether a racemic peptide mixture is “ripple-genic” (i.e., whether it forms a rippled sheet) or “pleat-genic” (i.e., whether it forms a pleated sheet) is likely governed by a complex interplay of thermodynamic and kinetic effects. Structural insights into rippled sheets remain limited to only a very few studies that combined sparse experimental structural constraints with molecular modeling. Crystal structures

of rippled sheets are needed so we can rationally design rippled sheet architectures. Here we report a high-resolution crystal structure, in which (L,L,L)-triphenylalanine and (D,D,D)-triphenylalanine form dimeric antiparallel rippled sheets, which pack into herringbone layer structures. The arrangements of the tripeptides and their mirror-images in the individual dimers were in excellent agreement with the theoretical predictions by Pauling and Corey. A subsequent mining of the PDB identified three orphaned rippled sheets among racemic protein crystal structures.

4.1 Introduction

Peptides with mixed chirality may be used to access frameworks with unique properties, including protease-resistant peptide drugs,[2,3] hydrogels with enhanced rigidity,[4,5] aggregation blockers,[6,7] amyloid oligomer-to-fibril converters,[8,9] and mechanistic tools.[10,11] Mirror-image proteins may also be used to enhance crystallization of proteins that are hard to crystallize, sometimes by creating unique interactions between the protein enantiomers.[12-15] A systematic incorporation of D-amino acids into proteins and peptides is expected to give access to a huge structure-function space that cannot be accessed in any other way.

In 1951, Pauling and Corey introduced the pleated β-sheet as a two-dimensional periodic layer configuration built from extended homochiral peptide strands.[16] The pleated β-sheet rapidly established itself as a key

protein structural motif that is commonly known in textbooks as the β-sheet. Thousands of protein structures have been published that contain β-sheets. This includes structures that may be as huge as a periodic, fibrillary β-sheet network on the one side and as small as a β-sheet dimer in the context of a globular protein on the other side. In 1953, Pauling and Corey introduced the rippled β-sheet as a configuration closely related to the pleated β-sheet, but with every alternate peptide chain mirrored, thus giving rise to unique structures.[17] Some of the key structural differences between pleated and rippled β-sheets, including differences in hydrogen bonding and relative side-chain disposition in the β-sheet frameworks, have been discussed very recently.[18] As illustrated in Figure 4.1, in an antiparallel pleated sheet, amino acid side chains are aligned in a vertical line orthogonal to the peptide backbones (Figure 4.1, left panel). In contrast, in an antiparallel rippled sheet, to reduce steric repulsion between the alternating enantiomeric peptides, the side chains are oriented diagonally across the peptidic network (Figure 4.1, right panel).

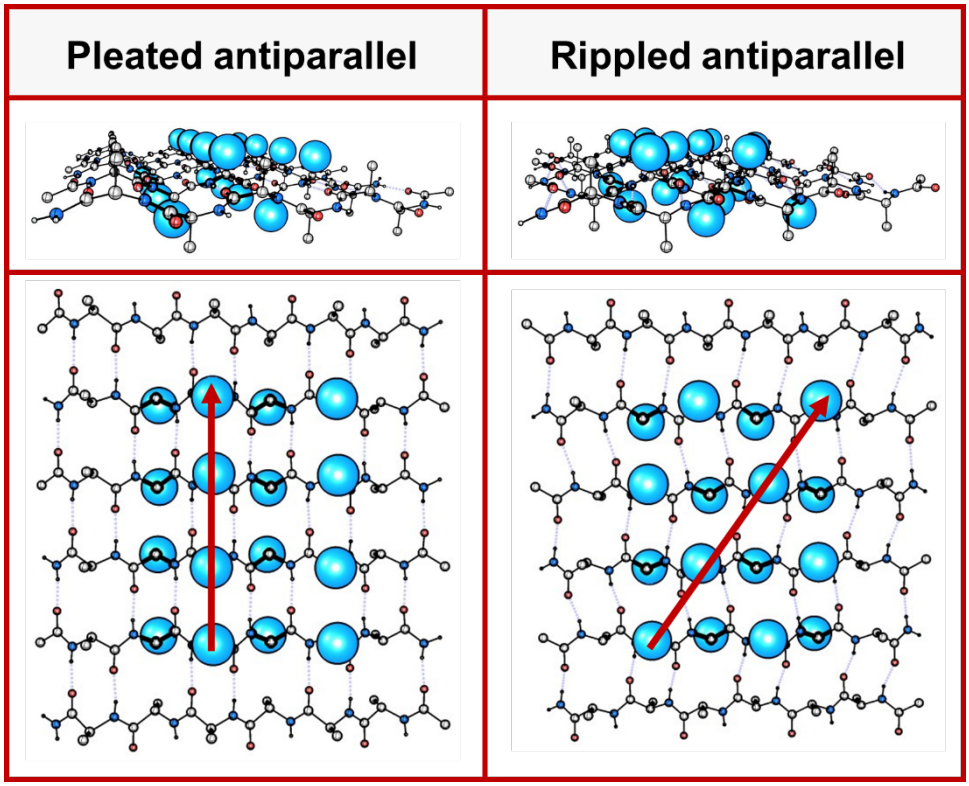

Figure 4.1 Left panel: Antiparallel pleated sheet in different projections. Right panel: Antiparallel rippled sheet in different projections. A selected number of amino acid side chains are depicted as blue spheres on the left panel (pleated, along red vertical line) and on the right (rippled, along red diagonal), to reduce steric repulsion in each case.

Unlike with the pleated β-sheet (now known as the β-sheet), the growth of our body of knowledge on the rippled β-sheet has been extremely sluggish. The first experimental observation of an (antiparallel) rippled sheet was made in the 1970s by Lotz, Moore and Krimm, on polyglycine I.[19–21] The authors used space group considerations to conclude that polyglycine I crystals contained rippled rather than pleated antiparallel sheets (monoclinic rather than orthorhombic unit cell geometry). Some three decades later, Lahav and co-workers used clever labeling strategies in conjunction with mass-spectrometry,

to produce evidence for rippled sheet formation, based on templated peptide replication.[22,23] Conversely, Chung and Nowick noted in their solution-phase NMR studies a thermodynamic preference for a dimeric pleated β-sheet, with the alternative rippled sheet observed as a minor diastereomer.[24] A more recent study by Liu and Gellman is broadly consistent with Chung and Nowick.[25] Our understanding of the interplay of thermodynamics and kinetics that underlie the formation of pleated vs rippled sheets remains extremely limited. Experiments performed in the laboratories of Schneider,[4,5] Nilsson,[26,27] Raskatov,[8,9] and Torbeev,[28] showed that mirror-image peptide strands may assemble into rippled sheets, but there is also evidence that some sequences may favor homochiral association.[29] The structural insights available for the MAX1/DMAX systems,[4] a short Amyloid-β (Aβ) segment, and, most recently, racemic full-length Aβ40[30] were obtained from theoretical calculations constrained by a fairly limited number of experimental data. These studies provide valuable insights into rippled sheets, but not experimental high-resolution structures.

It is interesting to note that not all racemic peptide mixtures form rippled sheets,[24,25,31] as self-sorting into pleated sheets may also occur.[31] We are just beginning to learn why some racemic peptide mixtures form rippled sheets (*i.e.*, are “ripple-genic”), whereas others prefer to form pleated sheets instead (*i.e.*, are “pleat-genic”). To systematically map out the structure-function space and to close this major knowledge gap, the field urgently needs high-resolution

structures of rippled sheets. Here we report the X-ray crystal structure of (L,L,L)-triphenylalanine that is hydrogen-bonded to (D,D,D-)-triphenylalanine in a dimeric antiparallel rippled sheet. We then draw comparisons with hitherto orphaned rippled sheet crystal structures that we discovered by searching the PDB for racemic proteins.

4.2 Experimental

4.2.1 Peptide Synthesis

The (L,L,L)-triphenylalanine (*i.e.*, FFF) and (D,D,D)-triphenylalanine (*i.e.*, fff) peptides were synthesized by standard Fmoc-based, solid-phase peptide chemistry, following previously reported protocols.[32,33] Both peptides were synthesized using preloaded, Fmoc-phenylalanine 4-alkoxybenzyl alcohol Wang resin: Fmoc-L-Phe-Wang (Sigma) or Fmoc-D-Phe-Wang (Fisher). All syntheses were performed manually at 0.2 mM scale relative to resin loading. An orbital shaker was used for mixing in both the deprotection and coupling steps. The resin was swelled in 3 mL of dimethylformamide (DMF) in a filter tube, housing 250 mg Fmoc-Phe Wang resin (0.796 mmol/g loading) for 20 min. For Fmoc-deprotection, 30% piperidine (Spectrum) in DMF was added to the resin, and allowed to shake on an orbital shaker for 20 min. The deprotection solution was rinsed with DMF (3x) and dichloromethane (DCM, 2x) and the deprotection step was repeated. Coupling reagents used were 4 eq. *N*,*N*-diisopropylethylamine (Fisher), 3 eq. *N*,*N*,*N*',*N*'-tetramethyl-O-(1*H*-

benzotriazol-1-yl)uronium hexafluorophosphate (Fisher) and 3 eq. hydroxybenzotriazole hydrate (Oakwood Products). For amino acid coupling, 3 eq. of either Fmoc-L-Phe-OH (Fisher) or Fmoc-D-Phe-OH (ChemPep) with coupling reagents listed above were dissolved in 3 mL DMF and added to the reaction vessel, and allowed to shake for 30 min. The coupling step was repeated for each amino acid addition to improve yield. The aforementioned steps were repeated to produce the resin-bound tripeptides, NH_2-L-FFF-COOH and NH_2-D-fff-COOH. The peptides were cleaved and deprotected with a mixture consisting of trifluoroacetic acid (10 mL, Fisher), tri-isopropylsilane (1 mL, Fisher), and liquefied phenol (0.5 mL, Sigma). The peptide identities were confirmed with mass spectrometry (Fig. S1-S2). Peptides were purified by reverse-phase high-performance liquid chromatography (HPLC) with PLRP-S columns (Agilent), as previously described,[32,33] yielding peptides with purities exceeding 95% (Figure S1-S2). HPLC was conducted under basic conditions (0.1% NH_4OH), to reduce aggregation and/or precipitation. Samples were lyophilized and stored as solid powders at –40 °C.

4.2.2 Crystallization

Solutions of L-FFF and D-fff peptides were prepared separately by dissolving 7 mg of each individual peptide in 4 mL of nanopure water. The resulting solutions were sonicated and transferred to an oil bath at 90 °C and kept under stirring for one hour. To enhance dissolution of the cloudy slurries,

80 µL of hexafluoroisopropanol (HFIP; Fisher) was added to the solutions (2% of total volume), but significant cloudiness was still observed. After an additional 1 h of heating in the oil bath, the two individual peptide solutions were combined by adding D-fff to the L-FFF solution, dropwise. The resulting cloudy solution was rapidly transferred to a Teflon lined stainless steel autoclave, which was sealed and placed on an oven at 75 °C for 10 d followed by a slow colling process at a rate of 0.1°C/min, leading to the formation of colorless, needle-like crystals.

4.2.3 Single-Crystal X-ray Diffraction

A suitable colorless needle with dimensions of 0.1 x 0.09 x 0.03 mm^3 was used for single-crystal X-ray diffraction data collection at 100 K on a Rigaku XtaLAB Synergy-S diffractometer using Cu K_α radiation (λ = 1.54 Å). Data collection, processing and reduction were performed with $CrysAlis^{Pro}$.[34] After face indexing, numerical absorption correction was applied using gaussian integration. Empirical absorption correction using spherical harmonics was applied using SCALE3 ABSPACK scaling algorithm. The structure was solved by intrinsic phasing using ShelXT and refined with ShelXL via Olex2.[35–37] All non-hydrogen atoms were refined anisotropically using standard procedures.[38] Atomic displacement parameters for hydrogen atoms in the terminal amine group were fixed to 1.5(U_{iso}) of the attached nitrogen atom. For all other hydrogen atoms, the values were fixed to 1.2(U_{iso}) of the atoms to which they

are attached. The N-H distances in the amine and amide groups were restrained to 0.91(2) Å and 0.88(2) Å, respectively. All other hydrogen atoms were placed at geometrically calculated positions and refined using a riding model.

4.2.4 Computational Chemistry

The input geometry for the optimization of FFF:fff was generated using the crystallographic data. The optimization was performed using ORCA 4.2.1, using Becke's 1988 exchange functional and Perdew's 1986 correlation functional (*i.e.*, BP86)[39,40] and the resolution of the identity approximation. Ahlrichs' def2-SVP basis set and the def2/J auxiliary basis set were used.[41,42] An atom-pairwise dispersion correction with the Becke-Johnson damping scheme was applied (D3BJ).[43,44] Implicit aqueous solvation was achieved using a conductor-like polarizable continuum model (CPCM=water).[45]

4.2.5 CSD Search

A systematic search of the CSD (version 5.41) was performed using ConQuest (version 2.0.4). Two queries were submitted simultaneously. The first searched for a C(C)C(O)NHC(C)C(O)NHC(C)C(O)NH fragment with all bond types set to "any", with both φ torsion angles from -180–0°, and with both ψ torsion angles within the range 0–180°. The second query required the presence of a distinct C(C)C(O)NHC(C)C(O)NHC(C)C(O)NH fragment with all

bond types set to “any”, with both φ torsion angles from 0–180°, and with both ψ torsion angles within the range -180–0°. The hits from this search were inspected manually and none featured a rippled sheet motif.

4.2.6 PDB Structural Database Mining

The PDB database was searched for the term “Racemic”, and the results were narrowed by selecting “protein” as the polymer entity type, producing a total of 387 hits. The majority of those hits were, however, not truly racemic protein structures, but rather, enantiomerically pure proteins complexed with racemic molecules or simply included racemic compounds used during synthesis. These were excluded from our search. From the remaining hits, we manually selected those, in which the mirror-image proteins had β-strands oriented in ways that made them potentially capable of forming rippled sheets. This eventually produced three structures that can be accessed through the PDB via reference codes 4WPY[46], 4IUZ[47], and 3ODV.[48]

4.2.7 Considerations Regarding Nomenclature

In the original theory papers Pauling and Corey introduced the concepts of the pleated sheet that since became textbook knowledge as the β-sheet, and the closely related, but understudied rippled sheet[17]. Those seminal papers discussed periodic layer structures, and the original definition of sheets originated from there. However, this nomenclature since evolved: it is now

common to refer to adequately paired peptide strands of the same handedness as pleated β-sheets. In this paper we follow analogy and refer to adequately paired peptide strands of opposite chirality as rippled β-sheets. The periodic β-sheets are discussed in the context of fibril structures, which is specified where necessary.

4.3 Results and Discussion

4.3.1 Choice of system

The significance of the oligomeric phenylalanine motif for amyloid formation is well-established. For example, it is known that the hydrophobic LVFFA segment that spans the amino acid residues 17-21 of the Amyloid β (*i.e.*, Aβ17-21) peptide is crucial for Aβ fibrillization.[49] Furthermore, Kiessling and coworkers have taken advantage of this by using the KLVFF segment for molecular recognition studies with Aβ.[49,50] Reductionist studies of Aβ by Gazit and co-workers demonstrated that the short diphenylalanine peptide is itself capable of forming amyloid nanostructures.[51] Unlike the dipeptide, FF, which has been shown to form water-filled nanovesicles and hollow tubes, the tripeptide, FFF, spontaneously assembles into a diverse set of supramolecular assemblies depending on conditions, such as solid nanospheres, nanorods, helical-ribbons, plates, dendrimers, and doughnuts,[52–54] similar to what has been reported for Aβ,[55] making it an interesting candidate from the standpoint of rippled sheet design. Additionally, Gazit and coworkers found that FFF

demonstrated improved stability and peptide-network propensity over FF.[54] The authors also reported Thioflavin T (ThT) positivity for the FFF assemblies, indicative of ordered β-sheet content.[54]

More recently, Nilsson and co-workers demonstrated that the Aβ16-22 segment, KLVFFAE, rapidly formed precipitates when mixed with its mirror-image counterpart klvffae, which the authors ascribed to rippled sheet formation based on isotope-edited FT-ICR mass spectrometric and solid state NMR spectroscopic experiments.[26]

Peptides containing bulky, hydrophobic amino acids Phe (F), Val (V), Ile (I) and Leu (L) are believed to be particularly prone to forming rippled sheets.[18] Phenylalanine stands out because of its relative rigidity, which should favor crystallization.[56] We chose a racemic mixture of (L,L,L)-triphenylalanine and (D,D,D)-triphenylalanine (*i.e.*, FFF:fff), as our model. The N- and C-termini of FFF and fff were kept as free amines and free carboxylates, respectively, to afford peptides that (a) are water-soluble and (b) favor a defined antiparallel arrangement due to Coulombic attraction. Peptides were made on solid support and purified using a procedure similar to one we previously developed for Aβ purification.[32]

4.3.2 The FFF:fff dimer structure

Combination of concentrated solutions of FFF and fff led to rapid formation of a fine precipitate. Optimization of conditions led to a protocol, in which

controlled cooling of a solution saturated with a racemic mixture of FFF and fff from 75 to 25 °C at a rate of 0.1 °C min^{-1} afforded single-crystal needles with length exceeding 3 mm. A short needle, suitable for single crystal X-ray diffraction was selected and the metric symmetry and Laue symmetry of the diffraction pattern obtained with Cu K_α radiation revealed that the crystal belonged to the monoclinic crystal system. Strict observance of Friedel's Law and the $<E^2 - 1>$ value of 1.008 indicate that the crystal is centrosymmetric, suggesting that the molecules had crystallized as the racemic compound. Centrosymmetry was confirmed by analysis of the systematic absences, which unambiguously confirmed the space group to be $P2_1/c$. The structure was solved using intrinsic phasing and refined against 0.84 Å-resolution data (Table 4.1). The resolution and quality of the data permitted anisotropic refinement of all non-H atoms and semi-free refinement of H-atom positions. The asymmetric unit contains a single tripeptide in its zwitterionic form (Figure 4.2).

Table 4.1 of FFF.fff dimers

Compound	Racemic triphenylalanine
Formula	$C_{27}H_{29}N_3O_4$
FW	459.53
T (K)	100(2)
λ (Å)	1.54184
Crystal System	Monoclinic
Space group	$P2_1/c$
a (Å)	11.3563(5)
b (Å)	16.7472(6)
c (Å)	12.6545(6)
β (°)	101.483(4)
Volume (Å^3)	2358.54(18)
Z	4
ρ_{calc} (Mg/m^3)	1.294
Size (mm^3)	0.10 × 0.09 × 0.03
θ range (°)	4.44 – 67.06
Total data	23314
Unique data	4187
Parameters	323
Completeness	99.7%
R_{int}	5.00%
R_1 (I > 2σ)	4.43%
R_1 (all data)	5.54%
wR_2 (I > 2σ)	11.22%
wR_2 (all data)	11.81%
S	1.036
Min, max (e Å^{-3})	–0.279, 0.295

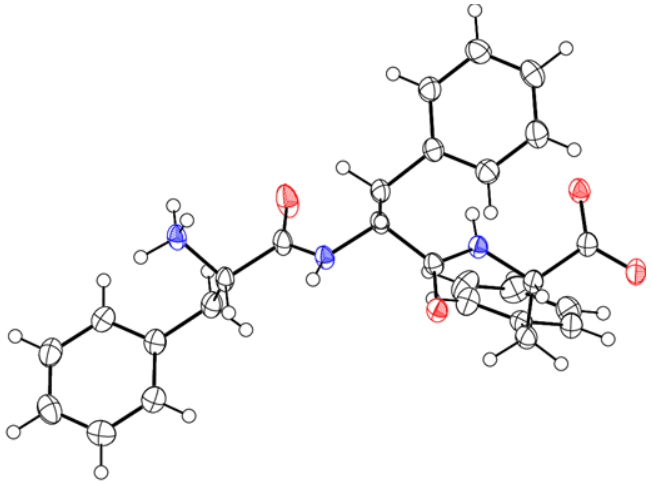

Figure 4.2 Molecular graph of FFF with 50% thermal ellipsoids and H atoms shown as spheres of arbitrary radius. Color code: O red, N blue, C grey, H white.

Both amides assume the expected *trans* configuration. The ψ angles of 114.6(2)° and 132.3(1)° and the φ angles of –124.7(4)° and –155.1(1)° for FFF fall within the range typically observed for β-pleated sheets. The side chains of the three residues assume, from N to C terminus, the *gauche*$^+$ (χ_1 = –63.2(2)°), *trans* (χ_1 = –175.1(1)°), and *gauche*$^-$ (χ_1 = 70.7(2)°) configurations.

The dimer resides on a crystallographic inversion center, across which FFF and fff form two symmetry-related pairs of hydrogen bonds (Figure 4.3). The terminal ammonium and carboxylate groups form a salt bridge with a N···O distance of 2.7660(18) Å and a N–H···O angle of 152.8(19)°. The hydrogen bond formed between the neutral amide units features an expectedly longer N···O distance of 2.9097(18) Å and a N–H···O angle of 157.4(17)°. The hydrogen bonds comprise the only significant intermolecular contacts between the components of the dimer; the torsion angles assumed by each of the

phenylalanine units allow them to effectively interleave given the inversion symmetry relating the two molecules. This arrangement of hydrogen bonds is in excellent agreement with the model put forward by Pauling and Corey (Figure 4.3 and Figure 4.4). In that original work, they model the antiparallel rippled sheet using a translation of 7.00 Å, which agrees well with the $C_{\alpha,1}\cdots C_{\alpha,3}$ distance of 6.888(2) Å in the present crystal structure.

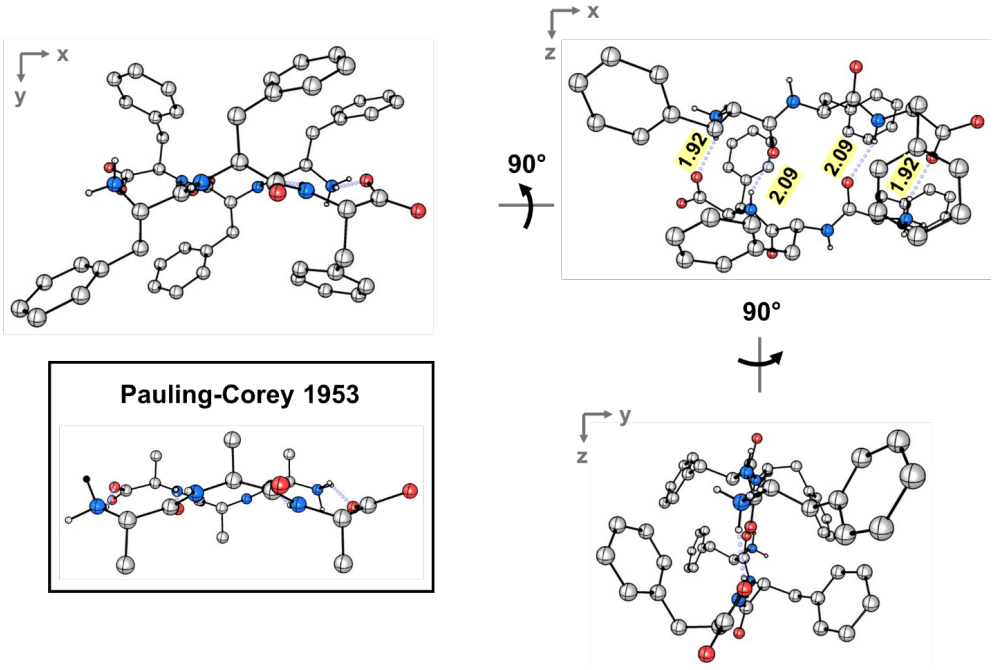

Figure 4.3 Ball-and-stick depiction of the experimental rippled antiparallel FFF:fff cross-β dimer, shown in three orthogonal projections. The Pauling-Corey rippled antiparallel backbone dimer is shown in the inset, with apical carbon atoms added geometrically to facilitate comparison; (color code: C, gray; O, red; N, blue).

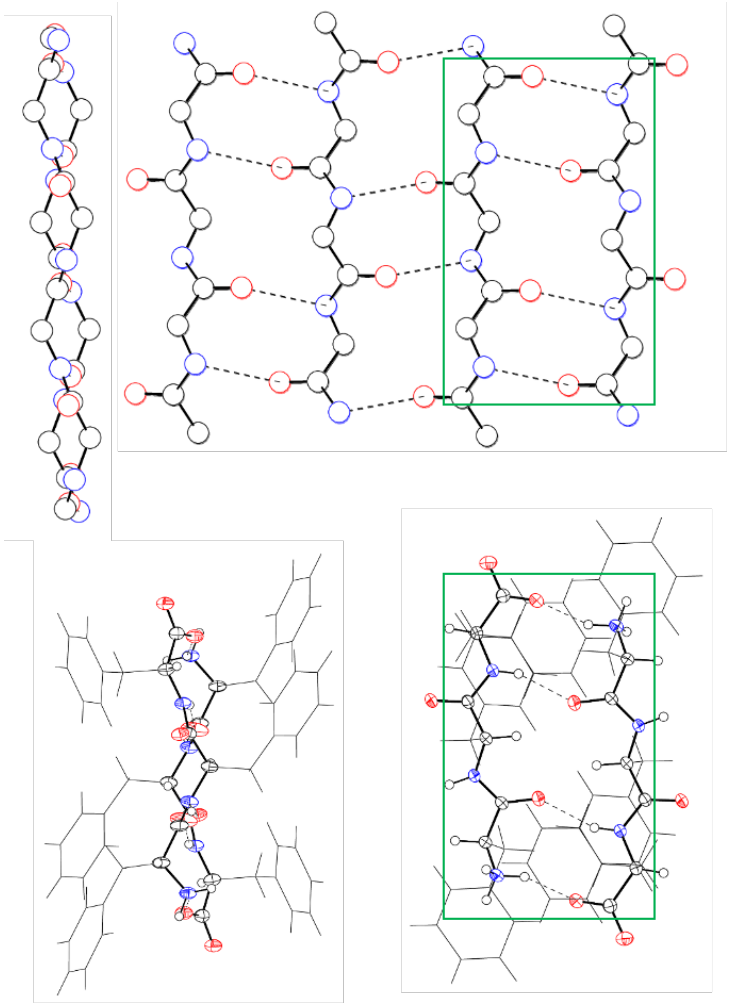

Figure 4.4 Top: Side and top views of the rippled antiparallel sheet structure predicted by Pauling and Corey [cf. Figure 1 from PNAS 1953, 39, 253]. Bottom: Side and top views of the rippled sheet structure formed by FFF:fff. Atoms of the polypeptide backbone are shown as ellipsoids (non-H) or spheres of arbitrary radius (H). Side-chain atoms are shown as sticks. Color code: O red, N blue, C grey, H white. Hydrogen bonds are shown as dashed lines. Boxed in green is the similar motif from the predicted (top) and experimentally observed (bottom) structure.

4.3.3 Crystal lattice analysis

The crystal is held together by a combination of interdimer hydrogen bonds, ionic interactions, and van der Waals interactions (Figure 4.5).

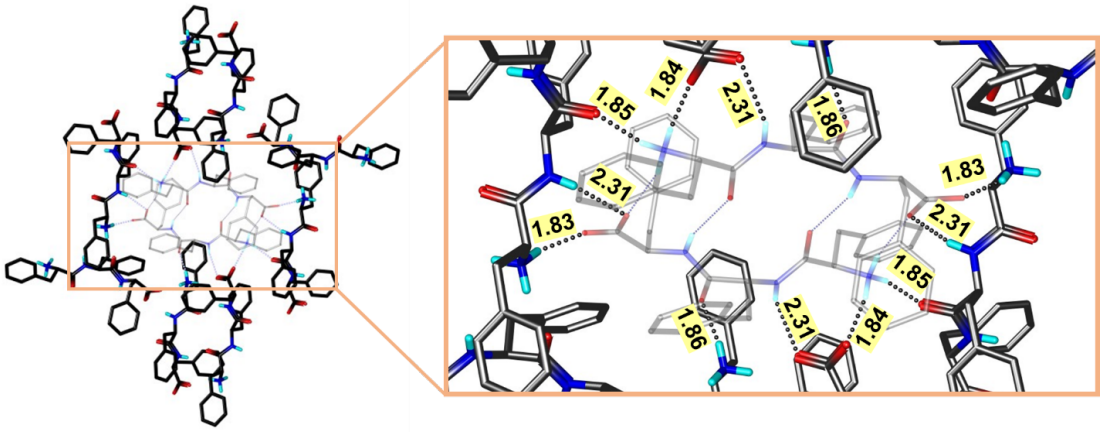

Figure 4.5 The rippled antiparallel FFF:fff cross-β dimer shown in contact with its direct neighbors.

In addition to interacting with the terminal carboxylate of the inversion-generated dimer mate, the terminal ammonium also forms hydrogen bonds to a glide-generated carbonyl of an enantiomeric tripeptide molecule (N···O = 2.7244(17) Å) and to the screw-generated terminal carboxylate of a molecule of identical handedness (N···O = 2.6645(18) Å). The internal amide N–H unit that is not involved in the antiparallel cross-β FFF:fff dimer also hydrogen bonds to this same screw-generated terminal carboxylate (N···O = 3.0168(17) Å). The H-atom positions in the final model are consistent with this hydrogen bonding pattern. These hydrogen bonds extend to form sheets parallel to the crystallographic *bc* plane (Figure 4.6).

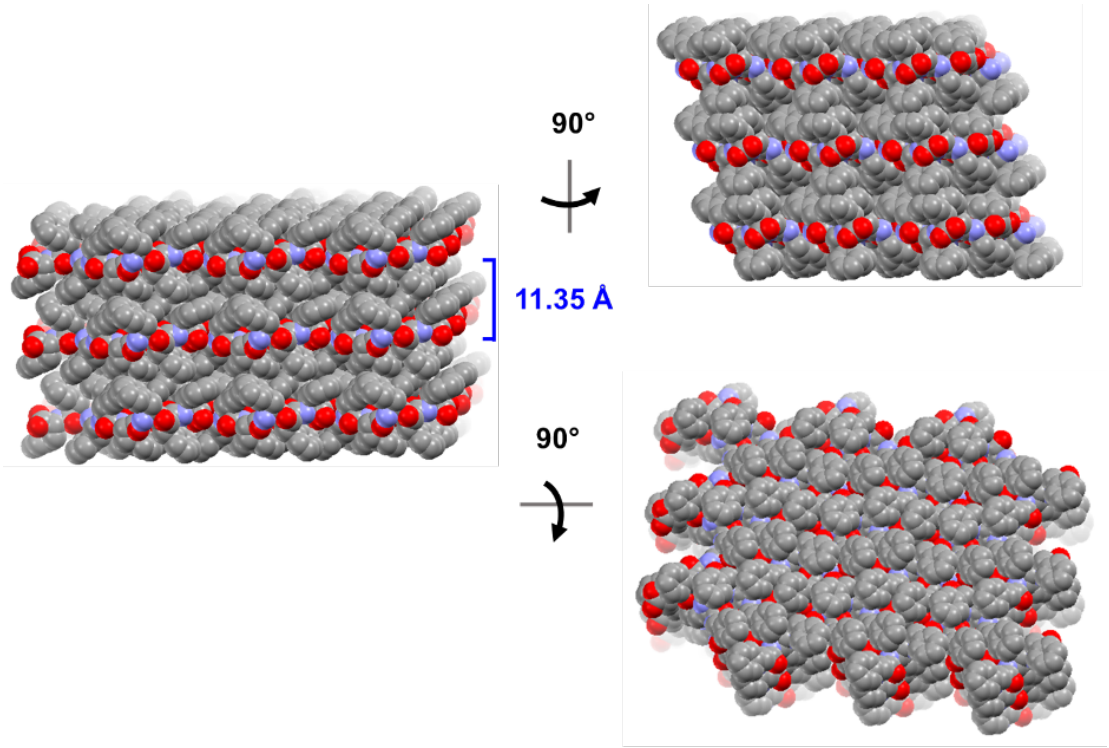

Figure 4.6 Long-range packing of the FFF:fff lattice, shown in three orthogonal projections. The layer-to-layer distance is indicated in blue.

These sheets feature a hydrophilic core bounded on both sides by hydrophobic layers. The layers stack on one another with an interlayer spacing corresponding to the crystallographic *a* lattice parameter of 11.3563(5) Å (Figure 4.7).

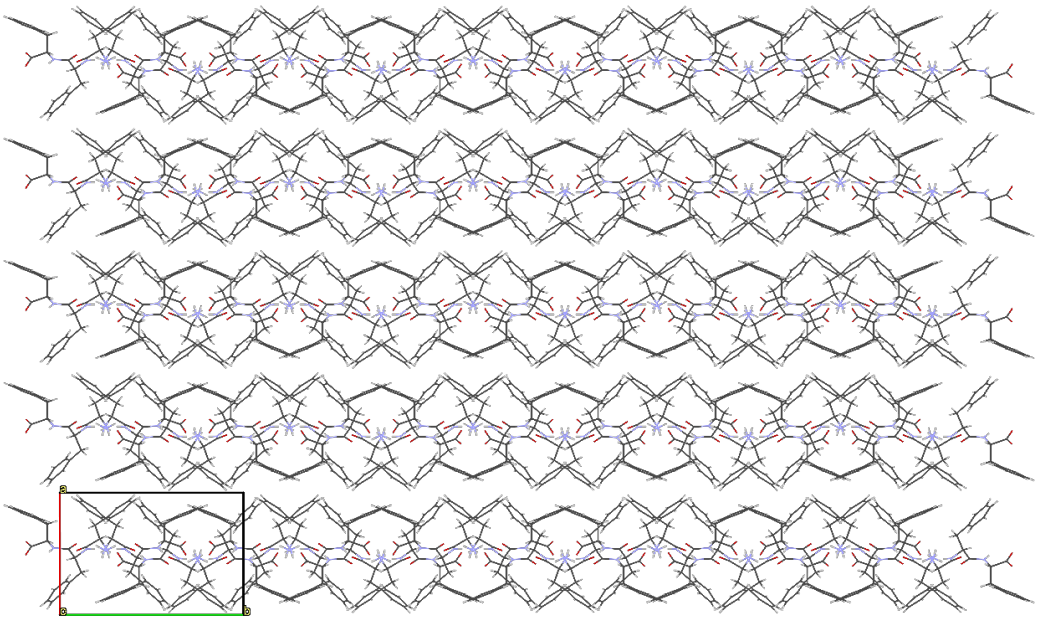

Figure 4.7 Packing diagram of FFF:fff highlighting that the layer-to-layer distance is the crystallographic lattice parameter a = 11.3563(5) Å.

This nanoscale architecture, with clear alternation between hydrophobic and hydrophilic layers, is reminiscent of a phase separation. The dimeric rippled sheets do not assemble into extended “fibrillary” rippled sheets with long-range order, packing into a classic herringbone pattern instead (Figure 4.8).

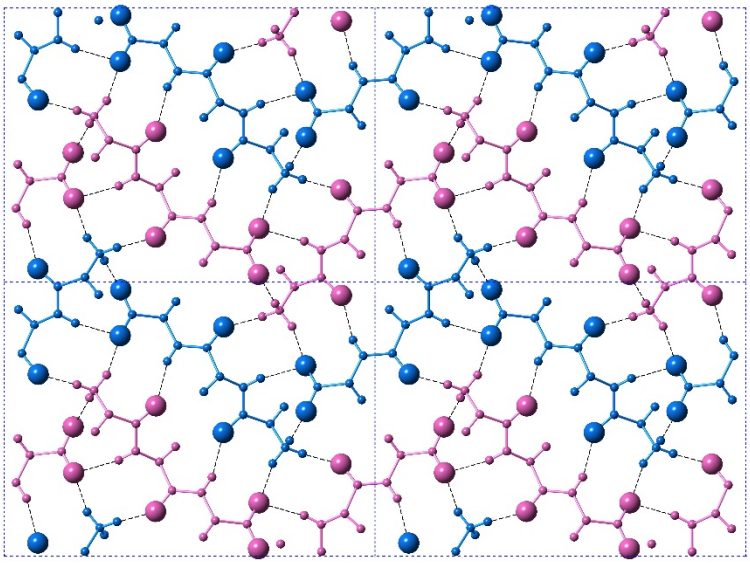

Figure 4.8 A top-on view of a single layer containing the peptidic backbones. Individual rippled antiparallel FFF:fff cross-β dimers are centered about the unit cell corners and center. L-peptides are shown in purple, and D-peptides are shown in blue.

To confirm that an isolated FFF:fff rippled antiparallel cross-β dimer is in itself a stable arrangement, the dimer was subjected to full geometry optimization using Density Functional Theory (DFT) methods. The optimization produced only marginal local structural changes (Figure 4.9, Table A.3), confirming that the structural features of the dimer are inherent to the β-rippled-sheet hydrogen bonding pattern and not crystal packing forces. This result stands in good agreement with the Raskatov group computational work on related rippled interfaces. [9,18,57,58]

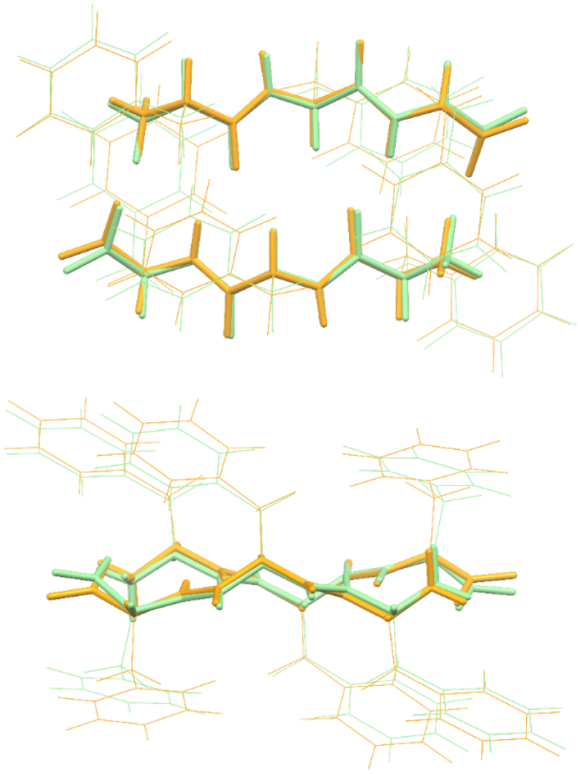

Figure 4.9 Overlay of the crystallographic (orange) and the optimized (green; BP86-D3BJ/def2-SVP-CPCMwater) structure of the FFF:fff dimer. The polypeptide backbone is shown as thick sticks and the sidechains as thin sticks.

4.3.4 Discussion

Above we presented a range of structural features we were able to glean from a crystal-structural analysis of the FFF:fff lattice. To the best of our knowledge, this is the first time that a rippled sheet crystal structure is being discussed in the literature. However, owing to the efforts of racemic protein crystallography, many crystal structures that contain potentially interacting mirror-image protein pairs are now available. It seemed plausible that the enantiomers in some of those structures might interact *via* rippled sheets. We

interrogated this possibility by searching the Cambridge Structural Database (CSD) and the Protein Data Bank (PDB), as described in the Materials and Methods section. The CSD search revealed no rippled sheet structures. The PDB search identified three racemic protein crystal structures with a qualitative appearance suggesting the presence of antiparallel rippled sheets. We analyzed the three structures and validated that dimeric rippled sheets were indeed present in all three cases (Figure 4.10).

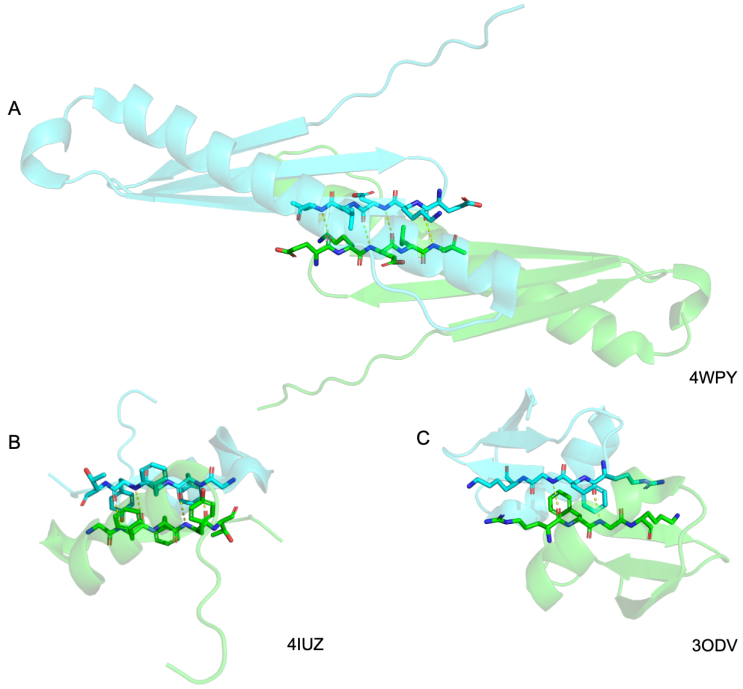

Figure 4.10 Detail of the antiparallel rippled motifs in the proteins selected by the PDB structural database mining. (**a)** glu-lys-glu-leu-val sequence in RV1738.[46] **(b)** phe-phe-tyr sequence in ester insulin.[47] **(c)** lys-gly-phe-arg sequence in Kaliotoxin.[48] PDB codes PDB codes are displayed on the bottom right.

In the racemic crystal structure of the Rv1738 protein, the protein enantiomers interact through an antiparallel rippled sheet formed by the Lys-Glu-Leu triad and its enantiomer (Figure 4.10a).[46] We also found that, in the racemic ester insulin crystal structure, the enantiomers are bridged by a rippled sheet formed between the Phe-Phe-Tyr triad and its enantiomer (Figure 4.10b).[47] Finally, we observed a very short rippled sheet segment of only one Phe residue and its enantiomer in the racemic crystal structure of kaliotoxin (Figure 4.10c).[48] Whereas in those three structural studies, the authors did recognize there were mirror-image interactions between their protein pairs, none of them identified those interactions as rippled sheets, which may be why those important structural insights appear to have escaped the attention of the rippled sheet community thus far. To gain deeper insights into the backbone conformations associated with the four rippled antiparallel sheet structures, we analyzed their Ramachandran angles (Figure 4.11).

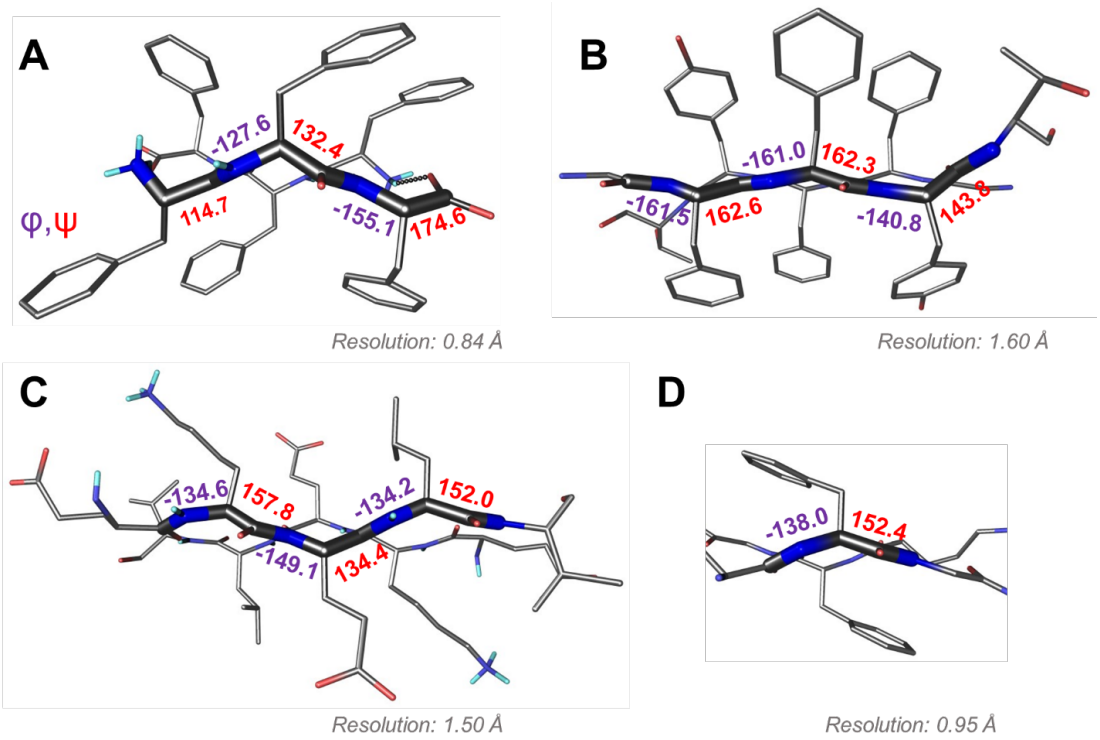

Figure 4.11 Ramachandran angle analysis for the rippled sheets noted with **(a)** the FFF:fff system; **(b)** racemic Ester Insulin (4IUZ)[47]; **(c)** racemic RV1738 (4WPY)[46]; D) racemic Kaliotoxin (3ODV).[48]

We noted that three of the rippled sheets contain internal L-Phe:D-Phe pairs, i.e., (F:::f). Their Ramachandran angles range from φ = -127.6° and ψ = 132.4 ° with FFF:fff (Figure 4.11a) to φ = -161.0° and ψ = 162.3° with racemic ester insulin (Figure 4.12b). This means that there is significant flexibility that is available to the (F:::f) pair in the context of the antiparallel rippled sheet, which may become a useful design element if the interest of the materials community to the rippled sheet motif continues to grow.

Pleated β-sheets are often observed in fibrils formed by aggregating enantiopure peptides, where they tend to display a one-dimensional long-range

order. Numerous structures are available through the work of the Eisenberg lab on steric zippers and related systems. [59–64] Some examples are shown in Figure 4.12.

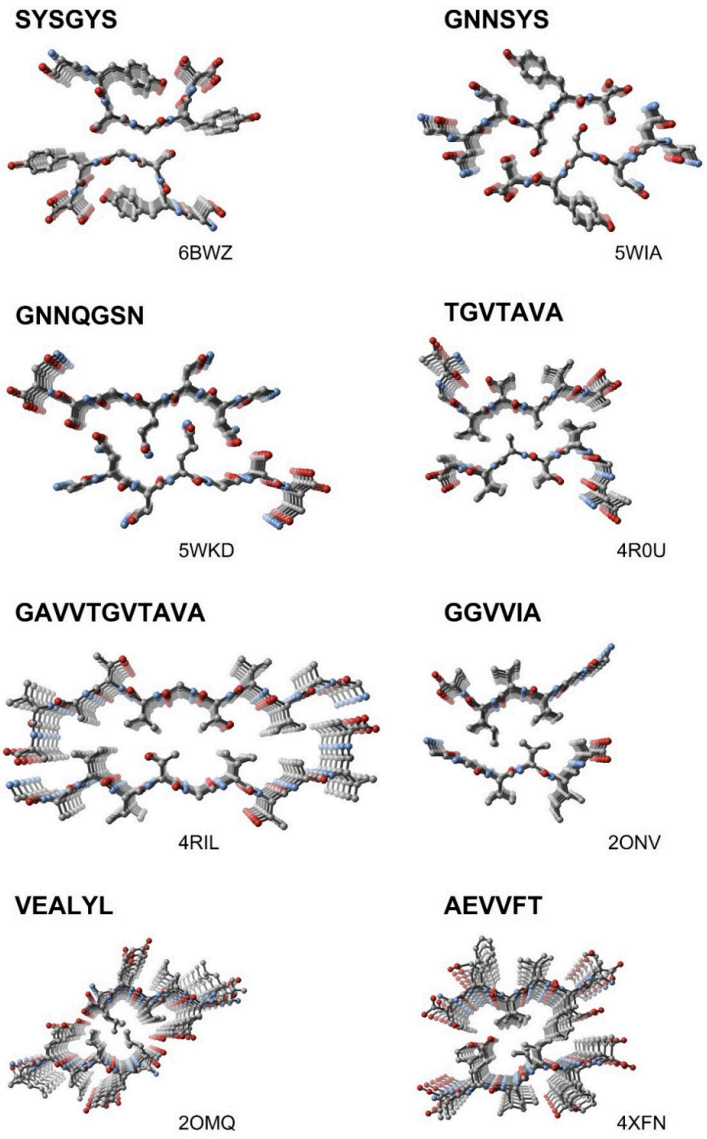

Figure 4.12 Selected examples from Eisenberg and coworkers, [59–64] of fibrils formed by aggregating enantiopure peptides in which pleated β-sheets display one-dimensional, long-range order. Color code: C, gray; O, red; N, blue. Water molecules and hydrogens are omitted for clarity. PDB codes are displayed on the bottom right of each structure.

In contrast to the long-range packing noted in the Eisenberg systems, we observed dimeric antiparallel rippled sheets with FFF:fff (Figure 4.2), but those dimers did not form extended rippled sheets (Figures 4.4 and 4.8). The lack of extended sheets may also be rooted in the hydrophobicity of the FFF:fff dimer that leads it to precipitate from water before it can mature into an extended fibrillary rippled sheet. Systematic optimization of crystallization parameters, including concentration, solvent identity, temperature, as well as variations in sequence, may allow the synthesis of extended fibrillary rippled sheet networks in the future. In that context it is interesting to compare our FFF:fff dimer structure with (a) the racemic Aβ40 structure, published in a recent collaborative study by the Raskatov and Tycko labs,[30] and (b) the hydrophobic Aβ16-22 segment in its interactions with its mirror-image, studied by the Nilsson lab. All three systems contain rippled antiparallel dimers, which is likely due, at least in part, to Coulombic attractions. However, there are important differences. Racemic Aβ40 forms fibrils with three Aβ40 units per layer and a fibril thickness of 7 ± 1 nm.[9] The crystalline Aβ16-22 aggregates, on the other hand, are micron-wide, which is consistent with the presence of thousands of peptides per layer.[25] Future X-ray structural studies of racemic Aβ16-22 should determine whether it (a) forms extended rippled sheets, (b) aggregates into rippled antiparallel cross-β dimers that then pack in ways similar to FFF:fff, or (c) packs in a way that is completely different.

Our findings have to be put in context with the recent paper by Liu and Gellman, where peptides designed to form two-stranded β-hairpins, composed of half L and half D residues did not exhibit any heterochiral stand pairing detectable by solution NMR.[25] It is noteworthy that one of the systems studied by the authors contained the VFF motif that is present in Aβ and is believed to be important for racemic Aβ fibrillization (*i.e.*, Aβ Chiral Inactivation, Aβ-CI).[8,26,30] The VFF motif is also very similar in terms of its size and hydrophobicity to the FFF motif studied here. A possible reason for the apparent discrepancy is that in Gellman's work, the L- and D- sequences were linked together, which may have induced a preference for homochiral strand pairing. Possibly more significantly, FFF:fff crystallization (similarly to Aβ-CI and the racemic Aβ16-22 model system studied by Nilsson) appears to occur under kinetic control, whereas the foldamers of the Gellman hairpin were monitored under thermodynamic equilibrium conditions. Similarly (albeit in the non-polar solvent $CDCl_3$), Chung and Nowick found that hydrophobic β-turn peptide mimics preferentially form homochiral (pleated) dimers.[24] Another important difference between our work and the two solution NMR studies is that, in our study, the rippled antiparallel FFF:fff dimers are packed into a three-dimensional crystal lattice that may, in itself, be a ripple-genic factor. In contrast, the solution NMR studies lacked evidence for the formation of higher order aggregates, and instead highlighted interactions between dimerizing peptide strands as isolated entities.

It may be tempting to ascribe the difference between the solution NMR experiments discussed above and our findings to the fact that solution NMR work studied systems as pure dimers, whereas our work produced extended layers, in which the individual dimers were stabilized through interactions with the crystal lattice. However, we are aware of a crystal structure of the GSTSTA peptide in a racemic mixture with its enantiomer, in which self-sorting into pleated fibrillary structures was observed, showing that racemic aggregating peptide mixtures are not ripple-genic *per se* either.[31] In this specific case, it may have been because GSTSTA lacks bulky, hydrophobic groups that appear to promote rippled sheet formation.[18] Yet it seems that the presence of bulky residues is not obligate either, as the first rippled sheet structure was reported for polyglycine I, which does not have sidechains.[19,20] It should also be noted that, in addition to sequence, aggregation conditions are important. As such, it was noted with the MAX1:DMAX system developed by the Schneider lab, that the rigidity of the hydrogels formed depended on whether peptides were aggregated under kinetic or thermodynamic control, with thermodynamically controlled assembly producing the most rigid hydrogel systems. [4,5,18] These are all conditions that should be explored in future research.

4.4 Conclusions and Future Directions

We presented crystal-structural insights into a rippled sheet-based nanostructure that we obtained by temperature-controlled crystallization of

FFF:fff. The structure consists of arrays of dimeric antiparallel rippled sheet, whose internal structural parameters agree well with the predictions by Pauling and Corey. The rippled dimers are arranged in a herringbone-pattern, into networks that are held together by in-plane salt bridges and hydrogen bonds and display lateral long-range segregation into hydrophobic and hydrophilic domains. Comparison of FFF:fff with the three orphaned rippled sheets identified by analyzing the racemic protein crystallography PDB supports the notion of Phe as a ripple-genic residue. Systematic exploration of Phe-containing racemic peptide mixtures may provide a rational framework on how to devise functional rippled sheet materials in the future.

4.5 References

(1) J. Kuhn, A.; Ehlke, B.; C. Johnstone, T.; J. Oliver, S. R.; A. Raskatov, J. A Crystal-Structural Study of Pauling–Corey Rippled Sheets. *Chemical Science* **2022**, *13* (3), 671–680. https://doi.org/10.1039/D1SC05731F.

(2) Schumacher, T. N. M.; Mayr, L. M.; Minor, D. L.; Milhollen, M. A.; Burgess, M. W.; Kim, P. S. Identification of D-Peptide Ligands Through Mirror-Image Phage Display. *Science* **1996**, *271* (5257), 1854–1857. https://doi.org/10.1126/science.271.5257.1854.

(3) Eckert, D. M.; Malashkevich, V. N.; Hong, L. H.; Carr, P. A.; Kim, P. S. Inhibiting HIV-1 Entry: Discovery of D-Peptide Inhibitors That Target the Gp41 Coiled-Coil Pocket. *Cell* **1999**, *99* (1), 103–115. https://doi.org/10.1016/S0092-8674(00)80066-5.

(4) Nagy-Smith, K.; Beltramo, P. J.; Moore, E.; Tycko, R.; Furst, E. M.; Schneider, J. P. Molecular, Local, and Network-Level Basis for the Enhanced Stiffness of Hydrogel Networks Formed from Coassembled Racemic Peptides: Predictions from Pauling and Corey. *ACS Cent. Sci.* **2017**, *3* (6), 586–597. https://doi.org/10.1021/acscentsci.7b00115.

(5) Nagy, K. J.; Giano, M. C.; Jin, A.; Pochan, D. J.; Schneider, J. P. Enhanced Mechanical Rigidity of Hydrogels Formed from Enantiomeric Peptide Assemblies. *J Am Chem Soc* **2011**, *133* (38), 14975–14977. https://doi.org/10.1021/ja206742m.

(6) Willbold, D.; Kutzsche, J. Do We Need Anti-Prion Compounds to Treat Alzheimer's Disease? *Molecules* **2019**, *24* (12), 2237. https://doi.org/10.3390/molecules24122237.

(7) van Groen, T.; Schemmert, S.; Brener, O.; Gremer, L.; Ziehm, T.; Tusche, M.; Nagel-Steger, L.; Kadish, I.; Schartmann, E.; Elfgen, A.; Jürgens, D.; Willuweit, A.; Kutzsche, J.; Willbold, D. The Aβ Oligomer Eliminating D-Enantiomeric Peptide RD2 Improves Cognition without Changing Plaque Pathology. *Sci Rep* **2017**, *7* (1), 16275. https://doi.org/10.1038/s41598-017-16565-1.

(8) Dutta, S.; Foley, A. R.; Warner, C. J. A.; Zhang, X.; Rolandi, M.; Abrams, B.; Raskatov, J. A. Suppression of Oligomer Formation and Formation of Non-Toxic Fibrils upon Addition of Mirror-Image Aβ42 to the Natural l-Enantiomer. *Angewandte Chemie International Edition* **2017**, *56* (38), 11506–11510. https://doi.org/10.1002/anie.201706279.

(9) Dutta, S.; Foley, A. R.; Kuhn, A. J.; Abrams, B.; Lee, H.-W.; Raskatov, J. A. New Insights into Differential Aggregation of Enantiomerically Pure and Racemic Aβ40 Systems. *Peptide Science* **2019**, *111* (6), e24139. https://doi.org/10.1002/pep2.24139.

(10) Foley, A. R.; Roseman, G. P.; Chan, K.; Smart, A.; Finn, T. S.; Yang, K.; Lokey, R. S.; Millhauser, G. L.; Raskatov, J. A. Evidence for Aggregation-Independent, PrPC-Mediated Aβ Cellular Internalization. *Proceedings of the*

National Academy of Sciences **2020**, *117* (46), 28625–28631. https://doi.org/10.1073/pnas.2009238117.

(11) Foley, A. R.; Raskatov, J. A. Understanding and Controlling Amyloid Aggregation with Chirality. *Current Opinion in Chemical Biology* **2021**, *64*, 1–9. https://doi.org/10.1016/j.cbpa.2021.01.003.

(12) Yeates, T. O.; Kent, S. B. H. Racemic Protein Crystallography. *Annual Review of Biophysics* **2012**, *41* (1), 41–61. https://doi.org/10.1146/annurev-biophys-050511-102333.

(13) Kurgan, K. W.; Kleman, A. F.; Bingman, C. A.; Kreitler, D. F.; Weisblum, B.; Forest, K. T.; Gellman, S. H. Retention of Native Quaternary Structure in Racemic Melittin Crystals. *J. Am. Chem. Soc.* **2019**, *141* (19), 7704–7708. https://doi.org/10.1021/jacs.9b02691.

(14) Zawadzke, L. E.; Berg, J. M. The Structure of a Centrosymmetric Protein Crystal. *Proteins: Structure, Function, and Bioinformatics* **1993**, *16* (3), 301–305. https://doi.org/10.1002/prot.340160308.

(15) Pentelute, B. L.; Gates, Z. P.; Tereshko, V.; Dashnau, J. L.; Vanderkooi, J. M.; Kossiakoff, A. A.; Kent, S. B. H. X-Ray Structure of Snow Flea Antifreeze Protein Determined by Racemic Crystallization of Synthetic Protein Enantiomers. *J. Am. Chem. Soc.* **2008**, *130* (30), 9695–9701. https://doi.org/10.1021/ja8013538.

(16) Pauling, L.; Corey, R. B. The Pleated Sheet, A New Layer Configuration of Polypeptide Chains. *Proceedings of the National Academy of Sciences* **1951**, *37* (5), 251–256. https://doi.org/10.1073/pnas.37.5.251.

(17) Pauling, L.; Corey, R. B. Two Rippled-Sheet Configurations of Polypeptide Chains, and a Note about the Pleated Sheets. *Proceedings of the National Academy of Sciences* **1953**, *39* (4), 253–256. https://doi.org/10.1073/pnas.39.4.253.

(18) Raskatov, J. A.; Schneider, J. P.; Nilsson, B. L. Defining the Landscape of the Pauling-Corey Rippled Sheet: An Orphaned Motif Finding New Homes. *Acc. Chem. Res.* **2021**, *54* (10), 2488–2501. https://doi.org/10.1021/acs.accounts.1c00084.

(19) Lotz, B. Crystal Structure of Polyglycine I. *Journal of Molecular Biology* **1974**, *87* (2), 169–180. https://doi.org/10.1016/0022-2836(74)90141-7.

(20) Colonna-Cesari, F.; Premilat, S.; Lotz, B. Structure of Polyglycine I: A Comparison of the Antiparallel Pleated and Antiparallel Rippled Sheets. *Journal of Molecular Biology* **1974**, *87* (2), 181–191. https://doi.org/10.1016/0022-2836(74)90142-9.

(21) Moore, W. H.; Krimm, S. Vibrational Analysis of Peptides, Polypeptides, and Proteins. I. Polyglycine I. *Biopolymers* **1976**, *15* (12), 2439–2464. https://doi.org/10.1002/bip.1976.360151210.

(22) Weissbuch, I.; Illos, R. A.; Bolbach, G.; Lahav, M. Racemic β-Sheets as Templates of Relevance to the Origin of Homochirality of Peptides: Lessons

from Crystal Chemistry. *Acc. Chem. Res.* **2009**, *42* (8), 1128–1140. https://doi.org/10.1021/ar900033k.

(23) Rubinstein, I.; Eliash, R.; Bolbach, G.; Weissbuch, I.; Lahav, M. Racemic β Sheets in Biochirogenesis. *Angewandte Chemie International Edition* **2007**, *46* (20), 3710–3713. https://doi.org/10.1002/anie.200605040.

(24) Chung, D. M.; Nowick, J. S. Enantioselective Molecular Recognition between β-Sheets. *J. Am. Chem. Soc.* **2004**, *126* (10), 3062–3063. https://doi.org/10.1021/ja031632z.

(25) Liu, X.; Gellman, S. H. Comparisons of β-Hairpin Propensity Among Peptides with Homochiral or Heterochiral Strands. *ChemBioChem* **2021**, *22* (18), 2772–2776. https://doi.org/10.1002/cbic.202100324.

(26) Urban, J. M.; Ho, J.; Piester, G.; Fu, R.; Nilsson, B. L. Rippled β-Sheet Formation by an Amyloid-β Fragment Indicates Expanded Scope of Sequence Space for Enantiomeric β-Sheet Peptide Coassembly. *Molecules* **2019**, *24* (10), 1983. https://doi.org/10.3390/molecules24101983.

(27) Swanekamp, R. J.; DiMaio, J. T. M.; Bowerman, C. J.; Nilsson, B. L. Coassembly of Enantiomeric Amphipathic Peptides into Amyloid-Inspired Rippled β-Sheet Fibrils. *J. Am. Chem. Soc.* **2012**, *134* (12), 5556–5559. https://doi.org/10.1021/ja301642c.

(28) Garcia, A. M.; Giorgiutti, C.; El Khoury, Y.; Bauer, V.; Spiegelhalter, C.; Leize-Wagner, E.; Hellwig, P.; Potier, N.; Torbeev, V. Aggregation and Amyloidogenicity of the Nuclear Coactivator Binding Domain of CREB-Binding

Protein. *Chemistry – A European Journal* **2020**, *26* (44), 9889–9899. https://doi.org/10.1002/chem.202001847.

(29) Torbeev, V.; Grogg, M.; Ruiz, J.; Boehringer, R.; Schirer, A.; Hellwig, P.; Jeschke, G.; Hilvert, D. Chiral Recognition in Amyloid Fiber Growth. *Journal of Peptide Science* **2016**, *22* (5), 290–304. https://doi.org/10.1002/psc.2861.

(30) Raskatov, J. A.; Foley, A. R.; Louis, J. M.; Yau, W.-M.; Tycko, R. Constraints on the Structure of Fibrils Formed by a Racemic Mixture of Amyloid-β Peptides from Solid-State NMR, Electron Microscopy, and Theory. *J. Am. Chem. Soc.* **2021**, *143* (33), 13299–13313. https://doi.org/10.1021/jacs.1c06339.

(31) Zee, C.; Glynn, C.; Gallagher-Jones, M.; Miao, J.; Santiago, C. G.; Cascio, D.; Gonen, T.; Sawaya, M. R.; Rodriguez, J. A. Homochiral and Racemic MicroED Structures of a Peptide Repeat from the Ice-Nucleation Protein InaZ. *IUCrJ* **2019**, *6* (2), 197–205. https://doi.org/10.1107/S2052252518017621.

(32) Warner, C. J. A.; Dutta, S.; Foley, A. R.; Raskatov, J. A. A Tailored HPLC Purification Protocol That Yields High-Purity Amyloid Beta 42 and Amyloid Beta 40 Peptides, Capable of Oligomer Formation. *J Vis Exp* **2017**, No. 121, 55482. https://doi.org/10.3791/55482.

(33) Kuhn, A. J.; Abrams, B. S.; Knowlton, S.; Raskatov, J. A. Alzheimer's Disease "Non-Amyloidogenic" P3 Peptide Revisited: A Case for Amyloid-α.

ACS Chem. Neurosci. **2020**, *11* (11), 1539–1544. https://doi.org/10.1021/acschemneuro.0c00160.

(34) Rigaku, 2020, CrysAlisPro 1.171.41.110a.

(35) Sheldrick, G. M. SHELXT – Integrated Space-Group and Crystal-Structure Determination. *Acta Cryst A* **2015**, *71* (1), 3–8. https://doi.org/10.1107/S2053273314026370.

(36) Sheldrick, G. M. Crystal Structure Refinement with SHELXL. *Acta Cryst C* **2015**, *71* (1), 3–8. https://doi.org/10.1107/S2053229614024218.

(37) Dolomanov, O. V.; Bourhis, L. J.; Gildea, R. J.; Howard, J. a. K.; Puschmann, H. OLEX2: A Complete Structure Solution, Refinement and Analysis Program. *J Appl Cryst* **2009**, *42* (2), 339–341. https://doi.org/10.1107/S0021889808042726.

(38) Müller, P. Practical Suggestions for Better Crystal Structures. *Crystallography Reviews* **2009**, *15* (1), 57–83. https://doi.org/10.1080/08893110802547240.

(39) Becke, A. D. Density-Functional Exchange-Energy Approximation with Correct Asymptotic Behavior. *Phys. Rev. A* **1988**, *38* (6), 3098–3100. https://doi.org/10.1103/PhysRevA.38.3098.

(40) Perdew, J. P. Density-Functional Approximation for the Correlation Energy of the Inhomogeneous Electron Gas. *Phys. Rev. B* **1986**, *33* (12), 8822–8824. https://doi.org/10.1103/PhysRevB.33.8822.

(41) Weigend, F.; Ahlrichs, R. Balanced Basis Sets of Split Valence, Triple Zeta Valence and Quadruple Zeta Valence Quality for H to Rn: Design and Assessment of Accuracy. *Phys. Chem. Chem. Phys.* **2005**, *7* (18), 3297–3305. https://doi.org/10.1039/B508541A.

(42) Weigend, F. Accurate Coulomb-Fitting Basis Sets for H to Rn. *Phys. Chem. Chem. Phys.* **2006**, *8* (9), 1057–1065. https://doi.org/10.1039/B515623H.

(43) Grimme, S.; Antony, J.; Ehrlich, S.; Krieg, H. A Consistent and Accurate Ab Initio Parametrization of Density Functional Dispersion Correction (DFT-D) for the 94 Elements H-Pu. *J. Chem. Phys.* **2010**, *132* (15), 154104. https://doi.org/10.1063/1.3382344.

(44) Grimme, S.; Ehrlich, S.; Goerigk, L. Effect of the Damping Function in Dispersion Corrected Density Functional Theory. *Journal of Computational Chemistry* **2011**, *32* (7), 1456–1465. https://doi.org/10.1002/jcc.21759.

(45) Garcia-Ratés, M.; Neese, F. Efficient Implementation of the Analytical Second Derivatives of Hartree–Fock and Hybrid DFT Energies within the Framework of the Conductor-like Polarizable Continuum Model. *Journal of Computational Chemistry* **2019**, *40* (20), 1816–1828. https://doi.org/10.1002/jcc.25833.

(46) Bunker, R. D.; Mandal, K.; Bashiri, G.; Chaston, J. J.; Pentelute, B. L.; Lott, J. S.; Kent, S. B. H.; Baker, E. N. A Functional Role of Rv1738 in Mycobacterium Tuberculosis Persistence Suggested by Racemic Protein

Crystallography. *Proceedings of the National Academy of Sciences* **2015**, *112* (14), 4310–4315. https://doi.org/10.1073/pnas.1422387112.

(47) Avital-Shmilovici, M.; Mandal, K.; Gates, Z. P.; Phillips, N. B.; Weiss, M. A.; Kent, S. B. H. Fully Convergent Chemical Synthesis of Ester Insulin: Determination of the High Resolution X-Ray Structure by Racemic Protein Crystallography. *J. Am. Chem. Soc.* **2013**, *135* (8), 3173–3185. https://doi.org/10.1021/ja311408y.

(48) Pentelute, B. L.; Mandal, K.; Gates, Z. P.; Sawaya, M. R.; Yeates, T. O.; Kent, S. B. H. Total Chemical Synthesis and X-Ray Structure of Kaliotoxin by Racemic Protein Crystallography. *Chem. Commun.* **2009**, *46* (43), 8174–8176. https://doi.org/10.1039/C0CC03148H.

(49) Ghanta, J.; Shen, C.-L.; Kiessling, L. L.; Murphy, R. M. A Strategy for Designing Inhibitors of β-Amyloid Toxicity*. *Journal of Biological Chemistry* **1996**, *271* (47), 29525–29528. https://doi.org/10.1074/jbc.271.47.29525.

(50) Lowe, T. L.; Strzelec, A.; Kiessling, L. L.; Murphy, R. M. Structure−Function Relationships for Inhibitors of β-Amyloid Toxicity Containing the Recognition Sequence KLVFF. *Biochemistry* **2001**, *40* (26), 7882–7889. https://doi.org/10.1021/bi002734u.

(51) Brahmachari, S.; Arnon, Z. A.; Frydman-Marom, A.; Gazit, E.; Adler-Abramovich, L. Diphenylalanine as a Reductionist Model for the Mechanistic Characterization of β-Amyloid Modulators. *ACS Nano* **2017**, *11* (6), 5960–5969. https://doi.org/10.1021/acsnano.7b01662.

(52) Guo, C.; Luo, Y.; Zhou, R.; Wei, G. Triphenylalanine Peptides Self-Assemble into Nanospheres and Nanorods That Are Different from the Nanovesicles and Nanotubes Formed by Diphenylalanine Peptides. *Nanoscale* **2014**, *6* (5), 2800–2811. https://doi.org/10.1039/C3NR02505E.

(53) Mayans, E.; Casanovas, J.; Gil, A. M.; Jiménez, A. I.; Cativiela, C.; Puiggalí, J.; Alemán, C. Diversity and Hierarchy in Supramolecular Assemblies of Triphenylalanine: From Laminated Helical Ribbons to Toroids. *Langmuir* **2017**, *33* (16), 4036–4048. https://doi.org/10.1021/acs.langmuir.7b00622.

(54) Tamamis, P.; Adler-Abramovich, L.; Reches, M.; Marshall, K.; Sikorski, P.; Serpell, L.; Gazit, E.; Archontis, G. Self-Assembly of Phenylalanine Oligopeptides: Insights from Experiments and Simulations. *Biophysical Journal* **2009**, *96* (12), 5020–5029. https://doi.org/10.1016/j.bpj.2009.03.026.

(55) Roychaudhuri, R.; Yang, M.; Hoshi, M. M.; Teplow, D. B. Amyloid β-Protein Assembly and Alzheimer Disease*. *Journal of Biological Chemistry* **2009**, *284* (8), 4749–4753. https://doi.org/10.1074/jbc.R800036200.

(56) Snatzke, G. J. Jaques, A. Collet, and S. H. Wilen: Enantiomers, Racemates, and Resolutions, J. Wiley & Sons, Inc., New York, Chichester, Brisbane, Toronto 1981. 447 Seiten, Preis: £ 38.75. *Berichte der Bunsengesellschaft für physikalische Chemie* **1982**, *86* (11), 1087–1087. https://doi.org/10.1002/bbpc.198200035.

(57) Raskatov, J. A. Conformational Selection as the Driving Force of Amyloid β Chiral Inactivation. *ChemBioChem* **2020**, *21* (20), 2945–2949. https://doi.org/10.1002/cbic.202000237.

(58) Raskatov, J. A. A DFT Study of Structure and Stability of Pleated and Rippled Cross-β Sheets with Hydrophobic Sidechains. *Biopolymers* **2021**, *112* (1), e23391. https://doi.org/10.1002/bip.23391.

(59) Sawaya, M. R.; Sambashivan, S.; Nelson, R.; Ivanova, M. I.; Sievers, S. A.; Apostol, M. I.; Thompson, M. J.; Balbirnie, M.; Wiltzius, J. J. W.; McFarlane, H. T.; Madsen, A. Ø.; Riekel, C.; Eisenberg, D. Atomic Structures of Amyloid Cross-β Spines Reveal Varied Steric Zippers. *Nature* **2007**, *447* (7143), 453–457. https://doi.org/10.1038/nature05695.

(60) Hughes, M. P.; Sawaya, M. R.; Boyer, D. R.; Goldschmidt, L.; Rodriguez, J. A.; Cascio, D.; Chong, L.; Gonen, T.; Eisenberg, D. S. Atomic Structures of Low-Complexity Protein Segments Reveal Kinked β Sheets That Assemble Networks. *Science* **2018**, *359* (6376), 698–701. https://doi.org/10.1126/science.aan6398.

(61) Guenther, E. L.; Cao, Q.; Trinh, H.; Lu, J.; Sawaya, M. R.; Cascio, D.; Boyer, D. R.; Rodriguez, J. A.; Hughes, M. P.; Eisenberg, D. S. Atomic Structures of TDP-43 LCD Segments and Insights into Reversible or Pathogenic Aggregation. *Nat Struct Mol Biol* **2018**, *25* (6), 463–471. https://doi.org/10.1038/s41594-018-0064-2.

(62) Li, D.; Jones, E. M.; Sawaya, M. R.; Furukawa, H.; Luo, F.; Ivanova, M.; Sievers, S. A.; Wang, W.; Yaghi, O. M.; Liu, C.; Eisenberg, D. S. Structure-Based Design of Functional Amyloid Materials. *J. Am. Chem. Soc.* **2014**, *136* (52), 18044–18051. https://doi.org/10.1021/ja509648u.

(63) Rodriguez, J. A.; Ivanova, M. I.; Sawaya, M. R.; Cascio, D.; Reyes, F. E.; Shi, D.; Sangwan, S.; Guenther, E. L.; Johnson, L. M.; Zhang, M.; Jiang, L.; Arbing, M. A.; Nannenga, B. L.; Hattne, J.; Whitelegge, J.; Brewster, A. S.; Messerschmidt, M.; Boutet, S.; Sauter, N. K.; Gonen, T.; Eisenberg, D. S. Structure of the Toxic Core of α-Synuclein from Invisible Crystals. *Nature* **2015**, *525* (7570), 486–490. https://doi.org/10.1038/nature15368.

(64) Saelices, L.; Johnson, L. M.; Liang, W. Y.; Sawaya, M. R.; Cascio, D.; Ruchala, P.; Whitelegge, J.; Jiang, L.; Riek, R.; Eisenberg, D. S. Uncovering the Mechanism of Aggregation of Human Transthyretin*. *Journal of Biological Chemistry* **2015**, *290* (48), 28932–28943. https://doi.org/10.1074/jbc.M115.659912.

Chapter 5 - Summary and Future Directions

5.1 Summary

This thesis presented three classes of extended materials obtained by distinct solvothermal methods. In Chapter 1, MAPOs and ionic liquids were introduced, followed by a literature review of the field. Chapter 2 discussed the variables involved in the ionothermal syntheses of AlPO-5 and MnAPO-5. Chapter 3 reported the hydrothermal synthesis of SLUG-53, a novel phase of coordination polymer [Ag(2,4'-bipyridine)] that presents superior adsorption capacity for perrhenate. Chapter 4 presented the first high-resolution single-crystal structure study of a rippled β-dimer motif. The structure of [FFF.fff], a racemic triphenylalanine mixture crystallized via solvothermal methods, is in agreement with the predictions made by Pauling and Corey in 1953. In this final chapter, future directions for each project are discussed.

5.2 Metal-doped Aluminophosphates Project

We successfully synthesized the zeolitic materials AlPO-5 and MnAPO-5 via the ionothermal route using DIPI or DIBU as ionic liquids. Further insights into these compounds' crystallization mechanism can be obtained by performing time-resolved PXRD, SS-NMR, and SEM studies. The temperature and reaction time of the ionothermal synthesis can be explored to obtain single-crystals for SCXRD analysis to determine if the DIPI and DIBU cations and/or

anions are occluded in the extra-framework structure of the as-synthesized MAPOs and, if so, which cavity they occupy. Such studies would highlight the factors leading to the stabilization of the AFI topology and help to rationalize the use of different strategies to increase phase selectivity, such as the use of co-OSDAs.

We have determined that the amount of HF added to the reaction medium significantly impacts framework formation. An exciting strategy would be to explore the use of different sources of the mineralizing ion. For example, fluoride precursors $[Me_4N]F$ and MnF_3 have been successfully used to obtain SOD, LTA or AFI topologies.[1] The use of different metal sources would also be interesting as it has been shown to affect phase formation of MnAPOs.[2]

Furthermore, more of the material's properties that affect its catalytic behavior can be elucidated. Calcination parameters for removing extra-framework species residing in the pores can be investigated. The pore availability for catalysis can be studied by determining the BET surface area. The Brønsted acidity can be elucidated by using NH_3-TPD.

Finally, MnAPO-5 can be directly tested as a catalyst in MTO reactions using a system similar to the one shown in Figure 5.1. The process conditions such as temperature, pressure, and gas flow can be explored for optimal catalytic turnover. The weight distribution of the obtained olefins can be used to better understand the synthesized AFI framework's shape selectivity and confinement behavior.

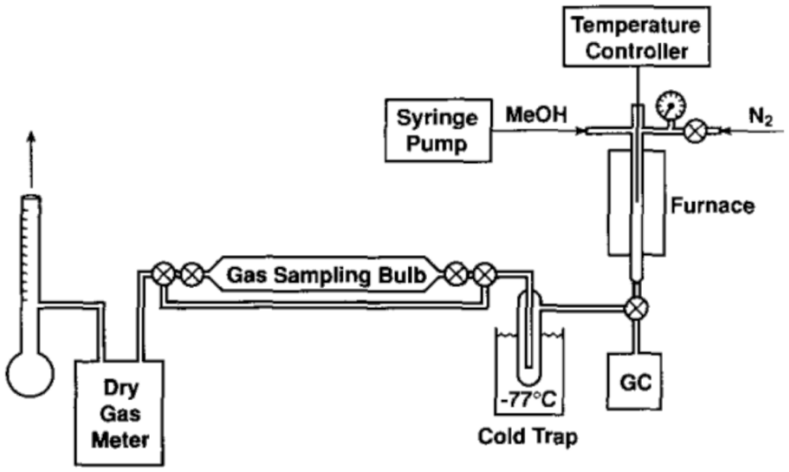

Figure 5.1 Scheme of a methanol conversion reactor to be used for testing MnAPO-5 as a catalyst in MTO reactions.[3]

5.3 Coordination Polymers Project

The synthesis and structural elucidation of a novel phase of the coordination polymer [Ag(2,4'-bipyridine)] (SLUG-53) has been determined. SLUG-53 is a soft porous crystalline material, with anisotropic deformations occurring due to temperature changes. In future studies, its dynamic framework may be more deeply investigated to determine if other perturbations - pressure or insertion of different guest ions in the extra-framework - can also cause deformations. Furthermore, elucidating the process's reversibility is also of interest, as SPCs can be used as sensors.[4,5] For example, the adsorption of O_2 by the SPC $[Zn_4O(bpz)_2(abdc)]$ causes a quenching in its photoluminescence, which allows for oxygen sensing.[6] Ion sensing in aqueous solutions has also been reported, with the adsorption order of $SCN^- > N_3^- > N(CN)_2^- > ClO_4^-$ leading to tunable luminesce in one-dimensional zinc SPCs.[7]

The material's superior adsorption capacity for perrhenate is very promising. A follow-up study on the use of pertechnetate itself will allow better determination of the applicability of SLUG-53 for the remediation of radioactive waste. Further investigations also include adsorption capacity studies in mediums containing ions commonly present in pertechnetate waste. A good strategy in that regard would be to use simulated high-level radioactive waste (HLW). The SLUG-53 stability when submitted to radiation or pH variations and the adsorption process' reversibility is of interest. These are promising studies as SBN ([Ag(4,4'-bipyridine]NO_3), a material analogous to SLUG-53, has been reported to retain its high adsorption capacity in a large range of pH.[8] Finally, the adsorption of perrhenate by SLUG-53 could be tested in a dynamic setting by performing column studies.

Further elucidation of coordination polymers containing bipyridine groups can be obtained by studying systems analogous to the one presented in Chapter 3. We recently reported the uptake of Cr(IV) species by SBA ([Ag(4,4′-bipy)][CH_3CO_2]·3H_2O) and SEN ([Ag(4,4′-bpe)][NO_3], bpe = 1,2-bis(4-pyridyl)ethane). Although both the materials show high Cr uptakes (533.48 mmol/mol and 481.28 mmol/mol for SBA and SEN, respectively), the anion exchange reaction presents different kinetics. SBA reaches it maximum adsorption capacity much faster than SEN.[9] Our group is currently investigating modular copper 4,4'-bipyridine amino acid coordination polymers for ion

exchange and the prediction of ion exchange thermodynamics of silver bipyridine coordination polymers using DFT.

5.4 Pauling-Corey Rippled β-dimers Project

The antiparallel rippled β-sheets formation is still incredibly unexplored, and many systems presenting this supramolecular feature are yet to be unveiled. After the publication of the work in Chapter 4, the Raskatov group reported three more polypeptide structures presenting rippled β-motifs: [FYF.fyf], [FWF.fwf], and [FWF.fyf]. Dimeric units similar to the ones observed in the triphenylalanine system were found. However, while in [FFF.fff] the dimers were terminally ordered in a herringbone fashion, in the new structures they further aggregate to form extended antiparallel rippled β-sheet layers. The replacement of the central phenylalanine by tyrosine or tryptophan possibly led to an end-to-edge interaction between the L and d polypeptides instead of the edge-to-edge observed for the [FFF.fff].[10]

The structures described represent a novel supramolecular arrangement. Future studies include expanding the tripeptide to larger or infinite polypeptide chains as our database mining showed rippled motifs were present in the glu-lys-glu-leu-val sequence of RV1738,[11] and in the lys-gly-phe-arg sequence of Kaliotoxin.[12] The study of longer chains will bring insights into why some systems preferred to arrange in a rippled over pleated fashion. The finds will sum to recent studies[13] that investigated the *rippled-genic* behavior of

polypeptides by NMR and will aid the rational design of materials presenting this novel supramolecular chemistry.

5.5 References

(1) Azim, M. M.; Stark, A. Ionothermal Synthesis and Characterisation of Mn-, Co-, Fe- and Ni-Containing Aluminophosphates. *Microporous Mesoporous Mater.* **2018**, *272*, 251–259. https://doi.org/10.1016/j.micromeso.2018.06.045.

(2) Liu, H.; Tian, Z.; Wang, L.; Wang, Y.; Li, D.; Ma, H.; Xu, R. Ionothermal Synthesis of MnAPO-SOD Molecular Sieve without the Aid of Organic Structure-Directing Agents. *Inorg. Chem.* **2016**, *55* (4), 1809–1815. https://doi.org/10.1021/acs.inorgchem.5b02700.

(3) Yuen, L.-T.; Zones, S. I.; Harris, T. V.; Gallegos, E. J.; Auroux, A. Product Selectivity in Methanol to Hydrocarbon Conversion for Isostructural Compositions of AFI and CHA Molecular Sieves. *Microporous Mater.* **1994**, *2* (2), 105–117. https://doi.org/10.1016/0927-6513(93)E0039-J.

(4) Horike, S.; Shimomura, S.; Kitagawa, S. Soft Porous Crystals. *Nat. Chem.* **2009**, *1* (9), 695–704. https://doi.org/10.1038/nchem.444.

(5) Schneemann, A.; Bon, V.; Schwedler, I.; Senkovska, I.; Kaskel, S.; Fischer, R. A. Flexible Metal–Organic Frameworks. *Chem. Soc. Rev.* **2014**, *43* (16), 6062–6096. https://doi.org/10.1039/C4CS00101J.

(6) Lin, R.-B.; Li, F.; Liu, S.-Y.; Qi, X.-L.; Zhang, J.-P.; Chen, X.-M. A Noble-Metal-Free Porous Coordination Framework with Exceptional Sensing Efficiency for Oxygen. *Angew. Chem. Int. Ed.* **2013**, *52* (50), 13429–13433. https://doi.org/10.1002/anie.201307217.

(7) Manna, B.; Chaudhari, A. K.; Joarder, B.; Karmakar, A.; Ghosh, S. K. Dynamic Structural Behavior and Anion-Responsive Tunable Luminescence of a Flexible Cationic Metal–Organic Framework. *Angew. Chem. Int. Ed.* **2013**, *52* (3), 998–1002. https://doi.org/10.1002/anie.201206724.

(8) Zhu, L.; Xiao, C.; Dai, X.; Li, J.; Gui, D.; Sheng, D.; Chen, L.; Zhou, R.; Chai, Z.; Albrecht-Schmitt, T. E.; Wang, S. Exceptional Perrhenate/Pertechnetate Uptake and Subsequent Immobilization by a Low-Dimensional Cationic Coordination Polymer: Overcoming the Hofmeister Bias Selectivity. *Environ. Sci. Technol. Lett.* **2017**, *4* (7), 316–322. https://doi.org/10.1021/acs.estlett.7b00165.

(9) Conour, C. S.; Droege, D. G.; Ehlke, B.; Johnstone, T. C.; Oliver, S. R. J. Selective Chromium(VI) Trapping by an Acetate-Releasing Coordination Polymer. *Inorg. Chem.* **2022**, *61* (51), 20824–20833. https://doi.org/10.1021/acs.inorgchem.2c03110.

(10) Hazari, A.; Sawaya, M. R.; Vlahakis, N.; Johnstone, T. C.; Boyer, D.; Rodriguez, J.; Eisenberg, D.; Raskatov, J. A. The Rippled β-Sheet Layer Configuration—a Novel Supramolecular Architecture Based on Predictions by Pauling and Corey. *Chem. Sci.* **2022**, *13* (31), 8947–8952. https://doi.org/10.1039/D2SC02531K.

(11) Bunker, R. D.; Mandal, K.; Bashiri, G.; Chaston, J. J.; Pentelute, B. L.; Lott, J. S.; Kent, S. B. H.; Baker, E. N. A Functional Role of Rv1738 in

Mycobacterium Tuberculosis Persistence Suggested by Racemic Protein Crystallography. *Proc. Natl. Acad. Sci.* **2015**, *112* (14), 4310–4315. https://doi.org/10.1073/pnas.1422387112.

(12) Pentelute, B. L.; Mandal, K.; Gates, Z. P.; Sawaya, M. R.; Yeates, T. O.; Kent, S. B. H. Total Chemical Synthesis and X-Ray Structure of Kaliotoxin by Racemic Protein Crystallography. *Chem. Commun.* **2009**, *46* (43), 8174–8176. https://doi.org/10.1039/C0CC03148H.

(13) Li, X.; Rios, S. E.; Nowick, J. S. Enantiomeric β-Sheet Peptides from Aβ Form Homochiral Pleated β-Sheets Rather than Heterochiral Rippled β-Sheets. *Chem. Sci.* 2022, *13* (26), 7739–7746. https://doi.org/10.1039/D2SC02080G**.**

Appendix

Table A.1 Cartesian coordinates (Å) of the optimized (BP86-D3BJ/def2-SVP-$CPCM_{water}$) structure of FFF:fff.

N	4.09370415118074	12.55158927464286	8.01951364412157
H	3.96372050731073	11.87945342785070	8.89432214522468
H	3.67631800795364	13.45649622333425	8.29311390077636
H	5.10684826815001	12.72465726857804	7.86526886151337
O	4.68579699986856	10.00514061707158	7.08428367684645
C	4.21448263423020	10.83662052651225	6.28704928091444
C	3.40980475436177	12.02854135266891	6.80005942484666
H	3.38849381951550	12.83743527898451	6.04322345172614
C	1.97814220013488	11.57525758215830	7.15655122642748
H	1.54884004221062	11.10109355234939	6.25346523955252
H	2.05396185690734	10.79648718941633	7.94155838244508
C	1.09701622979355	12.71237139894564	7.62055690280438
C	1.09001748865928	13.10851995683912	8.97692250143198
H	1.71128992818933	12.55279025588311	9.70001424570751
C	0.29689600869346	14.19002383941204	9.39669431116368
H	0.30059192960416	14.48984062825498	10.45650801618807
C	-0.50386245035868	14.88372023555253	8.47211911233997
H	-1.12640255974232	15.72951255555404	8.80337394705965
C	-0.50629168506993	14.49105974185670	7.12126056936911
H	-1.13393642246107	15.02638237004613	6.39177196518855
C	0.29214352294006	13.41473994354018	6.69959318764820
H	0.28717212918944	13.10692663820845	5.64159702917600
N	4.34294104144003	10.71642127776430	4.95139847892585
H	4.02617325620660	11.45980460038944	4.32051429068197
O	4.39183936657579	10.13695537762992	2.13900493459608
C	4.53310543154521	9.25649096794045	3.00946511222600
C	5.11461928813669	9.61794373703439	4.38145018136459
H	5.03142864014147	8.76479723071096	5.07907335395468
C	6.60638929528331	10.03204527673807	4.24216281816270
H	6.66557687589099	10.81001469482846	3.45165198777844
H	6.89946224238773	10.50545984207140	5.19887788497200
C	7.54254308228714	8.88459583473587	3.94395032674684
C	7.58844472576498	8.28365432032168	2.66674556186903
H	6.94541458912158	8.66743223090499	1.86030598840700
C	8.45406241058803	7.20893971981611	2.40909750515203
H	8.45866869918136	6.74144750394299	1.41303033853607

C	9.30756466458947	6.72918695577871	3.41817773094835
H	9.98108783486585	5.88275984854788	3.21748271978528
C	9.27910482335856	7.32382914438217	4.69135159978216
H	9.93367021228568	6.94739162654751	5.49237800535179
C	8.39410679692009	8.38361619037178	4.95215142881515
H	8.36419766813895	8.83646995965917	5.95638546896319
N	4.27663118712145	7.94432643547798	2.83632745682123
H	4.39016191615368	7.30690269470780	3.64608983816175
O	5.36980195556720	5.51211468406074	2.26698208562355
O	5.09304882803972	5.85257505134016	0.05486234185960
C	4.90057255794537	6.14531097208455	1.25187163274656
C	3.97434193707562	7.35780504501355	1.54693871462719
H	4.15988268217939	8.13603868377272	0.78141118168691
C	2.48655619546023	6.92138841586021	1.42477292423107
H	1.85209546270454	7.81224356928512	1.60606231857112
H	2.32724214528117	6.59796256665133	0.37609533953726
C	2.11097727051036	5.80620589219198	2.37244680421324
C	2.28383758162549	4.45495364572536	1.99379188158820
H	2.67080634096225	4.22534617366592	0.98911503166958
C	1.97216973402590	3.41055767808345	2.87910349859398
H	2.11294850143188	2.36460126016809	2.56553803860911
C	1.48716530888976	3.70102699174574	4.17042290894159
H	1.23529636180071	2.88618588539751	4.86589264946698
C	1.31363145278839	5.04280868136374	4.55795607578832
H	0.92521192817041	5.27458827729304	5.56116588140656
C	1.62688866751194	6.08414190438623	3.66815534639682
H	1.50038556562449	7.13045249278436	3.98520466935573
N	4.74703122774710	4.19342206535575	4.38663953239223
H	4.86982114067797	4.86859999022297	3.51236735404479
H	5.16572951866549	3.29077403479728	4.10731414188434
H	3.73588967731612	4.01485485660771	4.54727049323470
O	4.16396127954101	6.74099311505567	5.31970178886795
C	4.63668287937818	5.91001586461808	6.11657509188658
C	5.43805826522110	4.71658749571353	5.60216894786604
H	5.46305755532070	3.90877021067308	6.35997761795219
C	6.86792610873869	5.16821719136807	5.23686214111084
H	7.30324336496732	5.64298378557832	6.13686772890228
H	6.78863229433642	5.94642718974931	4.45160130783574
C	7.74531512969249	4.02995894798071	4.76861216913461
C	7.74620225810931	3.63468321238378	3.41199288294599
H	7.12226633738760	4.19134827437473	2.69196386862010
C	8.53610557380459	2.55234105284025	2.98827944757836
H	8.52777712362381	2.25340164652189	1.92824534422122
C	9.33923708665485	1.85655064983315	3.90916358454985

H	9.95906506252588	1.00998479980240	3.57486101451993
C	9.34747886624511	2.24803499228983	5.26035139643555
H	9.97688767485362	1.71100378114162	5.98706279816186
C	8.55257204045476	3.32541707508023	5.68587348668957
H	8.56224206367965	3.63190721945685	6.74422251177071
N	4.51052720974095	6.03229462726670	7.45220154621982
H	4.82651042328429	5.28942368673009	8.08403981081477
O	4.45232595927066	6.60889428488492	10.26408493469117
C	4.30897502190871	7.49022987865021	9.39504697506979
C	3.73597511114322	7.13021966374973	8.01935926195330
H	3.82437115588301	7.98469998990265	7.32401109400939
C	2.24330073099328	6.71538912344956	8.14594351566544
H	2.17747246094972	5.93349904559341	8.93207273703793
H	1.95932459305754	6.24640532392327	7.18443283902556
C	1.30292448053796	7.86019962901400	8.44063142782111
C	1.24628926054932	8.45719361506985	9.71925040002921
H	1.88425058064177	8.07248796859544	10.52931357266964
C	0.37671889880669	9.52946860213518	9.97359028393214
H	0.36398847124617	9.99405460084568	10.97094721913926
C	-0.47041059278953	10.01046241701172	8.95970510299747
H	-1.14694010497439	10.85507471550927	9.15804996991875
C	-0.43155406803901	9.41947292909609	7.68513411129953
H	-1.08076873075477	9.79703992510457	6.88030795999379
C	0.45762561067833	8.36233045564615	7.42775676507842
H	0.49635272347544	7.91346605546526	6.42204849777097
N	4.55794847339994	8.80345073438008	9.57209305360787
H	4.44090072447028	9.44241168791802	8.76417612467272
O	3.45773153209174	11.23195820553672	10.13619692761770
O	3.72372766929813	10.89370536486153	12.35022202628192
C	3.92218845055026	10.60018630256060	11.15420196520344
C	4.85142631989578	9.38888224494806	10.86400355769733
H	4.66304253740939	8.60924727106737	11.62747022693811
C	6.33799403486710	9.82787788232499	10.99427526631197
H	6.97470662291954	8.93916325253939	10.81038900872820
H	6.49410552636178	10.14606052384495	12.04506325579148
C	6.71402078474572	10.94844574207184	10.05328804868640
C	6.54366053238547	12.29762245682966	10.44049823518437
H	6.15815230682130	12.52157842727393	11.44705665043399
C	6.85585320690155	13.34711395800373	9.56158813110815
H	6.71736316114667	14.39123957898378	9.88217394534763
C	7.33815102249408	13.06412388275726	8.26764787422629
H	7.58955393048688	13.88299875538902	7.57680417956278
C	7.50710227758705	11.72451427242645	7.87058479718694
H	7.88968207936726	11.49728715754806	6.86407916177420

C	7.19436456586794	10.67803224808990	8.75476176529525
H	7.31699362953703	9.63366286271353	8.42976376320827

Table A.2 Chapter 2 synthetic details

Sample ID	Reagents	Formula weight (g/mol)	Target weight/ volume	Used weight/ volume	Temperature (°C)	Time (hours)
BE02_01	$Al(iPrO)_3$ $Mn(OAc)_2.4$ H_2O H_3PO_4 DIPI	187.56 245.09 97.99 233.15	0.1000 g 0.0150 g 50 µL 1.500 g	0.1002 g 0.0154 g 50 µL 1.518 g	135	2
BE02_02	$Al(iPrO)_3$ $Mn(OAc)_2.4$ H_2O H_3PO_4 DIPI	187.56 245.09 97.99 233.15	0.1000 g 0.0150 g 50 µL 1.500 g	0.1017 g 0.0161 g 50 µL 1.502 g	135	4
BE02_03A	$Al(iPrO)_3$ $Ni(OAc)_2.4$ H_2O H_3PO_4 HF DIBU	187.56 248.84 97.99 20.01 247.15	0.1000 g 0.0160 g 50 µL 2 µL 1.1627 g	0.1006 g 0.0169 g 50 µL 2 µL 1.158 g	135	117
BE02_03B	$Al(iPrO)_3$ $Ni(OAc)_2.4$ H_2O H_3PO_4 HF DIBU	187.56 248.84 97.99 20.01 247.15	0.1000 g 0.0160 g 50 µL 2 µL 1.1627 g	0.099 g 0.0168 g 50 µL 2 µL 1.163 g	135	120
BE02_04	$Al(iPrO)_3$ $Ni(OAc)_2.4$ H_2O H_3PO_4 HF DIBU	187.56 248.84 97.99 20.01 247.15	0.1000 g 0.0301 g 50 µL 2 µL 1.1627	0.108 g 0.0307 g 50 µL 2 µL 1.150 g	135	120
BE02_05	$Al(iPrO)_3$ $Ni(OAc)_2.4$ H_2O H_3PO_4 HF DIBU	187.56 248.84 97.99 20.01 247.15	0.1000 g 0.0460 g 50 µL 2 µL 1.1627 g	0.100 g 0.0465 g 50 µL 2 µL 1.158 g	135	120
BE02_07	$Al(iPrO)_3$ H_3PO_4 HF H_2O DIBU	187.56 97.99 20.01 18.02 247.15	0.1000 g 45 µL 2 µL 15 µL 1.3009 g	0.108 g 45 µL 2 µL 15 µL 1.294 g	135	120
BE02_08	$Al(iPrO)_3$ H_3PO_4 HF H_2O DIBU	187.56 97.99 20.01 18.02 247.15	0.1000 g 45 µL 2 µL 20 µL 1.3009 g	0.100 g 45 µL 2 µL 20 µL 1.296 g	135	120
BE02_10	$Al(iPrO)_3$ H_3PO_4 HF	187.56 97.99 20.01	0.1000 g 50 µL 2 µL	0.103 g 50 µL 2 µL	135	120

	H_2O	18.02	4.4 µL	4.4 µL		
	DIBU	247.15	1.2500 g	1.249 g		
BE02_11	$Al(iPrO)_3$	187.56	0.1000 g	0.101 g	135	120
	H_3PO_4	97.99	50 µL	50 µL		
	HF	20.01	2 µL	2 µL		
	H_2O	18.02	10.45 µL	10.45 µL		
	DIBU	247.15	1.2500 g	1.251 g		
BE02_11	$Al(iPrO)_3$	187.56	0.1000 g	0.100 g	135	120
	H_3PO_4	97.99	50 µL	50 µL		
	HF	20.01	2 µL	2 µL		
	H_2O	18.02	4.4 µL	4.4 µL		
	DIBU	247.15	1.2500 g	1.254 g		
BE02_13	$Al(iPrO)_3$	187.56	0.1000 g	0.100 g	135	120
	H_3PO_4	97.99	50 µL	50 µL		
	HF	20.01	2 µL	2 µL		
	H_2O	18.02	4.4 µL	4.4 µL		
	DIBU	247.15	1.2500 g	1.254 g		
BE02_14	$Al(iPrO)_3$	187.56	0.1000 g	0.101 g	135	120
	H_3PO_4	97.99	50 µL	50 µL		
	HF	20.01	2 µL	2 µL		
	H_2O	18.02	10.45 µL	10.45 µL		
	DIBU	247.15	1.2500 g	1.248 g		
BE02_15	$Al(iPrO)_3$	187.56	0.1000 g	0.100 g	135	120
	H_3PO_4	97.99	50 µL	50 µL		
	HF	20.01	2 µL	2 µL		
	H_2O	18.02	12.9 µL	12.9 µL		
	DIBU	247.15	1.2500 g	1.249 g		
BE02_16	$Al(iPrO)_3$	187.56	0.1000 g	0.101 g	135	120
	H_3PO_4	97.99	50 µL	50 µL		
	HF	20.01	2 µL	2 µL		
	H_2O	18.02	1.7 µL	1.7 µL		
	DIPI	233.15	1.7000 g	1.702 g		
BE02_17	$Al(iPrO)_3$	187.56	0.1000 g	0.101 g	135	120
	H_3PO_4	97.99	50 µL	50 µL		
	HF	20.01	2 µL	2 µL		
	H_2O	18.02	9.3 µL	9.3 µL		
	DIPI	233.15	1.7000 g	1.700 g		
BE02_18	$Al(iPrO)_3$	187.56	0.1000 g	0.101 g	135	120
	H_3PO_4	97.99	50 µL	50 µL		
	HF	20.01	2 µL	2 µL		
	H_2O	18.02	13.3 µL	13.3 µL		
	DIPI	233.15	1.7000g	1.701 g		
BE02_19	$Al(iPrO)_3$	187.56	0.9050 g	0.101 g	135	120
	$Ni(OAc)_2.4$	248.84	0.0118	0.0111 g		
	H_2O	97.99	50 µL	50 µL		
	H_3PO_4	20.01	2 µL	2 µL		
	HF	233.15	1.1600 g	1.160 g		
	DIPI					
BE02_20	$Al(iPrO)_3$	187.56	0.1000 g	0.100 g	135	120
	H_3PO_4	97.99	50 µL	50 µL		
	HF	20.01	2 µL	2 µL		
	H_2O	18.02	9.7 µL	9.7 µL		
	DIPI	233.15	1.7000g	1.703 g		

BE02_21	$Al(iPrO)_3$	187.56	0.1000 g	0.101 g	135	120
	$Mn(OAc)_2.4$	245.09	0.0150 g	0.0145 g		
	H_2O	97.99	50 µL	50 µL		
	H_3PO_4	20.01	2 µL	2 µL		
	HF	233.15	1.7000 g	1.703 g		
	DIPI					
BE02_25	$Al(iPrO)_3$	187.56	0.1000 g	0.103 g	135	120
	$Mn(OAc)_2.4$	245.09	0.0312 g	0.0307 g		
	H_2O	97.99	50 µL	50 µL		
	H_3PO_4	20.01	2 µL	2 µL		
	HF	233.15	1.5035 g	1.500 g		
	DIPI					
BE02_26	$Al(iPrO)_3$	187.56	0.1000 g	0.102 g	135	192
	$Mn(OAc)_2.4$	245.09	0.0470 g	0.0472 g		
	H_2O	97.99	50 µL	50 µL		
	H_3PO_4	20.01	2 µL	2 µL		
	HF	233.15	1.5045 g	1.500 g		
	DIPI					
BE02_27	$Al(iPrO)_3$	187.56	0.1019 g	0.101 g	135	264
	$Mn(OAc)_2.4$	245.09	0.0470 g	0.0467 g		
	H_2O	97.99	50 µL	50 µL		
	H_3PO_4	20.01	2 µL	2 µL		
	HF	233.15	1.5045 g	1.501 g		
	DIPI					
BE02_28	$Al(iPrO)_3$	187.56	0.1000 g	0.0999 g	135	120
	H_3PO_4	97.99	37 µL	37 µL		
	H_2O	18.02	5.6 µL	5.6 µL		
	DIBU	247.15	1.1440 g	1.4401 g		
BE02_29	$Al(iPrO)_3$	187.56	0.1000 g	0.0999 g	135	120
	H_3PO_4	97.99	37 µL	37 µL		
	HF	20.01	2 µL	2 µL		
	H_2O	18.02	4.5 µL	4.5 µL		
	DIBU	247.15	1.440 g	1.401 g		
BE02_30	$Al(iPrO)_3$	187.56	0.1000 g	0.1005 g	135	120
	H_3PO_4	97.99	37 µL	37 µL		
	HF	20.01	4 µL	4 µL		
	H_2O	18.02	3.4 µL	3.4 µL		
	DIBU	247.15	1.440 g	1.4394 g		
BE02_31	$Al(iPrO)_3$	187.56	0.1000 g	0.1001 g	135	120
	H_3PO_4	97.99	37 µL	37 µL		
	HF	20.01	6 µL	6 µL		
	H_2O	18.02	2.3 µL	2.3 µL		
	DIBU	247.15	1.440 g	1.4398 g		
BE02_32	$Al(iPrO)_3$	187.56	0.1000 g	0.1007 g	135	120
	H_3PO_4	97.99	37 µL	37 µL		
	HF	20.01	8 µL	8 µL		
	H_2O	18.02	1.1 µL	1.1 µL		
	DIBU	247.15	1.440 g	1.4402 g		
BE02_33	$Al(iPrO)_3$	187.56	0.1000 g	0.995 g	135	120
	H_3PO_4	97.99	37 µL	37 µL		
	HF	20.01	10 µL	10 µL		
	DIBU	247.15	1.440 g	1.4399 g		
BE02_34	$Al(iPrO)_3$	187.56	0.1000 g	0.1006 g	135	120

	$Mn(OAc)_2.4$	245.09	0.0130 g	0.0121 g		
	H_2O	97.99	37 µL	37 µL		
	H_3PO_4	18.02	5.3 µL	5.3 µL		
	H_2O	247.15	1.4515 g	1.4522 g		
	DIBU					
BE02_35	$Al(iPrO)_3$	187.56	0.1000 g	0.1006 g	135	120
	$Mn(OAc)_2.4$	245.09	0.0130 g	0.0129 g		
	H_2O	97.99	37 µL	37 µL		
	H_3PO_4	20.01	2	2		
	HF	18.02	4.2 µL	4.2 µL		
	H_2O	247.15	1.4515 g	1.4532 g		
	DIBU					
BE02_36	$Al(iPrO)_3$	187.56	0.1000 g	0.1005 g	135	120
	$Mn(OAc)_2.4$	245.09	0.0130 g	0.0125 g		
	H_2O	97.99	37 µL	37 µL		
	H_3PO_4	20.01	4	4		
	HF	18.02	3.15 µL	3.15 µL		
	H_2O	247.15	1.4515 g	1.4515 g		
	DIBU					
BE02_37	$Al(iPrO)_3$	187.56	0.1000 g	0.1002 g	135	120
	$Mn(OAc)_2.4$	245.09	0.0130 g	0.0132 g		
	H_2O	97.99	37 µL	37 µL		
	H_3PO_4	20.01	6	6		
	HF	18.02	2.1 µL	2.1 µL		
	H_2O	247.15	1.4515 g	1.533 g		
	DIBU					
BE02_38	$Al(iPrO)_3$	187.56	0.1000 g	0.998 g	135	120
	$Mn(OAc)_2.4$	245.09	0.0130 g	0.0134 g		
	H_2O	97.99	37 µL	37 µL		
	H_3PO_4	20.01	8	8		
	HF	18.02	3.15 µL	3.15 µL		
	H_2O	247.15	1.4515 g	1.4515 g		
	DIBU					
BE02_39	$Al(iPrO)_3$	187.56	0.1000 g	0.0998 g	135	120
	$Mn(OAc)_2.4$	245.09	0.0130 g	0.0133 g		
	H_2O	97.99	37 µL	37 µL		
	H_3PO_4	20.01	10	10		
	HF	247.15	1.4515 g	1.4541 g		
	DIBU					
BE02_40	$Al(iPrO)_3$	187.56	0.3000 g	0.2995 g	135	120
	$Ni(OAc)_2.4$	248.84	0.1300	0.1307 g		
	H_2O	97.99	125 µL	125 µL		
	H_3PO_4	20.01	6 µL	6 µL		
	HF	233.15	3.964 g	3.9647 g		
	DIPI(Ni)					
BE02_41	$Al(iPrO)_3$	187.56	0.3000 g	0.3003 g	135	120
	$Mn(OAc)_2.4$	245.09	0.0445 g	0.0448 g		
	H_2O	97.99	125 µL	125 µL		
	H_3PO_4	20.01	6 µL	6 µL		
	HF	247.15	4.2093 g	4.2099 g		
	DIBU					
BE02_42	$Al(iPrO)_3$	187.56	0.3000 g	0.3005 g	135	120
		248.84	0.1300	0.1297 g		

	$Ni(OAc)_2.4$	97.99	125 µL	125 µL		
	H_2O	20.01	6 µL	6 µL		
	H_3PO_4	233.15	3.964 g	3.9630 g		
	HF					
	DIPI(Ni)					
BE02_43	$Al(iPrO)_3$	187.56	0.3000 g	0.2997 g	135	120
	$Mn(OAc)_2.4$	245.09	0.0445 g	0.0443 g		
	H_2O	97.99	125 µL	125 µL		
	H_3PO_4	20.01	6 µL	6 µL		
	HF	247.15	4.2093 g	4.2136 g		
	DIBU					
BE02_45	$Al(iPrO)_3$	187.56	0.3000 g	0.2993 g	135	120
	$Ni(OAc)_2.4$	248.84	0.127	0.1271 g		
	H_2O	97.99	125 µL	125 µL		
	H_3PO_4	20.01	6 µL	6 µL		
	HF	233.15	3.964 g	3.968 g		
	DIPI(Ni)					
BE02_46	$Al(iPrO)_3$	187.56	0.3000 g	0.2994 g	135	120
	$Mn(OAc)_2.4$	245.09	0.0445 g	0.0453 g		
	H_2O	97.99	125 µL	125 µL		
	H_3PO_4	20.01	6 µL	6 µL		
	HF	247.15	4.2093 g	4.2011 g		
	DIBU					
BE02_48	$Al(iPrO)_3$	187.56	0.1000 g	0.0997 g	135	72
	H_3PO_4	97.99	67 µL	67 µL		
	HF	20.01	2 µL	2 µL		
	DIBU	247.15	1.1400 g	1.1397 g		
BE02_50	$Al(iPrO)_3$	187.56	0.1000 g	0.0994 g	135	120
	$Co(OAc)_2.4$	249.08	0.0140 g	0.0147 g		
	H_2O	97.99	37 µL	37 µL		
	H_3PO_4	20.01	2 µL	2 µL		
	HF	247.15	1.4512 g	1.4505 g		
	DIBU					
BE02_51	$Al(iPrO)_3$	187.56	0.3000 g	0.2992 g	135	120
	$Co(OAc)_2.4$	249.08	0.0420 g	0.0423 g		
	H_2O	97.99	111 µL	111 µL		
	H_3PO_4	20.01	24 µL	24 µL		
	HF	247.15	4.3500 g	4.3594 g		
	DIBU					
BE02_52	$Al(iPrO)_3$	187.56	0.3000 g	0.2997 g	135	120
	$Co(OAc)_2.4$	249.08	0.0420 g	0.0421 g		
	H_2O	97.99	111 µL	111 µL		
	H_3PO_4	20.01	24 µL	24 µL		
	HF	247.15	4.3500 g	4.3519 g		
	DIBU					
BE02_53	$Al(iPrO)_3$	187.56	0.3000 g	0.3004 g	135	120
	$Co(OAc)_2.4$	249.08	0.0420 g	0.0429 g		
	H_2O	97.99	111 µL	111 µL		
	H_3PO_4	20.01	24 µL	24 µL		
	HF	247.15	4.3500 g	4.3517 g		
	DIBU					
BE02_55	$Al(iPrO)_3$	187.56	0.3000 g	0.2992 g	135	120
		245.09	0.0445 g	0.0444 g		

	$Mn(OAc)_2.4$	97.99	111 µL	111 µL		
	H_2O	20.01	6 µL	6 µL		
	H_3PO_4	247.15	4.3500 g	4.3541 g		
	HF					
	DIBU					
BE02_58	$Al(iPrO)_3$	187.56	0.1000 g	0.0994 g	125	120
	H_3PO_4	97.99	67 µL	67 µL		
	HF	20.01	2 µL	2 µL		
	DIBU	247.15	1.1400 g	1.1451 g		
BE02_59	$Al(iPrO)_3$	187.56	0.1000 g	0.0993 g	100	120
	H_3PO_4	97.99	67 µL	67 µL		
	HF	20.01	2 µL	2 µL		
	DIBU	247.15	1.1400 g	1.1430 g		
BE02_60	$Al(iPrO)_3$	187.56	0.1000 g	0.0995 g	125	120
	H_3PO_4	97.99	67 µL	67 µL		
	HF	20.01	2 µL	2 µL		
	DIPI (I)	247.15	1.2000 g	1.196 g		
BE02_61	$Al(iPrO)_3$	187.56	0.1000 g	0.1008 g	100	120
	H_3PO_4	97.99	67 µL	67 µL		
	HF	20.01	2 µL	2 µL		
	DIPI (I)	247.15	1.2000 g	1.1970 g		
BE02_63	$Al(iPrO)_3$	187.56	0.1000 g	0.100 g	80	72
	H_3PO_4	97.99	67 µL	67 µL		
	HF	20.01	2 µL	2 µL		
	DIBU	247.15	1.1400 g	1.134 g		
BE02_64	$Al(iPrO)_3$	187.56	0.1000 g	0.099 g	100	20
	H_3PO_4	97.99	67 µL	67 µL		
	HF	20.01	2 µL	2 µL		
	DIBU	247.15	1.1400 g	1.131 g		
BE02_65	$Al(iPrO)_3$	187.56	0.3000 g	0.2992 g	135	120
	$Mn(OAc)_2.4$	245.09	0.0445 g	0.0445 g		
	H_2O	97.99	111 µL	111 µL		
	H_3PO_4	20.01	6 µL	6 µL		
	HF	247.15	4.3500 g	4.3488 g		
	DIBU					
BE02_69	$Al(iPrO)_3$	187.56	0.1000 g	0.1001 g	100	48
	H_3PO_4	97.99	67 µL	67 µL		
	HF	20.01	2 µL	2 µL		
	DIBU	247.15	1.1400 g	1.1449 g		
BE02_70	$Al(iPrO)_3$	187.56	0.1000 g	0.0999 g	100	120
	H_3PO_4	97.99	67 µL	67 µL		
	HF	20.01	2 µL	2 µL		
	DIBU	247.15	1.1400 g	1.1470 g		
BE02_71	$Al(iPrO)_3$	187.56	0.1000 g	0.1001 g	75	72
	H_3PO_4	97.99	67 µL	67 µL		
	HF	20.01	2 µL	2 µL		
	DIBU	247.15	1.1400 g	1.1495 g		
BE02_72	$Al(iPrO)_3$	187.56	0.1000 g	0.1009 g	100	120
	H_3PO_4	97.99	67 µL	67 µL		
	HF	20.01	2 µL	2 µL		
	DIPI	247.15	1.2000 g	1.2036 g		
BE02_73	$Al(iPrO)_3$	187.56	0.1000 g	0.1021 g	100	72
	H_3PO_4	97.99	67 µL	67 µL		

	HF	20.01	2 µL	2 µL		
	DIPI	247.15	1.2000 g	1.1995 g		
BE02_74	$Al(iPrO)_3$	187.56	0.1000 g	0.1009 g	100	120
	H_3PO_4	97.99	67 µL	67 µL		
	HF	20.01	2 µL	2 µL		
	DIPI	247.15	1.200 g	1.2036 g		
BE02_75	$Al(iPrO)_3$	187.56	0.1000 g	0.1004 g	135	120
	$Mn(OAc)_2.4$	245.09	0.0130 g	0.0133 g		
	H_2O	97.99	37 µL	37 µL		
	H_3PO_4	18.02	5.3 µL	5.3 µL		
	H_2O	247.15	1.4515 g	1.4542 g		
	DIBU					
BE02_76	$Al(iPrO)_3$	187.56	0.1000 g	0.1004 g	135	120
	$Mn(OAc)_2.4$	245.09	0.0130 g	0.0133 g		
	H_2O	97.99	37 µL	37 µL		
	H_3PO_4	18.02	5.3 µL	5.3 µL		
	H_2O	247.15	1.4515 g	1.4542 g		
	DIBU					
BE02_77	$Al(iPrO)_3$	187.56	0.1000 g	0.1000 g	135	120
	H_3PO_4	97.99	67 µL	67 µL		
	HF	20.01	10 µL	10 µL		
	DIPI	247.15	1.2000 g	1.2040 g		
BE02_78	$Al(iPrO)_3$	187.56	0.1000 g	0.1007 g	135	120
	H_3PO_4	97.99	67 µL	67 µL		
	HF	20.01	10 µL	10 µL		
	DIBU	247.15	1.1400 g	1.1423 g		

Table A.3 Chapter 3 synthetic details

Sample ID	Reagents	Molar ratio (mmol)	Formula weight (g/mol)	Target weight (g)	Used weight/ volume	Temperature (°C)	Time (hours)
BE02_79A	$AgNO_3$ 2,4'-bipy MilliQ H_2O	1 1	169.87 156.19	0.1699 0.1562	0.1687 g 0.1570 g 10 mL	RT	24
BE02_79B	$AgNO_3$ 2,4'-bipy MilliQ H_2O	1 1	169.87 156.19	0.1699 0.1562	0.1710 g 0.1571 g 10 mL	150	72
BE02_79C	$AgNO_3$ 2,4'-bipy MilliQ H_2O	1 1	169.87 156.19	0.1699 0.1562	0.1700 g 0.1576 g 10 mL	70	1
BE02_80	$AgNO_3$ 2,4'-bipy MilliQ H_2O	1 1	169.87 156.19	0.1699 0.1562	0.1702 g 0.1568 g 10 mL	150	24
BE02_82A	$AgNO_3$ 2,4'-bipy MilliQ H_2O	0.5 1.01	169.87 156.19	0.0849 0.1699	0.0854 g 0.1710 g 10 mL	Cycling condition	
BE02_82B	$AgNO_3$ 2,4'-bipy MilliQ H_2O	1.10 0.55	169.87 156.19	0.1869 0.0849	0.1872 g 0.0853 g 10 mL	Cycling condition	
BE02_83A	$AgNO_3$ 2,4'-bipy MilliQ H_2O	0.5 0.5	169.87 156.19	0.0849 0.0781	0.0853 g 0.0772 g 10 mL	Cycling condition	
BE02_83B	$AgNO_3$ 2,4'-bipy MilliQ H_2O	1 1	169.87 156.19	0.1699 0.1562	0.1707 g 0.1565 g 10 mL	Cycling condition	
BE02_84A	$AgNO_3$ 2,4'-bipy MilliQ H_2O	1 1	169.87 156.19	0.1699 0.1562	0.1690 g 0.1575 g 10 mL	100	120
BE02_84B	$AgNO_3$ 2,4'-bipy MilliQ H_2O	1 1	169.87 156.19	0.1699 0.1562	0.1698 g 0.1560 g 10 mL	119	120
BE02_85A	$AgNO_3$ 2,4'-bipy MilliQ H_2O	1 1	169.87 156.19	0.1699 0.1562	0.1701 g 0.1575 g 10 mL	150	120
BE02_85B	$AgNO_3$ 2,4'-bipy MilliQ H_2O	1 1	169.87 156.19	0.1699 0.1562	0.1701 0.1575 10	136	120
BE02_86	$AgNO_3$ 2,4'-bipy MilliQ H_2O	1 1	169.87 156.19	0.1699 0.1562	0.170 g 0.156 g 10 mL	150 Slow cooling 0.1 °C/min	120
BE02_87A	$AgNO_3$ 2,4'-bipy MilliQ H_2O DMF	1 1	169.87 156.19	0.1699 0.1562	0.169 g 0.156 g 5 mL 5 mL	150 Slow cooling 0.1 °C/min	120
BE02_87A	$AgNO_3$ 2,4'-bipy MilliQ H_2O DMF	1 1	169.87 156.19	0.1699 0.1562	0.170 g 0.156 g 9.5 mL 0.5 mL	150 Slow cooling 0.1 °C/min	120
BE02_88A	$AgNO_3$	1	169.87	0.1699	0.170 g	150	120

	2,4'-bipy MilliQ H_2O Acetonitrile	1	156.19	0.1562	0.156 g 5 mL 5 mL	Slow cooling 0.1 °C/min	
BE02_88B	$AgNO_3$ 2,4'-bipy MilliQ H_2O Acetonitrile	1 1	169.87 156.19	0.1699 0.1562	0.170 g 0.156 g 9.5 mL 0.5 mL	150 Slow cooling 0.1 °C/min	120
BE02_89A	$AgNO_3$ 2,4'-bipy MilliQ H_2O Acetonitrile	1 1	169.87 156.19	0.1699 0.1562	0.1693 g 0.1568 g 5 mL 5 mL	Cyclic condition	
BE02_89B	$AgNO_3$ 2,4'-bipy MilliQ H_2O Acetonitrile	1 1	169.87 156.19	0.1696 0.1566	0.170 g 0.156 g 9.5 mL 0.5 mL	Cyclic condition	
BE02_90	$AgNO_3$ 2,4'-bipy MilliQ H_2O	1 1	169.87 156.19	0.1699 0.1562	0.1691 g 0.1562 g 10 mL	150 Slow cooling 0.1 °C/min	120
BE02_100A	SLUG-53iso $KMnO_4$ MilliQ H_2O	0.2 0.2	326.06 158.04	0.0720 0.0318	0.0725 g 0.0318 g 10 mL	RT	24
BE02_100B	SLUG-53iso $NaReO_4$ MilliQ H_2O	0.2 0.2	326.06 273.14	0.0720 0.0546	0.0724 g 0.0552 g 10 mL	RT	24
BE02_101A	SLUG-53iso KCl MilliQ H_2O	0.2 0.2	326.06 74.5	0.0720 0.0149	0.0726 g 0.0151 g 10 mL	RT	24
BE02_101B	SLUG-53iso $NaClO_4.H_2O$ MilliQ H_2O	0.2 0.2	326.06 140.46	0.0720 0.0281	0.0724 g 0.0282 g 10 mL	RT	24
BE02_102A	$AgNO_3$ 2,4'-bipy MilliQ H_2O	1 1	169.87 156.19	0.1699 0.1562	0.170 g 0.156 g 10 mL	150	120
BE02_102B	$AgNO_3$ 2,4'-bipy MilliQ H_2O	1 1	169.87 156.19	0.1699 0.1562	0.170 g 0.156 g 10 mL	150	120
BE02_102C	$AgNO_3$ 2,4'-bipy MilliQ H_2O	1 1	169.87 156.19	0.1699 0.1562	0.169 g 0.157 g 10 mL	150	120
BE02_104A	SLUG-53iso KBr MilliQ H_2O	0.2 0.2	326.06 140.46	0.0720 0.0238	0.0724 g 0.0243 g 10 mL	RT	24

BE02_104B	SLUG-53iso NaI MilliQ H_2O	0.2 0.2	326.06 140.46	0.0720 0.0300	0.0718 g 0.0308 g 10 mL	RT	24
BE02_104C	SLUG-53iso K_2CrO_4 MilliQ H_2O	0.2 0.1	326.06 194.19	0.0720 0.0194	0.0722 g 0.0200 g 10 mL	RT	24
BE02_106	SLUG-53iso KCl KBr MilliQ H_2O	0.2 0.115 0.115	326.06 194.19	0.0843 0.0086 0.0137	0.0843 g 0.0086 g 0.0136 10 mL	RT	24
BE02_107	$AgNO_3$ 2,4'-bipy MilliQ H_2O	0.5 0.5	169.87 156.19	0.0849 0.0785	0.0849 g 0.0787 g 10 mL	145	24
BE02_108	$AgNO_3$ 2,4'-bipy MilliQ H_2O	0.5 0.5	169.87 156.19	0.0849 0.0785	0.0844 g 0.0784 g 10 mL	145	24
BE02_109	$AgNO_3$ 2,4'-bipy MilliQ H_2O	0.5 0.5	169.87 156.19	0.0849 0.0785	0.0850 g 0.0797 g 10 mL	145	24
BE02_110	$AgNO_3$ 2,4'-bipy MilliQ H_2O	0.5 0.5	169.87 156.19	0.0849 0.0785	0.0844 g 0.0791 g 10 mL	145	24
BE02_111	$AgNO_3$ 2,4'-bipy MilliQ H_2O	0.5 0.5	169.87 156.19	0.0849 0.0785	0.0846 g 0.0783 g 10 mL	145	24
BE02_113	$AgNO_3$ 2,4'-bipy MilliQ H_2O	4 1	169.87 156.19	0.6795 0.1562	0.670 g 0.156 g 10 mL	145 Slow cooling 0.1 °C/min	24
BE02_114	$AgC_2H_3O_2$ 2,4'-bipy MilliQ H_2O	1 1	166.19 156.19	0.6795 0.1562	0.670 g 0.156 g 10 mL	145 Slow cooling 0.1 °C/min	24
BE02_115	$Zn(NO_3)_2.6H_2O$ 2,4'-bipy MilliQ H_2O	1 1	297.48 156.19	0.2975 0.1562	0.295 g 0.157 g 10 mL	145 Slow cooling 0.1 °C/min	24
BE02_116	$AgNO_3$ 2,4'-bipy MilliQ H_2O	4 1	169.87 156.19	0.6795 0.1562	0.680 g 0.151 g 10 mL	185	24
BE02_117A	$AgNO_3$ 2,4'-bipy MilliQ H_2O	4 1	169.87 156.19	0.6795 0.1562	0.675 g 0.156 g 10 mL	145	24
BE02_117B	$AgNO_3$ 2,4'-bipy MilliQ H_2O	4 1	169.87 156.19	0.6795 0.1562	0.677 g 0.157 g 10 mL	145	24
BE02_117C	$AgNO_3$ 2,4'-bipy MilliQ H_2O	4 1	169.87 156.19	0.6795 0.1562	0.6800 g 0.1555 g 10 mL	145	24
BE02_117D	$AgNO_3$ 2,4'-bipy MilliQ H_2O	4 1	169.87 156.19	0.6795 0.1562	0.6798 g 0.1558 g 10 mL	145	24

BE02_117E	$AgNO_3$ 2,4'-bipy MilliQ H_2O	4 1	169.87 156.19	0.6795 0.1562	0.6785 g 0.1558 g 10 mL	145	24
BE02_118A	SLUG-53 $KMnO_4$ MilliQ H_2O	0.2 0.2	326.06 158.04	0.0720 0.0318	0.072 g 0.032 g 10 mL	RT	24
BE02_118B	SLUG-53 K_2CrO_4 MilliQ H_2O	0.2 0.2	326.06 194.01	0.072 0.039	0.073 g 0.040 g 10 mL	RT	24
BE02_120A	SLUG-53 $C_4H_6O_4$ MilliQ H_2O	0.2 0.1	326.06 118.09	0.0720 0.0118	0.072 g 0.011 g 10 mL	RT	24
BE02_120B	SLUG-53 $C_4H_4Na_2O_4$ MilliQ H_2O	0.2 0.1	326.06 162.05	0.0720 0.0162	0.070 g 0.016 g 10 mL	RT	24
BE02_121A	SLUG-53 $C_8H_6O_4$ MilliQ H_2O	0.2 0.1	326.06 166.13	0.0720 0.0166	0.073 g 0.017 g 10 mL	RT	24
BE02_121B	SLUG-53 $C_7H_4Na_2O_4$ MilliQ H_2O	0.2 0.1	326.06 210.09	0.0720 0.0219	0.072 g 0.022 g 10 mL	RT	24
BE02_122A	BE02_117 D $C_5H_8O_4$ MilliQ H_2O	0.2 0.1	326.06 132.11	0.0720 0.0132	0.071 g 0.015 g 10 mL	RT	24
BE02_122B	BE02_117 D $C_5H_6Na_2O_4$ MilliQ H_2O	0.2 0.1	326.06 176.08	0.0720 0.0176	0.071 g 0.018 g 10 mL	RT	24
BE02_123	$AgNO_3$ 2,4'-bipy MilliQ H_2O	1.5 1	169.87 156.19	0.255 0.1562	0.257 g 0.156 g 10 mL	145	24
BE02_124	$AgNO_3$ 2,4'-bipy MilliQ H_2O	2 1	169.87 156.19	0.340 0.1562	0.342 g 0.154 g 10 mL	145	24
BE02_125	$AgNO_3$ 2,4'-bipy MilliQ H_2O	2.5 1	169.87 156.19	0.425 0.1562	0.423 g 0.155 g 10 mL	145	24
BE02_126	$AgNO_3$ 2,4'-bipy MilliQ H_2O	3 1	169.87 156.19	0.510 0.1562	0.509 g 0.156 g 10 mL	145	24
BE02_127	$AgNO_3$ 2,4'-bipy MilliQ H_2O	3.5 1	169.87 156.19	0.595 0.1562	0.594 g 0.154 g 10 mL	145	24
BE02_128	$ZnC_2H_3O_2$ 2,4'-bipy MilliQ H_2O	4 1	219.50 156.19	0.878 0.1562	0.877 g 0.154 g 10 mL	150 Slow cooling 0.1 °C/min	120
BE02_129	$ZnC_2H_3O_2$ 2,4'-bipy MilliQ H_2O	1 1	219.50 156.19	0.2195 0.1562	0.218 g 0.154 g 10 mL	150 Slow cooling 0.1 °C/min	120

BE02_132	$AgNO_3$ 2,4'-bipy HNO_3 MilliQ H_2O	1 1	169.87 156.19 63.01	0.510 0.1562	0.509 g 0.156 g 2.42 µL 10 mL	Cycling condition	
BE02_133	$Cu(NO_3)_2.$ $2.5H_2O$ 2,4'-bipy MilliQ H_2O	4 1	232.59 156.19	0.9304 0.1562	0.933 g 0.154 g 10 mL	Cycling condition	
BE02_136A	$AgNO_3$ 2,4'-bipy MilliQ H_2O	4 1	169.87 156.19	0.6795 0.1562	0.6744 g 0.1554 g 10 mL	RT	24
BE02_136B	$AgNO_3$ 2,4'-bipy MilliQ H_2O	4 1	169.87 156.19	0.6795 0.1562	0.6751 g 0.1564 g 10 mL	RT	24
BE02_136C	$AgNO_3$ 2,4'-bipy MilliQ H_2O	4 1	169.87 156.19	0.6795 0.1562	0.6745 g 0.1557 g 10 mL	RT	24
BE02_137A	$AgNO_3$ 2,4'-bipy MilliQ H_2O	2 1	169.87 156.19	0.3397 0.1562	0.3381 g 0.1570 g 10 mL	RT	24
BE02_137B	$AgNO_3$ 2,4'-bipy MilliQ H_2O	2 1	169.87 156.19	0.3397 0.1562	0.3381 g 0.1571 g 10 mL	RT	24
BE02_137C	$AgNO_3$ 2,4'-bipy MilliQ H_2O	2 1	169.87 156.19	0.3397 0.1562	0.3377 g 0.1567 g 10 mL	RT	24
BE02_137D	$AgNO_3$ 2,4'-bipy MilliQ H_2O	2 1	169.87 156.19	0.3397 0.1562	0.3371 g 0.1564 g 10 mL	RT	24
BE02_137E	$AgNO_3$ 2,4'-bipy MilliQ H_2O	2 1	169.87 156.19	0.3397 0.1562	0.3374 g 0.1573 g 10 mL	RT	24
BE02_137D	$AgNO_3$ 2,4'-bipy MilliQ H_2O	2 1	169.87 156.19	0.3397 0.1562	0.3370 g 0.1565 g 10 mL	RT	24
BE02_137F	$AgNO_3$ 2,4'-bipy MilliQ H_2O	2 1	169.87 156.19	0.3397 0.1562	0.3370 g 0.1565 g 10 mL	RT	24
BE02_140	$AgNO_3$ 2,4'-bipy MilliQ H_2O	20 5	169.87 156.19	3.3749 0.7809	3.3747 g 0.7809 g 50 mL	RT	1
BE02_142	SLUG-53 $NaReO_4$ MilliQ H_2O	0.2 0.2	326.06 273.14	0.0652 0.0546	0.0655 g 0.0551 g 10 mL	RT	24
BE02_143_1	SLUG-53 $NaReO_4$ MilliQ H_2O	0.2 0.2	326.06 273.14	0.0652 0.0546	0.0653 g 0.0543 g 10 mL	RT	1
BE02_143_2	SLUG-53 $NaReO_4$ MilliQ H_2O	0.2 0.2	326.06 273.14	0.0652 0.0546	0.0654 g 0.0542 g 50 mL	RT	2
BE02_143_4	SLUG-53 $NaReO_4$ MilliQ H_2O	0.2 0.2	326.06 273.14	0.0652 0.0546	0.0653 g 0.0540 g 50 mL	RT	4

BE02_143_8	SLUG-53 $NaReO_4$ MilliQ H_2O	0.2 0.2	326.06 273.14	0.0652 0.0546	0.0648 g 0.0544 g 10 mL	RT	8
BE02_143_12	SLUG-53 $NaReO_4$ MilliQ H_2O	0.2 0.2	326.06 273.14	0.0652 0.0546	0.0653 g 0.0547 g 10 mL	RT	12
BE02_143_16	SLUG-53 $NaReO_4$ MilliQ H_2O	0.2 0.2	326.06 273.14	0.0652 0.0546	0.0654 g 0.0543g 10 mL	RT	16
BE02_143_20	SLUG-53 $NaReO_4$ MilliQ H_2O	0.2 0.2	326.06 273.14	0.0652 0.0546	0.0649 g 0.0546 g 10 mL	RT	20
BE02_143_24	SLUG-53 $NaReO_4$ MilliQ H_2O	0.2 0.2	326.06 273.14	0.0652 0.0546	0.0648 g 0.0547 g 10 mL	RT	24
BE02_144	$AgNO_3$ 2,4'-bipy MilliQ H_2O	20 5	169.87 156.19	3.3749 0.7809	3.3750 g 0.7809 g 50 mL	70	1
BE03_01A	$AgNO_3$ 2,4'-bipy MilliQ H_2O	4 1	169.87 156.19	0.6795 0.1562	0.6797 g 0.1565 g 10 mL	145	24
BE03_01B	$AgNO_3$ 2,4'-bipy MilliQ H_2O	4 1	169.87 156.19	0.6795 0.1562	0.6790 g 0.1570 g 10 mL	145	24
BE03_01C	$AgNO_3$ 2,4'-bipy MilliQ H_2O	4 1	169.87 156.19	0.6795 0.1562	0.6794 g 0.1565 g 10 mL	145	24
BE03_01D	$AgNO_3$ 2,4'-bipy MilliQ H_2O	4 1	169.87 156.19	0.6795 0.1562	0.6799 g 0.1570 g 10 mL	145	24
BE03_01E	$AgNO_3$ 2,4'-bipy MilliQ H_2O	4 1	169.87 156.19	0.6795 0.1562	0.6792 g 0.1568 g 10 mL	145	24
BE03_01F	$AgNO_3$ 2,4'-bipy MilliQ H_2O	4 1	169.87 156.19	0.6795 0.1562	0.6792 g 0.1561 g 10 mL	145	24
BE03_02A	SLUG-53p $C_4H_6O_4$ H_2O	0.2 0.1	326.06 118.09	0.0652 0.0118	0.0651 g 0.0114 10 mL	RT	24
BE03_02B	SLUG-53p $C_3H_4O_4$ H_2O	0.2 0.1	326.06 104.6	0.0652 0.0104	0.0650 g 0.0101 g 10 mL	RT	24
BE03_02C	SLUG-53p $C_5H_8O_4$ H_2O	0.2 0.1	326.06 132.11	0.0652 0.0132	0.0654 g 0.0132 g 10 mL	RT	24
BE03_03A	SLUG-53p $C_6H_{10}O_4$ H_2O	0.2 0.1	326.06 146.14	0.0652 0.0146	0.0654 g 0.0143 g 10 mL	RT	24
BE03_03B	SLUG-53p $NaReO_4$ H_2O	0.2 0.2	326.06 273.19	0.0652 0.0546	0.0655 g 0.0550 g 10 mL	RT	24
BE03_03C	SLUG-53p $NaBF_4$	0.2 0.2	326.06 109.79	0.0652 0.0220	0.0654 g 0.0228 g	RT	24

	H_2O				10 mL		
BE03_04A	SLUG-53p	0.2	326.06	0.0652	0.0654 g	RT	24
	$NaMnO_4$	0.2	159.94	0.0327	0.0326 g		
	H_2O				10 mL		
BE03_04B	SLUG-53p	0.2	326.06	0.0652	0.0651 g	RT	24
	$NaClO_4$	0.2	140.46	0.0281	0.0270 g		
	H_2O				10 mL		
BE03_04C	SLUG-53p	0.2	326.06	0.0652	0.0654 g	RT	24
	Na_2CrO_4	0.1	161.97	0.0162	0.0162 g		
	H_2O				10 mL		
BE03_05A	SLUG-53p	0.2	326.06	0.0652	0.0652 g	RT	24
	KBr	0.2	119.00	0.0238	0.0238 g		
	H_2O				10 mL		
BE03_05B	SLUG-53p	0.2	326.06	0.0652	0.0656 g	RT	24
	NaCl	0.2	58.44	0.0117	0.0115 g		
	H_2O				10 mL		
BE03_05C	SLUG-53p	0.2	326.06	0.0652	0.0656 g	RT	24
	NaI	0.2	149.89	0.0300	0.0302 g		
	H_2O				10 mL		
BE03_06A	SLUG-53	0.2	326.06	0.0652	0.0656 g	RT	24
	$C_4H_6O_4$	0.1	118.09	0.0118	0.0118		
	H_2O				10 mL		
BE03_06B	SLUG-53	0.2	326.06	0.0652	0.0653 g	RT	24
	$C_3H_4O_4$	0.1	104.6	0.0104	0.0104 g		
	H_2O				10 mL		
BE03_06C	SLUG-53	0.2	326.06	0.0652	0.0656 g	RT	24
	$C_5H_8O_4$	0.1	132.11	0.0132	0.0133 g		
	H_2O				10 mL		
BE03_07A	SLUG-53	0.2	326.06	0.0652	0.0653 g	RT	24
	$C_6H_{10}O_4$	0.1	146.14	0.0146	0.0149 g		
	H_2O				10 mL		
BE03_07B	SLUG-53	0.2	326.06	0.0652	0.0652 g	RT	24
	$NaReO_4$	0.2	273.19	0.0546	0.0546 g		
	H_2O				10 mL		
BE03_07C	SLUG-53	0.2	326.06	0.0652	0.0652 g	RT	24
	$NaBF_4$	0.2	109.79	0.0220	0.0227 g		
	H_2O				10 mL		
BE03_08A	SLUG-53	0.2	326.06	0.0652	0.0652 g	RT	24
	$NaMnO_4$	0.2	159.94	0.0327	0.0320 g		
	H_2O				10 mL		
BE03_08B	SLUG-53	0.2	326.06	0.0652	0.0652 g	RT	24
	$NaClO_4$	0.2	140.46	0.0281	0.0280 g		
	H_2O				10 mL		
BE03_08C	SLUG-53	0.2	326.06	0.0652	0.0654 g	RT	24
	Na_2CrO_4	0.1	161.97	0.0162	0.0164 g		
	H_2O				10 mL		
BE03_09A	SLUG-53	0.2	326.06	0.0652	0.0650 g	RT	24
	KBr	0.2	119.00	0.0238	0.0236 g		
	H_2O				10 mL		
BE03_09B	SLUG-53	0.2	326.06	0.0652	0.0656 g	RT	24
	NaCl	0.2	58.44	0.0117	0.0124 g		
	H_2O				10 mL		
BE03_09C	SLUG-53	0.2	326.06	0.0652	0.0658 g	RT	24

	NaI H_2O	0.2	149.89	0.0300	0.0300 g 10 mL		
BE03_10A	$AgNO_3$ 2,4'-bipy MilliQ H_2O	4 1	169.87 156.19	0.6795 0.1562	0.6793 g 0.1555 g 10 mL	145	24
BE03_10B	$AgNO_3$ 2,4'-bipy MilliQ H_2O	4 1	169.87 156.19	0.6795 0.1562	0.6797 g 0.1573 g 10 mL	145	24
BE03_10C	$AgNO_3$ 2,4'-bipy MilliQ H_2O	4 1	169.87 156.19	0.6795 0.1562	0.6798 g 0.1560 g 10 mL	145	24
BE03_10D	$AgNO_3$ 2,4'-bipy MilliQ H_2O	4 1	169.87 156.19	0.6795 0.1562	0.6798 g 0.1566 g 10 mL	145	24
BE03_11A	SLUG-53p $KMnO_4$ H_2O	0.2 0.2	326.06 158.04	0.0652 0.0318	0.0658 g 0.0315 g 10 mL	RT	24
BE03_11B	SLUG-53 $C_3H_4O_4$ H_2O	0.4 0.2	326.06 104.06	0.130 0.0208	0.0658 g 0.0208 g 10 mL	RT	24
BE03_11C	SLUG-53 $NaClO_4$ H_2O	0.6 0.6	326.06 140.46	0.1956 0.0843	0.1950 g 0.0861 g 10 mL	RT	24
BE03_11D	SLUG-53 $Na_2MoO_4.2H_2O$ H_2O	0.2 0.1	326.06 241.9	0.0652 0.0242	0.0656 g 0.0241 g 10 mL	RT	24
BE03_11E	SLUG-53p $Na_2MoO_4.2H_2O$ H_2O	0.2 0.1	326.06 241.9	0.0652 0.0242	0.0658 g 0.0246 g 10 mL	RT	24
BE03_14A	SLUG-53 $Na_2MoO_4.2H_2O$ H_2O	0.2 0.1	326.06 241.9	0.0652 0.0242	0.0661 g 0.0248 g 10 mL	RT	20
BE03_14B	SLUG-53p $Na_2MoO_4.2H_2O$ H_2O	0.2 0.1	326.06 241.9	0.0652 0.0242	0.0653 g 0.0248 g 10 mL	RT	20
BE03_15A	$AgNO_3$ 2,4'-bipy MilliQ H_2O	6 2	169.87 156.19	1.0192 0.3124	1.0146 g 0.3134 g 20 mL	80	1.5
BE03_15B	$AgNO_3$ 2,4'-bipy MilliQ H_2O	6 2	169.87 156.19	1.0192 0.3124	1.0185 g 0.3125 g 20 mL	80	10
BE03_16A	$AgNO_3$ 2,4'-bipy MilliQ H_2O	4 1	169.87 156.19	0.6795 0.1562	0.6799 g 0.1569 g 10 mL	145	24
BE03_16B	$AgNO_3$ 2,4'-bipy MilliQ H_2O	4 1	169.87 156.19	0.6795 0.1562	0.6799 g 0.1571 g 10 mL	145	24
BE03_16C	$AgNO_3$ 2,4'-bipy	4 1	169.87 156.19	0.6795 0.1562	0.6705 g 0.1571 g	145	24

	MilliQ H_2O				10 mL		
BE03_16D	$AgNO_3$	4	169.87	0.6795	0.6806 g	145	24
	2,4'-bipy	1	156.19	0.1562	0.1564 g		
	MilliQ H_2O				10 mL		
BE03_16E	$AgNO_3$	4	169.87	0.6795	0.6788 g	145	24
	2,4'-bipy	1	156.19	0.1562	0.1564 g		
	MilliQ H_2O				10 mL		
BE03_16F	$AgNO_3$	4	169.87	0.6795	0.6808 g	145	24
	2,4'-bipy	1	156.19	0.1562	0.1567 g		
	MilliQ H_2O				10 mL		
BE03_16G	$AgNO_3$	4	169.87	0.6795	0.6791 g	145	24
	2,4'-bipy	1	156.19	0.1562	0.1566 g		
	MilliQ H_2O				10 mL		
BE03_16H	$AgNO_3$	4	169.87	0.6795	0.6796 g	145	24
	2,4'-bipy	1	156.19	0.1562	0.1559 g		
	MilliQ H_2O				10 mL		
BE03_16I	$AgNO_3$	4	169.87	0.6795	0.6804 g	145	24
	2,4'-bipy	1	156.19	0.1562	0.1563 g		
	MilliQ H_2O				10 mL		
BE03_16J	$AgNO_3$	4	169.87	0.6795	0.6796 g	145	24
	2,4'-bipy	1	156.19	0.1562	0.1569 g		
	MilliQ H_2O				10 mL		
BE03_17	SLUG-53	0.4	326.06	0.1304	0.1308 g	RT	23
	$NaReO_4$	0.4	273.19	0.1093	0.1094 g		
	H_2O				20 mL		
BE03_18A	SLUG-53	0.4	326.06	0.1304	0.1308 g	RT	24
	$NaReO_4$	0.4	273.19	0.1093	0.1092 g		
	H_2O				20 mL		
BE03_18B	SLUG-53	0.4	326.06	0.1304	0.1306 g	RT	24
	$NaReO_4$	0.4	273.19	0.1093	0.1095 g		
	H_2O				20 mL		
BE03_18C	SLUG-53	0.4	326.06	0.1304	0.1306 g	RT	24
	$NaReO_4$	0.4	273.19	0.1093	0.1097 g		
	H_2O				20 mL		
BE03_19	SLUG-54	0.13	514.26	0.685	0.689 g	RT	24
	$AgNO_3$	40	169.87	6.795	6.7890 g		
	H_2O				20 mL		
BE03_20A	$AgNO_3$	4	169.87	0.6795	0.6771 g	145	24
	2,4'-bipy	1	156.19	0.1562	0.1560 g		
	MilliQ H_2O				10 mL		
BE03_20B	$AgNO_3$	4	169.87	0.6795	0.6703 g	145	24
	2,4'-bipy	1	156.19	0.1562	0.1554 g		
	MilliQ H_2O				10 mL		
BE03_20C	$AgNO_3$	4	169.87	0.6795	0.6725 g	145	24
	2,4'-bipy	1	156.19	0.1562	0.1571 g		
	MilliQ H_2O				10 mL		
BE03_20D	$AgNO_3$	4	169.87	0.6795	0.6796 g	145	24
	2,4'-bipy	1	156.19	0.1562	0.1563 g		
	MilliQ H_2O				10 mL		
BE03_20E	$AgNO_3$	4	169.87	0.6795	0.6753 g	145	24
	2,4'-bipy	1	156.19	0.1562	0.1571 g		
	MilliQ H_2O				10 mL		
BE03_20F	$AgNO_3$	4	169.87	0.6795	0.6754 g	145	24

	2,4'-bipy MilliQ H_2O	1	156.19	0.1562	0.1565 g 10 mL		
BE03_21	SLUG-54 $AgNO_3$ H_2O	0.076 15.2	514.26 169.87	0.0390 2582	0.0390 g 2.57 g 20 mL	80	1
BE03_22	SLUG-53p $NaReO_4$ H_2O	0.4 0.4	326.06 273.19	0.1304 0.1093	0.1308 g 0.1093 g 20 mL	RT	24
BE03_23A	SLUG-53 $NaReO_4$ Na_2SO_4 H_2O	0.4 0.4 20	326.06 273.19 142.04	0.1304 0.1093 2.8408	0.1306 g 0.1095 g 2.8393 20 mL	RT	24
BE03_23B	SLUG-53 $NaReO_4$ Na_2SO_4 H_2O	0.4 0.4 80	326.06 273.19 142.04	0.1304 0.1093 11.36	0.1306 g 0.1095 g 2.8393 50 mL	RT	24
BE03_24A	SLUG-53 $NaReO_4$ H_2O	0.2 0.2	326.06 273.19	0.0652 0.0546	0.0654 g 0.0546 g 10 mL	145	24
BE03_24B	SLUG-53 $NaReO_4$ H_2O	0.2 0.2	326.06 273.19	0.0652 0.0546	0.0659 g 0.0547 g 10 mL	145	24
BE03_24C	SLUG-53 $NaReO_4$ H_2O	0.2 0.2	326.06 273.19	0.0652 0.0546	0.0656 g 0.0558 g 10 mL	145	24
BE03_24D	SLUG-53 $NaReO_4$ H_2O	0.2 0.2	326.06 273.19	0.0652 0.0546	0.0660 g 0.0548 g 10 mL	145	24
BE03_24E	SLUG-53 $NaReO_4$ H_2O	0.2 0.2	326.06 273.19	0.0652 0.0546	0.0658 g 0.0558 g 10 mL	145	24
BE03_25A	SLUG-53 $NaReO_4$ Na_2SO_4 H_2O	0.4 0.4 20	326.06 273.19 142.04	0.1304 0.1093 2.8408	0.1306 g 0.1092 g 2.8316 20 mL	RT	24
BE03_25B	SLUG-53 $NaReO_4$ Na_2SO_4 H_2O	0.4 0.4 20	326.06 273.19 142.04	0.1304 0.1093 2.8408	0.1308 g 0.1094 g 2.8415 g 20 mL	RT	24
BE03_25C	SLUG-53 $NaReO_4$ Na_2SO_4 H_2O	0.4 0.4 80	326.06 273.19 142.04	0.1304 0.1093 11.36	0.1305 g 0.1096 g 11.3657 g 50 mL	RT	24
BE03_25C	SLUG-53 $NaReO_4$ Na_2SO_4 H_2O	0.4 0.4 80	326.06 273.19 142.04	0.1304 0.1093 11.36	0.1313 g 0.1090 g 11.3686 g 10 mL	RT	24
BE03_26A	$AgNO_3$ 2,4'-bipy MilliQ H_2O	20 5	169.87 156.19	3.3749 0.7809	3.3758 g 0.7814 g 50 mL	RT	1
BE03_26B	$AgNO_3$	10	169.87	1.6987	1.7001 g	RT	1

	2,4'-bipy	2.5	156.19	0.3920	0.3911 g		
	MilliQ H_2O				10 mL		
BE03_26C	$AgNO_3$	10	169.87	1.6987	1.6972 g	RT	1
	2,4'-bipy	2.5	156.19	0.3920	0.3935 g		
	MilliQ H_2O				10 mL		
BE03_28A	$AgNO_3$	4	169.87	0.6795	0.6798 g	145	24
	2,4'-bipy	1	156.19	0.1562	0.1577 g		
	MilliQ H_2O				10 mL		
BE03_28B	$AgNO_3$	4	169.87	0.6795	0.6797 g	145	24
	2,4'-bipy	1	156.19	0.1562	0.1567 g		
	MilliQ H_2O				10 mL		
BE03_28C	$AgNO_3$	4	169.87	0.6795	0.6793 g	145	24
	2,4'-bipy	1	156.19	0.1562	0.1574 g		
	MilliQ H_2O				10 mL		
BE03_28D	$AgNO_3$	4	169.87	0.6795	0.6794 g	145	24
	2,4'-bipy	1	156.19	0.1562	0.1576 g		
	MilliQ H_2O				10 mL		
BE03_28E	$AgNO_3$	4	169.87	0.6795	0.6792 g	145	24
	2,4'-bipy	1	156.19	0.1562	0.1577 g		
	MilliQ H_2O				10 mL		
BE03_33A	$AgNO_3$	4	169.87	0.6795	0.6716 g	145	24
	2,4'-bipy	1	156.19	0.1562	0.1574 g		
	MilliQ H_2O				10 mL		
BE03_33B	$AgNO_3$	4	169.87	0.6795	0.6753 g	145	24
	2,4'-bipy	1	156.19	0.1562	0.1567 g		
	MilliQ H_2O				10 mL		
BE03_33C	$AgNO_3$	4	169.87	0.6795	0.6720 g	145	24
	2,4'-bipy	1	156.19	0.1562	0.1571 g		
	MilliQ H_2O				10 mL		
BE03_33D	$AgNO_3$	4	169.87	0.6795	0.6793 g	145	24
	2,4'-bipy	1	156.19	0.1562	0.1569 g		
	MilliQ H_2O				10 mL		
BE03_36A	$AgNO_3$	4	169.87	0.6795	0.6768 g	145	24
	2,4'-bipy	1	156.19	0.1562	0.1565 g		
	MilliQ H_2O				10 mL		
BE03_36B	$AgNO_3$	4	169.87	0.6795	0.6763 g	145	24
	2,4'-bipy	1	156.19	0.1562	0.1569 g		
	MilliQ H_2O				10 mL		
BE03_36C	$AgNO_3$	4	169.87	0.6795	0.6782 g	145	24
	2,4'-bipy	1	156.19	0.1562	0.1569 g		
	MilliQ H_2O				10 mL		
BE03_37	$AgNO_3$	4	169.87	0.6795	0.6708 g	145	24
	2,4'-bipy	1	156.19	0.1562	0.1523 g		
	MilliQ H_2O				10 mL		
TV01_11A	$AgNO_3$	1	169.87	0.1699	0.1687 g	RT	24
	2,4'-bipy	1	156.19	0.1562	0.1570 g		
	MilliQ H_2O				10 mL		
TV01_11B	$AgNO_3$	1	169.87	0.1699	0.1710 g	150	72
	2,4'-bipy	1	156.19	0.1562	0.1571 g		
	MilliQ H_2O				10 mL		
TV01_11C	$AgNO_3$	1	169.87	0.1699	0.1700 g	120	1
	2,4'-bipy	1	156.19	0.1562	0.1577 g		
	MilliQ H_2O				10 mL		

TV01_12D	$AgNO_3$ 2,4'-bipy MilliQ H_2O	1 1	169.87 156.19	0.1699 0.1562	0.1708 g 0.1573 g 10 mL	120 Slow cooling 0.1 °C/min	24
TV01_13A	$AgNO_3$ 2,4'-bipy MilliQ H_2O	1 1	169.87 156.19	0.1699 0.1562	0.170 g 0.156 g 10 mL	150 Slow cooling 0.1 °C/min	120
TV01_13B	2,4'-bipy MilliQ H_2O	1	156.19	0.1562	0.155 g 10 mL	150 Slow cooling 0.1 °C/min	120
TV01_14	$AgNO_3$ 2,4'-bipy MilliQ H_2O	1 1	169.87 156.19	0.1669 0.1562	0.1704 g 0.1572 g 10 mL	150	24
TV01_15A	$AgC_2H_3O_2$ 2,4'-bipy MilliQ H_2O	1 1	166.91 156.19	0.1669 0.1562	0.1672 g 0.1567 g 10 mL	150	120
TV01_15B	$Zn(NO_3)_2.H_2O$ 2,4'-bipy MilliQ H_2O	1 1	297.48 156.19	0.2975 0.1562	0.2999 g 0.1567 g 10 mL	150	120
TV01_15C	$Cu(NO_3)_2.2.5H_2O$ 2,4'-bipy MilliQ H_2O	1 1	232.59 156.19	0.2326 0.1562	0.2332 g 0.1565 g 10 mL	150	120
TV01_17A	$Cu(NO_3)_2.2.5H_2O$ 2,4'-bipy MilliQ H_2O	1 1	232.59 156.19	0.2326 0.1562	0.2323 g 0.1568 g 10 mL	RT	120
TV01_17B	$Cu(NO_3)_2.2.5H_2O$ 2,4'-bipy MilliQ H_2O	1 1	232.59 156.19	0.2326 0.1562	0.2329 g 0.1573 g 10 mL	100	120
TV01_18C	$Cu(NO_3)_2.2.5H_2O$ 2,4'-bipy MilliQ H_2O	1 1	232.59 156.19	0.2326 0.1562	0.2324 g 0.1565 g 10 mL	70	1
TV01_19	$Cu(NO_3)_2.2.5H_2O$ 2,4'-bipy MilliQ H_2O	1 1	232.59 156.19	0.2326 0.1562	0.2324 g 0.1557 g 10 mL	100	168
TV01_20	$AgNO_3$ 2,4'-bipy MilliQ H_2O	1 1	169.87 156.19	0.1699 0.1562	0.1697 g 0.1562 g 10 mL	Cycling coondition	
TV01_21A	$AgNO_3$ 2,4'-bipy MilliQ H_2O Propanol	2 1	169.87 156.19	0.3397 0.1562	0.1687 g 0.1570 g 5 mL 5 mL	RT	24
TV01_21B	$AgNO_3$ 2,4'-bipy MilliQ H_2O DMSO	1 1	169.87 156.19	0.1699 0.1562	0.1687 g 0.1570 g 5 mL 5 mL	RT	24
TV01_21C	$AgNO_3$ 2,4'-bipy MilliQ H_2O	1 1	169.87 156.19	0.1699 0.1562	0.1687 g 0.1570 g 5 mL	RT	24

	Ethyl acetate				5 mL		
TV01_22A	$AgNO_3$ 2,4'-bipy MilliQ H_2O Acetonitrile	0.5 0.5	169.87 156.19	0.0849 0.0781	0.0858 g 0.0774g 5 mL 5 mL	Cycling condition	
TV01_22B	$AgNO_3$ 2,4'-bipy MilliQ H_2O Acetonitrile	0.1 0.1	169.87 156.19	0.0170 0.0156	0.0163 g 0.158 g 5 mL 5 mL	RT	24
TV01_23A	$AgNO_3$ 2,4'-bipy MilliQ H_2O Acetonitrile	0.5 0.5	169.87 156.19	0.0849 0.0781	0.1687 g 0.1570 g 9.5 mL 0.5 mL	RT	24
TV01_23B	$AgNO_3$ 2,4'-bipy MilliQ H_2O Acetonitrile	0.1 0.1	169.87 156.19	0.0170 0.0152	0.0175 g 0.0164 g 0.5 mL 0.5 mL	RT	24
TV01_24A	$AgNO_3$ 2,4'-bipy MilliQ H_2O	1 1	169.87 156.19	0.1699 0.1562	0.172 g 0.156 g 10 mL	150 Slow cooling 0.1 °C/min	120
TV01_24B	$AgNO_3$ 2,4'-bipy MilliQ H_2O	1 1	169.87 156.19	0.1699 0.1562	0.171 g 0.157 g 10 mL	150 Slow cooling 0.1 °C/min	120
TV01_24C	$AgNO_3$ 2,4'-bipy MilliQ H_2O	1 1	169.87 156.19	0.1699 0.1562	0.170 g 0.158 g 10 mL	150 Slow cooling 0.1 °C/min	120
TV01_25A	SLUG-53 $NaMnO_4$ H_2O	0.2 0.2	326.06 141.92	0.072 0.0316	0.0725 g 0.0313 g 10 mL	RT	24
TV01_25B	SLUG-53 K_2CrO_4 MilliQ H_2O	0.2 0.2	326.06 194.19	0.072 0.039	0.0725 g 0.0399 g 10 mL	RT	24